Behaviour of Ashes and Trace Substances During Chemical Looping Gasification of Biomass

Verhalten von Aschen und Spurenstoffen bei der Chemical-Looping-Vergasung von Biomasse

Von der Fakultät für Maschinenwesen der Rheinisch-Westfälischen Technischen Hochschule Aachen zur Erlangung des akademischen Grades eines Doktors der Naturwissenschaften genehmigte Dissertation

vorgelegt von

Florian André Lebendig

Berichter: Priv.-Doz. Dr. rer. nat. Michael Müller
Univ.-Prof. Dr.-Ing. habil. Manfred Christian Wirsum

Tag der mündlichen Prüfung: 20. Februar 2024

Diese Dissertation ist auf den Internetseiten der Universitätsbibliothek online verfügbar.

Fais de ta vie un rêve,
et d'un rêve, une réalité.
(Antoine de Saint-Exupéry)

List of Publications

Parts of this thesis have been published:

Journals

Lebendig, F.; Funcia, I.; Pérez-Vega, R.; Müller, M. Investigations on the Effect of Pre-Treatment of Wheat Straw on Ash-Related Issues in Chemical Looping Gasification (CLG) in Comparison with Woody Biomass. *Energies* **2022**, *15*, 3422.

Lebendig, F.; Müller, M. Effect of pre-treatment of herbaceous feedstocks on behaviour of inorganic constituents under chemical looping gasification (CLG) conditions. *Green Chemistry* **2022**, *24*, 9643–9658.

Lebendig, F.; Schmid, D.; Karlström, O.; Yrjas, P.; Müller, M. Influence of pre-treatment of straw biomass and additives on the release of nitrogen species during combustion and gasification. *Renewable and Sustainable Energy Reviews* **2024**, *189*, 114033.

Lebendig, F.; Müller, M. Laboratory Investigations on the Influence of Biofuel Blending on Inorganic Constituent Behavior under Fluidized-Bed Gasifier Conditions. Submitted to *Energy & Fuels* and under review.

Conferences

Lebendig, F.; Müller, M. Influence of pre-treatment of herbaceous biomass feedstocks on ash-related issues in chemical looping gasification, 29th European Biomass Conference and Exhibition (EUBCE), Marseille, 2021.

Lebendig, F.; Müller, Untersuchung von vorbehandelten halmgutartigen Biomassen in Bezug auf aschebedingte Probleme unter Vergasungsbedingungen, 30. Deutscher Flammentag, Hannover, 2021.

Lebendig, F., Influence of pre-treatment and the use of additives of herbaceous biomass feedstocks on the release of nitrogen species during combustion and gasification, 10th Liekkipäivä / Finnish Flame Days, Tampere, 2023.

Abstract

Regarding the discussion of the influence of carbon dioxide emissions on global warming, the development of sustainable, cleaner and more power-efficient technologies has become increasingly important in the last decade. Biomass gasification is a key technology for the energy transition towards transformation of the global energy sector from fossil-based to zero-carbon. During the gasification process, gaseous fuel compounds (synthesis gas) are produced, which can subsequently be converted to valuable synthesis products, such as transportation fuels, polymers or other essential chemicals, following different reaction paths. Chemical looping gasification (CLG) is a highly promising technology recognized for converting biomass into synthetic fuels. In this process, oxygen for gasification is provided through an oxygen carrier. During gasification itself, various issues related to ash produced from biomass can cause operational problems. A fundamental knowledge of the behaviour of inorganic, biomass-derived constituents is required in order to understand their impact on the chemical looping gasification process such as high-temperature corrosion, bed agglomeration, fouling and slagging, oxygen carrier poisoning or pollutant emissions.

This study offers a comprehensive overview of various biomass pre-processing methods, including thermal treatment (torrefaction), water-leaching, blending with Ca-based additives, and incorporation of different woody feedstocks. The aim of this work is to elaborate knowledge of the herbaceous/woody feedstocks. First, the release of K, S, P, Cl, and N species from high-temperature (950 °C) biomass gasification is investigated. Hence, in-situ analysis of the product gas was conducted using molecular beam mass spectrometry to gain insight into the fate of volatile species. The ash melting behaviour of fuel ashes was investigated by hot stage microscopy. XRD analysis was applied to clarify mineral phases formation. Additionally, thermodynamic equilibrium calculations were conducted to predict the gas phase chemistry, i.e. the condensation behaviour of inorganic compounds or the mineral compositions being formed under gasification conditions. The outcomes of both experimental investigations and thermodynamic predictions were compared.

Kurzfassung

Der Einfluss von CO_2-Emissionen auf die globale Erwärmung hat die Entwicklung nachhaltiger und energieeffizienter Technologien in den vergangenen Jahren beschleunigt. Biomassevergasung ist eine mögliche Option für die Energiewende, um den globalen Energiesektor von fossilen Brennstoffen auf kohlenstofffreie Energie umzustellen. Bei der Vergasung werden gasförmige Bestandteile (Synthesegas) erzeugt, welche anschließend über verschiedene Reaktionswege in Syntheseprodukte wie Kraftstoffe, Polymere oder andere Chemikalien umgewandelt werden können. Die Chemical Looping Vergasung (CLG) ist eine äußerst vielversprechende Technologie, die zur Umwandlung von Biomasse in synthetische Kraftstoffe eingesetzt wird. In diesem Prozess wird Sauerstoff für die Vergasung durch einen Sauerstoffträger bereitgestellt. Bei der Vergasung selbst entstehen jedoch etliche ascheinduzierte Probleme, welche den Prozess erheblich einschränken können. Daher sind grundlegende Kenntnisse über verschiedene Biomasseaschen unabdingbar, um ihre Auswirkungen auf den thermochemischen Prozess beurteilen zu können, beispielsweise Hochtemperaturkorrosion, Wirbelschichtagglomeration, Verschmutzung und Verschlackung, Vergiftung der Sauerstoffträger oder Schadstoffemissionen.

In dieser Arbeit wird eine Betrachtung verschiedener Vorbehandlungsmethoden, u.a. thermische Behandlung (Torrefizierung), Waschen, Ca-Additivierung oder Herstellung von Brennstoffmischungen erarbeitet. Das Ziel dieser Promotionsschrift besteht darin, fundamentale Kenntnisse über biomassebasierten Brennstoffen zu erarbeiten. Dazu wurde deren Zusammenhang in Bezug auf das Freisetzungsverhalten, hauptsächlich von K-, S-, P-, Cl- und N-Spezies während der Hochtemperaturvergasung (950 °C) aufgeklärt. In-situ-Analysen des erzeugten Produktgases wurden mittels Molekularstrahl-Massenspektrometrie durchgeführt, um Freisetzungen flüchtiger Spezies zu detaillieren. Das Ascheschmelzverhalten von Brennstoffaschen wurde mittels Erhitzungsmikroskopie untersucht. XRD-Analysen wurden zur Klärung von Phasenbildungen vollzogen. Zusätzlich wurden thermodynamische Berechnungen durchgeführt, um die Gasphasenchemie, u.a. das Kondensationsverhalten anorganischer Verbindungen, sowie entstehende Mineralphasen abzuschätzen. Die Resultate der experimentellen Untersuchungen wurden mit den numerischen Gleichgewichtsberechnungen verglichen.

Symbols and Index of Abbreviations

Symbols or Greek letters including units

λ	Air-fuel ratio	Dimensionless unit
Δ	Difference or change	Depending on expression
ν	Frequency	Hz
h	Planck's constant	$6.626\,070\,15 \times 10^{-34}\,\mathrm{J\,Hz^{-1}}$
u	Unified atomic mass unit or dalton	$1.660\,539\,068\,92 \times 10^{-27}\,\mathrm{kg}$

Chemical or physical formula and expressions

HHV	Higher heating value	$\mathrm{MJ\,kg^{-1}}$
m/z	Mass-to-charge ratio	$\mathrm{kg\,C^{-1}}$
NL	Normal litre	$0.001\,\mathrm{m^3}$
p_{O_2}	Oxgen partial pressure	bar or atm
ppmv	Parts per million by volume	1 ppmv ≡ 0.0001 vol%
T_G	Torrefaction grade or degree	%
T_{iso}	Isothermal temperature	°C
T_{max}	Maximum temperature	°C
vol%	Volume fraction	%
wt%	Mass fraction	%

Abbreviations and acronyms

+A	Sample blended with additive (Limestone or rather $CaCO_3$)
ar	Weight percentage or mass fraction from the material in its original form
ÅAU	Åbo Akademi University (Finland)
BtL	Biomass-to-Liquid
CENER	Centro Nacional de Energías Renovables (Spain)
CFD	Computational Fluid Dynamics
Chalmers	Chalmers University of Technology (Sweden)
CLARA	**C**hemical **L**ooping g**A**sification fo**R** sustain**A**ble production of biofuels
CLG	Chemical Looping Gasification
d.a.f.	Weight percentage or mass fraction from the dry and ash free material
d.b.	Dry basis
DFT	Density Functional Theory
FBR	Fluidised-Bed Reactor (Gasifier/Boiler)
FT	Fischer-Tropsch
FZJ	Forschungszentrum Jülich GmbH (Germany)
HSM	Hot Stage Microscopy
ICSD	Inorganic Crystal Structure Database
IR	Infrared
IWP	Industrial wood pellets
LUT	Lappeenranta University of Technology (Finland)
MBMS	Molecular Beam Mass Spectrometry
MW_{th}	Megawatts thermal

Abbreviations and acronyms

OB	Oak bark
PB	Pine bark
PFR	Pine forest residues
PV	Photovoltaic system
SPR	Single-Particle Reactor
Syngas	Synthesis gas
To	Torrefied sample
To-WL	i) Torrefied, then ii) water-leached sample (post-washed)
WL	Water-leached sample
WL-To	i) Water-leached, then ii) torrefied sample (pre-washed)
XRD	X-Ray Diffraction

Contents

Symbols and Index of Abbreviations i

List of Figures ix

List of Tables xv

1 Introduction 1

1.1 Motivation and challenges 1

1.2 Scope of the thesis 4

2 Fundamentals and Background 7

2.1 Biomass feedstocks for renewable fuel production 7

2.1.1 Nature of biomass 7

2.1.2 Biomass upgrading techniques for efficient gasification application 10

2.2 Gasification for sustainable biofuel production 14

2.2.1 Biomass-to-liquid process 14

2.2.2 Biomass gasification and gasifier reactor types 15

2.3 Ash-forming matter and ash-related problems in fluidised-bed gasification 23

2.3.1 High-temperature corrosion 23

2.3.2 Agglomeration 26

2.3.3 Fouling and slagging 30

2.3.4 Pollutant emissions: NO_x and its precursors, NH_3 and HCN . . . 32

2.3.5 Poisoning of oxygen carriers (in CLG applications) 33

3 Materials and Methods 35

3.1 Sample materials and pre-treatment 35

3.2 Preparation of fuel ashes for HSM and XRD investigations 41

3.3 Chemical characterisation and methods 45

3.3.1 Feedstock characterisation 45

3.3.2 Fundamentals of molecular beam mass spectrometry (MBMS) for hot gas analysis . . . 46
3.3.3 Analysis of hot gases using MBMS (batch-type experiments) . . . 48
3.3.4 Laboratory-scale fluidised-bed reactor for continuous release experiments . . . 52
3.3.5 Determination of N-species . . . 54
3.3.6 Hot stage microscopy (HSM) for ash fusion testing . . . 57
3.3.7 X-ray powder diffraction (XRD) . . . 60
3.4 Numerical thermodynamic equilibrium predictions . . . 63

4 Results and Discussions 67
4.1 Comparison of industrially pre-treated wheat straw with woody biomass 67
4.1.1 Chemical characterisation of fuels . . . 67
4.1.2 Analysis of hot gases using MBMS (batch-type experiments) . . . 69
4.1.3 Continuous release experiments conducted in a laboratory-scale fluidised-bed reactor . . . 74
4.1.4 Ash fusion testing and behaviour of ashes . . . 76
4.1.5 Thermodynamic prediction of gas phase chemistry . . . 82
4.1.6 Thermodynamic prediction of mineral phases formation . . . 88
4.1.7 Discussion on the impact on fluidised-bed gasification and CLG . 94
4.2 Influence of pre-treatment measures on behaviour of inorganic constituents 98
4.2.1 Chemical characterisation of fuels . . . 98
4.2.2 Analysis of hot gases using MBMS (batch-type experiments) . . . 102
4.2.3 Influence of pre-treatment measures on the release of N-species . . 106
4.2.4 Ash fusion testing and behaviour of ashes . . . 115
4.2.5 Thermodynamic prediction of gas phase chemistry . . . 121
4.2.6 Thermodynamic prediction of mineral phases formation . . . 124
4.2.7 Discussion on the impact on fluidised-bed gasification and CLG . 129
4.3 Influence of additives and blending on behaviour of inorganic constituents 133
4.3.1 Chemical characterisation of woody blend components . . . 133
4.3.2 Analysis of hot gases using MBMS (batch-type experiments) . . . 137
4.3.3 Ash fusion testing and behaviour of ashes . . . 146
4.3.4 Thermodynamic prediction of gas phase chemistry . . . 148
4.3.5 Thermodynamic prediction of mineral phases formation . . . 155
4.3.6 Discussion on the impact on fluidised-bed gasification and CLG . 162

5 Summary and Outlook **167**

Bibliography **173**

List of Figures

1.1 Shares of primary energy supply in 2015 and 2050 2

2.1 The key components and structure of lignocellulosic biomass begin with a plant cell 9
2.2 Electric conductivities of the extraction liquid pool (empty fruit bunch) . 12
2.3 Full thermochemical BtL route: from raw biomass to liquid fuel, summarising the most important steps 14
2.4 Schematic of CLG process 17
2.5 Schematic of a circulating fluidised-bed gasifier for syngas production . . 20
2.6 Schematic of an entrained flow gasifier for syngas production 21
2.7 Schematic of an updraft fixed bed gasifier for syngas production 22
2.8 Schematic mechanism of high-temperature corrosion 24
2.9 Schematic of agglomerate formation at the cold nozzles of the fluidised-bed diffusers 26
2.10 Calculated K_2O–SiO_2 binary phase diagram with experimentally determined data 27
2.11 Ternary phase diagram of the CaO–K_2O–SiO_2 system, presenting the high SiO_2 corner 28
2.12 Schematic of alkali vapour condensation on heat exchanger surfaces, illustrating deposit formation over time 30

3.1 Comparison of thermally treated colza straw 37
3.2 Overview of the water-leaching treatment process employed in this study 39
3.3 Sketch of the test setup for sample ash preparation in a gasification-like or reducing atmosphere 41
3.4 Example of sample ash prepared in a gasification-like atmosphere and subsequently reduced in a mixture of 4 % H_2 in argon 43
3.5 Cooling temperature plotted against water mass flow 44
3.6 Schematic setup of the molecular beam mass spectrometer 47

3.7 Schematic of the technical setup of the flow channel reactor furnace . . . 49
3.8 Representative intensity-time profiles of recorded species from the raw wheat straw data . . . 51
3.9 Schematic of the laboratory-scale fluidised-bed reactor used in this work 52
3.10 Lab-scale fluidised-bed reactor made of quartz glass . . . 53
3.11 Schematic of the single-particle reactor used in the experiments . . . 54
3.12 Overview of the working station, which comprises an electrically heated SPR unit and photometers for monitoring output gases . . . 55
3.13 Technical setup of the hot stage microscope, and a photograph of the working station . . . 57
3.14 Ash-based sample pellet for ash fusion testing by HSM . . . 58
3.15 Characteristic ash transformation points, which are typically observed at various temperature levels . . . 59
3.16 Schematic sketch of any crystal atomic plane, illustrating Bragg's reflection condition . . . 61
3.17 Schematic overview of the thermodynamic model conceptualised in this work, divided into three different main categories . . . 66

4.1 Illustration of the dominant species found in the CLARA project's samples, which are commonly associated with ash-related problems . . . 68
4.2 The mass spectra of $^{64}SO_2^+$ displays intensity profiles for the source material, as well as for torrefied and torrefied/post-washed wheat straw . . . 69
4.3 Averaged normalised peak areas of detected species released during devolatilization phase . . . 70
4.4 Averaged normalised peak areas of detected species released during the ash/char reaction phase . . . 71
4.5 Comparison of the normalised volatile peak area for KCl, HCl, and sulphur-containing species (H_2S, SO_2) in relation to the calcium concentration in (pre-treated) fuel samples or the molar ratio of Ca/K . . . 73
4.6 Mass spectra of primary gaseous species (He^+, CO^+, H_2O^+, CO_2^+, $^{17}O_2^{++}$ or $^{17}OH^+$, and $^{32}O_2^+$) . . . 74
4.7 Signal intensity versus gasification time for selected mass spectra of raw wheat straw . . . 75
4.8 Signal intensity of $^{34}O_2^+$ isotope versus gasification time for torrefied/water-leached wheat straw plus 2 wt% $CaCO_3$ . . . 76

4.9 Height profile of ashes plotted against temperature (HSM) 77
4.10 Photos (HSM) of straw and wood ash samples during the ash fusion test 78
4.11 XRD spectra of prepared sample ashes 79
4.12 XRD spectra of ilmenite and ash of treated (torrefied and post-washed) wheat straw with ilmenite 81
4.13 Condensation of alkali chlorides, primarily KCl, under both pyrolysis and gasification conditions 83
4.14 Condensation of carbonate, sulphide and slag-mixtures under both pyrolysis and gasification conditions 84
4.15 Predicted partial pressure of oxygen carrier constituents in contact with upgraded wheat straw samples, IWP, and PFR under isothermal gasification conditions (950 °C 87
4.16 Calculated mineral proportions of raw wheat straw ash under gasification conditions 88
4.17 Calculated mineral proportions of the ash of IWP, PFR, and pre-treated or $CaCO_3$-blended wheat straw under gasification conditions 89
4.18 Comparison of the ash fusibility of the biofuel samples under gasification conditions at 950 °C 90
4.19 Ternary phase diagram of the SiO_2–CaO–K_2O system 91
4.20 Chemical analysis of pre-treated herbaceous feedstocks, with a special focus on species that are critical to understanding ash-related issues . . . 100
4.21 Chloride content in washing water after first and second wash cycles for untreated and torrefied materials 101
4.22 Ash yields for raw, torrefied, water-leached, torrefied and pre-washed, or post-washed straw samples 101
4.23 Averaged normalised peak areas of detected species released during devolatilization phase for raw and pre-treated wheat, barley, corn and colza straw 103
4.24 Averaged normalised peak areas of detected species released during the ash/char reaction phase 104
4.25 Comparison potassium release during devolatilization in relation to the molar ratio of Si/K for the (treated) herbaceous fuels 105
4.26 Release of NO during combustion, gasification-like conditions, and devolatilization of raw wheat straw at 950 °C 106

4.27 Distribution of volatile-N, char-N, and removed-N (estimated based on fuel-N content in raw wheat straw, the source material) 107
4.28 A schematic illustration of the fate of the nitrogen in a fuel 108
4.29 NO emission in $\mu g\,g^{-1}$ dry fuel subject to different atmospheric conditions at 950 °C 109
4.30 Conversion of fuel-N to NO at 950 °C 111
4.31 Conversion of volatile-N to NO, NH_3, and HCN during devolatilization in 100 vol% N_2 at 950 °C 113
4.32 Comparison of NO release in various atmospheres and NH_3/HCN formation from devolatilization experiments (100 vol%) at 950 °C 113
4.33 Molar HCN/NH_3 ratio plotted against fuel-N or molar H/N ratio 114
4.34 Conversion of volatile-N to NH_3 and HCN plotted against fuel-Ca (left) or fuel-K (right) concentration in the pre-treated wheat straw samples . . 115
4.35 Height profile of ashes of raw and pre-treated colza, corn, wheat, and barley straw plotted against temperature (HSM) 116
4.36 Photos (HSM) of colza straw ash during the ash fusion test 117
4.37 Condensation of alkali chlorides, primarily KCl, under gasification conditions 121
4.38 Condensation of carbonate, sulphide, and slag-mixtures under both pyrolysis and gasification conditions 122
4.39 Calculated mineral proportions of ashes of upgraded straw varieties under gasification 124
4.40 Comparison of the ash fusibility of the upgraded biofuels under gasification conditions 126
4.41 The predicted molten slag fraction, expressed as wt% (100 wt%), is plotted against the molar Si/(Ca+Mg) ratio of the ash from pre-processed herbaceous fuels 127
4.42 Ternary phase diagrams for the SiO_2–CaO–K_2O system 128
4.43 Chemical analysis (blending materials PB and OB), with an emphasis on species which are playing a crucial role in ash-related issues 135
4.44 Averaged normalised peak areas of detected species released during pyrolysis/devolatilization phase 138
4.45 Comparison of the normalised peak area of KCl and SO_2 released during pyrolysis phase (pre-treated barley blended with $CaCO_3$ and without $CaCO_3$) in relation to the Ca concentration in (treated) feedstock 139

4.46 Comparison of molar Si/Ca ratios and the release of H_2S and SO_2 during devolatilization for the blended fuel series and their corresponding non-blended reference materials 142
4.47 Molar Ca/K ratio as a function of HCl release during devolatilization for blended fuels 143
4.48 Averaged normalised peak areas of detected species released during the ash/char reaction phase 145
4.49 Height profile of ashes of pre-processed and blended herbaceous biofuels plotted against temperature (HSM) 146
4.50 Condensation of alkali chlorides, primarily KCl, under gasification conditions 150
4.51 Condensation of carbonate and slag-mixtures under both pyrolysis and gasification conditions 153
4.52 Ternary phase diagrams for the SiO_2–CaO–K_2O system 157
4.53 Calculated mineral compositions of the ashes from the upgraded straw blend varieties were determined under gasification conditions 158
4.54 Comparison of the ash fusibility of the investigated ashes of the sample blend ashes under gasification conditions 161

5.1 Schematic overview of novel fuel characterisation tools, outcomes, and impacts on fluidised-bed gasification and CLG systems 170

List of Tables

2.1 Comparison of the primary products generated by the main fuel constituents in combustion and gasification 16

3.1 Biomass feedstocks analysed in this study 36
3.2 Moisture, ash content, and torrefaction grade T_G of FZJ project fuels . . 38
3.3 Mineral composition of oxygen carriers 40
3.4 The gasification gas composition 42
3.5 General setup parameters: recipient, cathode, and optical characteristics for the MBMS 48
3.6 This table presents the m/z ratios of various inorganic species investigated using MBMS 50

4.1 Ultimate analysis of the pre-treated wheat straw samples and woody biofuels obtained from the CLARA project partners 68
4.2 Overview of the main mineral phases, stable under gasification conditions at 950 °C 93
4.3 Ultimate analysis of the pre-treated fuel samples (wheat, barley, colza and corn straw) 99
4.4 Overview of the mineral phases present in the ashes of (treated) biofuels, which were found to be stable under gasification-like conditions 120
4.5 Ultimate analysis of both blend components pine bark and oak bark . . . 134
4.6 Ultimate analysis of the blended fuel sample series 136

1 Introduction

1.1 Motivation and challenges

In the last years, the demand for renewable and climate-friendly energies has increased significantly. Under the Paris Agreement, the priority decision was to limit global warming below 2 °C and, if possible, below 1.5 °C [1]. Fossil energy sources (oil, natural gas, lignite and hard coal) and nuclear energy are to be gradually replaced by renewable energies. Fossil fuels currently account for approximately 86 % of the global primary energy demand, a percentage that has been gradually increasing since 2015 [2]. It is projected that CO_2 emissions will increase from 38 gigatons CO_2 per year in 2015 to 75 gigatons CO_2 per year by 2035. Renewable energies, unlike fossil fuels and uranium ore, do not deplete and can be continuously produced as needed in a carbon-neutral manner. Bioenergy, solar energy, wind energy, hydropower as well as geothermal energy have turned out to be particularly promising energy sources. As from 2017, a quarter of all electrical energy worldwide was produced from renewable energy sources, however, the transition is not fast enough [3]. According to a comprehensive study which has been performed by the Energy Watch Group and the LUT University in 2019 [4], it might be even possible that a 100 % renewable energy system is cheaper than the current global energy supply. According to the pie charts in Figure 1.1, the primary energy supply will be met by a diverse mix of renewable sources, with solar PV accounting for 69 %, followed by wind energy (18 %), biomass and waste (6 %), hydropower (3 %), and geothermal energy (2 %) by 2050. According to the study published by the Energy Watch Group and the LUT University [4], solar PV and wind energy will make up 96 % of total electricity, and approximately 88 % of the total energy supply. This synergy is expected to provide a balanced energy mix.

Biofuels originating from biomass should be considered as an important part in the regenerative energy sector, even if as a non-dominant part. One reason is that large land areas are needed, however, estimates of areas that could be devoted to biomass energy production might vary greatly [5]. It should be also noted that ethanol produced from biogenic residues will not make a major contribution to global demand for liquid

fuels, as there will be only a low energy return [5]. However, besides direct combustion, biomass can be converted through other process routes to generate sustainable energy, like gasification to produce hydrogen and/or carbon monoxide [6].

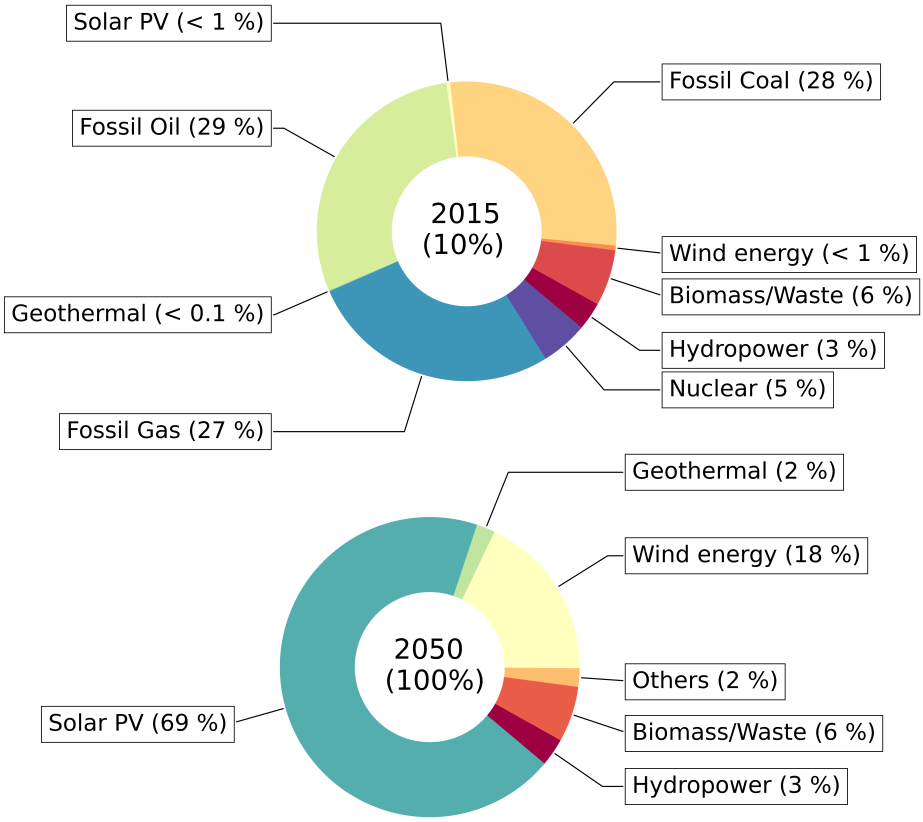

Figure 1.1: Shares of primary energy supply in 2015 (top pie chart) and 2050 (bottom pie chart). While the share of renewable energy was about 10 % in 2015, it is expected to be 100 % in 2050. Modified after Ram et al. [4].

One of the most widely used designs for biomass gasification is the fluidised-bed gasification process [7]. This technology offers several advantages, including uniform temperature distribution, high carbon conversion rates, and low tar production. Additionally, it provides the flexibility to select a wide range of biomass types, sizes, and feed rates. Furthermore, the fuel flexibility allows for the use of additives, such as those designed for in-situ pollutant removal (e.g., sulphur) or primary measures to enhance tar conversion rates [8]. However, fluidised-bed technology also has some drawbacks. When fuels with high levels of alkali metals and chlorine or high ash content are used, it can lead to changes in the hydrodynamics within the reactor. This can result in defluidisation and necessitate the shutdown of the power plant.

When combined with chemical looping technology (CLG), the fluidised-bed gasifier becomes even more efficient. This is achieved through the use of oxygen carriers, which enable thermochemical fuel conversion in the absence of air and allow for autothermal operation [9]. Chemical looping technology also offers several benefits, including lower CO_2 emissions and the production of high-quality syngas [10].

1.2 Scope of the thesis

The European research project CLARA (**C**hemical **L**ooping G**A**sification fo**R** Sustain**A**ble Production of Biofuels, Horizon 2020 framework programme, G.A. 817841), in which this study was conducted, suggests that the use of biogenic residues as a CO_2-neutral fuel in CLG should be encouraged. The overall goal of the CLARA project is to focus on the concept route, from biomass to biofuel, as outlined on the project's website [11]:

> "The overall aim of the CLARA project is to develop an efficient technology for the production of liquid fuels based on chemical looping gasification (CLG) of biogenic residues. The major objective of this project is thus to further develop and test CLG up to 1 MW_{th} scale in an industrially relevant environment. Furthermore, the project aims at developing and optimizing innovative technologies for biomass pre-treatment and syngas cleaning. The entire process chain will be demonstrated by pilot tests including hydrocracking of FT wax for drop-in fuel production. Finally, the process will be evaluated with respect to risks, economics, as well as its impact on environment and society."

Fluidised-bed systems are often versatile and can be used with various types of fuels. Therefore, CLG can be considered a suitable process for feedstocks with high levels of impurities, such as residues from agriculture and forestry [11]. In particular, herbaceous biomass such as straw is a promising lignocellulosic material due to its abundance and renewability. However, biogenic residues like straw have some undesirable properties that hinder their use in fluidised-bed gasification [12–16]. Specifically, they have low energy density, which increases transportation costs and poses difficulties in feeding, as well as low ash melting points that lead to agglomeration and slagging. Additionally, their high content of volatile inorganics promotes corrosion and fouling. As a result, handling, transporting, and storing these materials can be challenging, which limits their commercial use. Consequently, it is necessary to perform pre-treatment on the feedstock before the gasification step to overcome these issues.

Work Package 2 of the CLARA project, which this PhD thesis was primarily involved in, focused on investigating the influence of pre-treatment methods and additives on biofuel behaviour under gasification conditions. It is worth noting that whenever the term "gasification-like conditions" is used in this study, it refers to experiments performed under laboratory-scale conditions that are similar to those found in gasification processes.

In contrast, "gasification conditions" implies the use of thermodynamic modelling approaches or calculations of phase equilibria using FactSage™, which involves predictive methods under well-defined model conditions.

In this study, various biofuel upgrading methods were investigated and compared with the goal of using these pre-treated fuels for fluidised-bed gasification, with the aim of minimising the ash-related risks mentioned earlier. It is essential to note that some aspects of this work are specifically relevant to CLG applications, such as continuous release experiments with oxygen carriers (Chapter 4.1.3) or thermodynamic predictions of gas phase chemistry or mineral phases formation when herbaceous feedstocks are blended with oxygen carriers (Chapter 4.1.5 and 4.1.6). However, the majority of the findings presented in this work will be beneficial for both fluidised-bed gasification and fluidised-bed gasification combined with chemical looping technology.

Chapter 4.1 of this study compares industrially upgraded wheat straw with woody biomass, samples provided by CLARA project partners. In contrast, Chapters 4.2 and 4.3 delve into the pre-treatment methods and additive blending techniques used for herbaceous feedstocks, which are closely related to the CLARA project's approaches. In Chapters 4.2 and 4.3, the author explores their own ideas to increase and broaden the sample variation and results, ultimately aiming to provide a comprehensive overview and enhance comparability. A summary of the selected fuels and a description of the upgrading methods can be found in Chapter 3.1.

In summary, the challenges associated with ash-related issues in biomass gasification systems are similar to those encountered in combustion systems [17]. However, the behaviour of new biomass fuels under gasification conditions is not yet fully understood. Therefore, it is essential to conduct a comprehensive fuel characterisation that focuses on fuel properties relevant to gasification. This study examines the ash-related problems that arise from particle and nitrogen-related pollutant emissions, high-temperature corrosion, deposit formation, ash melting on grates, bed agglomeration in fluidised-bed systems, and SO_2 and HCl emissions. Unfortunately, traditional "state-of-the-art" fuel characterisation methods are insufficient to adequately address these issues. As a result, advanced investigative strategies are necessary for detailed evaluations. The discussion of these points and suggested future research directions can be found in the final chapter of this work, "Summary and Outlook" (see Chapter 5).

2 Fundamentals and Background

2.1 Biomass feedstocks for renewable fuel production

The following chapter provides a concise introduction to the chemical properties and characteristics of biomass, along with the basics of biomass pre-processing for industrial (chemical looping) gasification applications.

2.1.1 Nature of biomass

Biomass, typically considered as a renewable organic natural resource, belongs to the category of carbon-based renewable fuels, which can be utilised directly or through primary processing [18]. According to the American Society for Testing and Materials (ASTM International) [19], biomass has been defined to be "any material, excluding fossil fuel, which was a living organism that can be used as a fuel either directly or after a conversion process". Simplified it can be said that photosynthesis creates biomass in the form of cell wall polymers (that is cellulose, hemicellulose and lignin), which can be converted to renewable and clean energy [18]. There are a variety of possible ways given, ranging from simple burning to complex bioconversion processes for accessing the energy stored in the above-mentioned polymers [20]. This implies that biomass is generated from available atmospheric CO_2, water and sunlight through biological photosynthesis. Equation 2.1 describes the simplified net equation of oxygenic photosynthesis, which can be physically understood as an intermediate storage process of solar energy.

$$6\,CO_2 + 6\,H_2O \xrightarrow{\text{Light } (h\nu)} C_6H_{12}O_6 + 6\,O_2 \tag{2.1}$$

There are different categories of processing technologies for biomass-derived feedstocks given. The most important ones may generally be classified into three categories: biochemical, thermochemical and physicochemical processing [21]. An important aspect, that should be considered, is the heating value of biomass, which describes the energy content and determines the design of a thermal conversion system [22, 23]. It is generally well-known that both, composition and heating value of biomass are significantly

different from that of coal [24]. The variations between the heating value as well as the chemical composition of biomass were also found to be greater than that of coal [24]. Technically, generations of biofuels can generally be divided into the two following classes:

i) **First-generation biofuels.** The so-called first-generation fuels lead to a fuel and food competition, as they are produced from crop materials such as palm oil, corn and sugarcane [25]. The first-generation fuels increase in turn the price of food grains and other allied products [26]. Consequently, the competition of fuel and food results in the exploration of alternative feedstocks for biofuels, i.e. lignocellulosic-based material [27].

ii) **Second-generation biofuels.** The second-generation biofuels are more promising as the former ones. Unlike the first generation-fuels, they do not lead to any fuel/food competition. These types of biofuels are based on lignocellulosic feedstock. Lignocellulosic feedstocks are understood to be the stems as well as leaves of the above-ground plant body [27]. Some biofuel crops such as switchgras, eucalyptus or miscanthus are described to be adapted to poor soils and marginal agricultural land, hence reducing land-use competition for food crops [28]. Moreover, agricultural and industrial waste, which are unsuitable plant organs for human consumption, are promising sources of lignocellulosic materials. Different straw varieties such as wheat, barley, corn, soya or rice are the main sources of agricultural waste that can be suitable for biofuel production.

Figure 2.1 displays the structure and main components of lignocellulosic biomass, which is mainly composed of the three polymers: lignin, cellulose and hemicellulose together with small amounts of other components such as minerals, acetyl groups and phenolic substituents [29].

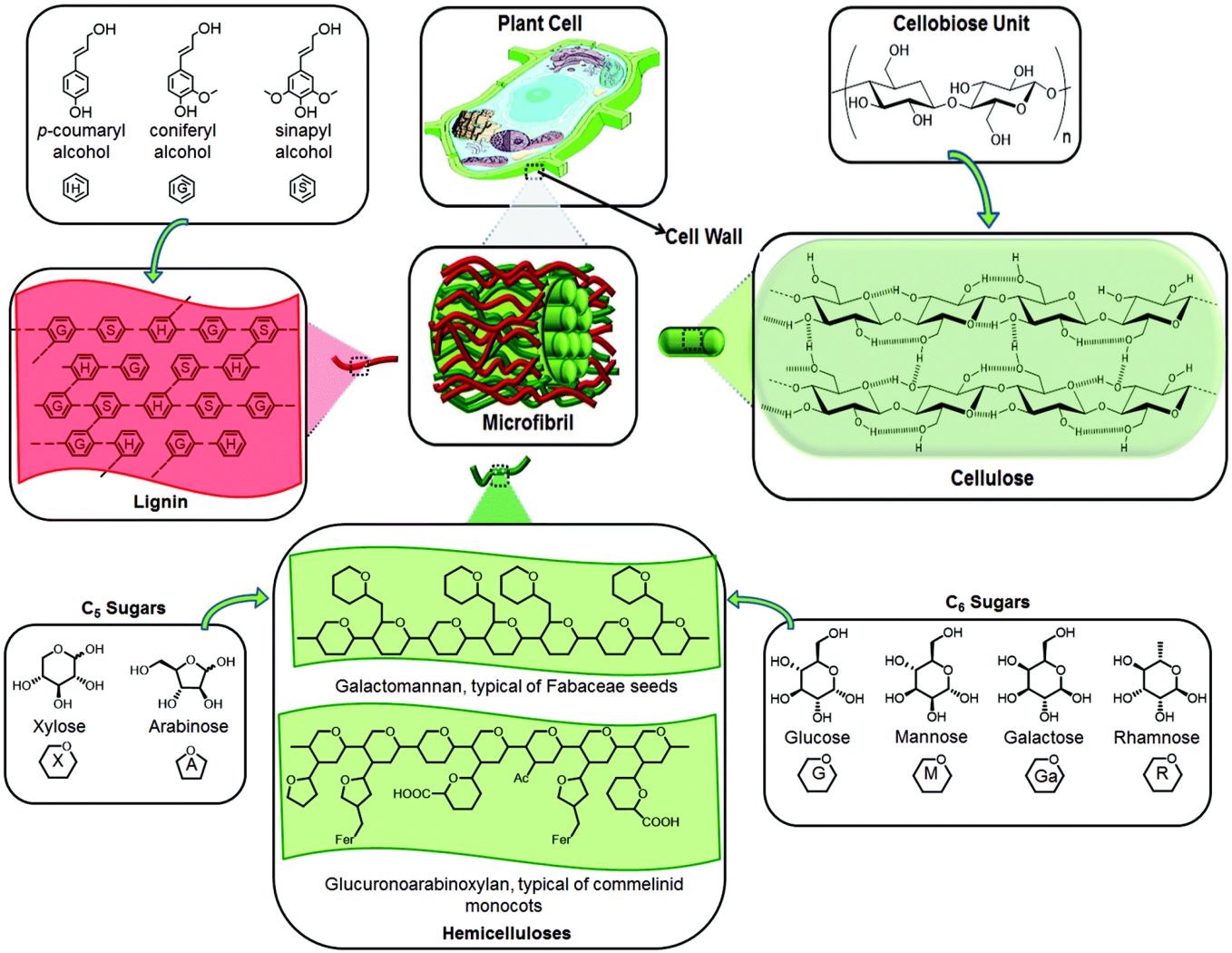

Figure 2.1: The key components and structure of lignocellulosic biomass begin with a plant cell. "Gl" represents glucuronic acid and "Fer" represents esterification with ferulic acid, which is characteristic of xylans in commelinid monocots [30]. Adapted and modified after Isikgor et al. [29].

The aforementioned polymers are usually organised into complex, non-uniform and three-dimensional structures, depending on the lignocellulosic biomass type (microfibril structure, Fig. 2.1). It is known that lignocellulose has evolved to resist degradation. The robustness of lignocellulose itself stems from the crystallinity of cellulose, the encapsulation of cellulose by the lignin–hemicellulose matrix and the hydrophobicity of lignin [31–33]. Lignocellulosic biomass is mainly based on cellulose. Approximately half of the organic carbon in the biosphere is present in the form of cellulose, which in turn means that the conversion of cellulose into fuels and valuable chemicals has a paramount importance [34–36]. The second most abundant polymer is hemicellulose, which is composed of several heteropolymers. Hemicellulose is mainly responsible for providing structural strength by linking cellulose fibres into microfibrils and cross-linking with lignin (as can be seen in Fig. 2.1). Lignin functions as the cellular glue which provides stiffness to the cell wall of the plant and compressive strength to its tissue and the individual fibres as well [20].

2.1.2 Biomass upgrading techniques for efficient gasification application

The inherent characteristics or low quality of biomass, such as low energy density, high moisture content, irregular size and shape, low bulk density or relatively high alkali salts content are described to be the main reasons for its under exploitation [37]. Following this, the previously stated factors make biomass in its natural form difficult to use for the purpose of energy production. Biomass pre-treatment leads to chemical, physical and structural changes, which plays a crucial role in order to improve and solve ash-related issues during thermochemical conversions [37, 38].

There are many upgrading approaches which have been studied previously, and are still in development thus far [32]. Thermal treatment such as torrefaction is one leading method to produce bio-coal, resulting in the removal of unbound water, improving heating values, better ignition, and combustion properties [39]. Moreover, torrefaction has shown the potential ability to significantly reduce the chlorine content of raw biomass [40]. Using water as a solvent for leaching biomass has been recognized as a successful technique for the removal of problematic species like potassium, sodium, and chlorine [41–43]. This method serves to enhance the properties of biomass feedstock for high-temperature processes. The nature of biomass ash has a strong impact on the ash melting behaviour. The negative effect of low-temperature ash melting can be over-

come by adding calcium-based additives, that can better prevent sintering of biomass ash [44]. Most research is focused on analysing fuel properties by leaching or (dry and wet) torrefaction treatment [41, 45–47], however, there are only few studies on the combination of those methods plus using (Ca-based) additives. The major pre-processing methodologies are listed in the following:

Torrefaction

The torrefaction process consists of a thermal treatment of biomass in absence of oxygen, which converts biomass into a coal-like material. It can be considered as a mild form of pyrolysis carried out at a temperature range typically between 200 °C to 300 °C. Herbaceous biomass usually contains high quantities of chlorine, a part of which would be released to the gas phase during thermochemical conversion [48]. Generally, it is recognised that both, concentration and forms of Cl have a significant effect on the release and transformation of the alkali and alkali earth metals [49, 50]. Some part of Cl would release to the gas phase during torrefaction and organochlorine (C–Cl) compounds are formed, most as methyl chloride [40, 48]. The combustion of torrefied biomass proceeds preferable to raw biomass: torrefied fuels provide a higher calorific value as well as a lower moisture content. Despite the lower content of volatile components, torrefied biomass ignites faster than untreated raw material [51].

Water-leaching

Tukey [52] defined leaching as the removal of substances (inorganic and organic) from plants by aqueous solutions including rain, dew, mist, and fog. For thermochemical looping processes, proceeding at elevated gasification temperatures (generally >800 °C), many different problems such as ash fouling or environmental impacts can be reduced by systematic modification of fuel compositions. For most applications in terms of the chemical looping process, typically high content of inorganics (ash constituents) cause problems such as high-temperature corrosion or adverse ash melting behaviour and proceed accordingly slagging and agglomeration issues (Chapter 2.3). Particularly, alkali metal cations, such as potassium and sodium or the corresponding alkali salts KCl/NaCl, but also sulphates and carbonates are proven to be problematic species. Those species can be easily removed by leaching the feedstock with water due to their very good solubility. An in-depth study in 1996 [53] characterised the effect of aqueous extraction of inorganic constituents on straw ash fusibility. It was found that without

leaching, ash was observed to fuse between 900 °C and 1000 °C, however, no ash fusion was observed with well leached samples at temperatures up to 1600 °C.

Following those observations, this emphasises that leaching of biomass is one effective method, which is known to improve fuel properties or affect some physico-chemical properties of the formed leachates [54]. Insoluble inorganic components are not removed by water-leaching because they are bound differently, particularly the cations are mostly bound with active sites of lignin, cellulose, or hemicellulose, and in order to remove them, an acidic environment is required, e.g. HCl or HNO_3 [55, 56].

In a previous study performed by Meesters et al. [57], several tests were executed on oil palm empty fruit bunch and sugar cane field trash. Extraction experiments with empty fruit bunch and sugar cane trash have shown that potassium and chloride concentrations can be reduced by 80 % and 90 % respectively, after four consecutive extractions with fresh water, bringing Cl and K down or close to acceptable levels. The electric conductivity of the extraction liquid pool (empty fruit bunch) was constantly measured within an hour and the obtained results are displayed in Figure 2.2.

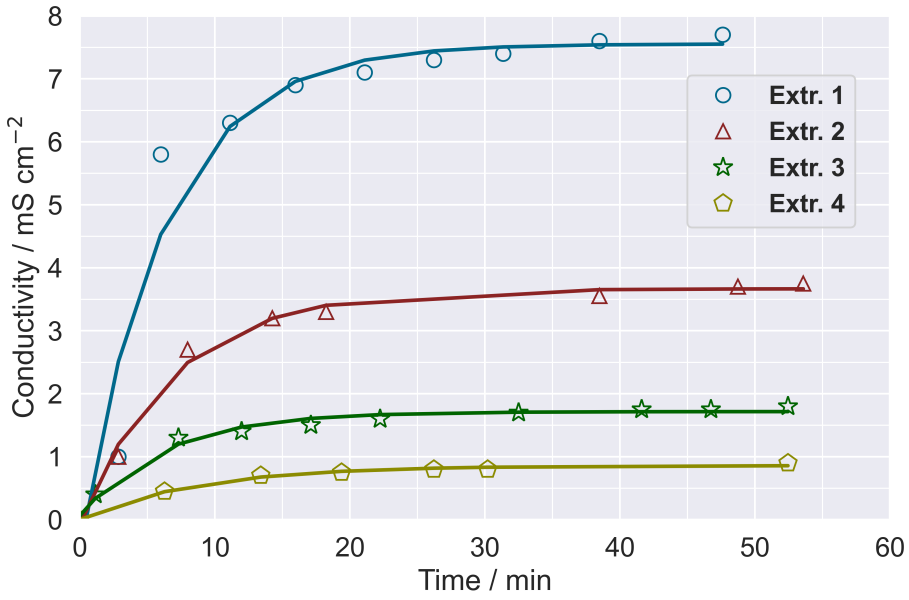

Figure 2.2: Electric conductivities of the extraction liquid pool (empty fruit bunch). Adapted and modified after Meesters et al. [57].

The extraction experiments with empty fruit bunch and trash have shown that the conductivity of the extracted fluid is reduced by almost 90 % in four consecutive extraction steps with fresh water, and the equilibrium was presumably achieved after 30 min.

Co-blending or additives

Apart from water-leaching, co-blending or additive applications are supposed to be universal approaches for increasing of biomass ash fusion temperature, thereby reducing problems during gasification of biomass feedstocks [58, 59]. Regarding the ash melting behaviour, both Ca and Mg are known to increase the ash fusion temperature noticeably, whereas Na and K decrease it [14, 60]. Beyond that, low melting alkali- and alumina silicates and chlorides can also significantly decrease the ash melting point [61]. Several studies have already previously demonstrated that the addition of oxides or inorganic salts to the initial biomass can raise its melting behaviour and change its thermal behaviour [62–65]. From the information given it follows that, based on the knowledge of the SiO_2–CaO–K_2O system, the fusibility tendencies can be predicted [66]. Blending can improve the quality of the feedstock by shifting the ratio of problematic constituents. Ray et al. [67] reported on a great promise to enable more cost-effective downstream processing regarding both blending and densification. An increased availability of feedstocks and shorter transportation costs, and lower total costs for the biorefinery feedstock, blending of multiple biomass types could increase the overall land base available for biomass production [68]. Previous studies reported on the opportunities to deliver a satisfactory feedstock for biorefineries at lower total costs, and thus improve the overall process economics by blending high quality feedstocks with marginal quality feedstocks [69–71].

Chapter 2.3.2 provides an in-depth explanation of how additives like calcium interact with other ash constituents such as potassium or silicon. It discusses ash-related problems such as agglomeration and addresses them in detail.

2.2 Gasification for sustainable biofuel production

This chapter delves into the biomass-to-liquid process, biomass gasification, and the underlying process engineering background, with a specific focus on gasifier reactor technologies.

2.2.1 Biomass-to-liquid process

Biofuels or synthetic hydrocarbon fuels can be produced via a thermochemical route, a multi-step process known as biomass-to-liquid (BtL) process [72]. The thermochemical route has been extensively applied for energy conversion worldwide, since it provides a higher conversion efficiency than that of conventional biochemical technologies [24]. The thermochemical route approves an appropriate destructive ability of organic compounds and requires a shorter reaction time [24]. In summary, thermochemical conversion technologies include mainly combustion, pyrolysis, gasification, liquefaction, and torrefaction [73, 74].

In 1996, the first biomass-to-liquid process was developed and mentioned by CHOREN industries in Freiberg, Germany, with an annual plant capacity of 15 000 t of liquid fuel per year [75]. Figure 2.3 exemplifies a simplified scheme of a full BtL chain process.

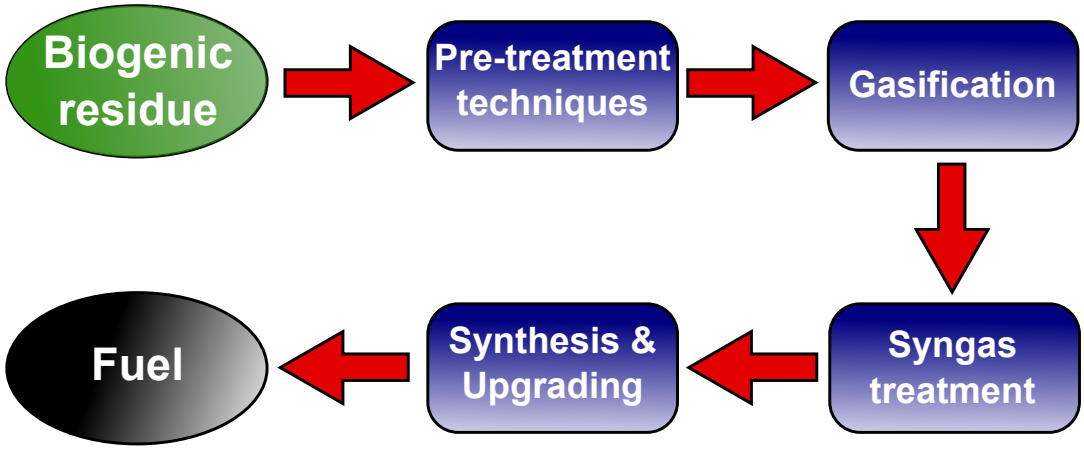

Figure 2.3: Full thermochemical BtL route: from raw biomass to liquid fuel, summarising the most important steps.

The multi-step process can be broadly described in general terms, comprising four fundamental steps, starting from the raw source material and ending with the liquid fuel. The steps are outlined below.

Biomass upgrading

Pre-treatment of biogenic residues is expected to contribute to a decline in ash-related issues, which will have a positive impact on both economical and ecological aspects. Biofuel upgrading can improve the gasification characteristics of biomass, thereby enhancing the utilisation of cheap domestic biomass resources.

Gasification

Gasification is the main process in which biomass fuel-based carbonaceous materials are converted into gases (Chapter 2.2.2). The reaction process typically occurs at elevated temperatures above 800 °C. Throughout the entire process, only small amounts of oxygen and/or steam are present in the reaction environment. Syngas is the resulting target gas mixture.

Syngas treatment

The raw syngas produced from the gasification process requires purification and conditioning to meet the specific requirements of the subsequent synthesis step, for example, Fischer-Tropsch (FT) synthesis. Typically, the purification process involves reducing inert species, such as CO_2, to minimise unnecessary gas flows and removing condensable gases, including tars and particles, as well as impurities (H_2S, COS, HCN, NH_3) to a concentration of less than 0.1 ppmv.

Synthesis and upgrading

In the final step, the treated syngas is converted to a liquid mixture comprising paraffinic hydrocarbons (C_nH_{2n+2}) through the exothermic FT synthesis:

$$n\,\mathrm{CO} + 2n{+}1\,\mathrm{H_2} \longrightarrow \mathrm{C}_n\mathrm{H}_{2n+2} + n\,\mathrm{H_2O} \tag{2.2}$$

2.2.2 Biomass gasification and gasifier reactor types

Gasification is a thermal process that converts biomass into a combustible gas, commonly referred to as syngas, which is composed of carbon monoxide, hydrogen, water, and methane. This process involves a chemical reaction that occurs through the partial oxidation of a fuel, typically in the absence of sufficient oxygen. The air-to-fuel ratio λ

plays a crucial role in determining whether the conditions are combustion- or gasification-like. When the air-to-fuel ratio is high (λ >1), the conditions are more conducive to combustion, while a lower air-to-fuel ratio ($\lambda \ll 1$) favours gasification. In comparison with combustion which uses an excess of oxidant, gasification typically uses one-fifth to one-third of the theoretical oxidant [76].

In contrast to combustion, gasification is a slower and endothermic reaction. Combustion, on the other hand, is a chemical reaction that takes place between a fuel and oxygen, in the presence of heat. It is a rapid and exothermic reaction that releases energy in the form of heat.

Table 2.1 provides a comparison of the products obtained from gasification and combustion, highlighting the significant change in reaction products that occurs when the air-to-fuel ratio is altered from combustion to gasification conditions.

Table 2.1: Comparison of the primary products generated by the main fuel constituents in combustion and gasification [77].

Species	**Combustion**	**Gasification**
Carbon	CO_2	CO
Hydrogen	H_2O	H_2
Nitrogen	NO, NO_2	HCN, NH_3 or N_2
Sulphur	SO_2 or SO_3	H_2S or COS
Water	H_2O	H_2

A primary distinction between combustion and gasification lies in the amount of heat released by the chemical reactions. In combustion, the chemical energy of the fuel is fully released as thermal energy, whereas in gasification, most of the fuel's chemical energy is not converted into heat [77].

A pioneering gasification method is chemical looping gasification (CLG), which enables the production of a high-calorific, nitrogen-free synthesis gas from solid hydrocarbon feedstocks without the need for a costly air separation unit [9]. The primary difference between regular gasification and CLG lies in the reactor design and the way the oxygen is introduced into the reaction. Figure 2.4 illustrates a conventional mechanism operation of CLG.

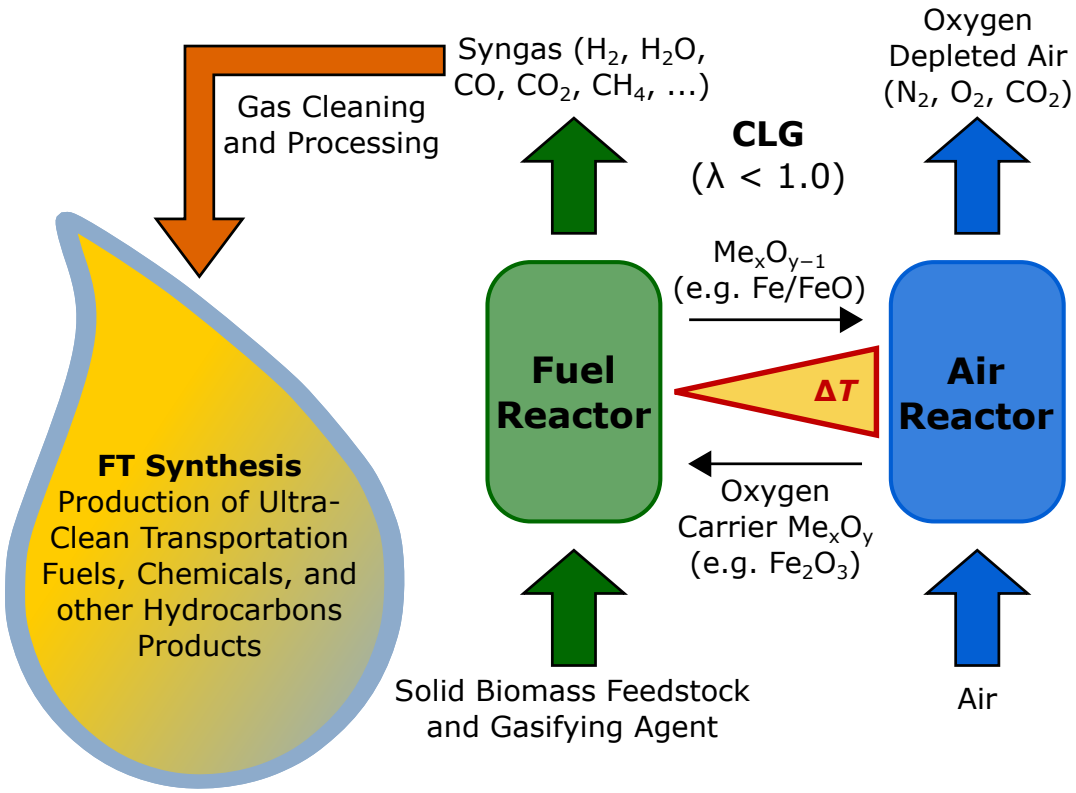

Figure 2.4: Schematic of CLG process. The reduced metal oxide Me_xO_{y-1} is circulated to the air reactor unit to be re-oxidised before a new cycle starts. The exothermic heat resulting from the metal reaction with oxygen provides endothermic energy ΔT needed for the fuel reactor. Modified after Nguyen et al. [10].

The reactor unit is comprised of two primary sections: the air reactor and the fuel reactor. Within the fuel reactor, the gasification and subsequent fuel conversion processes occur. A metal oxide, designated as Me_xO_y, serves as an oxygen carrier and is reduced to provide a specified amount of lattice oxygen for fuel conversion. Following reduction, the metal oxide is circulated back to the air reactor, where it is re-oxidised, thereby initiating a new cycle. The general redox reaction can be summarised as follows:

$$\text{Feedstock} + Me_xO_y \longrightarrow Me_xO_{y-1} + H_2 + CO + CO_2 + CH_4 + H_2O + \ldots \tag{2.3}$$

and

$$Me_xO_{y-1} + \frac{1}{2}O_2 \longrightarrow Me_xO_y \tag{2.4}$$

Equation 2.3 describes the reduction of the metal oxide and Equation 2.4 the re-oxidation of the reduced metal oxide in the air reactor.

The essential reactions of the gasification process are primarily endothermic, requiring energy for their occurrence. This energy is typically supplied by the oxidation of part of the biomass, either through an allothermal or autothermal process design [78]. In CLG, the heat generated in the air reactor can be transferred to the fuel reactor through oxygen carriers, enabling autothermal operation [9]. Below, the steps involved in the gasification process are briefly summarised in chronological order [78, 79].

Dehydration

Biomass typically contains a relatively high amount of moisture, depending on the type of feedstock material (i.e., either herbaceous or woody feedstocks). Any water content in the feedstock evaporates and leaves dry material. The water vapor may then enter into later chemical reactions.

Pyrolysis

Pyrolytic reactions occur when the feedstock is exposed to rising temperatures in the gasifier. Pyrolysis is understood as the thermal decomposition of biomass that occurs in the absence of oxygen, and volatile gases are released during this stage. This process involves particularly the breaking of weaker chemical bonds and devolatilization [80]. The resulting product is a molecular-weight char that will undergo gasification reactions in a subsequent stage.

Combustion

Some of the formed char, as well as the volatile products (e.g., tar vapours, hydrogen, or methane), will react with limited oxygen to form both CO_2 and CO. This reaction provides thermal energy in the form of heat, which is needed for subsequent gasification reactions.

Gasification

The most relevant stage is the gasification reaction, where CO_2 and steam react with the remaining char to produce the target molecules H_2 and CO, which serve as precursors for further synthesis.

Water-gas-shift reaction and methanation

Based on gasifier conditions, these separate reversible gas-phase reactions take place simultaneously. The water-gas shift reaction is a chemical process that involves the conversion of CO and H_2O into CO_2 and H_2:

$$CO + H_2O \rightleftharpoons CO_2 + H_2 \qquad \Delta H^0_{298} = -41.1\,\mathrm{kJ\,mol^{-1}}, \tag{2.5}$$

The following reactions describe the methanation of carbon monoxide and carbon dioxide:

$$CO + 3\,H_2 \longrightarrow CH_4 + H_2O \qquad \Delta H^0_{298} = -206\,\mathrm{kJ\,mol^{-1}} \tag{2.6}$$

and

$$CO_2 + 4\,H_2 \longrightarrow CH_4 + 2\,H_2O \qquad \Delta H^0_{298} = -165\,\mathrm{kJ\,mol^{-1}}\cdot \tag{2.7}$$

The methanation reactions are classified as exothermic [81]. Depending on the desired product, these reactions can be kinetically controlled, playing an important role in industrial applications and contributing to a decrease in the H_2O/CO ratio.

There are various types of reactors, including fixed-bed, circulating (or bubbling) fluidised bed, and entrained-flow gasifiers. Almost any type of organic feedstock can be gasified, depending on the design of the gasifier. Several gasifier types are available for commercial use. The most important gasifiers are discussed in the following paragraphs.

Fluidised bed (FBR)

One of the simplest fluidised-bed reactors developed for power generation applications is the bubbling FBR, with its first reported use for gasification by Winkler in 1921 [82, 83]. Fluidised-bed reactors are among the most commonly used reactor configurations for reactions involving biomass-derived reactants [84]. Figure 2.5 illustrates a schematic of a common circulating FBR gasifier for biomass, as commonly used in industrial applications.

The suspension of solid particles in a fluid is described as fluidisation. The fluidisation agent is supplied from the bottom, and the gasification occurs accordingly within the bed. The feedstock material undergoes fast pyrolysis, yielding rise to a component mixture of gaseous materials. The bed of inert solid material behaves like a liquid, and is continuously stirred by the presence of gas bubbles.

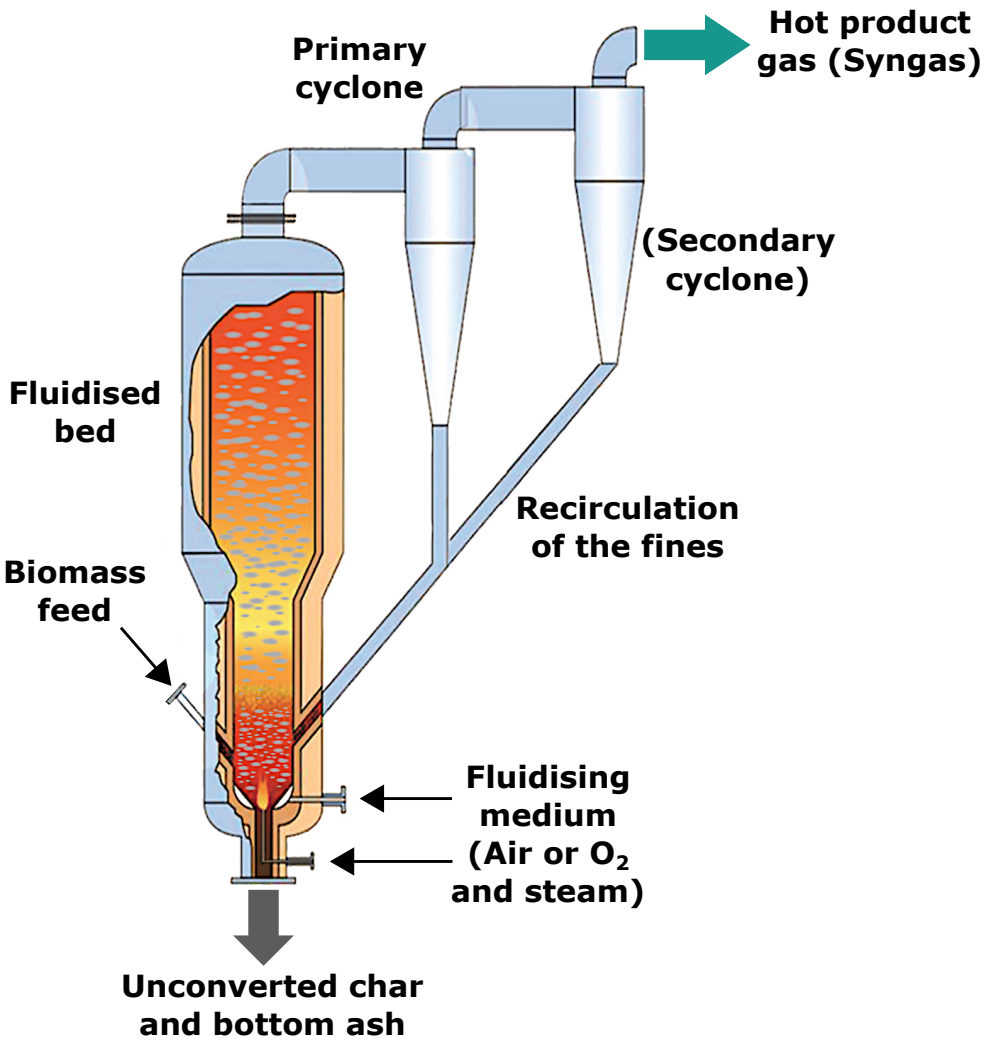

Figure 2.5: Schematic of a circulating fluidised-bed gasifier for syngas production. Adapted and modified from Lalou [85].

The main advantage of a FBR is its ability to transport heat within and out of the reactor very rapidly, resulting in an even temperature distribution [86, 87]. The mechanism facilitates high levels of contact between gases and solids. The fluidising medium in an FBR can be either a gas or a liquid, while the material being fluidised is almost always solid.

However, there are some critical disadvantages of fluidised beds, particularly those caused by ash-derived species. For example, alkaline- and Si-rich biomass may lead to the formation of low-temperature melting phases such as silicates, carbonates, or molten salts, resulting in the production of molten slag [88]. This can promote bed agglomeration, followed by defluidisation (see Chapter 2.3.2).

Entrained bed

In entrained flow reactors, biomass particles are rapidly gasified as they are transported through the reactor. This process requires high temperatures and small particle sizes and to ensure that gasification reactions are completed quickly [89]. The operating temperatures typically exceed 1200 °C, and the operation can easily proceed at higher pressures, such as 25 bar. The configuration of an entrained flow gasifier is shown in Figure 2.6.

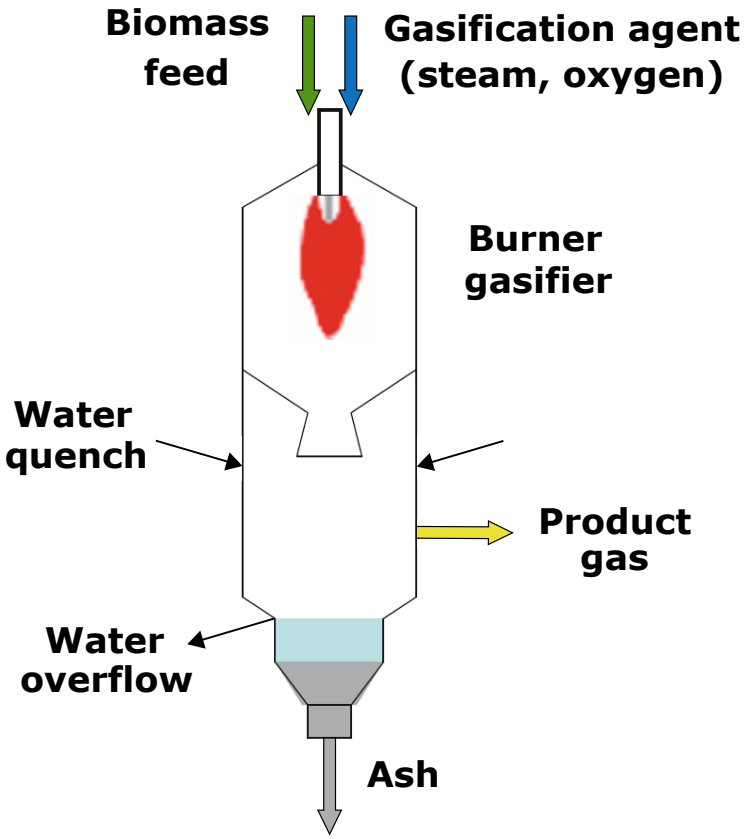

Figure 2.6: Schematic of an entrained flow gasifier for syngas production. Adapted and modified from Hofbauer et al. [89].

Fuel and gasification agents are typically fed into the reactor from the top. Gasification occurs in the upper part of the reactor, while the lower part is where the product gas is cooled and separated from ash particles. The ash is collected in granulated form at the bottom of the reactor. The product gas, which can be upgraded to syngas, exits the reactor at the lower part.

The main advantage of an entrained flow reactor is the very low tar content in the product gas [89].

Fixed bed

Fixed bed gasifiers come in three main types: updraft (counter-current), downdraft (co-current), and crossdraft gasifiers. Updraft gasifiers are a widely used and straightforward type of gasifier for biomass [90]. In the past, only updraft operation has been used for large-scale gasifiers [89]. This means that the gasification agent flows from the bottom to the top, while biomass flows from the top to the bottom. Different zones are set up within the gasifier, with a drying zone at the top followed by a pyrolysis zone, reduction zone, and an oxidation zone at the bottom where the gasification agent enters. The temperature within the fixed bed increases from top to bottom. Figure 2.7 illustrates a schematic of a typical fixed bed gasifier.

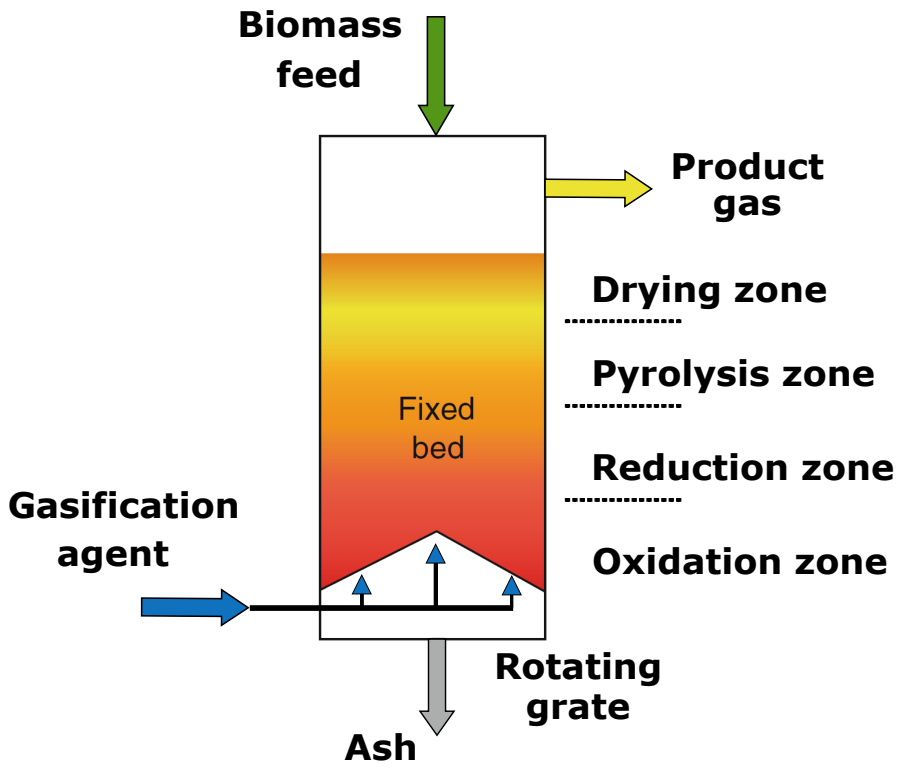

Figure 2.7: Schematic of an updraft fixed bed gasifier for syngas production. Adapted and modified from Hofbauer et al. [89].

The main advantages of updraft gasifiers include the simplicity of the gasifier configuration and operation, less complex feedstock preparation compared to entrained flow gasifiers, feedstock flexibility, and a relatively low oxidant requirement.

2.3 Ash-forming matter and ash-related problems in fluidised-bed gasification

This chapter focuses on the most common characteristics of ash-forming matter and the associated issues that arise in gasifiers, with a particular emphasis on fluidised-bed systems. The inorganic components of biomass ash can lead to significant impairments and key challenges during the gasification process. Furthermore, preventive measures are highlighted and elaborated to mitigate these issues.

2.3.1 High-temperature corrosion

Both high-temperature and complex gas environment are significant driving forces, commonly causing a non-ideal oxidation behaviour of alloys. For example, high carbon activities and low oxygen partial pressures might induce carburisation, whereas alkali metal compounds (mainly potassium and sodium salts) may form problematic eutectic melts on different surfaces [14, 91]. Sulphur may react to cause sulphidation of the reactor material components and so forth. Steel is predominantly used in heat transferring surfaces due to its good thermal conductivity. However, taking into account the water-enriched atmosphere under gasification conditions, water vapour can adversely affect the oxidation resistance of stainless steels. From the thermodynamic perspective, the Gibbs free energy of formation ΔG is the driving force for the oxidation of a metal in gaseous environments [92]. Consequently, this means that the occurrence of an oxidation chemical reaction depends on the magnitude of ΔG. At constant pressure, ΔG is mathematically defined by

$$\Delta G^0 = -RT\,ln(K), \tag{2.8}$$

where K is the equilibrium constant.

Biomass, especially fast growing species such as herbaceous plants, contains in general a high amount of chlorine in contrast to fossil fuels, which has in turn a negative effect on the metal behaviour, e.g. the rector wall unit [93]. This phenomenon is understood as chlorine-induced corrosion, which is the most important corrosion process in power plants, firing waste, coal and/or biomass [94]. Therefore, the effects and interactions of chlorine-rich fuels on the behaviour of steel should be clearly elucidated. Both the origin source and the amount of chlorine vary noticeably between different types of fuels. The chlorine concentration in coal varies generally between $50\,mg\,kg^{-1}$ and $2000\,mg\,kg^{-1}$, whereas in biomass the content can vary between $<100\,mg\,kg^{-1}$ and $7000\,mg\,kg^{-1}$ [95]. The cellular liquid of the plants is known to be the source of chlorine [96].

According to Kahn et al. [97], three different types of corrosion processes were identified:

- **gas phase corrosion**,
- **liquid induced corrosion**, and
- **solid-phase corrosion** (or **high-temperature corrosion**).

The gas phase corrosion is described by a process in which Cl_2 reacts directly with the wall material of the reactor or the heat exchanger surfaces. The liquid induced corrosion occurs upon condensation of HCl or aqueous solutions, whereas the solid phase corrosion is caused by a series of chemical reactions (chain reaction): chlorine is enriched within the slag deposits, which consequently leads to high corrosion rates. Figure 2.8 displays the mechanism of high-temperature corrosion while Equations 2.9 and 2.10 show the appropriate reaction pathways.

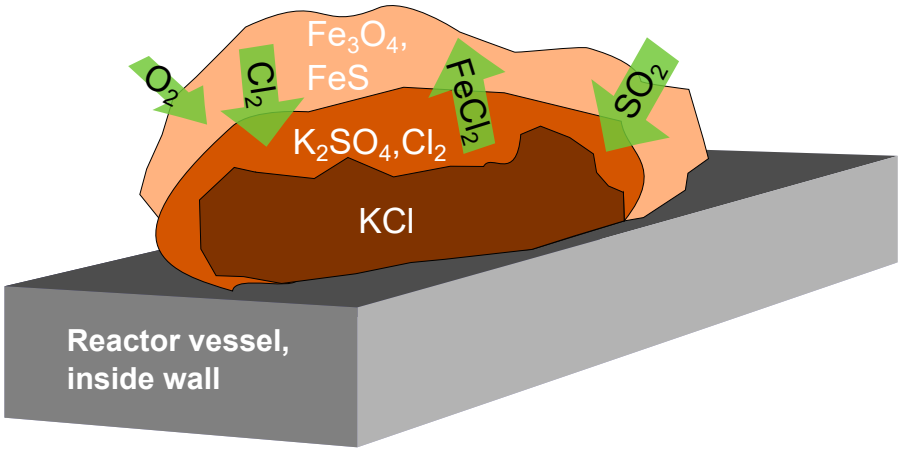

Figure 2.8: Schematic mechanism of high-temperature corrosion. Modified after Gatternig [96] and Karl [98].

It should be pointed out here that the following reactions basically describe the corrosion mechanisms for combustion conditions, as commonly described in the literature or hereinafter. Nevertheless, the reaction mechanisms are in principle proceeding quite similar under gasification conditions. Vaughan [99] described the reaction in a water-containing atmosphere, starting from an alkali metal chloride:

$$2\,KCl + SO_2 + \frac{1}{2}\,O_2 + H_2O \longrightarrow 2\,HCl + K_2SO_4. \tag{2.9}$$

Reaction 2.9 depends on the availability and quantity of water in the flue gas. If no water is present, then the reaction is possible nonetheless and results in the formation of gaseous chlorine as described by Kautz et al. [100]:

$$2\,KCl + SO_2 + O_2 \longrightarrow K_2SO_4 + Cl_2 \tag{2.10}$$

The generated chlorine gas forms highly volatile $FeCl_2$ (Equation 2.11) with the reactor wall material and is transported by diffusion to the outer surface of the deposit.

$$Fe + Cl_2 \rightleftharpoons FeCl_2 \tag{2.11}$$

Finally, the iron reacts to the more stable or thermodynamically preferred oxide and sulphide components (Equation 2.12 and 2.13). The critical vapour pressure of metal chloride is already reached at temperatures lower than 300 °C or more precisely, the equilibrium between solid $FeCl_2$ and gaseous $FeCl_2$ is favoured [101]:

$$3\,FeCl_2 + 2\,O_2 \rightleftharpoons Fe_3O_4 + 3\,Cl_2 \tag{2.12}$$

and

$$4\,FeCl_2 + SO_2 + O_2 \rightleftharpoons FeS + Fe_3O_4 + 4\,Cl_2, \tag{2.13}$$

resulting in a release of chlorine to return to the inner deposit layer, which leads to a critical chain reaction. It is assumed that certain oxygen activities are required for the conversion of gaseous chlorides to oxides at constant Cl_2-activity [102]. According to Equation 2.12, from a thermodynamic point of view the required oxygen partial pressure p_{O_2} for the conversion of bivalent gaseous metal chloride to trivalent oxide is described by [102, 103]:

$$p_{O_2} = \left(\frac{p_{Cl_2}^2}{p_{FeCl_2(g)}^2 \cdot K_{chloride/oxide}} \right)^{\frac{3}{2}} \tag{2.14}$$

In conclusion, it can be seen that a rapid destruction of the reactor wall unit is caused by the enrichment of chlorine at the wall of the boiler surface.

2.3.2 Agglomeration

A major obstacle is the phenomenon of bed agglomeration, which is mainly caused by melting of the ash. The agglomeration can be understood as the partial fusion or reaction of ash particles and the fuel bed, forming new larger particles, so called agglomerates [104]. This phenomenon is based on adhesion, the ability of a substance to stick to an unlike substance. Low melting points are causing sticky coatings around the bed material particles, which are changing the fluid dynamics of a fluidised bed. Finally, the formation of agglomerates can lead to poor combustion or gasification conditions, de-fluidisation of fluidised beds, decreased mass and heat transport. A decreased heat transport causes concurrently an uneven temperature distribution, which leads to local over-heating and thus, the amount of formed molten ash results in accelerated agglomeration as indicated in Figure 2.9.

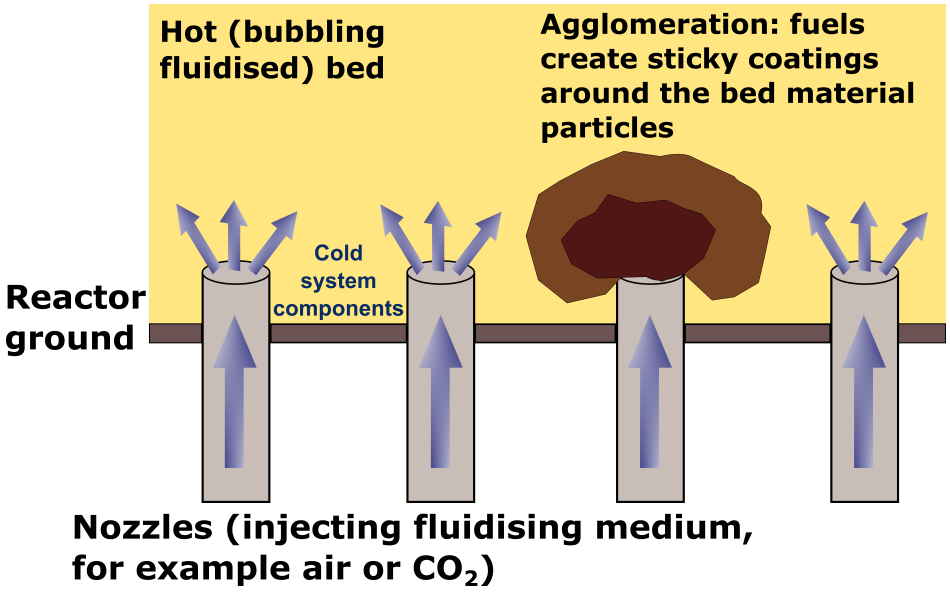

Figure 2.9: Schematic of agglomerate formation at the cold nozzles of the fluidised-bed diffusers. Modified after Ottmann [105].

Moreover, problems with the ash removal system and the downstream ash handling equipment can cause significant problems [106]. Consequently, several shutdowns of boiler operations are inducing unfavourable ecological and economic challenges.

When the uniting forces of the bed material overcome the separating ones, stable agglomerates start to form at a critical point. It is worth nothing that a crucial fraction of obtained alkali containing ashes can result as a critical point. The tendency of agglomeration is strongly dependent upon temperature sensitive interactions between bed material and ash particles.

Ash with high alkali content (primarily potassium and sodium salts) are typically revealing lower melting points because of the formation of potassium or sodium silicates that have low melting points due to eutectic effects [14]. A calculated K_2O–SiO_2 binary phase diagram is shown in Figure 2.10.

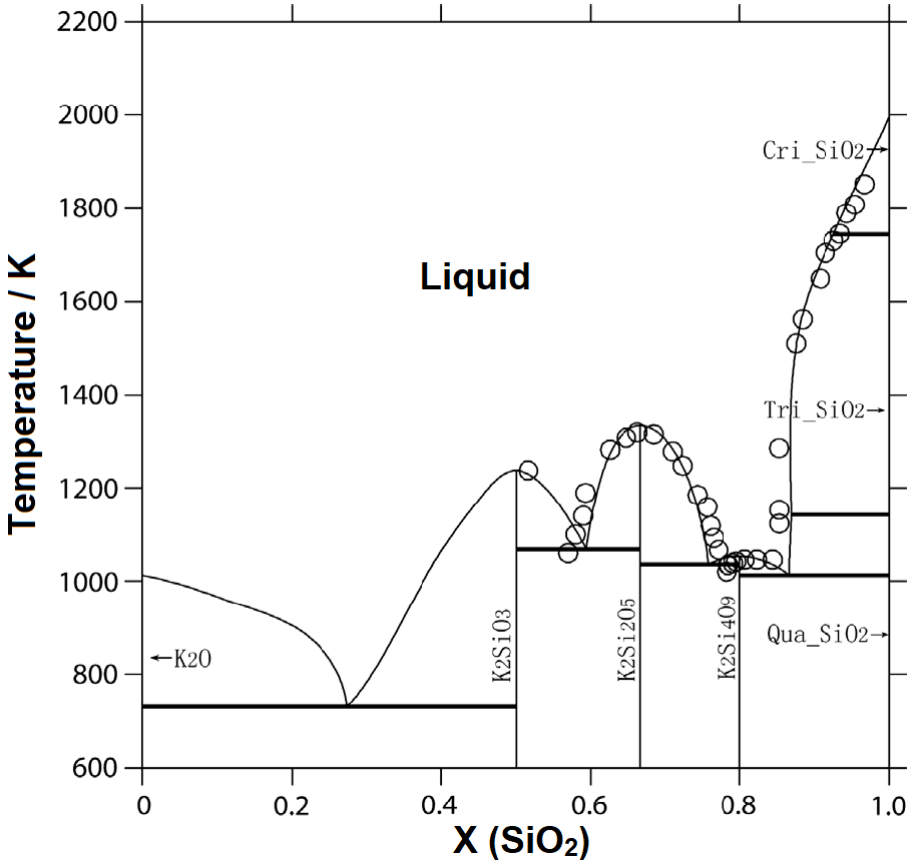

Figure 2.10: Calculated K_2O–SiO_2 binary phase diagram with experimentally determined data (Kracek et al. [107], denoted by circles). Mineral polymorphs of SiO_2 are denoted as follows: Cri = Cristobalite, Tri = Tridymite and Qua = Quartz. Modified after Zhang et al. [108].

Silica is the main component of common bed materials (such as olivine or quartz sand), and potassium oxide is a main constituent of herbaceous biomass ash [109]. It is important to mention that the oxygen carrier itself is used as bed material for CLG, which implies that reactions with ash constituents are highly assumed to occur.

Sintered products of the fluidised bed are formed at higher temperatures. Once the softening temperature is close to or even lower than the reaction temperature of the bed material, the ash starts to stick with the inert material, and this is described by the phenomenon of coating and agglomeration. Deposits are formed on cold plant com-

ponents such as nozzle bottoms, combustion chamber walls and other heating surfaces (Fig. 2.9) [61, 110]. The ash melting behaviour strongly depends on the ratio between potassium and silicon oxide. Depending on their relative concentrations, the melting temperature may be as low as about 740 °C as can be seen in Fig. 2.10. The solidus of the resulting quartz and potassium tetrasilicate increases when much more silicon oxide is present than potassium oxide (see right hand site of the binary phase diagram in Fig. 2.10). Potassium silicates can be formed when potassium is present in a form that is thermodynamically less stable than the latter [111–113].

As opposed to alkali silicates, alkaline earth silicates show different effects on the melting behaviour. The ternary phase diagram of $CaO–K_2O–SiO_2$ in Figure 2.11 demonstrates that adding calcium silicates or calcium oxide to potassium silicates increases the melting point of the obtained mixture.

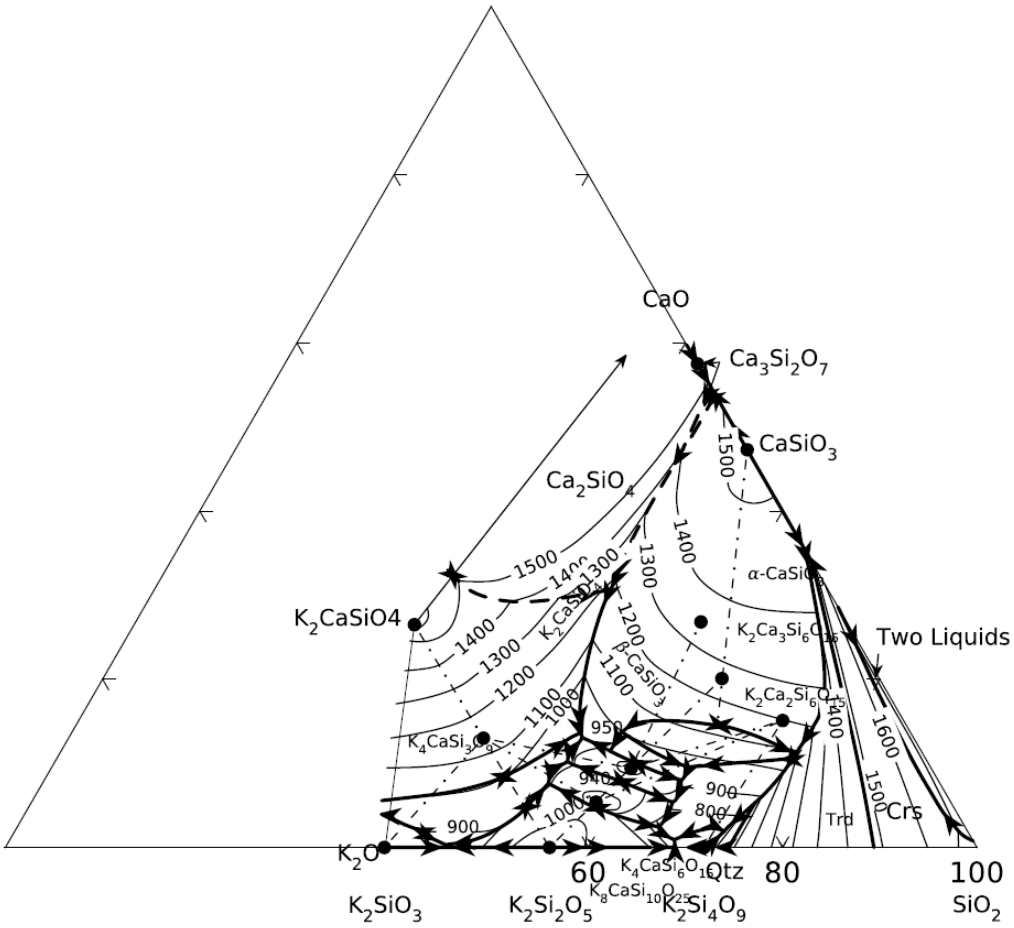

Figure 2.11: Ternary phase diagram of the $CaO–K_2O–SiO_2$ system, presenting the high SiO_2 corner. Adapted from Morey et al. [114].

According to Figure 2.11 and the calculated binary phase diagram proposed by Jung et al. [115], the lowest solidus temperature for CaO–SiO_2 is 1437 °C, which is much higher than the typical operating conditions of a FBR. The presence of both calcium and magnesium silicates increases the melting point of silicate mixtures, as Jung et al. [115] showed that the lowest solidus temperature for MgO–SiO_2 is above 1500 °C, and the lowest eutectic for CaO–MgO–SiO_2 is above 1350 °C.

Several preventive measures can be taken into account in order to avoid bed agglomeration. The gasification temperature can be adjusted, either by increasing or decreasing. The latter option may prevent salt melt formation, however, it might be difficult to reach an ideal thermal fuel gasification in that case. If the former alternative is selected, relatively high temperatures are required so that salt formation no longer occurs and that formed salt melt has preferably low viscosity that it will not cause technical problems anymore (the "stickiness" is related to temperature) [106]. On the downside, the risk of reaction introduced adhesion is enhanced by increase of temperature, and the formation of glass melt at reaction with a pure bed material might be initialised [106]. The replacement of the bed material with a material that is more resistant to high temperatures and the formation of glass melt might be another option. Herbaceous biomass, e.g. straw, is correlated with higher risks in connection with agglomeration, as those species are melt forming itself [109].

A promising strategy is the use of additives that increase the ash melting point, thus preventing the formation of eutectics [106]. For example, additives that can be used are commonly alkaline earth carbonates such as dolomite or limestone. If dolomite is used, calcium-magnesium-silicates are formed, and there are no chemical interactions between dolomite itself and potassium from the ash believed to take place [116]. Residual, Ca/Mg/Si-rich waste products from the industry can be used instead of pure additives in the sense of ecological and economic purposes. Last but not least, co-gasification of problematic fuels with the use of ash fraction containing aluminosilicate that capture alkali and thus counteracts the melting process under operating temperatures of a fluidised bed has been reported to be promising and effective [117].

2.3.3 Fouling and slagging

Due to the distinct nature of the mineral and phase composition of biomass ash, fouling and slagging are common problems associated with biomass firing. The risk tendencies are inherently linked to the composition of biomass fuels. As previously mentioned, biomass tends to have a lower ash content than coal; however, it is often rich in volatile alkalis, primarily K and/or Na [118]. The phenomenon of both fouling and slagging occurs when the ash particles are molten and adhere to the boiler surface. At lower temperatures, inorganic vapours may condense on solid particles, resulting in a sticky molten film coating their surface. Fouling and slagging are complex processes that have been extensively studied in various publications [119–122]. The mechanism of fouling can be primarily explained by the condensation of volatile species vaporised in previous boiler sections, which are loosely bonded [121]. The main transport mechanisms leading to ash deposition on surfaces have been described in various publications elsewhere [123, 124]. The mechanism of slag formation involves adhesiveness, ash melting and sintering effects. Slagging deposits are consisting of an inner powdery layer, which is followed by silicate and alkali compounds [121, 125]. Figure 2.12 illustrates the deposition of ash and the resulting chemical reactions on a heat exchanger.

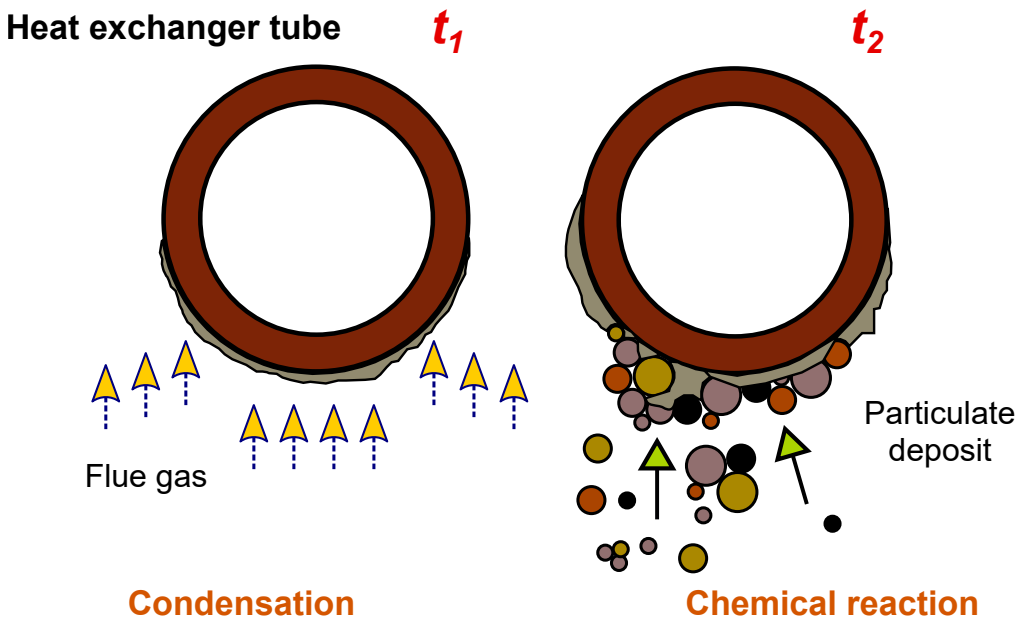

Figure 2.12: Schematic of alkali vapour condensation on heat exchanger surfaces, illustrating deposit formation over time (t_1: condensation of inorganic species; t_2: chemical reactions resulting in the formation of slagging deposits) on a heat exchanger tube. Modified after Kleinhans et al. [124].

The ash deposition rate is enhanced by low melting alkali chlorides contained in the fuel, since they condense on boiler and refractory walls, resulting in creating molten, sticky layers to which flue gas particles can adhere [126, 127]. Miles et al. [128] proposed an alkali index to monitor the amount of alkali in fuels and to minimise fouling and slagging occurrence, as reported in [129]:

$$\text{Alkali index} = \frac{(K_2O + Na_2O) \cdot \text{Ash}\,(\text{wt}\%)}{\text{HHV}} \tag{2.15}$$

In Equation 2.15, HHV represents the higher heating value (MJ/kg) at $H = 0\,\%$ (which refers to anhydrous HHV, where the moisture content is $0\,\%$), while both K_2O and Na_2O are expressed as the percentage of these components in the feedstock composition in dry weight (d.b.). According to the alkali index previously mentioned, following conclusions can be drawn in order to estimate fouling risks:

- alkali index $> 0.17\,\text{kg}$ alkali/MJ → probable fouling
- alkali index $> 0.34\,\text{kg}$ alkali/MJ → fouling is certain to occur

This index should be taken as an approximate reference value. Besides alkali species, chlorine also plays an essential role, facilitating the transfer of potassium in the gas phase, where it participates in further reactions or is deposited on cold surfaces [130]. Chlorine is substituted by sulphur on the surface, resulting in formation of potassium sulphate deposits and/or reacting with the protective oxide layers of the metals, thereby initiating corrosion [121, 131]. The following values were established by Bryers [132] and Pronobis [133] in order to limit chlorine-based fouling and slagging in biomass fuels, where chlorine simply represents the chlorine content of the sample dry weight:

- $\text{Cl} < 0.2\,\text{wt}\%$ → low slagging trend is expected
- $0.2\,\text{wt}\% < \text{Cl} < 0.3\,\text{wt}\%$ → medium slagging trend is expected
- $0.3\,\text{wt}\% < \text{Cl} < 0.5\,\text{wt}\%$ → high slagging trend is expected
- $\text{Cl} > 0.5\,\text{wt}\%$ → very high slagging trend is expected

A more conservative threshold was proposed by Obernberger et al. [134], which suggests that when the chlorine content exceeds $0.1\,\text{wt}\%$, there may be a risk of corrosion and HCl emissions.

2.3.4 Pollutant emissions: NO_x and its precursors, NH_3 and HCN

Nitrogen oxide emissions are a known problem under combustion conditions. Nitrogen oxides (NO_x) are also produced during gasification, as the biomass is thermochemically converted. The exact composition of nitrogen oxides depends on the gasification process, which can include fixed bed gasifiers, fluidised-bed gasifiers, or entrained flow gasifiers. However, NO_x emissions from gasification are generally lower than those from direct combustion. A previous study has thoroughly explored the mechanisms of NO_x formation in combustion processes [135], but there is still a lack of understanding regarding the specific behaviour of NO_x formation under gasification conditions.

Some biofuels contain significant amounts of nitrogen, which is an essential nutrient for plant growth. As a vital component, nitrogen plays a crucial role in plant function and is a fundamental element of amino acids, serving as the primary building block for the synthesis of plant enzymes and proteins [136]. During the gasification process, nitrogen molecules bound to the fuel are transformed into ammonia and other nitrogen-containing compounds [137]. When these compounds are combusted, they undergo oxidation to produce NO_x. As a result, they contribute to the formation of acid rain, photochemical smog, and other environmentally harmful byproducts [138, 139]. Consequently, strict emission limits have been established for nitrogen oxides in flue gases from combustion processes [140].

The form in which nitrogen is bound in the biomass influences the release of nitrogen during thermal conversion [140–143]. The nitrogen in the fuel (fuel-N) can be divided into nitrogen released during devolatilization (volatile-N) and nitrogen released during char conversion (char-N). Volatile-N compounds comprise typically NO, N_2, NH_3, HCN and HNCO [144]. The distribution of nitrogen compounds during devolatilization depends on several factors, such as the temperature and ash composition [144–147]. The primary precursors of NO_x and N_2O during biomass gasification are NH_3 and HCN [148]. Ammonia can act as a reducing agent for NO_x reduction. Equation 2.16 denotes the main global reaction [149]:

$$4\,NO + 4\,NH_3 + O_2 \longrightarrow 4\,N_2 + 6\,H_2O \tag{2.16}$$

The mechanism in Eq. 2.16 underlines the correlation between the ammonia concentration in the fuel and the formation of NO. The higher the ammonia concentration, the more dominant the de-NO_x mechanism as demonstrated by Koger et al. [150]. There are several detailed NO_x reduction reaction mechanisms available in the litera-

ture, e.g. [151] and [152]. It is worth noting that the nitrogen chemistry is distinct for either combustion or gasification conditions, as the formation of the NO_x precursors strongly depends on the oxygen partial pressure during the process.

The catalytic effect of fuel ash is of great interest, particularly as the presence of Ca, Mg, K, Fe, and Na may catalyse the reduction of NO and NO_2 [62, 149, 153]. Ash-forming matter influences the nitrogen chemistry; recent studies have reported, for example, that Ca and K catalyse the reduction reaction between NO and char [147, 154–156]. Based on the catalytic effects originating from the ash, it can be assumed that biofuel upgrading should impact the emissions of N-containing compounds. However, so far, there are only a few studies that have investigated the influence of pre-treatments on fuel-N release and the mechanisms are not yet fully understood [144, 157].

2.3.5 Poisoning of oxygen carriers (in CLG applications)

The backbone of any CLG application is the oxygen carrier material, which provides the required oxygen for fuel gasification through its lattice oxygen. In addition to the problems and risks discussed earlier, the oxygen carriers are also susceptible to unwanted side reactions with ash-forming compounds. The composition of ash-forming species in any feedstock can vary depending on the source of biomass [158, 159]. Syngas contains varying amounts of reactive compounds, including alkali metals, alkaline earth metals, and sulphur compounds. Some species may influence the behaviour of certain oxygen carriers depending on the redox pair used. Oxygen carrier materials are exposed to extreme conditions, including elevated temperatures, constant temperature fluctuations, high-velocity impacts with other particles and reactor surfaces [160]. Sulphur contained in biomass-derived feedstocks is known to poison the oxygen carrier activity [161]. Notable cases where sulphur poisoning causes significant difficulties include Ni-based oxygen carriers, which form thermodynamically stable Ni_3S_2, and Ca-containing Mn-based perovskites, which form $CaSO_4$ and CaS [162, 163]. In contrast, common oxygen carriers based on Mn and Fe oxides are not deactivated by sulphur compounds [164]. Cu-based materials have been found to exhibit reduced stability, with some copper sulphide detected inside the oxygen carrier, but only when the H_2S concentration in the gas was extremely high (sour gas with 0.3 vol% to 15 vol% of H_2S) [164, 165].

In addition to sulphur poisoning, the impact of chlorine on oxygen carrier performance was investigated by Dai et al. [166]. They found that the formation of HCl also leads to the deactivation of oxygen carriers due to the formation of gaseous products from

side reactions between the oxygen carrier and Cl-based species. According to Dai et al. [166], Cu_2O may be converted into gaseous CuCl and Cu_3Cl_3 in the presence of HCl, deactivating the oxygen carrier in the fuel reactor. The Cu-Cl interaction is primarily governed by the relative quantities of HCl and H_2O in the gas stream. In contrast, high steam concentrations inhibit the formation of CuCl and Cu_3Cl_3.

Besides sulphur and chlorine poisoning compounds, researchers have also focused on the impact of alkali metal salts and alkaline earth salts on oxygen carriers [167–172]. However, their effects may differ and depend strongly on the chemistry of the oxygen carrier. For example, Ca-based compounds have been shown to exhibit higher reactivity towards iron oxides than Mg-based compounds, and observations have confirmed the formation of Ca-Fe-based oxides, whereas no formation of Mg-Fe oxides was observed [173].

3 Materials and Methods

3.1 Sample materials and pre-treatment

This chapter provides a detailed description of the biofuel samples and the (combined) pre-treatment approaches employed in this study. The batch of samples studied in this work was split into three distinct parts, as shown in Table 3.1. One part of the samples was obtained from project partners in Spain (CENER, partners in the European research project CLARA, for details refer to Chapter 1.2). The CLARA project aims to compare industrially pre-treated herbaceous fuels with woody biomass. In order to classify the effectiveness of the measures, industrial wood pellets were taken as benchmark material and pine forest residues were chosen as alternative woody waste biomass. In addition to the project samples, various commercial herbaceous straw varieties were purchased in Germany (Futtermittel Louven, North Rhine-Westphalia), pre-treated and analysed to broaden the scope of fuel/ash composition. These fuels are hereafter referred to as FZJ project fuels.

The sample materials were analysed as received from the project partners, without further processing (except for milling and sieving to facilitate analysis). The project partners' treatment parameters were as follows: raw wheat straw from Spain's Navarre province was initially chopped, then milled and pelleted. The pellets were torrefied at 260 °C in a nitrogen atmosphere over a 30 min to 40 min period using a lab-scale rotating batch reactor designed by CENER (part of the CLARA project). To ensure uniform thermal treatment, the torrefaction process was performed in this reactor. For water leaching, torrefied samples were washed for 24 h at room temperature (20 °C) with deionized water (1:10 ratio), followed by overnight drying at 45 °C. The detailed procedures for the applied pre-processing methods can be found in a project publication by the project partners [174]. The samples were subsequently milled and sieved, resulting in particles with diameters less than or equal to 0.56 mm.

Table 3.1: Biomass feedstocks analysed in this study. Pre-treatment methods differed between the CLARA project's fuels and the FZJ project's fuels. Pine forest residues were used as both a biofuel and an additive for co-blending.

CLARA project's fuels (Chapter 4.1)	**Pre-treatment method (abbreviation)**
Wheat straw	Source material (Raw), Torrefied (To), Torrefied + water-leached (To-WL), Torrefied + 2 wt% $CaCO_3$ blended (To+A), Torrefied + post-washed + 2 wt% $CaCO_3$ blended (To-WL+A)
Pine forest residues	Raw, not pre-treated (PFR)
Industrial pine pellets	Raw, not pre-treated (IWP)
FZJ project's fuels (Chapter 4.2 and 4.3)	**Pre-treatment method (abbreviation)**
Wheat straw	Source material (Raw), Torrefied (To), Water-leached (WL), Pre-washed + torrefied (WL-To), Torrefied + post-washed (To-WL)
Barley straw	—*dito*—
Colza straw	—*dito*—
Corn straw	—*dito*—
FZJ project's additives (Chapter 4.3)	**Pre-treatment method (abbreviation)**
Oak bark	Raw, not pre-treated (OB)
Pine bark	Raw, not pre-treated (PB)
Pine forest residues	Raw, not pre-treated (PFR)
Limestone	Raw, not pre-treated (A)

For the FZJ project fuels, various pre-treatment methods were applied, including torrefaction, water leaching, and blending with limestone or cost-effective woody components. These methods were used either individually or in combination. Detailed procedures for these pre-treatment methods are described in the following sections.

Torrefaction pre-treatment

In this work, a dry torrefaction method without the use of water vapor has been employed. As previously noted, biomass torrefaction occurs in a non-oxidising atmosphere. Consequently, argon with a purity of 99.9992 % was used as an inert gas due to its higher gas density compared to nitrogen. A photograph of the raw material as well as the sample after thermal treatment is exemplified in Figure 3.1.



Figure 3.1: Comparison of thermally treated colza straw: raw material (left) vs. torrefied colza straw (right).

The raw material was positioned in the centre of the furnace chamber to ensure even heat distribution. The chamber was then flushed with argon for two hours to achieve a low oxygen partial pressure (p_{O_2} ≤0.70 %). Prior to torrefaction, the feedstock was heated to 110 °C and maintained at this temperature for three hours to facilitate the evaporation of any remaining moisture and ensure proper drying. Following the drying process, the chamber was automatically heated to 250 °C at a rate of 5 K min^{-1} and maintained at this temperature for one hour under a constant argon atmosphere.

The torrefaction grade T_G was also investigated gravimetrically. Table 3.2 presents the torrefaction grades, moisture content, and ash content of the raw (non-treated) straw samples.

Table 3.2: Moisture, ash content, and torrefaction grade T_G of FZJ project fuels (note: T_G includes residual moisture content). Moisture and ash content represent the source material as received (ar).

Feedstock	**Moisture** (wt% ar)	**Ash** (wt% ar)	**Torref. grade** (wt%)
Colza straw	10.37 ± 0.11	8.15 ± 0.05	36.90 ± 2.60
Corn straw	7.85 ± 0.11	9.79 ± 0.18	28.46 ± 0.97
Wheat straw	6.41 ± 0.04	5.32 ± 0.12	27.84 ± 1.60
Barley straw	7.46 ± 0.04	5.63 ± 0.04	26.50 ± 1.35

The torrefaction grade was determined by calculating the percentage of mass loss of the torrefied biomass (m_t) in relation to the initial mass (m_0) of the untreated material. This can be expressed mathematically as shown in Equation 3.1:

$$T_G = \frac{m_0 - m_t}{m_0} \times 100 \tag{3.1}$$

Both the moisture and ash content were analysed gravimetrically. To determine the moisture content, the samples were dried in an oven at 110 °C for 48 h. The ash content was determined by ashing samples in a normal laboratory atmosphere at 550 °C for 36 h according to DIN EN ISO 18122, until a constant mass loss was achieved.

Water-leaching pre-treatment

A water-leaching treatment was applied to the herbaceous feedstocks, using only deionised water, for both the source and torrefied materials. Building on the research by Meesters et al. [57], a two-step washing procedure was developed in this study. Consistent with the findings of [57], washing twice with deionised water was found to be more effective in removing soluble salts compared to a single-step washing process. The FZJ feedstocks listed in Table 3.1 (Chapter 3.1) were washed with deionised water at a constant temperature of approximately 20 °C (room temperature). The washing procedure consisted of the steps outlined below, presented in chronological order.

1) 50 g of the raw or torrefied material was placed in a plastic bottle and 0.5 L of deionised water was added, resulting in a weight ratio of 1:10 between sample and washing water.

2) The bottle was then placed on an electric reel, where the water-feedstock mixture was gently rotated at a constant rate and room temperature for one hour.

3) After step 2), the washing water was decanted, and vacuum filtration was applied to remove any residual water from the sample material. This step aimed to achieve a fast and effective separation of washing water containing impurities or water-soluble salts.

4) The same procedures as steps 1) and 2) were repeated one-to-one again, resulting in two water-leaching cycles in total.

5) The same vacuum filtration procedure as step 3) was repeated, and the water-leached material was subsequently rinsed with a defined amount of deionised water, resulting in a weight ratio of 1:5 between sample and washing water.

6) Finally, the water-leached samples were stored for at least 24 h inside a fume hood to facilitate the evaporation of residual moisture.

Figure 3.2 illustrates the procedure schematically and in chronological order, showing the steps outlined above. The raw and torrefied samples were washed in their raw form and subsequently milled and sieved.

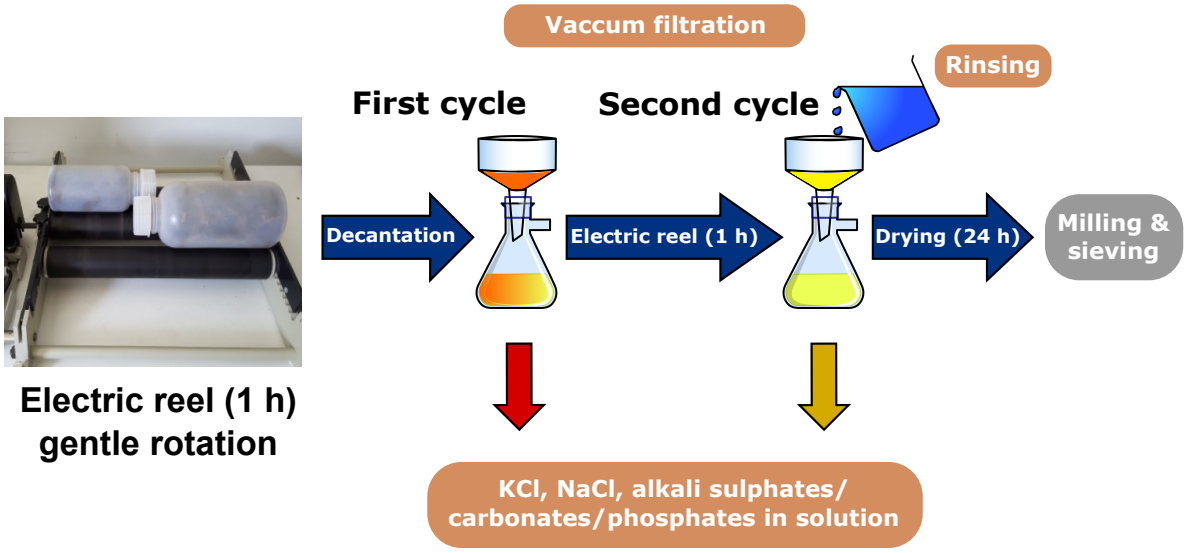

Figure 3.2: Overview of the water-leaching treatment process employed in this study.

Three different oxygen carriers were provided by project partners at Chalmers, as listed in Table 3.3.

Table 3.3: Mineral composition of oxygen carriers in wt%. Ilmenite also contains 5.5 wt% of inert materials, which are not included in the thermodynamic modelling.

Oxygen carrier	**MnO_2**	**Fe_2O_3**	**SiO_2**	**Al_2O_3**	**CaO**	**Fe_2TiO_5**	**TiO_2**
LD Slag	5.42	26.85	14.08	1.29	52.36	-	-
Sibelco (calcined)	72.99	9.05	7.31	7.97	2.67	-	-
Ilmenite (calcined)	-	11.2	-	-	-	54.7	28.6

Thermodynamic equilibrium calculations were conducted to numerically investigate the interactions between the oxygen carriers and fuel-derived ash at 950 °C, considering both gas and mineral phases. LD Slag, also known as basic oxygen furnace slag or steel converter slag, is a by-product of the steel industry, where pig iron from the blast furnace is converted into steel [175]. Sibelco is a manganese-based oxygen carrier, named after its manufacturer [176]. Ilmenite is a common titanium-iron oxide mineral.

For the experimental investigations using a fluidised-bed reactor, pure iron oxide was chosen as the oxygen carrier material and added to the pre-treated samples at a defined ratio of $0.48\,\mathrm{g\,g^{-1}}$ Fe_2O_3 to feedstock. It is worth noting that this assumption is based on the complete reduction of fully oxidised oxygen carrier, which is not the case in real-world processes. However, the actual amount of oxygen supplied is similar, allowing for a reasonable syngas composition to be achieved. The biofuel and oxygen carrier were mixed in a bottle and placed on an electric wheel, which was gently rotated to ensure a homogeneous mixture.

3.2 Preparation of fuel ashes for HSM and XRD investigations

This chapter provides a concise overview of the preparation of sample ashes from the feedstocks, which is essential for further studies involving hot stage microscopy (HSM) and XRD. The ash melting behaviour is a critical aspect for understanding interactions and allows for conclusions about ash slagging and agglomeration of the fluidised-bed material. Prior to analysis, pre-treated samples were initially ashed in a gasification-like environment and subsequently reduced in a mixture of argon and 4 % hydrogen for 3 h. This reduction step was employed to maintain the stability of crystalline phases, which are essential for XRD investigations.

Figure 3.3 presents a technical schematic of the designed test setup for ash sample preparation in a gasification-like environment. The argon/hydrogen mixture for subsequent reduction was introduced only after the ashing process, and the other gases were shut off simultaneously. The ash was prepared at 550 °C throughout the entire procedure, in accordance with the standard procedure outlined in DIN EN ISO 18122. This temperature ensured that alkali metal compounds were not evaporated.

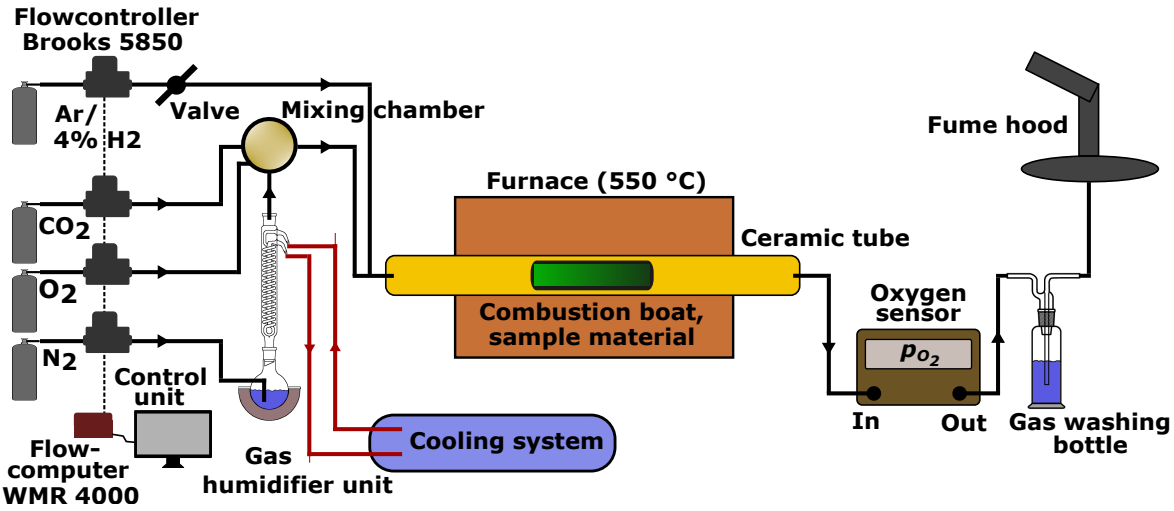

Figure 3.3: Sketch of the test setup for sample ash preparation in a gasification-like or reducing atmosphere (4 % H_2 in Ar).

The duration of ashing was found to be strongly influenced by the sample weight, which was determined by the carbon content of the fuel. A small amount of oxygen was initially introduced to enhance the rate of carbon conversion. The total gas flow rate was 100 mL min^{-1}, with the exact composition detailed in Table 3.4.

Carbon dioxide was introduced as a substitute for the oxygen carrier material. The defined volume flow rate, $\dot{V}$, was set to 5 vol%, based on preliminary thermodynamic equilibrium calculations performed using FactSage software.

Table 3.4: The gasification gas composition, consisting of N_2, CO_2, and water vapour, was mixed in a mixing chamber prior to entering the tube furnace. Subsequently, a separate gas stream consisting of 4 % H_2 in Ar was introduced to create a reducing environment, although the flow rate was not calibrated.

Process	**N_2**	**H_2O**	**CO_2**	**O_2**	**Ar/4 % H_2**
Gasification	70 mL min^{-1}	15 mL min^{-1}	5 mL min^{-1}	10 mL min^{-1}	–
Reduction	–	–	–	–	>100 mL min^{-1}

An oxygen sensor was integrated into the test setup to continuously monitor the oxygen partial pressure. Once the oxygen partial pressure reached a level of 0.30 % or greater, the reaction was promptly halted and the gas supply was switched to a mixture of 4 % Ar in H_2. This ensured a reducing environment and prevented further oxidation or combustion of the biogenic sample material. Assuming that oxygen is constantly depleted and converted into CO or CO_2, the oxygen partial pressure would increase constantly. The reaction progress of p_{O_2} depends on the reaction time of ashing, assuming that oxygen is continuously depleted during the reaction under ideal conditions. However, this idealised assumption is not applicable under real-world conditions, and the reaction rather exhibits a step-like progress. This behaviour can be attributed to the inhomogeneous composition of the feedstock and kinetic limitations. Furthermore, the sample materials were neither stirred nor rotated during ashing, which means that uniform mixing was not provided.

The ashed fuels were weighed afterwards, yielding an average yield of ±15 wt% (ar). The high ash content indicated a relatively high residual carbon content, which was not completely converted. Figure 3.4 shows exemplarily a photo of prepared sample ash, highlighting the carbon distribution in the sample. The colour gradient in Fig. 3.4 indicates a clear trend of residual carbon distribution, explained by the gas flow direction (denoted by the blue arrow). The gas flow was non-uniform, resulting in carbon not being completely depleted and thus, nonetheless distributed in the fuel sample ash. The further the sample material away from the gas inlet (ceramic tube furnace) was, the higher the fraction of carbon content was, as shown in Fig. 3.4. In addition, an increased carbon

content was found in the lower layers of the ash samples afterwards, due to unfavourable reaction or kinetic conditions. Before chemical characterisation or further processing, samples were homogenised in a mortar.

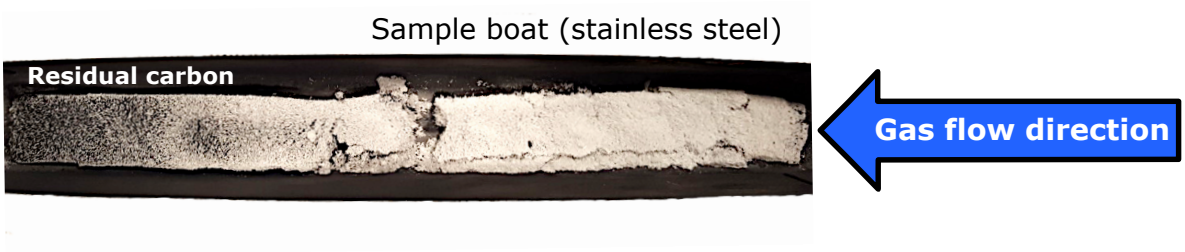

Figure 3.4: Example of sample ash prepared in a gasification-like atmosphere and subsequently reduced in a mixture of 4 % H_2 in argon.

The ash samples were prepared in a gasification-like environment, following the guidelines of the CLARA project partners. The use of steam as a gasification agent was motivated by its reputation as a preferred and effective agent for thermochemical conversion of biomass [177]. The steam gasification process aims to convert biomass into a combustible gas mixture (syngas) through partial oxidation at high temperatures. To ensure optimal humidification of the carrier gas, it is crucial to consider the gas flow rate when calculating the water flow rate. Pure nitrogen was used as the carrier gas, which was humidified with water. According to the ideal gas law, presented in Equation 3.2, the water vapour pressures can be directly converted into mass flow rates ($\dot{m}$). For the calculation of the flow rate, specific saturated vapour pressures (p^0) dependent on the temperature T were taken from tabulated literature values in the standard *CRC Handbook of Chemistry and Physics* [178]. The mass flow rate was calculated using Equation 3.2:

$$\dot{m} = \frac{\dot{V} \cdot p^0 \cdot M}{T \cdot R} \tag{3.2}$$

The defined volume flow rate $\dot{V}$ was set to 15 vol% aqueous vapour, based on preliminary thermodynamic equilibrium calculations with FactSage. The pressure p was equal to atmospheric pressure, and M denotes the molar mass of water, which is 18 g mol^{-1}. Figure 3.5 exhibits the water mass flow rate in dependence on the humidification temperature. As can be seen in Fig. 3.5, a water mass flow of 0.723 g h^{-1} correspondingly yields a humidification temperature of 66.6 °C. In practical terms, it is worth mentioning that water was evaporated using a reflux condenser, while excess water was condensed in the cooler unit to achieve the desired concentration.

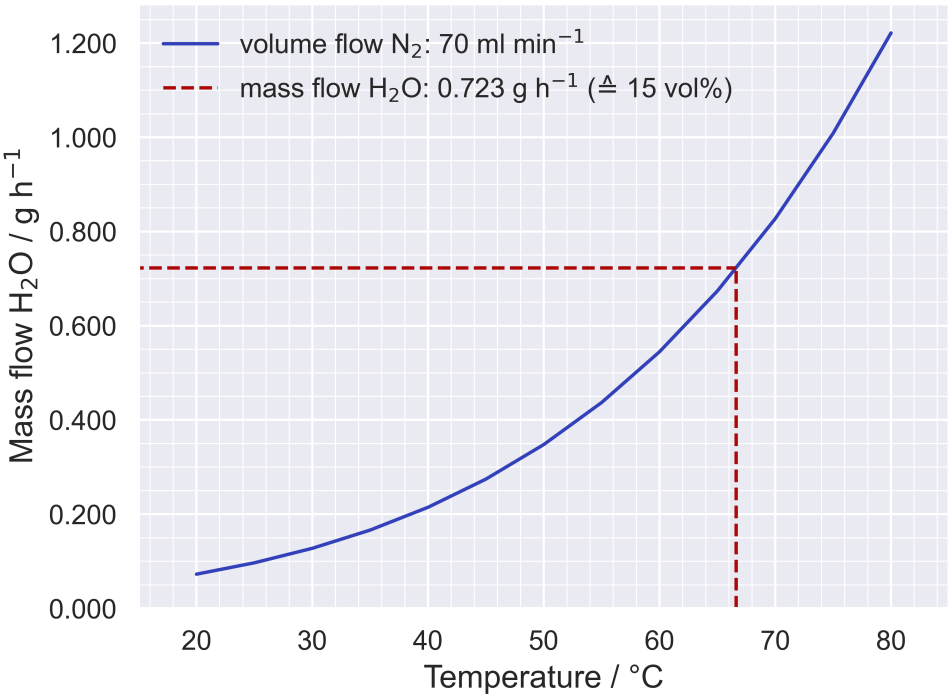

Figure 3.5: Cooling temperature plotted against water mass flow. The volume fraction of steam was maintained at 15 vol%, which corresponds to a mass flow rate of 0.723 g h^{-1} (the calculation assumes a volume flow rate of nitrogen at 70 mL min^{-1}).

3.3 Chemical characterisation and methods

The subsequent chapters offer detailed descriptions of the applied methods for experimental investigations. The final chapter outlines the numerical approaches or thermodynamic equilibrium calculations conducted in this study.

3.3.1 Feedstock characterisation

The ultimate analysis of the biofuels listed in Table 3.1 (Chapter 3.1) was carried out in an institute at FZJ[1]. The major elements were analysed using CHNOS elemental analysis method (Leco 600): approximately 2.5 mg of sample material was burned in the CHN mode for three times, approximately 2 mg sample was burned in the O mode for three times and approximately 20 mg was burned in the S mode for three times in the elemental analyser. For the determination of C and S, the sample was burned in flowing oxygen by radiofrequency heating after the addition of combustion aids and, if necessary, substances making it electrically conductive. The reaction products CO – after conversion into CO_2 and SO_2 were determined via their infrared absorption. For the analysis of O, N, and H, the samples were heated in flowing helium gas in a graphite crucible by means of resistance heating. Oxygen was determined as CO_2, hydrogen was determined as H_2O by infrared absorption, and nitrogen by thermal conductivity detection.

The minor elements were detected by atomic emission spectroscopy (ICP-OES, Thermo Scientific iCAP7600): two weights of each 50 mg were mixed with 0.25 g lithium borate in Pt/Au crucibles and heated up to 1000 °C in a muffle furnace within 3 h. The mixture was then digested for approximately 30 min at this temperature. Each melt was subsequently dissolved in 30 mL HCl (5 %) and filled up with water to 50 mL volume. For the determination, two aliquots of the obtained sample solution were diluted in a ratio of 1:20 and analysed afterwards.

The trace elements, mainly composed of heavy metals, were analysed by inductively coupled plasma mass spectrometry (ICP-MS). The digestion solutions were adopted from the ICP-OES section. Three aliquots per sample were analysed by ICP-MS.

[1]Forschungszentrum Jülich, Central Institute of Engineering, Electronics and Analytics (ZEA), Division Analytics (ZEA-3)

The chloride content was analysed by ion chromatography. The sample preparation was as follows: approximately 150 mg sample was shaken upside down in 10 mL Milli-Q water for 24 h, then centrifuged, filtered and analysed by ion chromatography (setup information: anions: Dionex ICS-3000; column AS23; eluent 0.8 mmol $NaHCO_3$ plus 4.5 mmol Na_2CO_3).

3.3.2 Fundamentals of molecular beam mass spectrometry (MBMS) for hot gas analysis

Molecular **B**eam **M**ass **S**pectrometry (MBMS) was employed for real-time determination of gaseous species in the release experiments (as thematised in the following Chapters 3.3.3 and 3.3.4) in this work. The general technique of a MBMS is based on common mass spectrometry, which analyses the mass-to-charge ratios (m/z) of ionised molecules in an electromagnetic field. More specifically, the correct mass m unit is expressed as unified atomic mass unit u.

The mass spectrometer basically consists of four major components: the sample inlet, the ionisation unit, the mass analyser and the detector. A schematic setup of the MBMS is illustrated in Figure 3.6. A sample inlet system is used to introduce the sample directly into the mass spectrometer. Regardless of whether the sample is a liquid or solid, it must always be vaporized before proceeding with the subsequent analysis steps. Following this, the gas is ionized, which can be achieved through various methods, such as chemical ionization or electron impact. Once the molecules are ionized, they are accelerated by an electric field towards the mass analyser. There are two primary types of mass analysers: sector field or quadrupole mass spectrometer. Subsequently, the ions are separated in an electromagnetic field based on their mass-to-charge ratios (m/z). After the ions have been separated, they are collected by a detector, e.g. an electron multiplier or a Faraday cup. The generated ion flux is converted into an electrical current, before it is recorded by appropriate computer software and translated into signal intensities. The main advantage of MBMS is that it allows for the continuous analysis of gases at higher pressures and temperatures. [179].

The multistage setup of the recipient consists of three differentially pumped vacuum chambers. This setup allows mass spectrometric studies of condensable (gaseous) species. Two Osaka Helical Groove turbomolecular pumps evacuate the first chamber to 10^{-2} mbar. Four additional Pfeifer turbomolecular pumps are connected to the second and third chambers. They evacuate the two subsequent chambers to 10^{-6} mbar and

10^{-8} mbar, respectively. The gas to be analysed is sucked into the first chamber according to the vacuum through a front opening with a diameter of 0.3 mm. The gas entering through the nozzle expands abruptly and tries to adapt to the lower chamber pressure, during this process the thermal energy of the gas is converted into kinetic energy. This adiabatic free-jet expansion is the basis for the formation of a molecular beam in the MBMS system [180, 181]. A comprehensive analysis of the technical functioning of an MBMS instrument and the underlying physical principles governing its operation can be found in the literature [182–184].

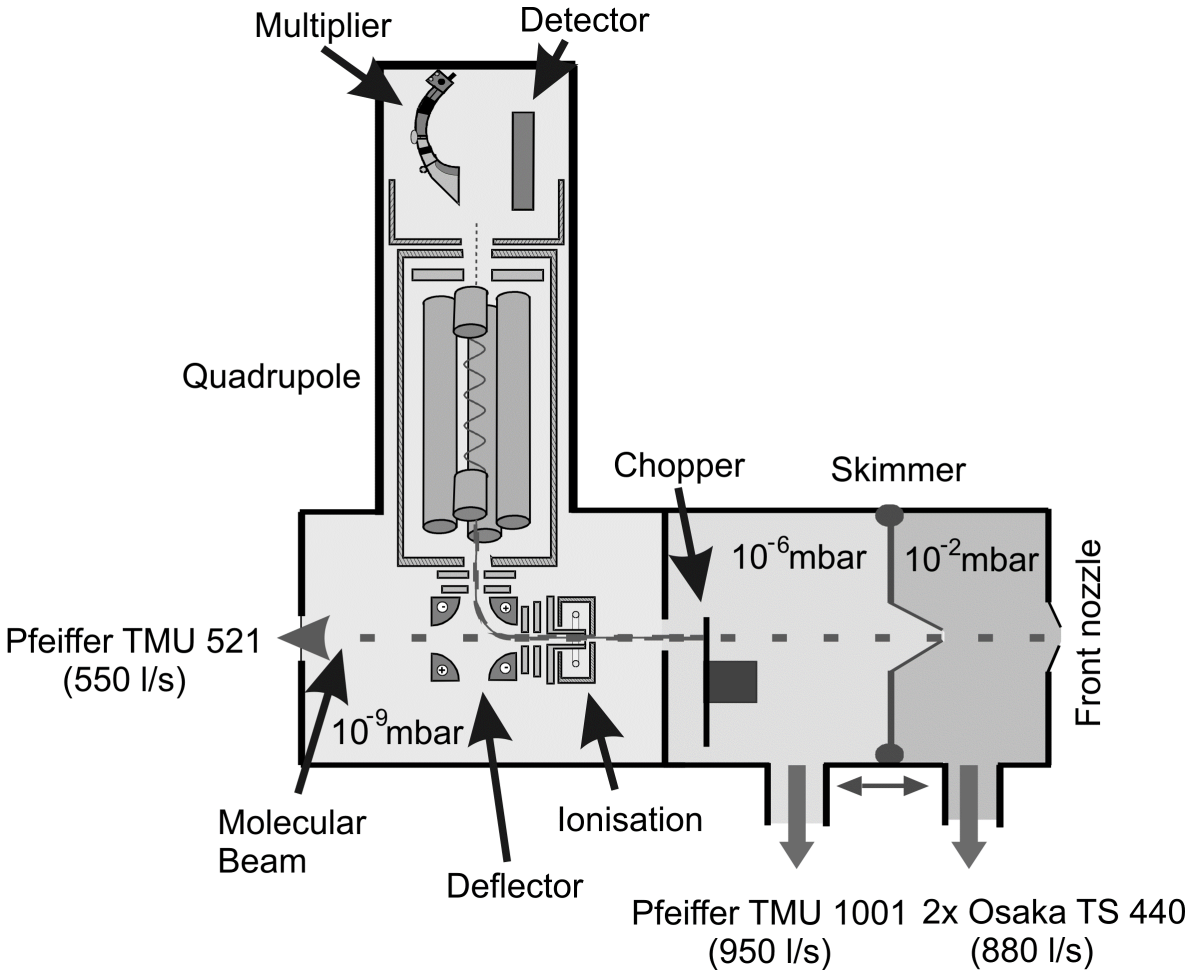

Figure 3.6: Schematic setup of the molecular beam mass spectrometer. Adapted from Bläsing [185].

3.3.3 Analysis of hot gases using MBMS (batch-type experiments)

A MBMS system was employed to determine the product gas composition. The fundamental principles and technical and physical background are described in Chapter 3.3.2. The key setup parameters of the MBMS are listed in Table 3.5. The multiplier voltage ranged from 1600 V to 2500 V throughout the study.

Table 3.5: General setup parameters: recipient, cathode, and optical characteristics for the MBMS.

Recipient	Front nozzle	0.3 mm
	Skimmer	1.0 mm
	Aperture chamber	1.5 mm
Ionisation (Cathode)	Electron energy	−70 V to −50 V
	Electron emission	0.8 mA
Lens (Optic)	Ion region	12.5 V to 30.0 V
	Extractor	−46 V to −29 V
	Lens 1/3	−245 V to −62 V
	Lens 2	11 V to 23 V
	Quadrupole entrance	−1 V
	Quadrupole exit	−62 V to −2 V
	Dynode voltage	4000 V to 5000 V
	Dynode polarity	negative

It is noteworthy that the setup parameters were remarkably similar for both batch-type and continuous release experiments, as described in Chapter 3.3.4.

Small batch-type release experiments were conducted in a flow channel reactor furnace, where the electrical heated flow channel reactor was coupled to the MBMS system for the analysis of product gas composition. The experiments simulate the thermal conversion of biofuels under gasification-like conditions. The experimental setup of the flow channel furnace is schematically illustrated in Figure 3.7.

The experiments were conducted in a gasification-like atmosphere at a constant temperature of 950 °C. The ceramic tube, situated inside the furnace, was directly connected to the MBMS nozzle, where the hot gas entered the MBMS. Within the first two zones at 950 °C, the gasification of the biofuel samples was carried out. A small amount of weighed fuel sample (80 mg in each case) was placed in a small platinum bowl and in-

serted airtight using a corundum slide bar into the temperature-calibrated zone. To ensure semi-quantitative analysis, the weight of the samples was kept constant throughout the measurements. The penultimate temperature zone was set at 1400 °C to crack hydrocarbons, as only inorganic compounds were of interest. The gas composition was determined under gasification-like conditions, resulting in 15 vol% steam and 5 vol% CO_2 (as mentioned in Chapter 3.2). In addition to these gases, helium (80 vol%) was chosen as an inert carrier gas to increase the resolution of the MBMS and was humidified with water. The total gas flow rate was 4 L min^{-1}. The residence time of the gas until it reached the MBMS unit was approximately 0.7 s. This was calculated considering a ceramic tube (Fig. 3.7) with a diameter of 25 mm and a length of 870 mm, with the sample placed in the middle of the tube. The calculation also took into account a temperature difference of 925 K relative to room temperature (298 K).

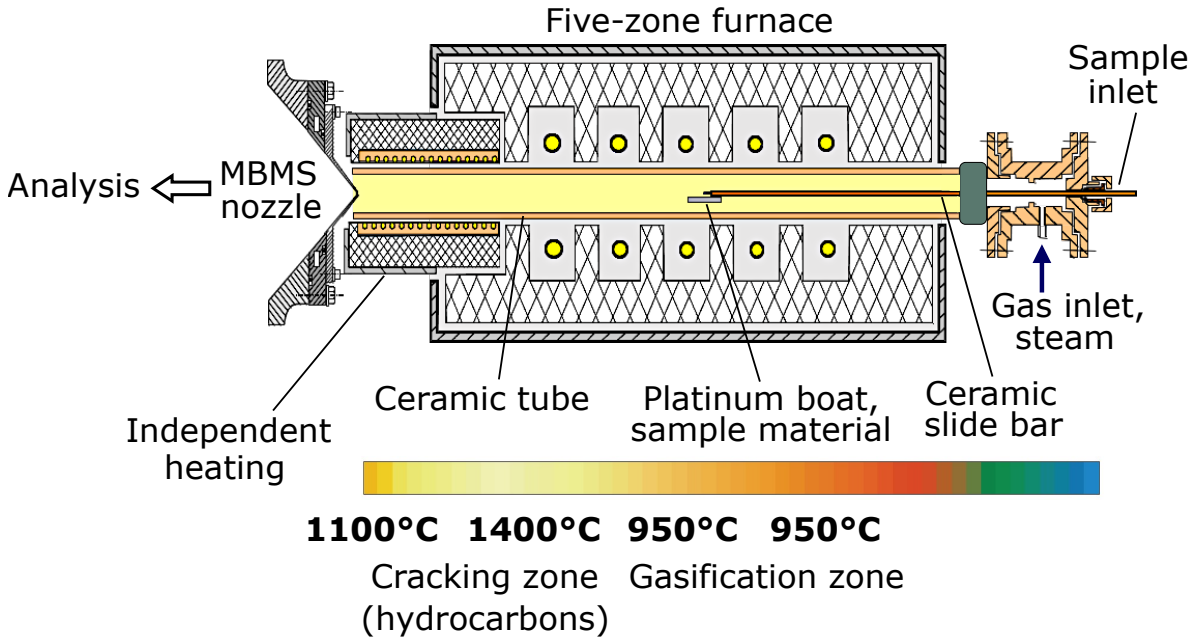

Figure 3.7: Schematic of the technical setup of the flow channel reactor furnace, showing the placement of the sample within a ceramic tube. Adapted and modified from Porbatzki [186].

Three measurements were performed for each fuel sample, and an additional full spectrum was recorded for a general overview. The species of particular interest, along with their mass-to-charge ratios (m/z), are listed in Table 3.6.

Due to software limitations, 20 different species had to be set for each measurement campaign. However, the determined species were consistently maintained throughout the study. The scanning parameters were monitored using the ABB Extrel Merlin Automation Data System (version 4.0) software, providing ultimate control over the process. The collected multiplier signals were evaluated as a function of time and mass-to-charge ratio.

Table 3.6: This table presents the m/z ratios of various inorganic species investigated using MBMS. Additionally, certain isotopes were also considered in the analyses.

Element	**Ionised species and corresponding m/z ratios**
C	$^{23}CO_2{}^{++}$ (taking account of ^{18}O isotope), $^{60}COS^{+}$
K	$^{39}K^{+}$, $^{74}KCl^{+}$, $^{55}KO^{+}$, $^{97}NaKCl^{+}$, $^{113}K_2Cl^{+}$
Na	$^{23}Na^{+}$, $^{39}NaO^{+}$, $^{58}NaCl^{+}$, $^{60}NaCl^{+}$ (taking account of ^{37}Cl isotope), $^{81}Na_2Cl^{+}$, $^{97}NaKCl^{+}$
P	$^{47}PO^{+}$, $^{62}P_2{}^{+}$, $^{63}PO_2{}^{+}$, $^{110}P_2O_3{}^{+}$, $^{126}P_2O_4{}^{+}$, $^{142}P_2O_5{}^{+}$
S	$^{34}H_2S^{+}$, $^{60}COS^{+}$, $^{64}SO_2{}^{+}$
Cl	$^{35}Cl^{+}$, $^{37}Cl^{+}$, $^{36}HCl^{+}$, $^{38}HCl^{+}$ (taking account of $^{37}Cl^{+}$ isotope)

The standard $CO_2{}^{+}$ peak intensities, as well as those of the corresponding double ionized peaks, were excessively high due to the necessary adjustment of the multiplier voltage. As a result, the intensity of CO_2 containing one ^{18}O isotope ($^{23}CO_2{}^{++}$ with a mass-to-charge ratio of 23) was used as a normalisation signal. In addition to qualitative analysis, semi-quantitative analysis via peak integration was also performed. The inorganic species of particular interest are listed in Table 3.6, and exemplary intensity-time profiles for each species are presented in Figure 3.8. As evident in Fig. 3.8, many species exhibit a significant release behaviour, as seen in the spectrum of m/z 39 ($^{39}K^{+}$) and other examples. In contrast, some species appear only as background noise, such as the m/z 47 signal ($^{47}PO^{+}$). This suggests that the background noise does not correspond to any reaction or release.

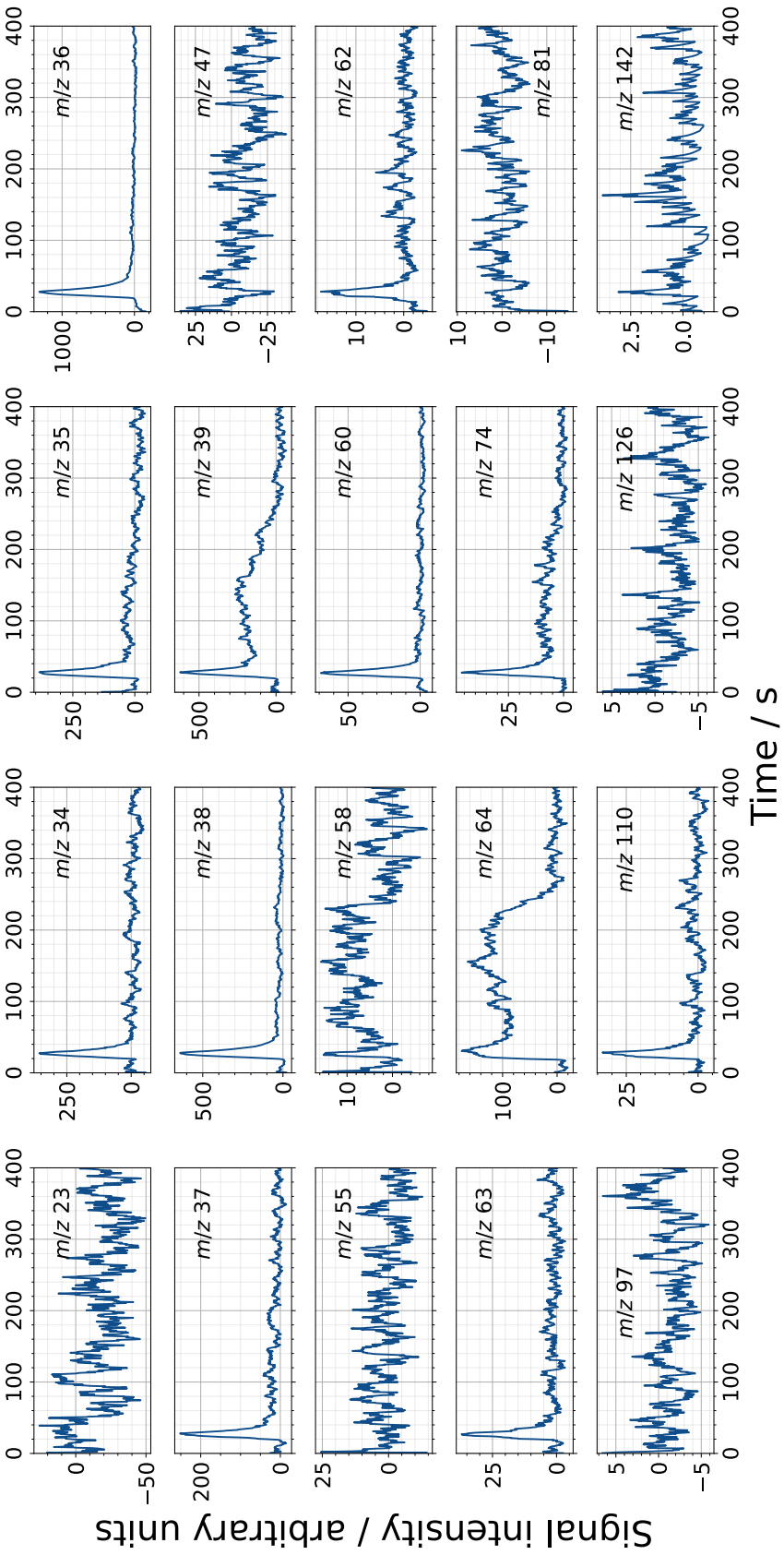

Figure 3.8: Representative intensity-time profiles of recorded species from the raw wheat straw data, as listed in Table 3.6. This figure illustrates exemplary the spectral data collected from the analysis.

3.3.4 Laboratory-scale fluidised-bed reactor for continuous release experiments

Building on the small-batch experiments that focused exclusively on the release of inorganic compounds (Chapter 3.3.3), this work also conducted continuous release experiments using an oxygen carrier. To achieve this, a fluidised-bed reactor was designed to simulate the CLG process.

The reactor comprised two main components: a lower glass section with a feeding and mixing zone, and an upper alumina section featuring a fluidised bed and a cracking zone for hydrocarbons. A detailed illustration of the entire fluidised-bed laboratory reactor is presented in Figure 3.9.

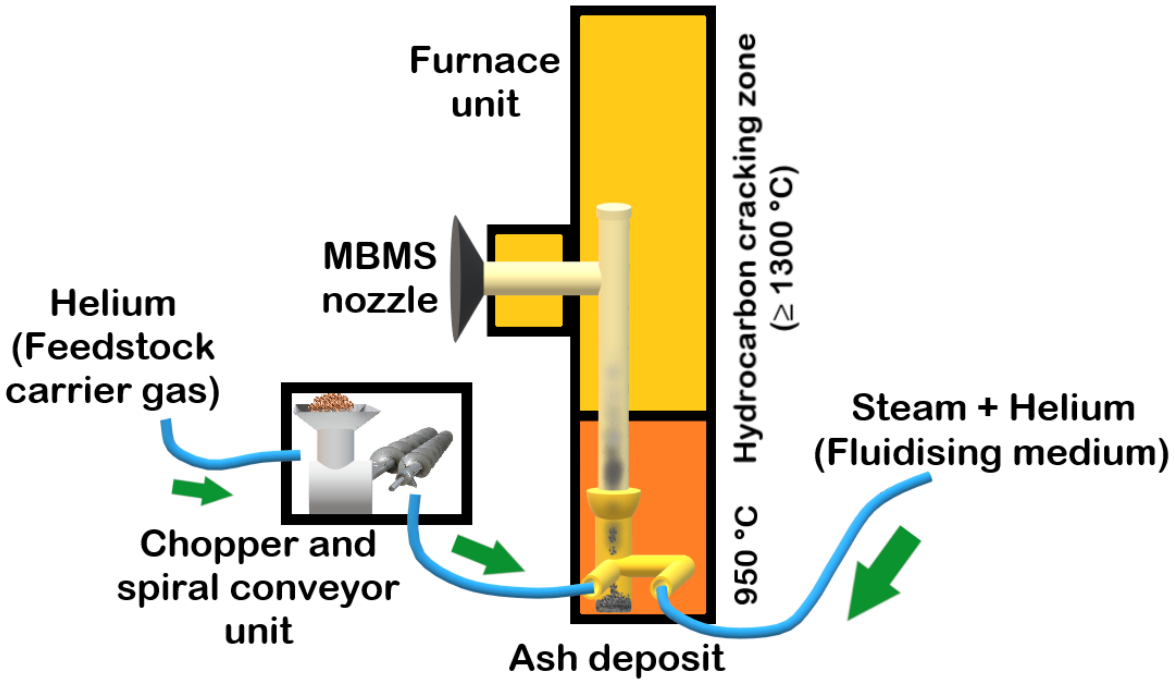

Figure 3.9: Schematic of the laboratory scale fluidised-bed reactor used in this work, featuring a chopper and spiral conveyor unit on the left side. The quartz glass reactor is situated at the base of the reactor and is centrally located within the gasification zone, which operated at a temperature of 950 °C.

The reactor was constructed from heat-resistant quartz glass and was designed for continuous operation under high-temperature conditions, specifically at 950 °C. The fuel inlet was water-cooled to prevent or mitigate pyrolytic reactions during the feeding process. The feedstock was blown towards the reactor core unit, where a metal pipe was inserted to ensure a consistent fuel transport mechanism. The metal pipe, which

was constantly cooled with water, allowed for a higher pressure to be applied to the fuel transport, thereby enhancing the mechanism. The fuel transport was supplied with helium gas at a rate of 2.5 L min^{-1}, and the velocity of the fluidisation medium (helium and 15 % steam) was maintained at 2.5 L min^{-1}. The total gas flow rate was 5 L min^{-1}, taking into account the necessary pressure for the MBMS system. The fluidising medium was introduced through the bottom of the core unit, where it suspended the solid particles and created a fluidised state. The fluidised bed was located in the lower part of the alumina reactor, which was mounted on top of the glass part. The upper part of the reactor was made of ceramic to minimise unfavourable chemical side reactions with volatile alkali compounds. After gasification, the formed ash fell through the side of the funnel and deposited on the reactor floor. Figure 3.10 shows images of the quartz glass reactor.



Figure 3.10: Left: overview of the quartz glass reactor, designed for laboratory-scale fluidised-bed reactor experiments. The injector was constantly water-cooled to prevent pyrolysis of the fuel. Centre: close-up of the reactor core unit, showcasing both the reaction zone and the ash deposition zone, which is located beneath the glass funnel. Right: top-view illustration of the reactor core unit.

As is typical in the CLG process, the oxygen carrier itself served as the bed material. Iron oxide (Fe_2O_3) was selected as oxygen carrier material, and fuel samples were blended with iron oxide with a weight ratio of 0.48 wt%/wt%. The diameter of the oxygen carrier grains amounted to 100 µm. The gasification temperature was set at 950 °C, and the hydrocarbon cracking zone in the upper part of the reactor was set at ≥1300 °C (as only inorganic species were focused on in this study). The fuel samples, blended with iron oxide, were filled into a pulsating metal funnel in order to let the pulverised material enter the chopper unit, where a uniform mixing was provided. A spiral conveyor unit was designed for uniform fuel transport, and the feeding rate was set to 0.5 g min^{-1}. The conveyor mechanism (left-hand part in Fig. 3.9) was placed inside an airtight box made of acrylic glass, and the box had to be opened before new sample material was filled

in and analysed. The chamber was constantly flushed with helium carrier gas in order to built up a pressure and thus, providing a constant feedstock transport into the inner part of the glass reactor. Thus, a steady state operation was maintained. A ceramic tube was connected with the nozzle of the MBMS in order to let the gaseous species entering the MBMS system for analysis. All species were analysed in real-time, according to their mass-to-charge ratios (analogous to the batch-type experiments expounded in Chapter 3.3.3).

3.3.5 Determination of N-species

A quartz glass single-particle reactor (SPR) was used to investigate the combustion and gasification-like properties of biomass-based fuels. The technical setup of the SPR is illustrated in Figure 3.11.

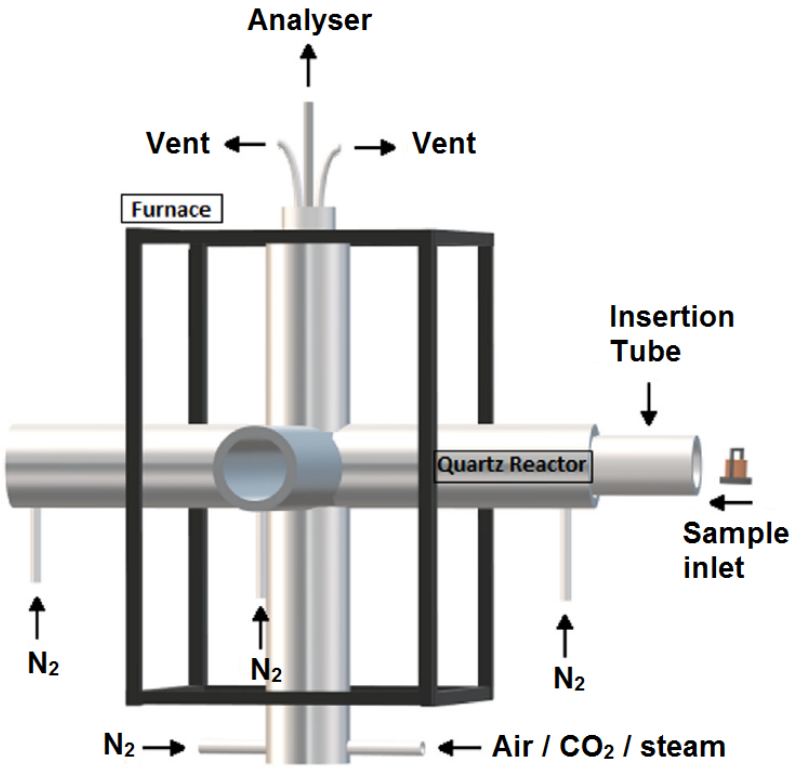

Figure 3.11: Schematic of the single-particle reactor (SPR) used in the experiments (designed by ÅAU, Finland). The black frame represents the electrically heated furnace (T_{iso} = 950 °C). The gas supply was varied to produce either oxidising or reducing atmospheres. Modified after Schmid et al. [144].

The quartz tube reactor was inserted in a heated ceramic furnace. The reaction gases were fed with a constant flow rate of 100 $NL\,h^{-1}$ from the bottom of the reactor and inert gas (nitrogen) from the sides of the reactor with a flow of 120 $NL\,h^{-1}$, resulting in a total flow of 220 $NL\,h^{-1}$. The product gases left at the top of the reactor. Figure 3.12 presents an overview (including the photometers) of the working station.



Figure 3.12: Overview of the working station, which comprises an electrically heated SPR unit on the left and photometers for monitoring output gases on the right.

For experiments with the SPR, samples were pressed into uniform, cylindrical pellets (with a fixed pressure of 49 kN) having a diameter of 8 mm and a mass of 200 mg (for NO quantification) and 400 mg (for NH_3 and HCN quantification). The sample pellets were

placed at the center of the quartz reactor using an insertion tube. To minimise potential effects of varying temperature gradients, the size of the sample pellet was maintained constant. The concentrations of the product gases were measured continuously: CO, CO_2, O_2, and NO. Oxygen was measured using a combined IR and paramagnetic analyser, CO and CO_2 using an on-dispersive IR analyser, and NO using a chemiluminescence analyser. The residence time from the reactor to the gas analyser was 3 s.

The SPR reactor has been used in several previous studies. A more detailed description can be found elsewhere [144, 187–189]. The char content was determined gravimetrically in pure nitrogen atmosphere and at 950 °C, while the char-N content was determined from the remaining nitrogen in the char afterwards. The present work used a special setup for collecting both NH_3 and HCN, based on a wet chemistry method, which is also described in [144]. For the analysis of released NH_3, the flue gas was directed to an ice-cooled HCl solution ($1\,mol\,L^{-1}$) in order to collect NH_3 in the form of NH_4^+. HCN was collected in an ice-cooled NaOH solution ($1\,mol\,L^{-1}$). For determination of the release of NH_3 and HCN during devolatilization, each experiment with the 400 mg pellets was repeated 20 times to ensure sufficient amounts of absorbed NH_3 and HCN in the solutions (HCl or NaOH) for subsequent chemical analysis. Both ammonium and cyanide ions were quantified by spectrophotometry.

Three types of thermal experiments were conducted: gasification, combustion and devolatilization experiments. The devolatilization experiments were conducted in 100 vol% N_2, the gasification-like experiments in 14.5 vol% steam and 5 vol% CO_2, and the combustion experiments in 3 vol% O_2. Additional experiments were conducted using various gas compositions, including 5 vol% CO_2 and 3 vol% O_2, as well as 14.5 vol% steam, 5 vol% CO_2 and 3 vol% O_2. These intermediate gas mixtures were selected to enable conclusions about the individual effects of each gas component and the specific interactions between the components on nitrogen chemistry. In each experiment, N_2 was used as the balance gas to ensure that all gas mixtures were at the same total volume.

For each experiment, a single pellet was placed on a glass sample holder and inserted into the reaction zone, which was set at 950 °C. The pellet was kept in the reactor until the combustion or gasification process was complete. The reaction sequence was validated by monitoring the NO concentration in the product gas. The amount of NO released was quantified through peak integration and partitioned into two distinct parts, devolatilization and char conversion/ash reaction. Each experiment was repeated three times, and the standard deviation of the NO concentration emitted was calculated to estimate the error dispersion. The consistency of the NO concentration deviations throughout the sequence of experiments indicates a homogeneous sample composition.

The devolatilization experiments were conducted in pure N_2 for 2 min. The residual char was collected and subsequently analysed using CHNS analysis to determine the remaining nitrogen content. Both the nitrogen content in the residual char (char-N) and the volatile nitrogen (volatile-N) released during devolatilization were investigated. Additionally, the amount of nitrogen removed from each sample was quantified through CHNS analysis of the pre-treated samples.

3.3.6 Hot stage microscopy (HSM) for ash fusion testing

Hot stage microscopy (HSM) enables the determination of the melting behaviour of ashes according to DIN 51730. HSM is a valuable tool for studying the physical features and morphology of a sample under investigation, taking into account environmental conditions and temperature. Figure 3.13 shows the technical setup of the HSM used in this work.

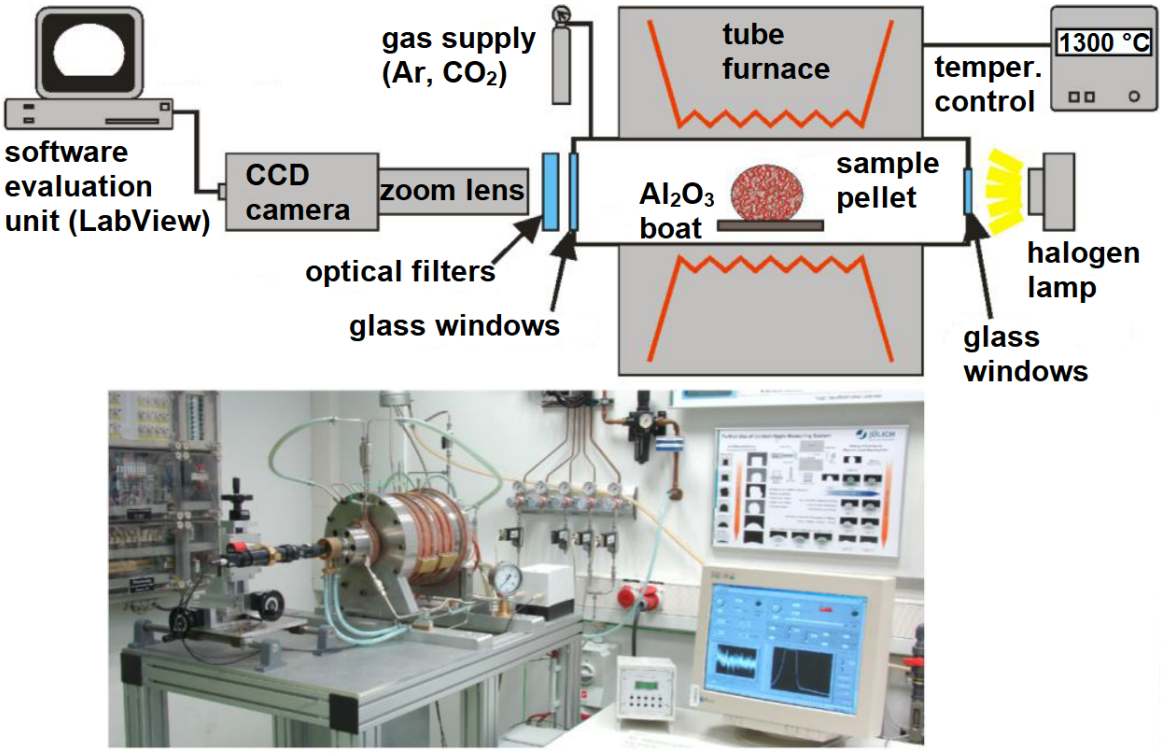

Figure 3.13: Technical setup of the hot stage microscope (top), and a photograph of the working station (bottom). Adapted and modified from Schupsky [190].

Based on the collected data indicating changes in the sample geometry, HSM enables observation of the wetting behaviour of melts – such as slags or molten salts – on various materials, as well as the corrosion of those materials by the melts. The primary objective was to identify and characterise the temperature-dependent phases, which correspond to changes in the sample geometry and cross-sectional area, as ash samples were heated up to 1300 °C.

Sample pellets were prepared from the ashes of pre-treated biomass fuels (refer to Chapter 3.2). The ash was pressed into cylindrical pellets with a diameter of 5 mm (left-hand photo in Figure 3.14). A constant load of 1.5 kN was applied to each sample series throughout the study. Preliminary tests revealed that the ash pellets tended to crumble upon pressing, which is why one drop of pure isopropanol was added as a surfactant to maintain pellet stability during pressing and placement in the testing setup. The carbon content of the ash samples varied (which affects the bulk density of the sample material), resulting in a sample height range of 4 mm to 7 mm. To ensure consistency, the same amount of ash was weighed for each sample preparation. The cylindrical sample pellet was placed centrally within a temperature-calibrated tube furnace. Most of the ash samples were fully molten after measurement completion at a temperature of $T_{max} = 1300\,°C$, exhibiting a glass-like structure (right-hand photo in Figure 3.14)



Figure 3.14: Left: ash-based sample pellet for ash fusion testing. The dark shade of the material suggests a relatively high carbon content in the ash. Right: the molten sample after measurement at $T_{max} = 1300\,°C$.

The gas flow was introduced from the furnace inlet, and a mixture of pure argon gas (87 vol%) was added to create an inert gas environment during the measurements. Additionally, based on preliminary thermodynamic equilibrium calculations, a defined amount of 13 vol% CO_2 was mixed with argon gas to maintain the stability of any possibly formed carbonates. The tube furnace was heated at a constant rate of $5\,K\,min^{-1}$ from room temperature to 1300 °C. A CCD camera was positioned behind the furnace outlet, and one sample image was captured per degree Celsius, starting from 550 °C.

The evaluation of the results was conducted in accordance with the work of Pang et al. [191], and the coefficient h_x/h_0 was calculated based on the height change of the sample specimen (h_0 = initial height of the pellet). A customised LabView program by Dohrn [192] (National Instruments, Austin, U.S.) was used to evaluate the change in sample shape (height ratio of the pellet) as a function of temperature change. Based on this information, essential conclusions can be drawn about the ash melting behaviour. The sample specimens exhibited diverse characteristic shapes during the measurement, which corresponded to the temperature level and provided indications on the melting process, as shown in Figure 3.15.

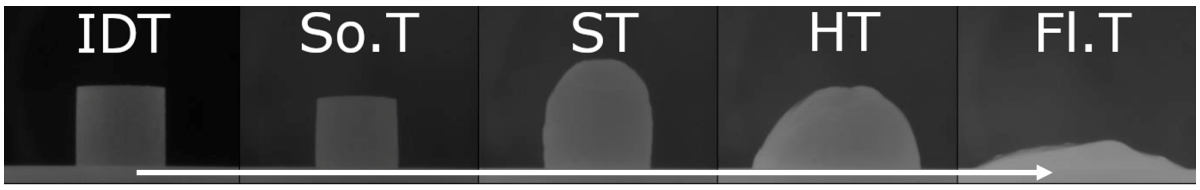

Figure 3.15: Characteristic ash transformation points, which are typically observed at various temperature levels, are shown. The points include the initial deformation temperature (IDT), softening temperature (So.T), spherical temperature (ST), hemispherical temperature (HT), and flow temperature (Fl.T). The arrow indicates the increasing temperature from left to right. Adapted and modified from Dohrn [192].

The following characteristic ash transformation points were identified: initial deformation temperature, softening temperature, spherical temperature, hemispherical temperature, and flow temperature. It is crucial to note that DIN 51730 represents ideal conditions, implying that each biofuel exhibits a unique ash melting behaviour. This can sometimes pose challenges when interpreting or comparing data, as the detailed understanding of the results requires careful consideration of the sample geometry and temperature profiles. The temperature profiles are defined by the sample geometry and are described in detail in references [193–195]:

- **Initial deformation temperature** or **softening temperature**. Temperature at which first signs of rounding occur, due to melting of either the tip or edges of the sample specimen.
- **Spherical temperature**. Temperature at which the edges of the pellet become completely round, and the height is becoming equal to the width of the baseline.

- **Hemispherical temperature**. Temperature at which the sample becomes approximately hemispherical, the height being equal to half the pellets base diameter.

- **Flow temperature**. Temperature at which the sample material has spread out so that its height is about one-third of that at the hemispherical temperature.

The sample shrinks slightly until it reaches the softening temperature. A further increase in temperature intensifies the melting process, and the geometry of the sample reaches a spherical shape, followed by a hemispherical shape. It is likely that most of the ash is molten in this state. Once the flow temperature is reached, the sample is found to be completely molten ("liquid state").

3.3.7 X-ray powder diffraction (XRD)

The application of X-ray diffraction investigation is an indispensable tool for the structure determination of crystalline solids. A crystal represents a natural diffraction grating, since the wavelength of X-rays corresponds to the interplanar spacings of a crystal lattice. The wavelength of X-rays is typically in the range of 1 nm to 30 pm [196]. The smaller the wavelength, the greater the frequency and thus the energy of the radiation particle. Figure 3.16 displays two X-rays incident on a atomic plane in parallel to each other at any diffraction angle θ. A specified distance of the atomic plane is defined as d. If the path difference $2\,\Delta$ corresponds to the integer multiple of the irradiated wavelength of the X-rays, constructive interference results. This means that destructive interference occurs when the waves are out of phase.

Figure 3.16 shows the Bragg's reflection condition, which is mathematically described by Bragg's equation (Equation 3.3). The equation gives the conditions for constructive interference [197]:

$$n \cdot \lambda = 2\ d \cdot sin(\theta) \text{ where } n = 0, 1, 2, 3\ ... \tag{3.3}$$

The diffraction order is defined by the integer variable n, and the wavelength of the X-rays is given by λ. The primary focus of the diffractometric investigations in this work was the identification of the crystalline phase compositions of the biofuel ash samples. The lattice constant of the crystallographic unit cell can be derived from the determined lattice plane spacing d_{hkl}, provided that the crystal system is known. The Laue indices hkl indicate the position of the array of parallel lattice planes in the crystal lattice,

and at the same time the diffraction order n. For a standard cubic crystal system, Equation 3.4 describes the Laue indices accordingly:

$$\frac{1}{d_{hkl}^2} = \frac{h^2 + k^2 + l^2}{a^2} \tag{3.4}$$

If the spacing of the atomic plane d is known, the lattice constant a of the unit cell can be calculated by assigning the reflections to the individual atomic planes (hkl-reflections).

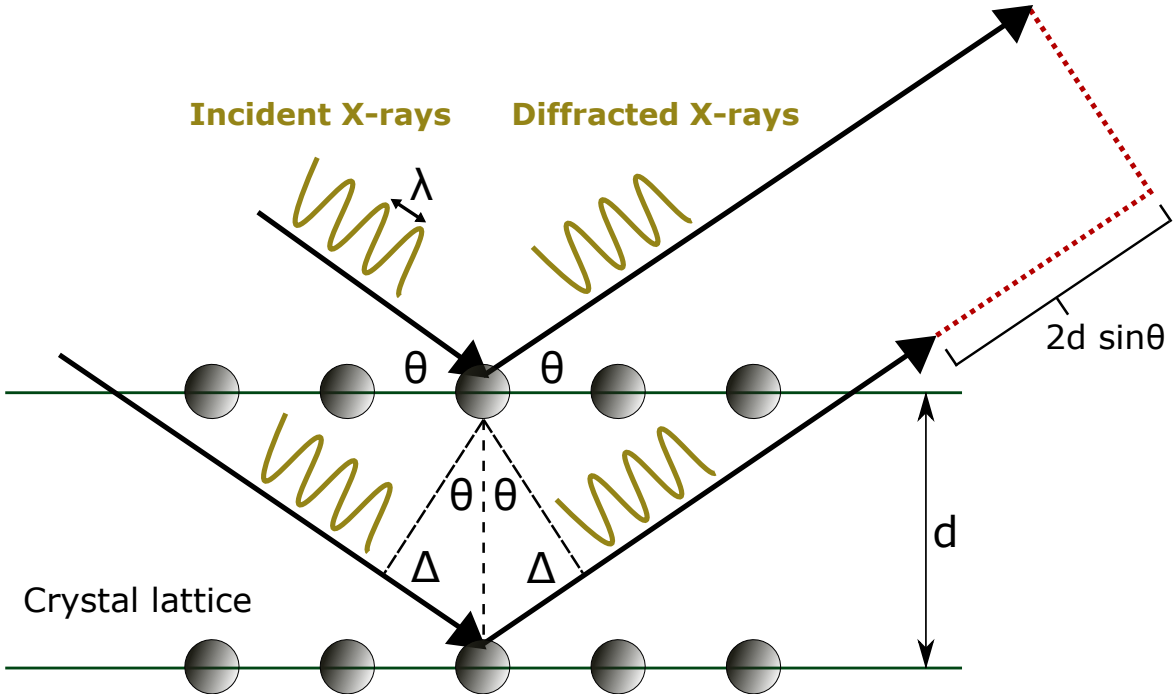

Figure 3.16: Schematic sketch of any crystal atomic plane, illustrating Bragg's reflection condition, as seen in [198].

Several measurements of pre-treated biofuel samples were conducted using XRD analysis to determine the crystallized phases structurally. Both diffractometers, D8 ADVANCE (Bruker) and EMPYREAN (PANalytical) were employed, and a copper K_α anode X-ray tube (Cu-LFF-tube, 40 kV, 40 mA) was installed during the measurements. A conventional parafocusing Bragg–Brentano geometry was used, which gives well-defined diffraction angles for finite slit widths and beam divergences [199]. Both time per step and step size were dynamically adjusted to the sample requirements and were generally between 0.5 s and 30 s or 0.013° and 0.05°, respectively.

Each sample was investigated in powder form, and the sample analyses were performed in-house[2]. The detected spectra for each sample were compared with datasets from the ICSD (Inorganic Crystal Structure Database, FIZ Karlsruhe, Germany) in order to determine the crystallised phases in the corresponding samples. In the case of quantitative phase analysis, Rietveld refinements were performed (software TOPAS v.6, Bruker AXS, generally using crystal structures published in the ICSD). In the Rietveld method, the whole pattern of diffracted intensity, the diffraction profile, as a function of the diffraction angle 2θ is computed for the model [200].

[2]Forschungszentrum Jülich, Institute of Energy and Climate Research, Structure and Function of Materials (IMD-1), Division Scanning and Analytical Electron Microscopy

3.4 Numerical thermodynamic equilibrium predictions

Numerical thermodynamic prediction is considered as a low-cost and fast generation method for understanding the release and fate of inorganic gaseous species as well as mineral phases formation. This method can be applied to compute the equilibrium composition of one investigated system under clearly defined conditions (in compliance with consistent parameters, such as temperature, atmosphere, pressure or volume).

In thermodynamics, the Gibbs free energy G is regarded as a thermodynamic potential that quantifies the acquired or process-initialising work from an isobaric and isothermal thermodynamic system. Hereby, G combines enthalpy and entropy into a single value. Equation 3.5 represents the classical Gibbs-Helmholtz-equation, where ΔG equals the change in Gibbs free energy and H the enthalpy, the absolute temperature T and the entropy S:

$$\Delta G = \Delta H - T \cdot \Delta S. \tag{3.5}$$

Using Equation 3.5, the change of free energy ΔG allows to predict essential information about any chemical reaction as listed in the following:

- $\Delta G < 0$: exergonic process, indicating a spontaneous reaction,
- $\Delta G > 0$: endergonic process, indicating an unfavourable or non-spontaneous reaction,
- $\Delta G = 0$: reaction is in equilibrium.

In order to obtain the minimum of the Gibbs energy of one system (in due consideration of constant temperature and pressure), taking account of the number of moles of each component in each phase n_i^k, the phase equilibrium can be calculated for a system with the number of NP phases and NC components [201]:

$$G = \sum_{k=1}^{NP} \sum_{i=1}^{NC} n_i^k \mu_i^k \tag{3.6}$$

The number of moles of component i in k phase is represented by n_i^k, and μ_i^k represents the chemical potential of component i in k phase. Thus, μ_i^k is a function of k phase composition, temperature and pressure.

FactSage™ is a powerful thermodynamic computation tool for determining gaseous, solid or liquid phase formations as well as reaction equilibria. It is a thermochemical software and database package developed jointly between Thermfact/CRCT (Montreal, Canada) and GTT-Technologies (Aachen, Germany). The computer package consists

of a series of information, calculation and manipulation modules that enables to access and manipulate compound and solution databases [202]. The thermodynamic databases integrated in FactSage are based on CALPHAD (**Cal**culation of **Pha**se **D**iagrams) predispositions and cover the entire spectrum from oxides to metallic alloys, salts or aqueous solutions [203]. The operating principle is based on different types of algorithms, e.g. the *Equilib* module, which is used for treating complex heterogeneous equilibria and grounded on Gibbs free energy minimisation. With the aid of Gibbs energy minimisation, computation of the most stables phases assemblages in a heterogeneous system (i.e. multiphase and multicomponent equilibrium) can be completed easily. The chemical equilibria represent a temporal indefinitely state where the properties remain stable. Incomplete or slow reaction sequences can therefore not be solved numerically. In addition, the results depend on the quality of the substance databases [204].

All calculations performed in this work were conducted using FactSage™ 7.3 (**F**acility for the **A**nalysis of **C**hemical **T**hermodynamics) thermochemical software and databases [202]. The FactSage package consists of a broad series of calculation modules as well as commercial databases. The commercial database SGPS was used for pure gaseous and some solid stoichiometric compounds. Those data originate from a collection of thermochemical data of pure substances of the SGTE organisation (Scientific Group Thermodata Europe). Additionally, the latest version of the GTox database was implemented for calculations. GTox is a private database [205, 206], developed by a cooperation of FZJ[3] and GTT-Technologies (Aachen, Germany). The chemical compositions of the corresponding fuel ashes (as obtained from the ultimate analysis, Chapter 3.3.1) were taken for thermodynamic equilibrium calculations. The data was normalised to 100 wt% before in order to allow direct comparisons of the final results. Equilibrium (*Equilib* module) calculations were conducted in the temperature range of 400 °C to 1300 °C. It is important to mention that if the calculated temperature of a compound fell outside the specified temperature range listed in the corresponding database, the thermodynamic variables were extrapolated.

In order to asses ash-related issues, which were previously discussed in Chapter 2.3, several numerical approaches were designed. Figure 3.17 presents a schematic flowchart in which the calculations substeps altogether are displayed. The thermodynamic model outline comprises a sequence of several equilibrium reactors which were designed to describe crucial parallel operations of the CLG process, with the focus on ash chemistry.

[3]Forschungszentrum Jülich, Institute of Energy and Climate Research, Structure and Function of Materials (IMD-1), Division Thermochemistry

It shall be noted, that only the gasification part of the process is represented by the model, whereas the air reactor for re-oxidation of the oxygen carrier materials is not considered. Moreover, only the stoichiometric lattice oxygen from the oxygen carrier itself has been considered for the equilibrium calculations.

The gas phase composition was predicted to enable the determination of the condensation of volatile inorganics, primarily alkali salts and slag, at operating temperature. The results facilitate drawing conclusions regarding slagging and fouling issues. Ternary phase diagrams featuring the main oxides K_2O, CaO, and SiO_2, as well as phase maps, were predicted to elucidate the formation of mineral phases and the amount of molten slag, which is essential for estimating agglomeration risks. The interactions between oxygen carrier materials and fuel ashes were also predicted to assess the likelihood of oxygen carrier poisoning. All calculations were performed under isobaric conditions at atmospheric pressure.

Both pyrolysis and gasification conditions were of particular interest in evaluating the thermochemical process as a whole. Therefore, phases formation under pyrolysis condition were calculated without addition of steam and oxygen, whereas the phases formation under gasification condition were calculated by adding water (steam:feedstock ratio = $0.5\,\mathrm{g\,g^{-1}}$) and oxygen (Fe_2O_3:feedstock ratio = $0.48\,\mathrm{g\,g^{-1}}$), and these ratios were exactly based on those which have been considered for the experimental investigations or ash sample preparations (Chapter 3.1).

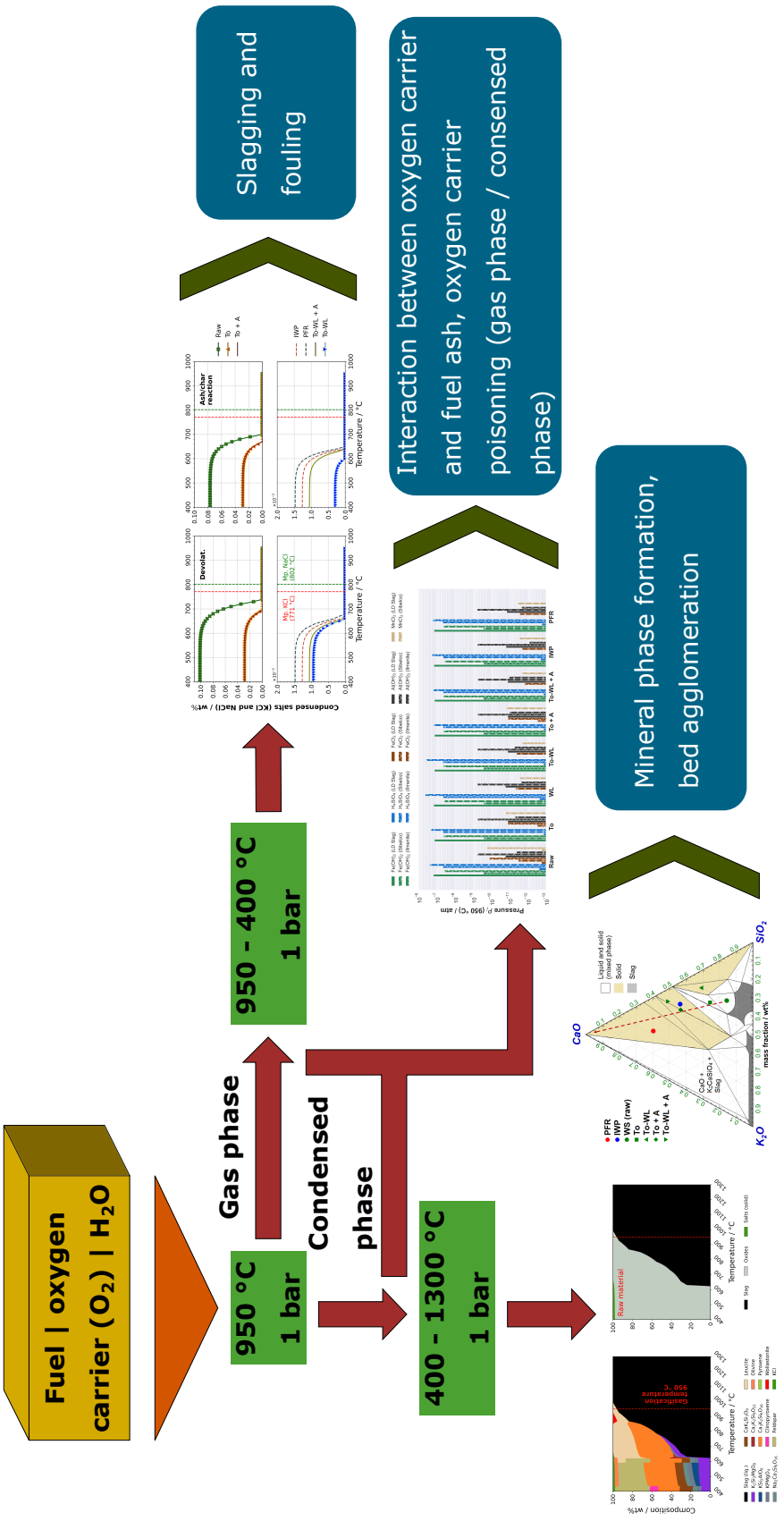

Figure 3.17: Schematic overview of the thermodynamic model conceptualised in this work, divided into three different main categories. All calculation parts were performed under isobaric conditions at atmospheric pressure.

4 Results and Discussions

4.1 Comparison of industrially pre-treated wheat straw with woody biomass

The following chapter provides an overview of the investigations on ash-related issues during gasification conditions, with the main focus on the comparison between industrially treated wheat straw samples and woody biomass in terms of benchmark criteria.

4.1.1 Chemical characterisation of fuels

Pre-treated wheat straw samples and woody feedstocks were provided by project partners from Spain (CENER) within the CLARA project. The ultimate analysis of the upgraded fuels is listed in Table 4.1.

Figure 4.1 presents a summary of the dominant species that are commonly associated with ash-related issues. These inorganic species can be significantly impacted by pre-treatment, as they are primarily present in the form of water-soluble salts.

Raw wheat straw showed a high potassium content, which could be effectively decreased, when the sample was torrefied and post-washed. Likewise, the content of chlorine and sulphur has also been decreased after treatment. Both species, chlorine as well as potassium could be significantly decreased by washing the feedstocks due to their high solubility in water. Sulphur could only be removed partly due to different solubility of several sulphur compounds, e.g. organic sulphur, alkali sulphates and alkaline earth sulphates. It is not surprising that the industrial wood pellets showed in general a noticeably lower fraction of inorganic species compared to the wheat straw feedstock. PFR revealed an increased fraction of calcium as opposed to the other samples, and might therefore be taken into consideration as promising blending component in order to compensate for the calcium content of calcium-poor biomass residues.

Table 4.1: Ultimate analysis of the pre-treated wheat straw samples and woody biofuels obtained from the CLARA project partners in wt% or mg kg^{-1}. The results were not normalised.

wt%	**Raw**	**To**	**To-WL**	**To+A**	**To-WL+A**	**IWP**	**PFR**
Ash (d.b.)	5.70	5.80	5.10	7.30	8.20	0.70	2.00
C (d.a.f.)	48.80	56.40	56.00	54.50	57.50	50.80	52.70
H (d.a.f.)	6.20	5.90	6.10	6.10	6.00	6.00	6.40
N (d.a.f.)	0.40	0.45	0.50	0.30	0.32	0.07	0.34
O (d.a.f.)	44.60	37.30	37.40	39.10	36.20	43.20	40.50
S (d.a.f.)	0.05	0.07	0.04	0.03	0.03	0.01	0.05
Cl (d.a.f.)	230	145	50	50	200	60	70
mg kg^{-1} (d.b.)	Ash forming components (major elements only)						
Al	846	1090	943	1540	1220	62	174
Ca	4060	5550	5140	11700	13700	1300	3390
Fe	860	7890	672	1430	1690	82	134
K	4720	5995	2070	7190	3970	486	1370
Mg	460	1001	775	944	909	232	453
Na	129	116	75	328	418	13	34
P	313	417	223	441	383	94	217
Si	7205	9455	7725	10500	14000	1050	958

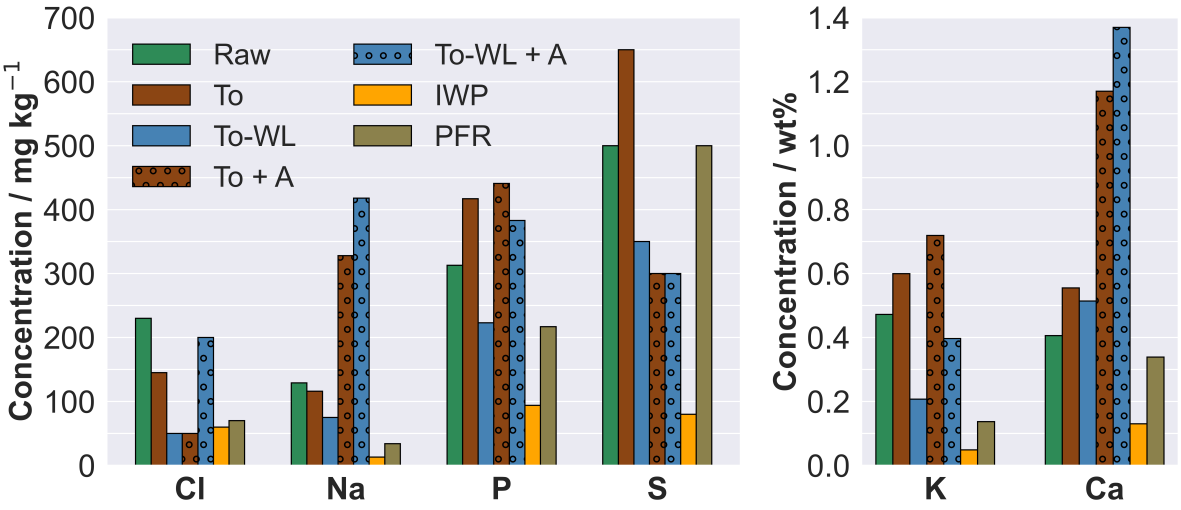

Figure 4.1: Illustration of the dominant species found in the CLARA project's samples, which are commonly associated with ash-related problems. The data is sourced from Table 4.1.

The distinction of ash content displays a clear disparity between woody (IWP or PFR) as well as herbaceous biomass (Table 4.1). As expected, the addition of an inorganic additive, such as 2 wt% $CaCO_3$, to upgraded wheat straw samples has significantly increased the ash content.

4.1.2 Analysis of hot gases using MBMS (batch-type experiments)

Figure 4.2 presents exemplary mass spectra of sulphur dioxide (wheat straw) and demonstrates the impact of the pre-treatment method used. Initially, a short, volatile peak is observed, which corresponds to the devolatilization peak, indicating the rapid release of easily vaporized compounds. In the subsequent step, a significantly broader signal area emerges, attributed to the release of less-volatile matter. This mass signal is indicative of the char gasification and ash reactions that typically occur after devolatilization. The devolatilization peak is characterized by a fast reaction kinetic rate, whereas the char gasification and ash reaction exhibit a slower kinetic rate in contrast.

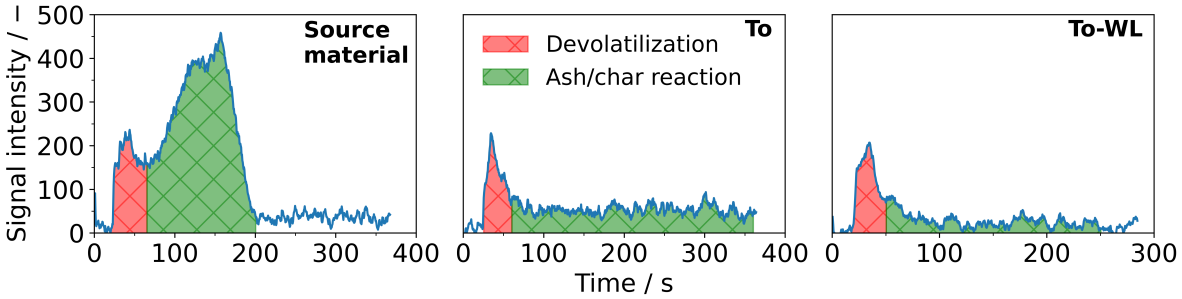

Figure 4.2: The mass spectra of $^{64}SO_2^+$ displays intensity profiles for the source material, as well as for torrefied and torrefied/post-washed wheat straw. The graph clearly distinguishes between devolatilization and ash/char reactions.

The intensity-time profiles clearly demonstrate the influence of both torrefaction and water-leaching. Each sample exhibits a short peak at the onset (red area), which is characteristic of the devolatilization reaction. The raw material shows a distinct secondary release reaction in the form of a broader ash/char reaction peak (green area). In contrast, the torrefied and torrefied/post-washed samples exhibit a significantly reduced intensity range of the char gasification and ash reaction. Fig. 4.2 suggests that water-leaching was effective in removing sulphur compounds, likely in the form of inorganic sulphates. Furthermore, torrefaction also had a notable impact on the release behaviour of SO_2. As reported by Knudsen et al. [207], sulphur is typically released in a moder-

ate temperature range (torrefaction temperature), coinciding with the decomposition of cysteine and methionine (170 °C to 190 °C), which are primary S-containing precursors for plant proteins [40].

In Figure 4.3 and 4.4, normalised results for both peak areas are presented as bar charts, illustrating the results of devolatilization and char gasification/ash reaction for both herbaceous and woody feedstocks.

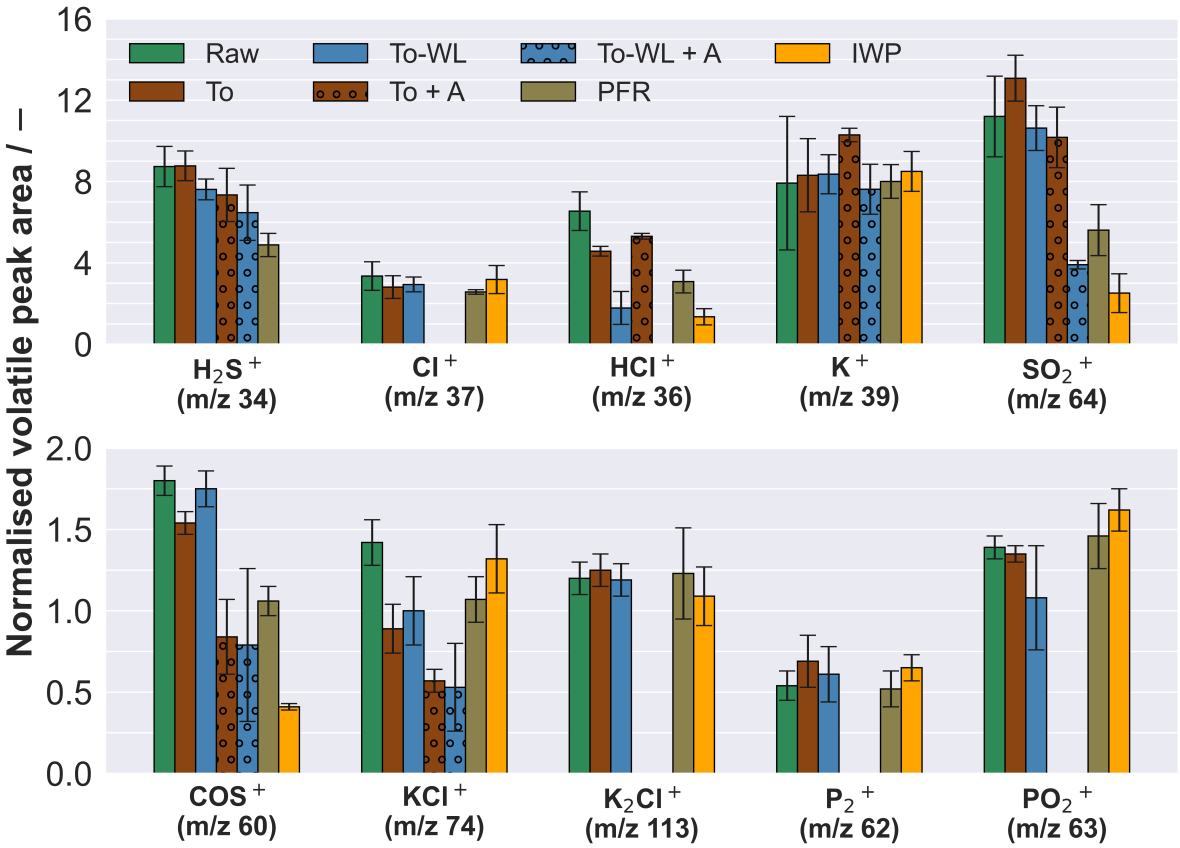

Figure 4.3: Averaged normalised peak areas of detected species released during devolatilization phase.

Normalisation was performed using the $^{23}CO_2{}^{++}$ signal, as CO_2 supply was constant throughout the measurement (see Chapter 3.3.3). Each sample was analysed three times. The relatively large error bars in the figures reflect the high inhomogeneity of herbaceous feedstocks in general. Despite this variability, some trends can be observed. It is important to note that the amounts released should be considered semi-quantitative. This means that the results do not provide absolute numerical values, but rather convey a trend through the pre-treatments, allowing for comparative analysis and the drawing of conclusions between the different results.

The release of hydrochloric acid (m/z 36) decreased significantly when the sample was post-washed, and torrefaction also showed a decrease in HCl release. This finding is consistent with the study by Keipi et al. [208], which reported a decrease in chlorine concentration during torrefaction due to the reactivity of chlorine in biomass fuels at torrefaction temperatures. As expected, the amount of potassium chloride (m/z 74) released from the torrefied/water-leached sample was lower compared to the raw material itself. Interestingly, woody feedstocks generally exhibited low levels of released sulphur species (COS, SO_2 and H_2S) during pyrolysis reactions, despite having similar sulphur content in their ash to that of herbaceous feedstocks. COS is typically formed under pyrolytic conditions and glowing temperatures or incomplete oxidation condition after

$$\mathrm{CO + S \longrightarrow COS} \tag{4.1}$$

and

$$\mathrm{2\,C + 2\,S + O_2 \longrightarrow 2\,COS.} \tag{4.2}$$

Partial oxidation produces CO and SO_2 (char gasification/ash reaction). If water vapour is present, it hydrolyses to CO_2 and H_2S. For IWP, the amount of released HCl was nearly the same as for the torrefied and post-washed material, which represented an suitable result in terms of benchmark quality at first appearance.

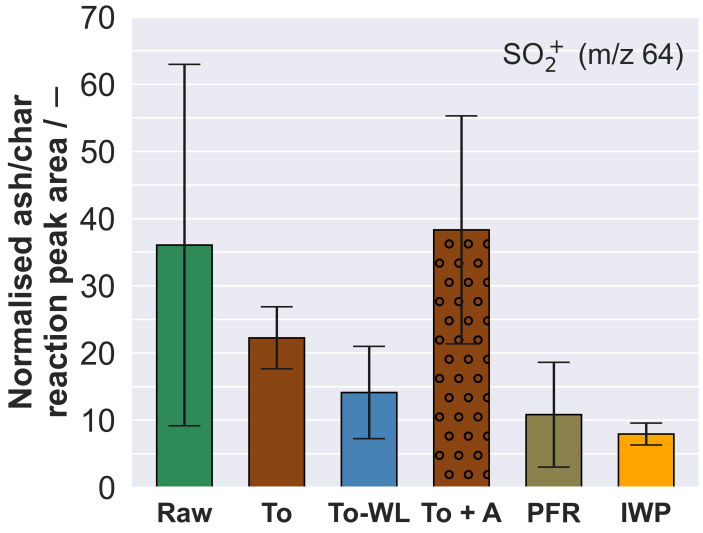

Figure 4.4: Averaged normalised peak areas of detected species released during the ash/char reaction phase. For To-WL + A, no char gasification/ash reaction was observed.

During the char gasification/ash reaction phase (Fig. 4.4), only the release of sulphur dioxide (m/z 64) was observed, which originated from the decomposition and reaction of sulphates contained in the ash. Due to a short residence time in the flow-channel reactor, it was not reduced to H_2S in the gas phase despite the relatively low oxygen partial pressure and high water concentration. This in turn indicated that the hydrogen sulphide released during devolatilization phase should mainly originate from sulphidic, primarily organically bounded sulphur. Likewise, the wide dispersion of the error bars indicated a relatively high inhomogeneity of the raw material, meaning that the sulphur content varied from sample to sample. Both torrefaction and torrefaction/water-leaching decreased the amount of sulphur dioxide tendentiously. Industrial pine pellets have shown the lowest amount of released sulphur dioxide during char gasification/ash reaction. Upon torrefaction and post-washing of the straw sample, the amount of SO_2 released during the char gasification or ash reaction phase was comparable to that from IWP.

In addition to the torrefied and water-leached samples, Fig. 4.3 presents a semi-quantitative analysis of the $CaCO_3$-blended samples with a 2 wt% $CaCO_3$-to-fuel ratio. Notably, a slight reduction in the release of sulphur-containing compounds such as H_2S, SO_2, and COS was observed. Furthermore, a slight decrease in the release of KCl was seen compared to the samples without additive (To and To-WL). Despite the inhomogeneous nature of the fuels investigated, a discernible trend emerged, and the Ca additive demonstrated a noticeable effect on the release behaviour of certain species.

Figure 4.5 illustrates the impact of Ca or the ratio of Ca to K in the sample on the amount of KCl, HCl, and sulphur-containing species released during the devolatilization phase. The increased amount of Ca in the fuel has led to a decrease in the amount of released KCl. Interestingly, IWP, which had a relatively low Ca content compared to To-WL + A, showed a correspondingly higher amount of released KCl. Moreover, the higher the ratio of Ca to K, the lower was the amount of HCl, H_2S, and SO_2 released. It is reasonable to assume that fuel-Ca forms CaO instead of $CaCO_3$ and is likely the dominant ash component at high operating temperatures (950 °C). CaO may act as HCl sorbent according to

$$CaO + 2\,HCl \longrightarrow CaCl_2 + H_2O. \tag{4.3}$$

Similar observations were reported by Shemwell et al. [209], where HCl gas was treated using CaO, $CaCO_3$, and calcium formate with the result that high removal efficiencies were determined. In comparison with To-WL + A, To + A showed a stronger release of HCl. According to the ultimate analysis (Table 4.1, Chapter 4.1.1), To + A showed

a significantly higher content in K, which means that a higher KCl content must have been present in the fuel sample. Possibly, CaO also reacted with KCl, according to Equation 4.4:

$$\mathrm{CaO} + 2\,\mathrm{KCl} \longrightarrow \mathrm{CaCl_2} + \mathrm{K_2O}. \tag{4.4}$$

Potassium chloride (KCl) is recognised as the primary source of hydrogen chloride (HCl) formation [210]. This suggests that it could potentially be responsible for a decrease in HCl formation, in addition to the reaction outlined in Equation 4.3. A plausible explanation for the correlation between Ca and sulphur content may be attributed to the fact that Ca is an active suppressor of the release of S species, specifically H_2S and SO_2 [210].

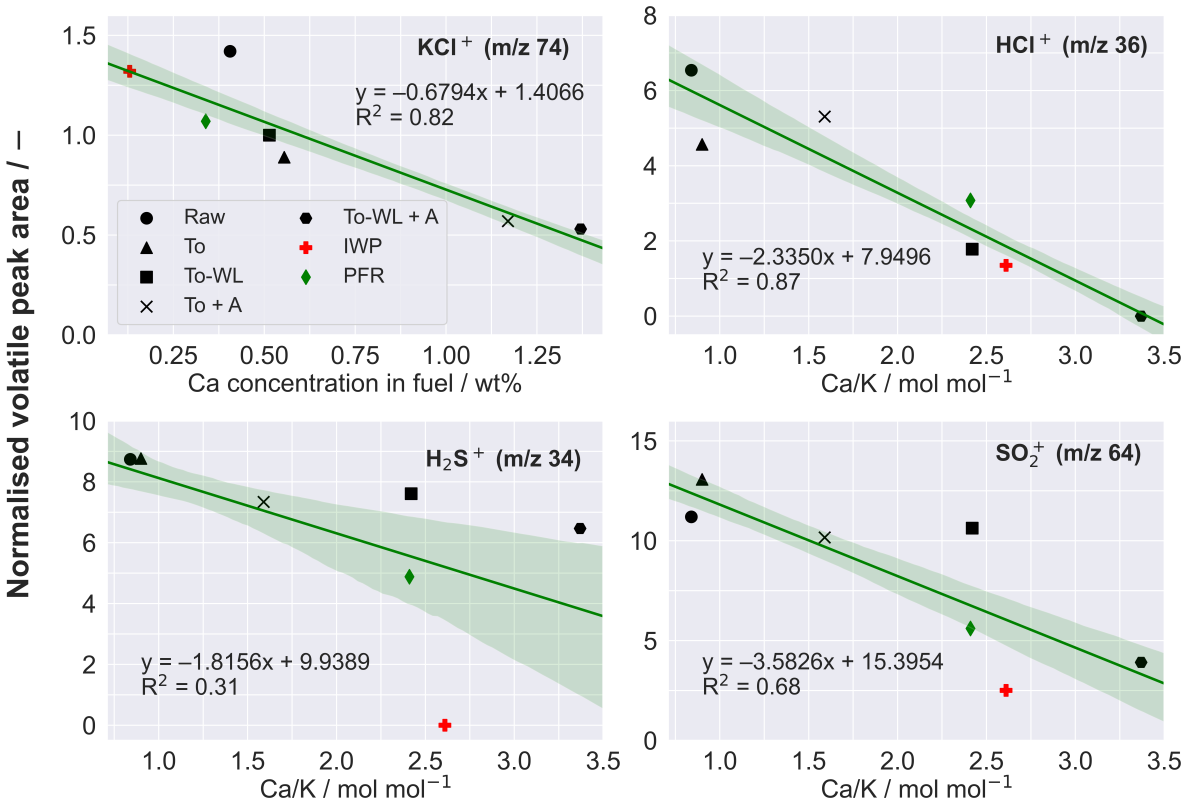

Figure 4.5: Comparison of the normalised volatile peak area (Fig. 4.3) for KCl, HCl, and sulphur-containing species (H_2S, SO_2) in relation to the calcium concentration in (pre-treated) fuel samples (top left) and the molar ratio of Ca/K. The confidence interval is set at 68 %.

4.1.3 Continuous release experiments conducted in a laboratory-scale fluidised-bed reactor

In addition to the batch-type release experiments described in the previous chapter, continuous experiments were conducted using a quartz glass fluidised-bed reactor (Chapter 3.3.4). The goal was to investigate continuous chemical reactions and elucidate the release and fate of inorganic gaseous species under continuous operation using an oxygen carrier. These experiments were performed on a laboratory scale (Chapter 3.3.4). The species of interest were the same as those listed in Table 3.6 (Chapter 3.3.3). Since no gas tracer was used to normalise the signals, $^{23}CO_2{}^{++}$ was chosen as the reference peak, similarly to the batch-type release experiments. At m/z 55, a H_2O-cluster $[(H_2O)_3\text{-}H]^+$ was detected, which demonstrated the accuracy and measurement sensitivity of the spectrometer. As shown in Figure 4.6, a full mass spectrum of PFR was recorded from m/z 2 to 70 to clarify the course of the carrier gas flow (helium) and the gasification medium (H_2O) as well as the syngas components CO and CO_2.

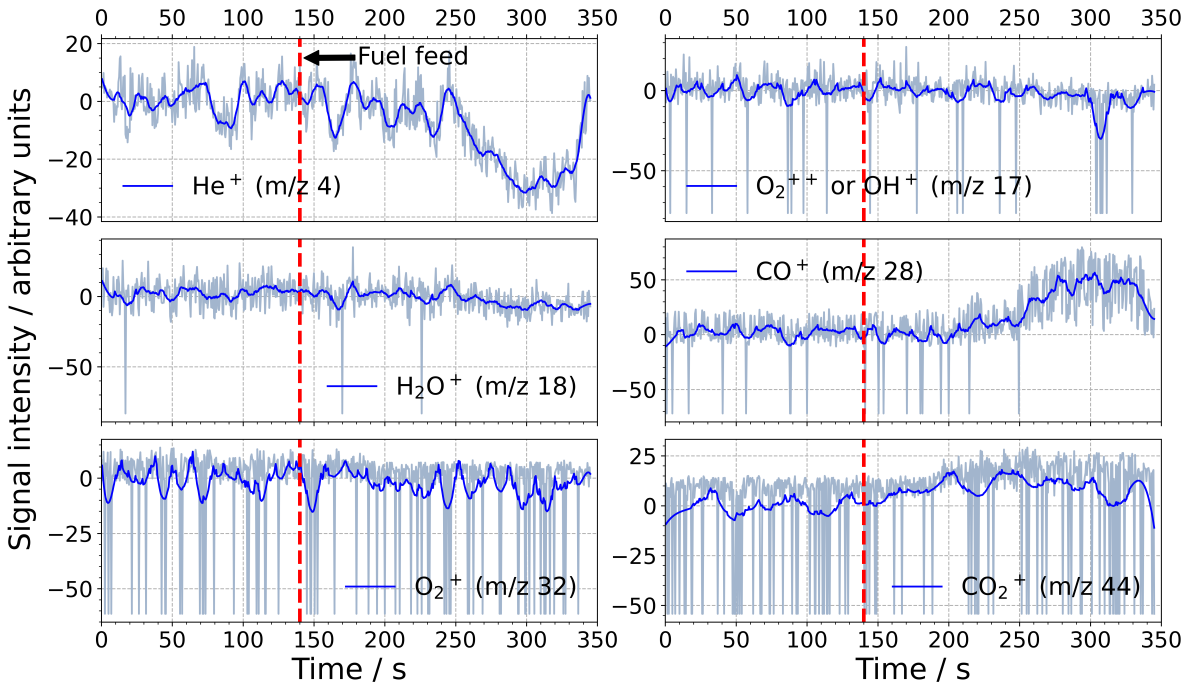

Figure 4.6: Mass spectra of primary gaseous species (He^+, CO^+, H_2O^+, $CO_2{}^+$, $^{17}O_2{}^{++}$ or $^{17}OH^+$, and $^{32}O_2{}^+$), He was used as carrier gas. The grey line presents the original spectrum, and the blue line the fitted signal accordingly. The curves were smoothed using a filter due to relative noisy signal intensities.

The fuel feed was initiated around 140 s into the experiment. Upon initiation, the $^{4}He^{+}$ signal intensity rapidly decreased, while $^{28}CO^{+}$ and $^{22}CO_2{}^{+}$ signal intensities increased noticeably. Water and oxygen signals also decreased slightly, with the doubly ionized oxygen isotope ($^{17}O_2{}^{++}$) showing a more pronounced effect. Notably, the decrease in oxygen signals suggests that oxygen was depleted in the formation of carbon monoxide, indicating that a gasification reaction likely occurred. However, despite recording mass spectra of inorganic species, the signals were predominantly noisy, making semi-quantitative evaluations impossible.

Shortly after the fuel reached the reactor unit, the sample reached the temperature necessary for devolatilization. The released volatile organic and inorganic matter immediately reacted with oxygen, resulting in a significant decrease in oxygen availability, as evident from the intense drop-off in $^{34}O_2{}^{+}$ signal intensity in Figure 4.7.

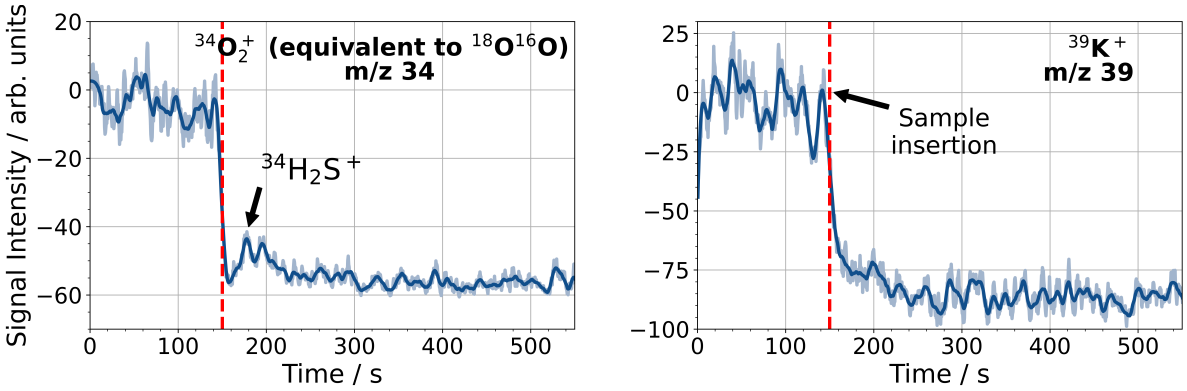

Figure 4.7: Signal intensity versus gasification time for selected mass spectra of raw wheat straw. Left: $^{34}O_2{}^{+}$ isotope incl. $^{34}H_2S^{+}$, right: $^{39}K^{+}$. The red dashed line denotes the time, when the fuel was gasified.

As shown in Fig. 4.7, the signal intensity at m/z 34 exhibited a sudden increase during the devolatilization phase of the gasification experiments at around 180 s. This phenomenon can be attributed to the formation of H_2S instead of SO_2, resulting in an overlapped spectrum due to the similar mass-to-charge ratios of $^{34}H_2S^{+}$ and $^{34}O_2{}^{+}$. The quadrupole system employed in this study had insufficient resolution to distinguish between these two species, as also observed by Bläsing et al. [185]. A sector field mass spectrometer would be necessary for higher resolution and accurate determination of $^{34}H_2S^{+}$ and $^{34}O_2{}^{+}$.

Notably, Figure 4.8 provides additional evidence of sorption, as it shows that no H_2S release was observed in the sample with additive, in contrast to the sample without additive (Fig. 4.7). This observation aligns with the findings presented in Fig. 4.5, further supporting the hypothesis that Ca acts as an active suppressor for the release of S species.

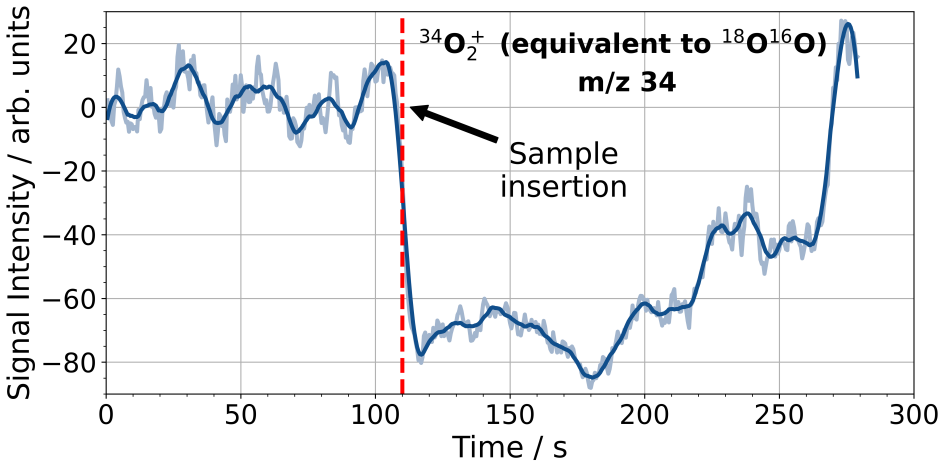

Figure 4.8: Signal intensity of $^{34}O_2{}^+$ isotope versus gasification time for torrefied/water-leached wheat straw plus 2 wt% $CaCO_3$. No $^{34}H_2S^+$ release was observed.

The $^{39}K^+$ spectra of all investigated samples exhibited a substantial decrease in intensity following fuel gasification, likely due to unwanted side reactions within the reactor (as indicated by the arrow in Fig. 4.7, right-hand chart). This phenomenon may be attributed to a reaction between potassium and already-formed ash residues, although the underlying mechanism remains unclear.

4.1.4 Ash fusion testing and behaviour of ashes

In Figure 4.9, the coefficients h_x/h_0 of pre-treated herbaceous and woody samples are plotted against temperature. The coefficient shows an indirect correlation with phase formation or transitions, which was determined by measuring the shrinkage of the pellet. The results generated by HSM are valuable indicators of the ash melting behaviour, particularly in terms of relative behaviour. As previously discussed in Chapter 3.3.6, the coefficient values should not be taken as absolute values because of the inherent inhomogeneity of biomass-derived fuels, which often exhibit unique characteristics and effects in their ash melting behaviour [211]. The composition or chemistry of the ash plays a crucial role in determining the melting characteristics. However, the progression

of melting can be clearly tracked by HSM. The photos of the sample specimens were taken at each temperature increment, corresponding to the determined height profile coefficients h_x/h_0, as shown in Figure 4.10).

Raw wheat straw ash started shrinking slightly at 720 °C. However, no influence on agglomeration was expected in that case. The steep decrease of the coefficient at 1020 °C indicated the start of melting whereas increases thereafter were likely caused by gas formation. In contrast, both IWP and PFR showed in a temperature range between 700 °C to 800 °C noticeable, initial deformations in the form of a pellet shrinkage, however, the size of the pellets remained stable until the end of the course of the test (the final temperature was 1300 °C). For the pre-treated samples, it was observed that the slight initial deformation was shifted to approximately 750 °C, and the severe deformation to 1050 °C. Moreover, a decrease in size was observed in a temperature range of 800 °C to 950 °C for the torrefied sample, where the ash fusion behaviour may become more problematic.

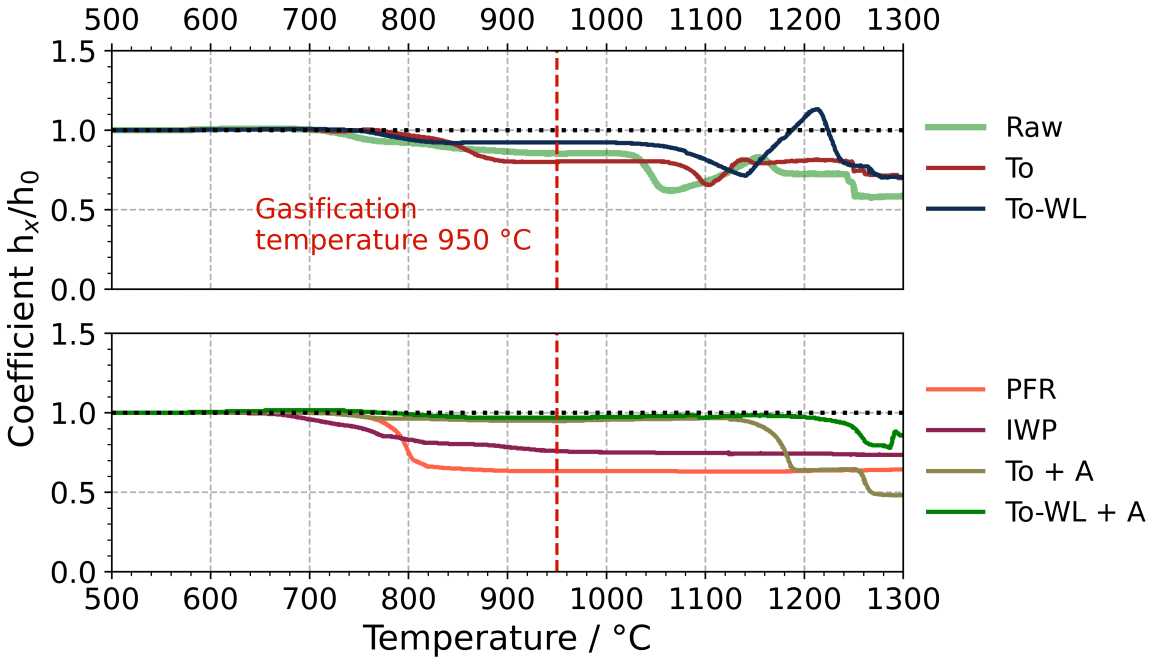

Figure 4.9: Height profile of ashes plotted against temperature (HSM). The red dashed line denotes the defined gasification temperature of 950 °C.

It is not unexpected that the most promising results were obtained with $CaCO_3$-blended feedstocks. Both torrefied and post-washed samples exhibited a relatively stable geometric profile up to temperatures of 1120 °C and 1240 °C, respectively. Consequently,

they appear to be the most promising candidates. Interestingly, this suggests that the melting point has also increased. Notably, however, the stability of the woody ash pellets seems to be highest at 1300 °C.

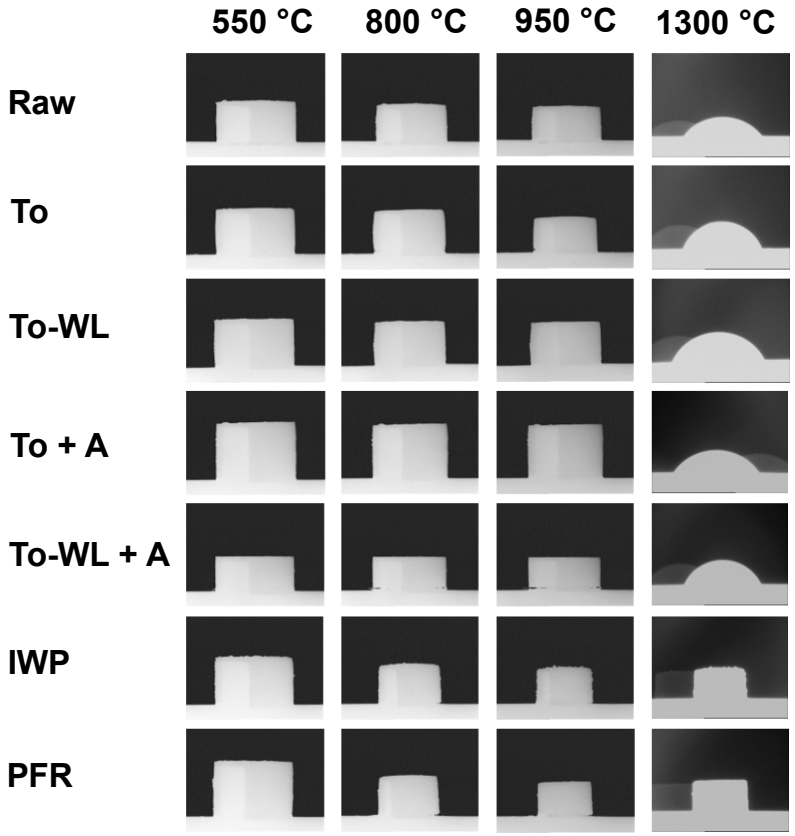

Figure 4.10: Photos (HSM) of straw and wood ash samples during the ash fusion test, showing geometric transformations that indicate the initial reactions and melting points.

Characterisation of mineral phases in sample ashes

Samples were prepared in a gasification-like environment at 550 °C, as described in Chapter 3.2, and analysed diffractometrically to elucidate the phases formed during thermal conversion. Figure 4.11 presents XRD spectra, which show the crystalline main phases present in the herbaceous fuel ashes as well as the woody samples (IWP and PFR).

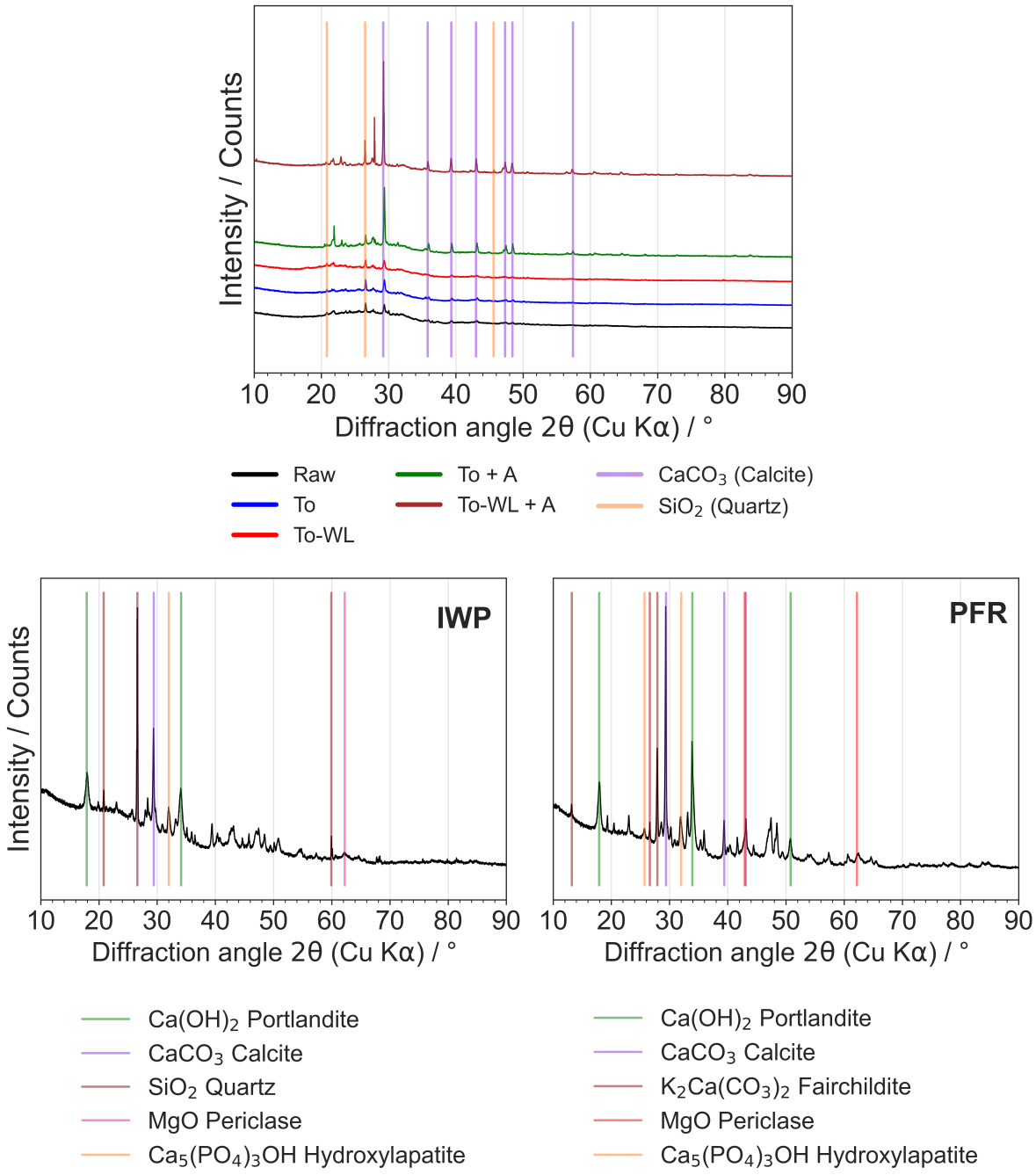

Figure 4.11: XRD spectra of prepared sample ashes: pre-treated wheat straw samples (top Figure), IWP (bottom left Figure), and PFR (bottom right Figure).

The XRD spectra (Fig. 4.11) show a significant presence of amorphous phases. The low-temperature feedstock ash primarily consisted of non-crystalline compounds, which are challenging to detect using the XRD method [212]. Consequently, a quantitative

phase analysis by Rietveld method becomes difficult and inaccurate. Given that the investigated ash samples had a relatively high amount of amorphous content, it can be assumed that they have a strong impact on ash deposition formation, but they cannot be detected by the XRD method [213, 214]. However, the major phases such as $CaCO_3$ or SiO_2 in quartz form could be clearly evaluated. SiO_2 has been frequently detected in ashes produced from agricultural residues [116, 215, 216]. The ashes of the $CaCO_3$-blended feedstocks (torrefied and torrefied/post-washed) exhibited the highest calcite peak intensities. No potassium chloride was detected in the samples, which may be attributed to the low chlorine content in the investigated samples (Table 4.1, Chapter 4.1.1). The chlorine content in all fuels was slightly above the measurement limit, suggesting that most of it was already washed out; for example, the wheat straw feedstock may have been lying in the field for an extended period. Mason et al. [217] investigated the potassium content in the solid phase of various biomass materials, including wheat straw. They found that in relation to K content, it is inferred that where KCl is present, it is not necessarily the dominant species in the solid phase.

Both IWP and PFR samples exhibited the presence of hydroxylapatite or portlandite. $Ca(OH)_2$ typically forms when CaO reacts with water, and therefore, CaO is likely to be formed when $CaCO_3$ decomposes at elevated temperatures. Phosphorus is primarily found in the form of hydroxylapatite $Ca_5(PO_4)_3(OH)$ or calcium whitlockite (β-$Ca_3(PO_4)_2$) in the ashes from woody biomass [218]. Ca phosphates, such as hydroxylapatite or whitlockite, are more stable than K-Ca phosphates and are therefore likely to be the final product [219].

It is worth noting that the formation of crystalline phases depends heavily on the ashing temperature, with increasing temperature leading to the formation of certain phases (such as silicates or aluminosilicates) while others decompose, like chlorides and carbonates [172]. Additionally, the heating rate can have a significant impact on the thermal characteristics of ash samples. Yang et al. [220] discovered that varying heating rates had a substantial effect on fusion characteristics.

In addition to the upgraded biofuels, oxygen carrier poisoning interactions using XRD analysis were investigated. Figure 4.12 presents the main mineral phases identified through X-ray diffraction analysis.

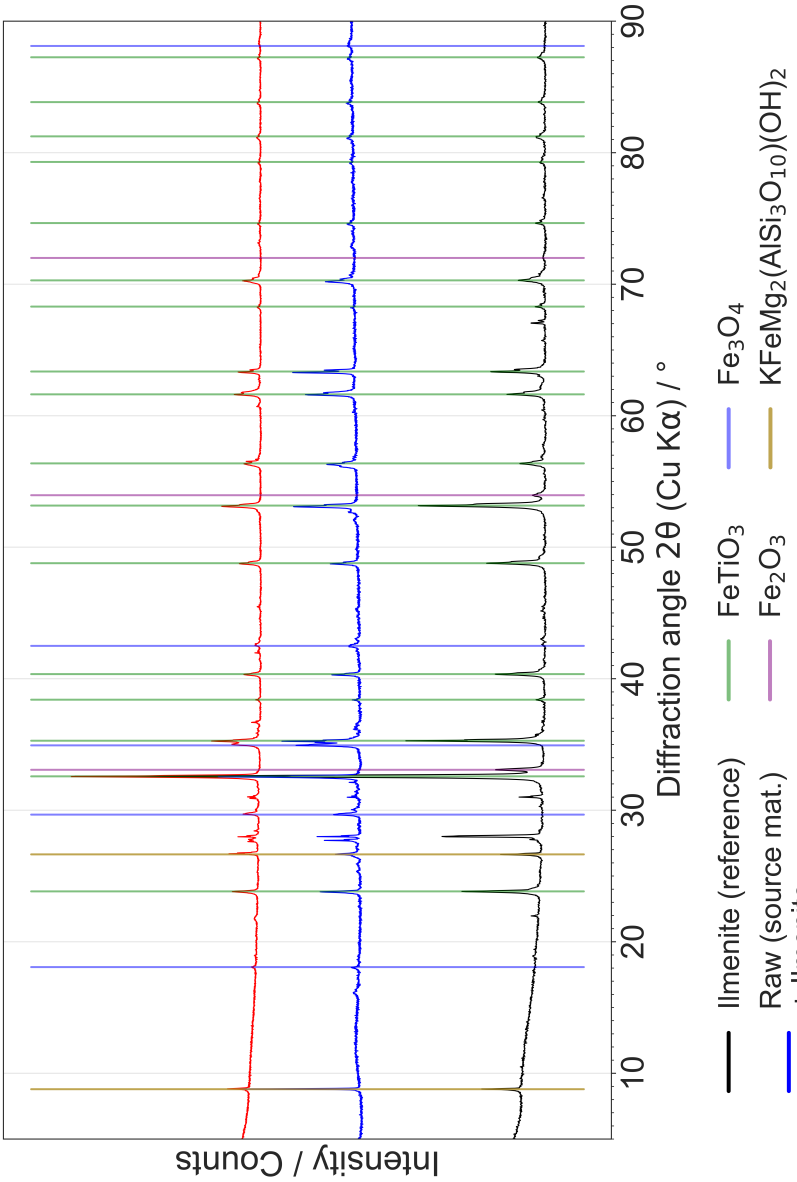

Figure 4.12: XRD spectra of ilmenite and ash of treated (torrefied and post-washed) wheat straw with ilmenite. Same investigations revealed no changes in the torrefied or calcium-blended materials.

Preliminary equilibrium calculations revealed undesired interactions between the ash constituents of wheat straw and the oxygen carrier ilmenite. The results of these predictions are discussed in Chapter 4.1.6 and presented in Table 4.2. Therefore, treated samples mixed with ilmenite were ashed in situ in a gasification-like atmosphere (Chapter 3.2), but at 950 °C instead of 550 °C. The weight ratio of ilmenite to biofuel was 0.48 g/g, matching the Fe_2O_3/feedstock ratio specified in Chapter 3.4. Ilmenite itself exhibited characteristic phases such as $FeTiO_3$ or Fe_2O_3 (hematite). It is worth noting that the investigation of ilmenite used the material as received from the CLARA project partners. Unlike pre-treated wheat straw samples, the oxygen carrier itself was not subjected to high-temperature gasification-like conditions. In contrast, straw ash samples mixed with ilmenite formed Fe_3O_4 (magnetite) phases, indicating partial reduction of iron. Mica mineral phases were also observed, likely attributed to biotite with the chemical formula $KFeMg_2(AlSiO_{10})(OH_2)$. The formation of biotite phases was likely due to sample contamination, as they were found in all samples, including the reference material ilmenite. This phase formation may have been caused by impurities originating from the corundum tube of the tube furnace (Chapter 3.2), and it is possible that manufacturing reasons may have contributed as well.

4.1.5 Thermodynamic prediction of gas phase chemistry

Calculations were conducted to study the condensation of inorganic compounds, specifically alkali chlorides, carbonates, and slag-mixtures, for both pyrolysis and gasification conditions up to 950 °C. The detailed conditions used in these calculations are presented in Chapter 3.4. The primary difference between pyrolysis and gasification lies in the absence of oxygen and steam during pyrolysis, whereas oxygen and steam were present during gasification.

The model calculations were designed to investigate the release of inorganic compounds during thermochemical conversion, primarily focusing on the condensation behaviour of volatile inorganic species from the gas phase, released during gasification. Notably, no significant differences were observed between pyrolysis and gasification regarding the fraction of condensed alkali chlorides. The only distinction between the two conditions was the temperature range in which salts started to condense, with a lower condensation temperature observed for gasification. It was found that alkali chlorides remaining in the gas phase decreased with increasing temperature until reaching a constant level.

Figure 4.13 illustrates that the condensation temperature of alkali chlorides released during gasification of pre-treated wheat straw (both torrefied and torrefied/water-leached samples) shifted towards lower temperatures. Additionally, the quantity of formed salts decreased when wheat straw was treated. Torrefaction is known to reduce the chlorine content of feedstocks [208], which in turn results in a lower content of alkali chloride. This observation is consistent with the results obtained by chemical characterisation (as evident from the comparison of Cl content in Table 4.1, Chapter 4.1.1). Notably, the condensation temperature of alkali chlorides was found to be lower than their corresponding melting points, indicating that the salts are not excessively sticky.

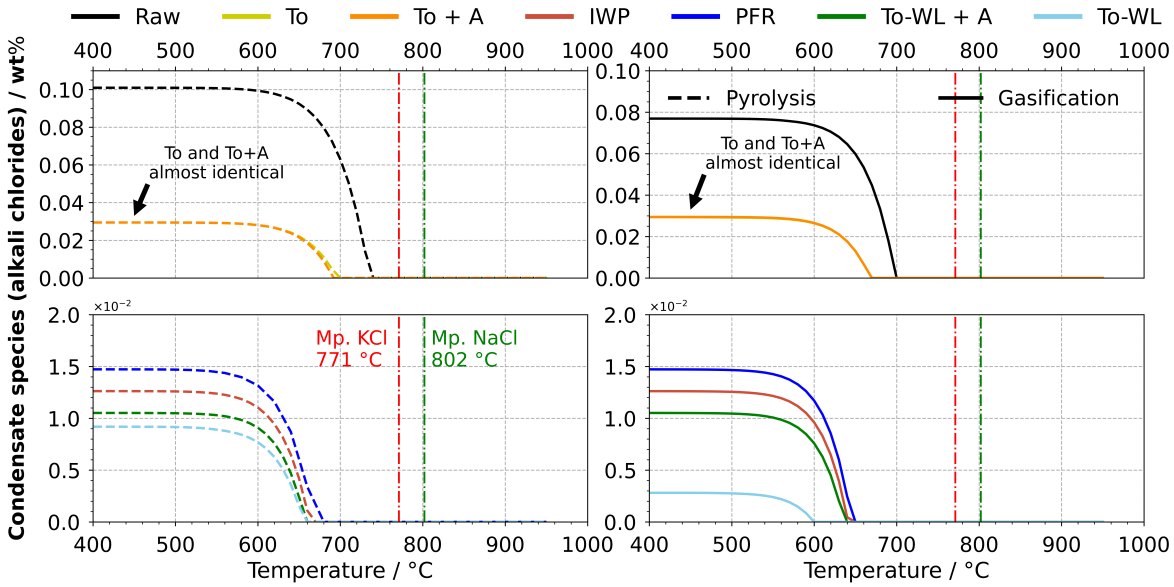

Figure 4.13: Condensation of alkali chlorides, primarily KCl, under both pyrolysis (left Figure) and gasification conditions (right Figure). The red and green dashed lines indicate the melting temperatures of KCl and NaCl, respectively. The gasification temperature is 950 °C.

Another notable finding was the reduction in the amount of formed salts in both the torrefied sample and the post-washed sample, compared to the raw source material. In contrast, no significant quantitative effect was observed on the formation of alkali chlorides KCl and NaCl for Ca-blended and pre-treated samples. Interestingly, the calculated fraction of condensed salts for PFR and IWP was significantly lower than for wheat straw.

From a thermodynamic perspective, it is suggested that KCl is the most stable K-containing compound in the gas phase, existing primarily as vapour at temperatures above 800 °C [221]. This would explain why a higher fraction of alkali chloride was formed instead of alkali carbonates.

In contrast to the alkali salts, the release of carbonates was characterised by relatively minor differences, which depended on whether pyrolysis or gasification conditions were applied. Figure 4.14 displays the predicted data for carbonates, sulphides, and slag-mixtures (intermediates).

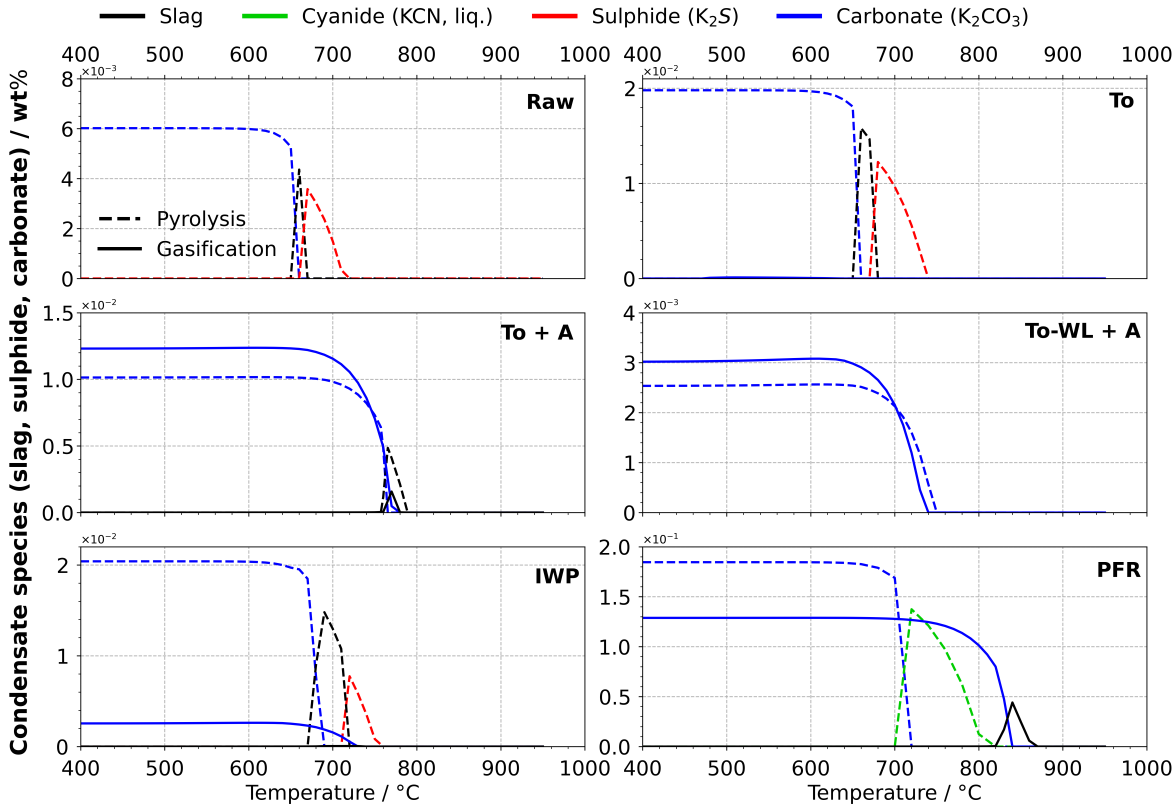

Figure 4.14: Condensation of carbonate, sulphide, and slag-mixtures under both pyrolysis and gasification conditions. No condensate species were identified in the To-WL sample other than KCl and NaCl (Fig. 4.13). The gasification temperature is 950 °C.

For the upgraded samples, the formation of condensed carbonates (primarily K_2CO_3) was found to be higher than in raw wheat straw, with PFR exhibiting a notably high quantity of condensed carbonates. While torrefied and torrefied/water-leached samples also showed the presence of condensed carbonates, no carbonates were predicted to

condense for the torrefied/water-leached fuel without the addition of $CaCO_3$. In addition to alkali salts, small amounts of condensed slag were observed prior to the formation of carbonates. According to the predicted activities, potassium sulphide was primarily found in the slag, with small amounts of sulphides also present. Notably, sulphide formation only occurred in the absence of oxygen (pyrolysis), whereas it did not form under gasification conditions due to its reactivity with water and/or oxygen. The shapes of the condensation curves suggested a typical, smooth phase transition, indicating that potassium sulphide decomposed and subsequently formed potassium carbonate. This phenomenon was also observed in torrefied biofuel and IWP, with potassium sulphide becoming unstable both above and below its melting point, explaining the observed phase transition.

Besides alkali chlorides, carbonates, and sulphides, liquid potassium cyanide was found to condense in PFR, exclusively under pyrolysis conditions. A thermodynamic equilibrium was observed in the temperature range between 700 °C and 820 °C, which favoured the formation of KCN. Notably, Hansson et al. [222] reported that nitrogen-containing species such as hydrogen cyanide, ammonia, and isocyanic acid were identified during the pyrolysis of biomass-based feedstocks, including bark pellets, at temperatures between 700 °C and 1000 °C.

Assessing the risk of oxygen carrier poisoning (gas phase)

To assess the poisoning risk of oxygen carrier materials – LD Slag, Sibelco, and ilmenite (introduced in Table 3.3, Chapter 3) – when exposed to fuel ashes, the resulting gas phase composition was predicted using FactSage. As shown in the thermodynamic flow chart presented in Figure 3.17 (Chapter 3.4), calculations were performed under gasification conditions, considering the following ratios, which were agreed upon by the CLARA project partners:

- Oxygen carrier:fuel = 40:1
- Steam:fuel = $0.6\,\mathrm{g\,g^{-1}}$
- Air-fuel ratio $\lambda = 0.3$

The gasification temperature was maintained at 950 °C, and the partial pressures p_i of oxygen carrier constituents were calculated for the most notable species. The results, shown in Figure 4.15, indicate that the partial pressures are generally very low, ranging from 10^{-12} atm to below 10^{-6} atm. Although these pressures may seem insignificant at

first glance, they can have a significant impact on pilot-plant operation. Over time, as the oxygen carriers react with ash constituents, the poisoning risk increases. Moreover, fouling issues and corrosion risks will also escalate, with corrosion being exacerbated by the buildup of metal chlorides.

As shown in Figure 4.15, both ferrous hydroxide and aluminium hydroxide remained constant in the gas phase and were not affected by the pre-treatment methods applied to the samples. Since Sibelco had the lowest iron and highest aluminium content among the oxygen carriers, its partial pressure reflected this relative ratio. Interestingly, the partial pressure of orthosilicic acid was significantly lower in the case of LD Slag compared to Sibelco or ilmenite. This is because calcium binds silicon primarily as calcium silicates [223], which suppresses the formation of orthosilicic acid. Since LD Slag is nearly half composed of calcium oxide, silica is fully bound as calcium silicates, resulting in lower orthosilicic acid formation.

The analysis also showed that chlorine in wheat straw fuel reacts with iron/manganese to form chloride compounds (except for ilmenite, which does not contain manganese). The torrefied and post-washed sample showed a notable reduction in the formation of volatile salts compared to the untreated source material, which is a promising outcome.

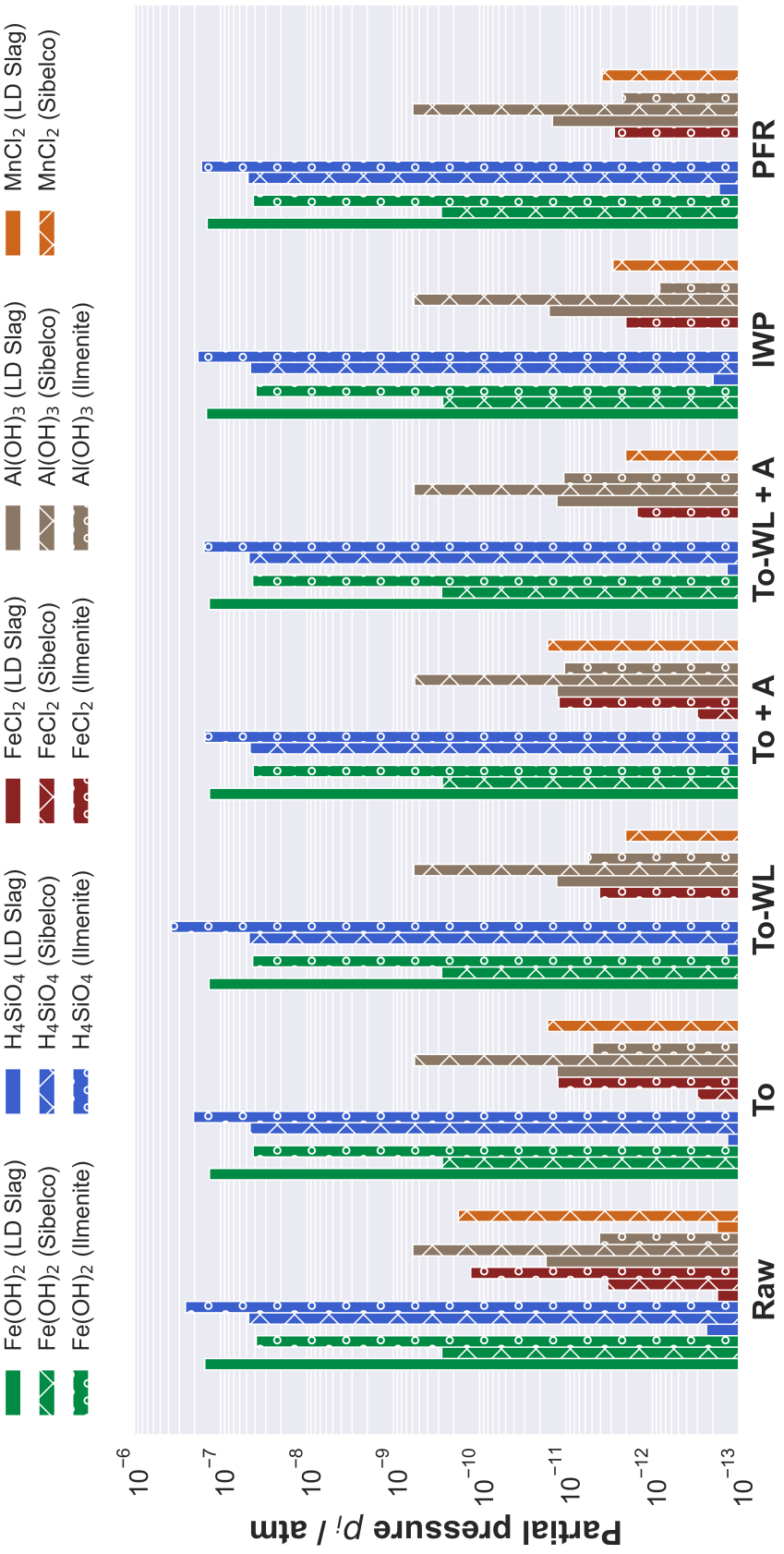

Figure 4.15: Predicted partial pressure of oxygen carrier constituents in contact with upgraded wheat straw samples, IWP, and PFR under isothermal gasification conditions (950 °C). The species of primary interest, with partial pressures ranging from 10^{-12} atm and above, are highlighted for each type of added oxygen carrier.

4.1.6 Thermodynamic prediction of mineral phases formation

A detailed prediction of mineral phases was conducted for both pyrolysis and gasification conditions, taking into account the lattice oxygen from the carrier material and steam. With regard to the formation of mineral phases, no principal differences were observed between pyrolysis and gasification in general. This means that both conditions appeared to reveal a similar reaction sequence. For clarity, only the predicted results of inorganic phase formation under gasification conditions are presented below. The prediction of each phase was numerically calculated, depending on the gasification temperature, starting from 400 °C and ending at 1300 °C. The dominant phases were summarised and sorted to provide a structural overview of the main compounds, including alkali chlorides, sulphides, carbonates, and oxides/silicates. Figure 4.16 illustrates the calculated phase map of the ash of untreated wheat straw, displaying each individual phase as well as the consolidated phase groups.

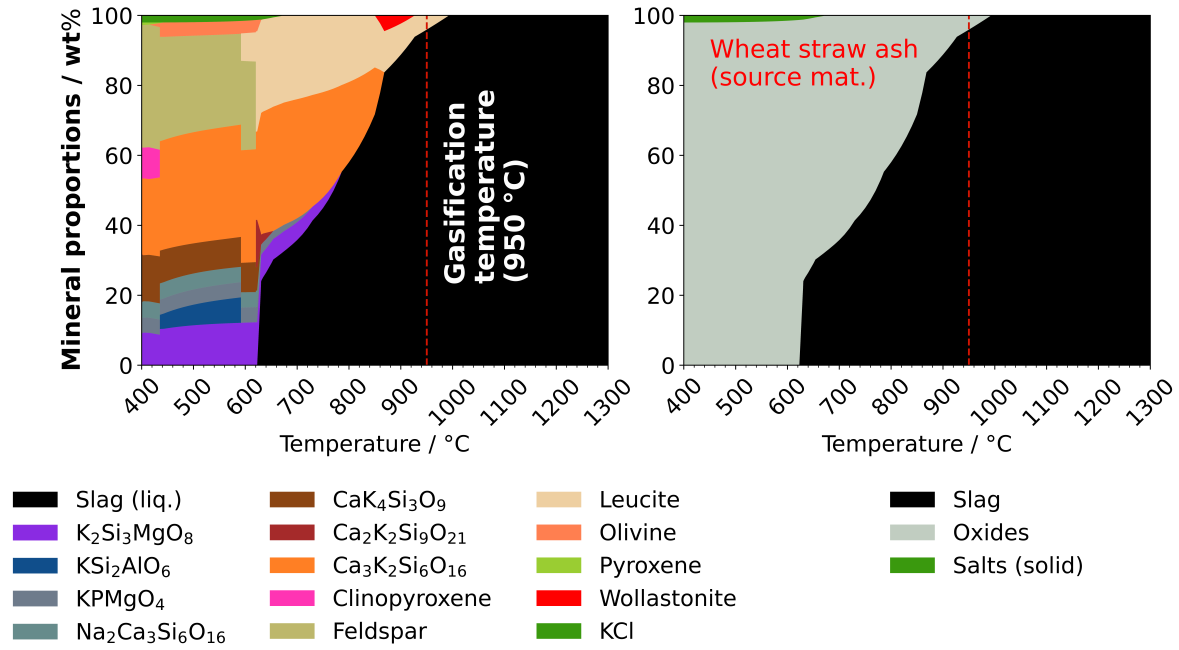

Figure 4.16: Calculated mineral proportions of raw wheat straw ash under gasification conditions. Left: the overview phase map displays each predicted mineral phase of the sample ash. Right: the summarised phases are presented, primarily consisting of oxides, alkali salts, and molten slag.

The shape of the black area in Figure 4.16 represents the molten slag fraction and can be viewed as a "pseudo-melting curve". The raw material exhibited more than 90 wt% molten slag at 950 °C, whereas at 600 °C, mainly oxides in the solid state and small

amounts of alkali metal salts were predicted. It is not unexpected that the amount of molten slag increased in parallel with increasing operating temperature. Figure 4.17 illustrates the predicted phase proportions of each sample listed in Table 4.1 in Chapter 4.1.1.

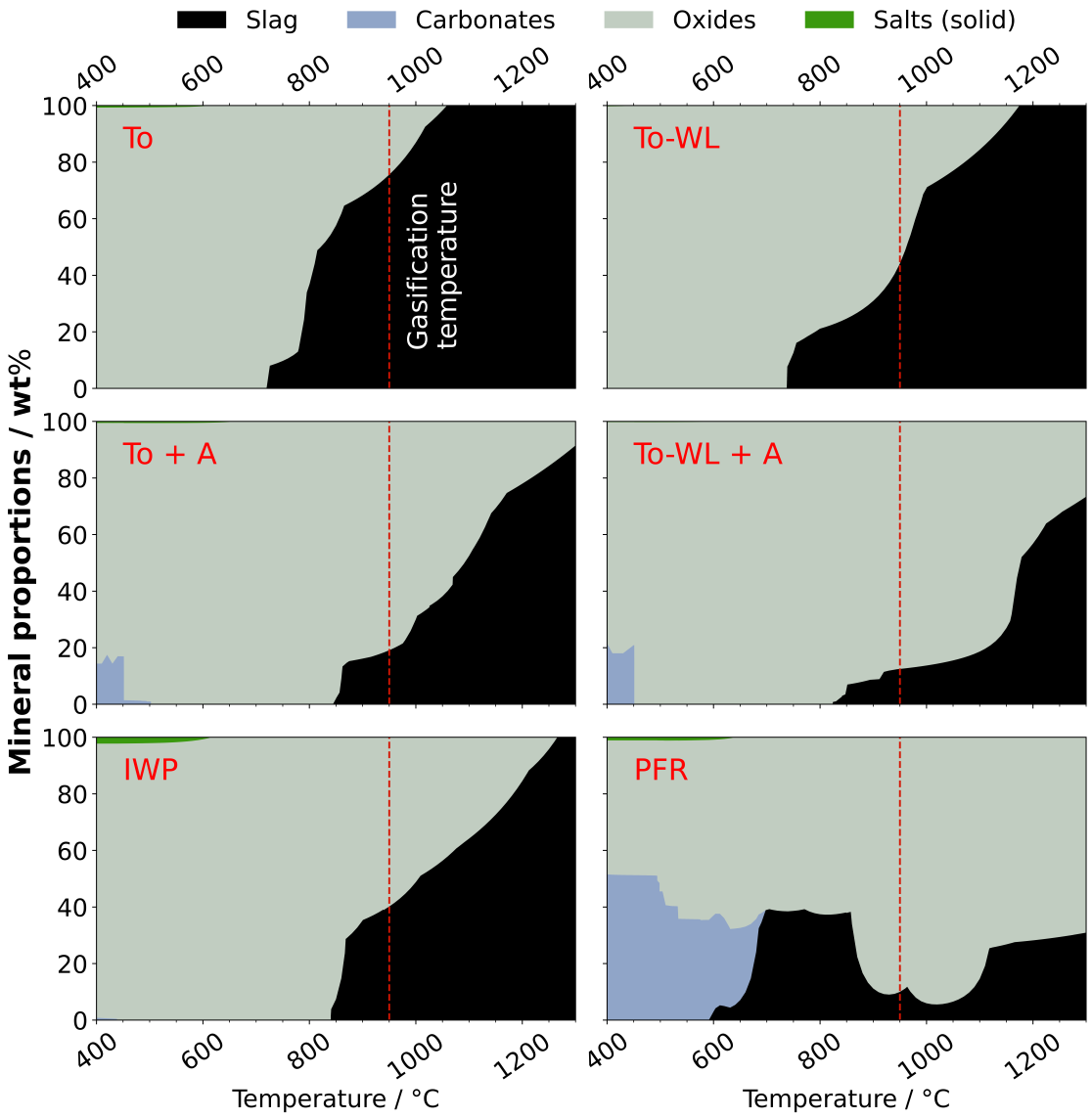

Figure 4.17: Calculated mineral proportions of the ash of IWP, PFR, and pre-treated or $CaCO_3$-blended wheat straw under gasification conditions.

IWP, selected as the benchmark material for this study, exhibited less than 40 wt% molten slag at 950 °C. In contrast, the torrefied straw sample showed a shifted slag formation towards higher temperatures, approximately 100 °C, compared to the raw material. Additionally, the content of alkali metal chlorides and the amount of slag

at gasification temperature were lower in the torrefied feedstock compared to the raw feedstock. Although this effect was noticeable, it was not satisfactory for the gasification process, which typically operates above 900 °C. Torrefaction and subsequent post-washing of the feedstock yielded more promising results, bringing the quality of the benchmark material close to what was expected. Notably, the most reliable results were achieved when the torrefied or torrefied/water-leached material was blended with 2 wt% $CaCO_3$. Under these conditions, a molten slag content of less than 20 wt% was achieved. For the Ca-blended feedstock, a small amount of calcium-rich carbonates was found at lower temperatures. Since the calcium content in the ash increased significantly due to the addition of the blending component, the formation of carbonates was consequently favoured. PFR showed a relatively high content of carbonates compared to herbaceous feedstocks. The slag consisted mainly of liquid carbonates, which explained why the transition between carbonates and slag seemed to proceed smoothly in this case. No carbonates were found above 800 °C, as carbonates typically thermally decompose in this range. A summary comparison of the ash fusibility of the (pre-treated) feedstocks is presented in Figure 4.18.

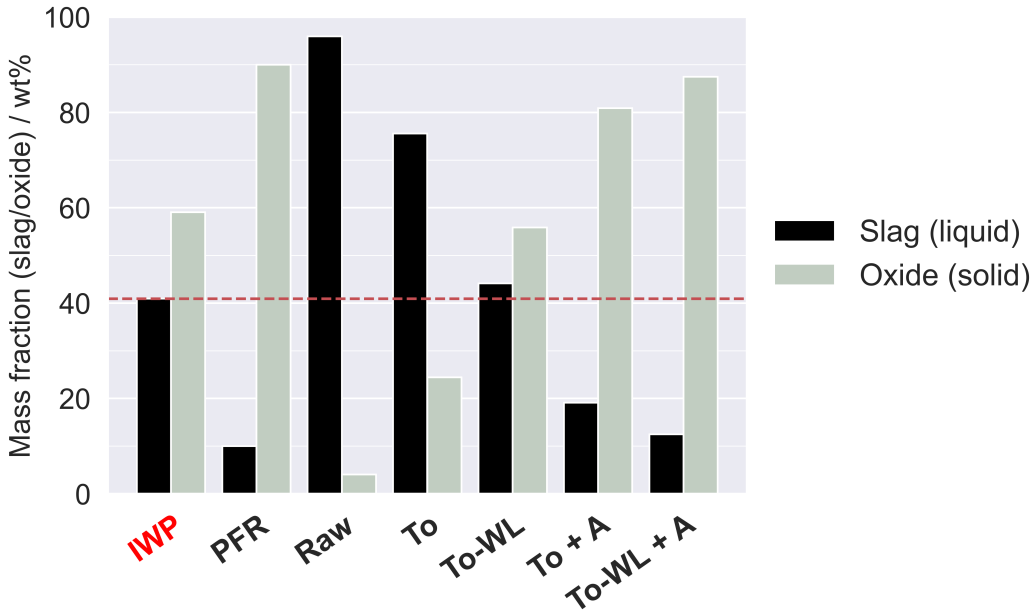

Figure 4.18: Comparison of the ash fusibility of the biofuel samples under gasification conditions at 950 °C. The data is sourced from Fig. 4.17 and 4.16.

The information given in the bar chart were taken from the calculated phase maps in Figure 4.16 and 4.17. The formed amount of slag/oxides was calculated at gasification conditions (950 °C). The higher the slag part, the lower the amount of solid oxides and

thus, the stickier the sample was. With approximately 10 wt%, PFR showed a relatively low amount of molten slag in comparison to the other samples.

It is important to emphasise that merely considering the quantity of molten slag is not a sufficient indicator for estimating slagging risks, as molten slag has a complex nature. The operating conditions and configuration of the gasifier are also relevant in this context. Additionally, viscosity is a crucial factor to consider, as it plays a significant role in determining slag stickiness [224]; however, it has not been the focus of this work.

A ternary phase diagram was computed to enable the prediction of the formation of inorganic phases in the upgraded material (Figure 4.19).

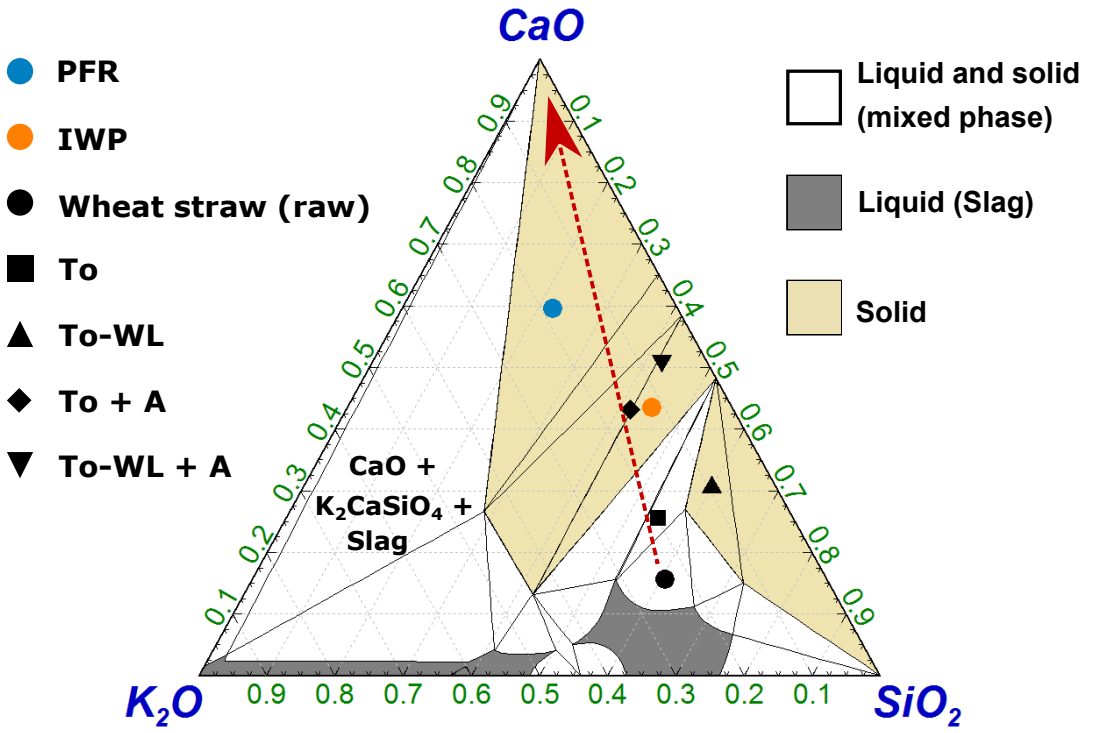

Figure 4.19: Ternary phase diagram of the SiO_2–CaO–K_2O system, predicted using FactSage [202]. The phases were predicted for treated wheat straw, IWP and PFR. The calculation was performed under isothermal and isobaric conditions, at a temperature of 950 °C and at atmospheric pressure.

The sum of the inorganic compounds estimated from these calculations provides an approximation of the ash content, but may differ significantly from experimentally determined results (Table 4.1, Chapter 4.1.1). This discrepancy is likely due to the presence of impurities and residual carbon content. By leveraging the understanding of the SiO_2-CaO-K_2O system, the fusibility tendencies were predicted as presented in Fig. 4.19; it is known that Ca, K, and Si are key elements responsible for agglomeration difficulties [66].

The ash of the herbaceous source material is situated in the liquid-solid two-phase region, relatively close to the slag phase, whereas the ashes of the woody biofuels IWP and PFR are found in the solid area. The woody biomass exhibits a noticeably lower K and Si content compared to wheat straw (Table 4.1, Chapter 4.1.1), which favours a high-melting point of the ash. Torrefaction did not appear to affect the ash melting behaviour, as observed in experimental investigations conducted by HSM (Chapter 4.1.4). In contrast, the other pre-treated samples displayed a distinct behaviour in terms of their phase states. According to model calculations, torrefaction alone did not produce the desired effect on ash melting; however, subsequent post-washing of the sample revealed a positive effect on ash melting. The results suggest that torrefaction of the sample and adding 2 wt% of $CaCO_3$ could potentially suppress ash melting, as the ash of the sample is located in the solid phase area.

Assessing the risk of oxygen carrier poisoning (mineral phases)

The gas phase was investigated in the previous chapter, with one goal being to understand possible chemical interactions between ash and oxygen carriers (Fig. 4.15, Chapter 4.1.5). Additionally, mineral phases formation were numerically predicted to estimate the poisoning risk of oxygen carriers LD Slag, Sibelco, and ilmenite (listed in Table 3.3, Chapter 3) with fuel ashes. The results are presented in Table 4.2. The respective ratios of oxygen carriers (oxygen carrier/fuel, steam/fuel, and air-fuel ratio λ; see Chapter 4.1.5) remained unchanged and were consistent with calculations of gas phase activities (Fig. 4.15, Chapter 4.1.5).

The results suggest that the pre-treated samples did not undergo chemical reactions with the oxygen carriers compared to the untreated material, with the exception of ilmenite. Primarily, magnesium and potassium from the ash interacted with mineral phases to form intermediates or mixtures. Raw wheat straw in combination with ilmenite showed the thermodynamically favoured formation of potassium titanate, whereas in the torrefied/leached sample, no potassium titanate was found. The fact that leached samples exhibited only small amounts of potassium may explain the suppression of $K_2Ti_6O_{15}$ formation. The quantity of K_2O-rich liquid phase plays a crucial role in the formation of potassium titanate during heating calcination [225]. However, the experimental results obtained by XRD analysis (Fig. 4.12, Chapter 4.1.4) did not confirm any interaction between the ash constituents and ilmenite, and potassium titanate phases were not observed in the diffractograms. This is likely explained by the fact that the formation of potassium or sodium titanate is kinetically limited. Bao et al. [225] reported

on the formation steps of potassium titanate: at temperatures above 1100 °C, $K_2Ti_6O_{13}$ is generated from $K_2Ti_4O_9$, accompanied by the continuous melt of K_2O-rich liquid phase.

Table 4.2: Overview of the main mineral phases, stable under gasification conditions at 950 °C. The interactions of the phases are compared with each other, depending on the oxygen carrier added to the fuel. The "original" sample is for comparison and denotes the ash-free composition of the source material.

Sample	**LD Slag**	**Sibelco Calcined**	**Ilmenite Calcined**
Original (C, H, N, O only) source material	Metal oxides (MeO); Olivine; alpha-prime Ca_2SiO_4; Rhodonite	Spinel; Wollastonite; Olivine; Bixbyte; Rhodonite	Corundum, Rutile, Pseudobrookite
Source material	MeO + Mg; Olivine + Mg; alpha-prime + Ca_2SiO_4 (P, Mg); Rhodonite + Mg	Spinel + Mg; Wollastonite + Mg; Leucite + K; Olivine + Mg; Rhodonite + Mg	Corundum + (Al, Mg); Pseudobrookite + (Al, Mg); Leucite with Al/Fe; Perowskite + Ca; Potassium titanate ($K_2Ti_6O_{13}$); Titanite/Sphene ($CaTiSiO_5$)
To	—*dito*—	—*dito*—	—*dito*—
To-WL	—*dito*—	—*dito*—	no potassium titanate found
To + A	—*dito*—	—*dito*—	see source material
To-WL + A	—*dito*—	—*dito*—	see source material

To summarise, the assessment of all the modelling steps reveals that the results obtained by thermodynamic modelling were generally consistent with the experimental ones, although some deviations were observable in certain cases, particularly when estimating the poisoning risk. It should be noted that the calculations were based on ideal thermodynamic conditions and did not always correspond to kinetically controlled, experimental conditions.

4.1.7 Discussion on the impact on fluidised-bed gasification and CLG

In this chapter, various investigation methods have been employed and combined to clarify the impact of industrial pre-treatment techniques and Ca-blending on the inorganic constituents of wheat straw. Additionally, valuable insights on the effects of these treatments on (chemical looping) gasification can be assessed.

It is not surprising that the torrefied material exhibited a slightly higher ash content compared to the raw material, while the torrefied and post-washed sample showed a lower content. The ash content of the Ca-blended fuels was also significantly higher. These results align with the outcomes of the chemical characterisation, as ash only represents non-combustible inorganic compounds. The woody fuels, both IWP and PFR, displayed a relatively low ash content, as expected, due to their limited amount of inorganic compounds. A lower ash content is associated with a lower risk in terms of reactor operation. In the following sections, the most critical ash-related issues in (chemical looping) gasification are discussed, comparing both experimental and calculated data. Based on the obtained results, conclusions will be drawn about fouling and slagging, agglomeration, high-temperature corrosion, and poisoning of oxygen carriers.

High-temperature corrosion

Biomass-based fuels contain a significant amount of chlorine in the form of salts, particularly alkali chlorides, which has a negative impact on metal behaviour due to its inherent correlation with chlorine-induced corrosion [93]. It is well-known that small quantities of potassium chloride can greatly accelerate the oxidation of austenitic alloys, highlighting the corrosive nature of potassium chloride [226].

The present batch-type release experiments have demonstrated that the method of torrefaction/water-leaching significantly influences the amount of chlorine released during devolatilization and char gasification/ash reactions. Notably, To-WL samples ex-

hibited a lower ash content than the raw material, resulting in a decreased amount of reactive inorganic species remaining in the feedstock. In contrast, the benchmark material IWP showed a similar quantity of HCl released, but the effect of torrefaction or torrefaction/water-leaching on release behaviour was still evident. The combination of both torrefaction and water-leaching effectively decreased the fraction of problematic inorganic species in the ash. Therefore it can be concluded that, torrefaction alone is not sufficient for industrial-scale applications, as it does not effectively remove all problematic constituents. In contrast, the combination of torrefaction and water-leaching appears to be a promising approach for removing these impurities, making it a viable option for industrial-scale use.

In addition to influencing the ash melting behaviour, the $CaCO_3$ additive showed a slight effect on the release behaviour of inorganic compounds, primarily sulphur-containing species. From a thermodynamic perspective, CaO or $CaCO_3$ can react with sulphur oxides in the temperature range 800 °C to 950 °C [227–230]. Calcium is known to react with SO_2 to form calcium sulphate, thereby reducing SO_2 emissions [231].

Moreover, a slight decrease in the quantitative release of KCl was observed. Research suggests that Ca, S, and P may contribute to capturing and depositing gaseous alkali chlorides (KCl or NaCl) [232–234]. The formation of sulphates from the $CaCO_3$ additive and various sulphur species (H_2S, SO_2, COS) originating from the fuels could also lead to a decreased release of KCl. The formation of alkali chlorides through different sulphation reactions can be mitigated by sulphur-based additives [235–237].

It is worth noting again that corrosion mechanisms for biomass gasification systems are assumed to be largely similar to those for combustion conditions [17].

Bed agglomeration

Bed agglomeration, a phenomenon where molten or sticky ash compounds interact with bed material, is a significant issue that can cause defluidisation and shutdown of the reactor unit. Ash fusion tests and thermodynamic modelling revealed that torrefaction reduced the melt fraction at 950 °C and increased the ash melting point, but not enough for industrial applications. In contrast, torrefaction followed by water-leaching showed more promising results, with a more pronounced increase in melting point. The pre-treatment of fuels also reduced the amount of ash, decreasing the risk of bed agglomeration. In comparison to the benchmark IWP, the ashes of torrefied and post-washed fuels exhibited nearly identical melting behaviour. When blended with 2 wt% $CaCO_3$, the torrefied and torrefied/post-washed fuels demonstrated suitable melting behaviour,

with experimental results from HSM and thermodynamic modeling showing consistent agreement. At a gasification temperature of 950 °C, melting is unlikely to be a concern in this scenario. The predicted amount of molten slag for both samples was found to be even lower than that of the benchmark material. Despite IWP indicating a slag-to-oxide ratio of 40:60, the torrefied sample with added $CaCO_3$ showed a ratio of 20:80, and the torrefied and water-leached sample with additive displayed a nearly 10:90 ratio. The results were consistent across both experimental and modelling methods. The presence and concentration of alkali metals have a significant impact on melting temperatures, which can lead to low-melting eutectics formation [172].

Another viable alternative would be to use To-WL feedstocks without any Ca-based additives. However, considering the predicted results, it may be more advantageous to decrease the gasification temperature from 950 °C to 900 °C or lower. This should eliminate ash-related problems and result in phase formations similar to those of the benchmark IWP.

Fouling and slagging

The formation of deposits on heat transfer surfaces, such as heat exchangers and boiler walls, is a common issue in biomass fuel utilisation, often resulting in fouling and slagging problems. These deposits typically consist of alkali compounds [118]. Mineral deposits found on heat transfer surfaces are frequently composed of alkali compounds. Batch-type release experiments and thermodynamic equilibrium calculations indicate that alkali chlorides and carbonates are primarily released under typical CLG conditions, which then condense in colder areas of the plant. As a result, biomass with higher levels of volatile alkali compounds poses a greater risk of condensation. Notably, both torrefied and water-leached wheat straw samples exhibited the greatest shift in predicted alkali salt condensation temperature compared to the raw feedstock, “mimicking” the behaviour of the benchmark IWP. This is promising, as the condensation temperatures of KCl (and partially NaCl) were lower than their melting points, suggesting that the deposits will not be excessively sticky for industrial-scale applications.

Poisoning of oxygen carrier materials

At the heart of any CLG application is the oxygen carrier material, which, in addition to the previously mentioned issues, is also susceptible to reactions with ash-derived particles and gas phase components. For instance, it is well-known that sulphur can poison the oxygen carrier activity [238]. Thermodynamic equilibrium calculations suggest that chlorine, derived from the gas phase, may react with iron and manganese in LD Slag, Sibelco, and ilmenite to form volatile chlorides. This issue can be mitigated by torrefying and/or water-leaching the samples, as chlorine can be effectively removed from the feedstock. Consequently, the reduced chlorine content also reduces the risk of poisoning. Furthermore, thermodynamic calculations indicate that alkali and alkaline earth oxides can be incorporated into various solid phases of oxygen carriers. In the case of ilmenite, alkali titanates are likely to form. Notably, torrefied and post-washed wheat straw has shown the most promising results in reducing this risk.

4.2 Influence of pre-treatment measures on behaviour of inorganic constituents

This chapter examines the laboratory-scale pre-treatment technologies of torrefaction and water-leaching, as well as their combination in various sequences, on the behaviour of inorganic constituents. Four selected herbaceous feedstocks, listed in Table 3.1 (Chapter 3.1), were investigated and compared with one another.

4.2.1 Chemical characterisation of fuels

Four straw varieties – colza, barley, corn, and wheat – were chosen as biomass-based fuel samples due to their widespread availability and potential use in Europe and globally. The goal was to investigate and compare a diverse range of pre-treated herbaceous samples. By pursuing this objective, numerous outcomes were obtained that allow for detailed conclusions about the ash melting behaviour (mineral phases) and the fate and release behaviour of inorganics (gas phase). The results of the ultimate analysis for all feedstock samples are presented in Table 4.3.

Figure 4.20 presents the results of the ultimate analysis, with a primary focus on inorganic species. These species are particularly sensitive to pre-treatment technologies such as torrefaction and water-leaching. The chemical analysis outcomes underscore the complexity of biomass as a natural material, which exhibits enormous chemical and inorganic variability.

It can be generally stated that torrefied samples exhibited a higher weight percentage of critical inorganic species, specifically alkali metals, compared to the original material. In contrast, corn straw showed a higher average concentration of Mg and Si, which may be attributed to the fact that it was contaminated with soil impurities.

The torrefaction process increases the bulk density of the material by eliminating volatile organic compounds and water (in the form of moisture), which in turn enhances the fixed carbon content and increases the calorific value of the feedstock [239, 240]. Water-leaching has a notable impact on reducing the Cl content, whereas no effect is observed on Si content due to its insolubility. As potassium is primarily present in the form of KCl in the fuel, water-leaching also has a positive effect on K content, as it effectively removes it with the washing water. Additionally, sulphur and phosphorus can be removed to some extent due to the different solubility of various sulphur or phosphorus compounds.

Table 4.3: Ultimate analysis of the pre-treated fuel samples (wheat, barley, colza and corn straw) in wt% or mg kg^{-1}. The results were not normalised. Blue colour marks the source material.

wt% (ar)	Wheat	To	WL	To-WL	WL-To	Barley	To	WL	To-WL	WL-To
C	43.80	50.50	45.20	49.30	51.30	43.40	50.30	44.30	47.10	49.50
H	6.18	5.83	6.39	5.83	5.96	6.20	5.91	6.37	5.85	5.95
N	0.39	0.44	0.30	0.47	0.34	0.56	0.73	0.39	0.37	0.63
O	44.20	37.00	45.40	39.40	39.20	43.80	37.70	44.70	39.70	40.20
S	0.18	0.17	0.10	0.10	0.10	0.13	0.12	0.10	0.10	0.10
mg kg^{-1} (ar)	Ash forming components (major elements only)									
Cl	3360	424	127	298	113	618	1076	42	60	100
Al	20	20	20	61	20	20	20	20	40	20
Ca	2010	1747	340	2640	845	3010	4310	2820	4400	4130
Fe	10	7	7	76	7	7	7	7	49	7
K	13000	17840	2360	6400	3214	15600	19550	3600	7170	4610
Mg	468	716	248	588	358	377	550	271	515	405
Na	90	90	90	200	90	90	140	90	200	90
P	220	320	78	210	96	890	1258	490	980	1010
Si	7840	10130	7410	10200	10640	7480	10720	7000	10710	10800
wt% (ar)	Colza	To	WL	To-WL	WL-To	Corn	To	WL	To-WL	WL-To
C	41.20	46.90	44.00	47.60	50.10	41.40	49.00	42.90	48.10	48.40
H	6.01	5.77	6.38	5.98	6.02	6.11	5.74	6.21	5.90	5.27
N	0.51	0.54	0.30	0.36	0.34	0.60	0.50	0.49	0.57	0.52
O	44.10	41.00	45.00	42.20	41.50	44.30	37.60	41.80	40.30	38.00
S	0.33	0.36	0.10	0.10	0.11	0.11	0.13	0.10	0.10	0.11
mg kg^{-1} (ar)	Ash forming components (major elements only)									
Cl	8340	915	588	349	341	3434	989	228	273	310
Al	31	20	20	40	20	1010	610	1251	550	1215
Ca	8430	8920	4730	4760	6284	6110	3270	3070	3110	4209
Fe	7	7	7	18	7	686	224	758	270	574
K	22370	24570	3147	3250	3990	11400	25000	5970	4470	9070
Mg	552	662	227	253	304	2800	2480	1652	1740	2033
Na	1199	1710	185	200	235	86	196	155	100	147
P	242	413	63	130	78	940	1293	700	573	909
Si	98	47	30	70	30	17100	10130	21200	10800	19210

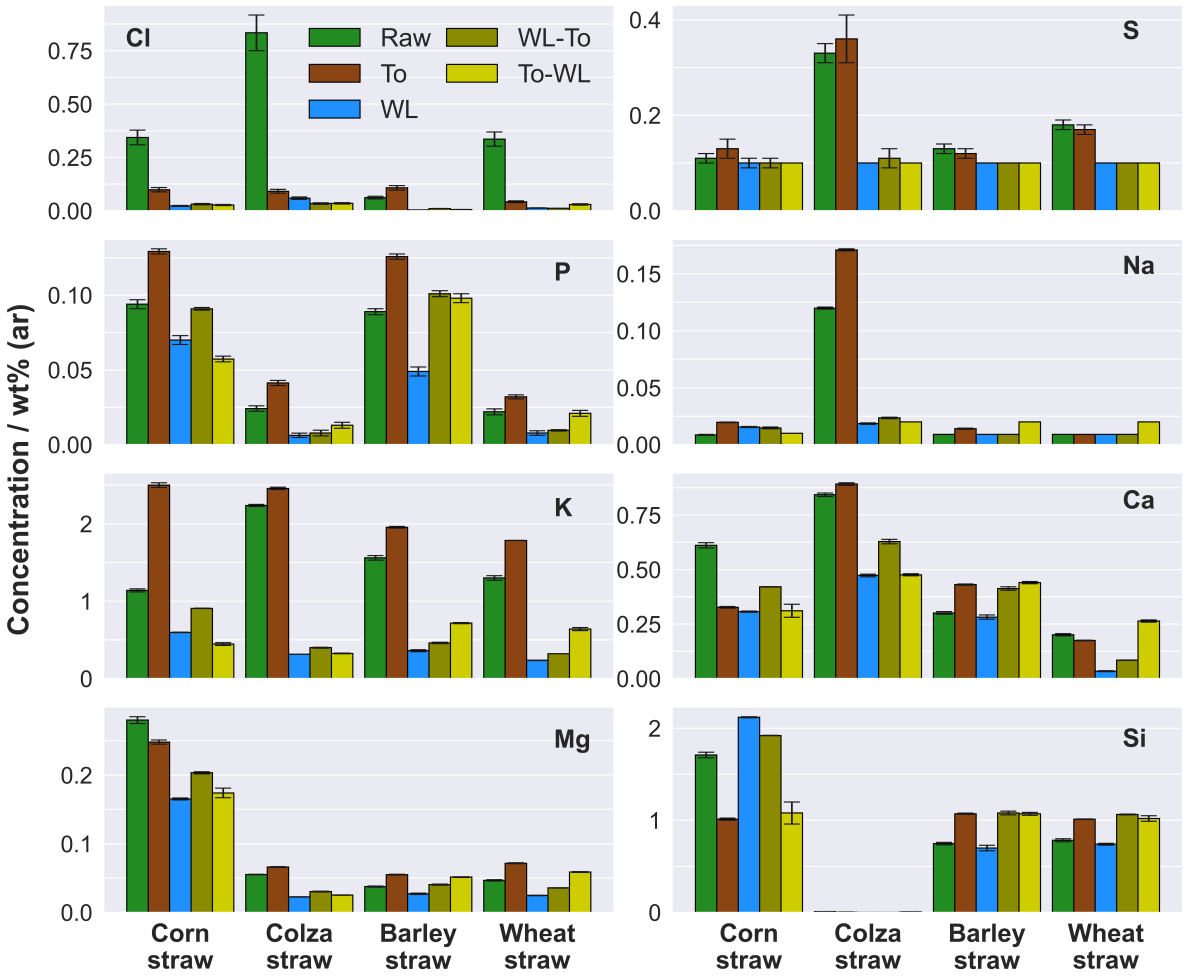

Figure 4.20: Chemical analysis of various pre-treated herbaceous feedstocks, with a special focus on species that are critical to understanding ash-related issues. The data is sourced from Table 4.3.

A comparison of the first and second washing cycles in Figure 4.21 reveals that the effect of decreasing Cl content becomes more pronounced after the second wash. A significant reduction in chlorine levels was observed in the washing water after the second cycle. In the case of torrefied samples, particularly those made from corn straw, the chlorine content after the first wash cycle was lower compared to the original material. It is likely that some of the fuel-bound Cl was released during the thermal pretreatment, as seen in previous studies [48, 208], which would explain the decrease in leached Cl. However, after the second wash cycle, it appears that the chlorine fraction remained consistent with that of the untreated source material. This suggests that some of the Cl had become chemically bound to a different matrix, possibly an organic one.

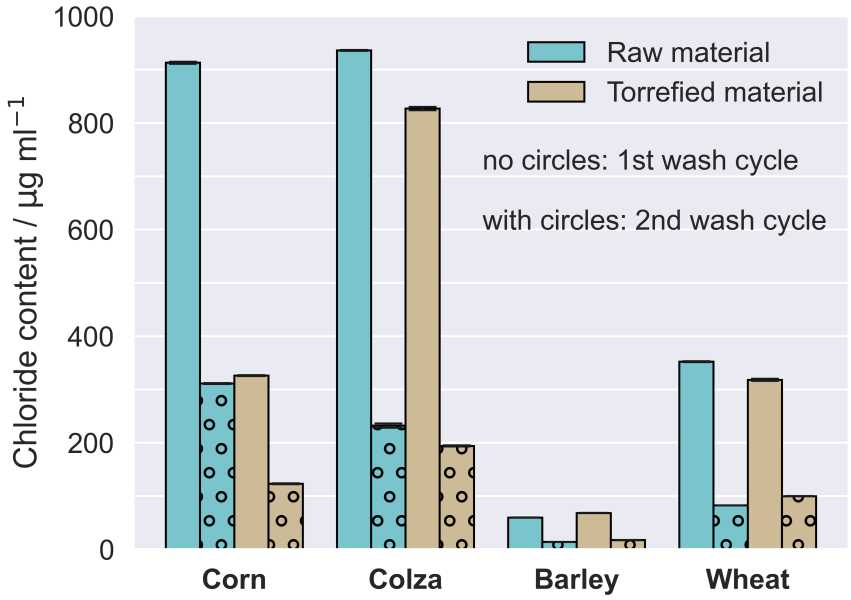

Figure 4.21: Chloride content in washing water after first and second wash cycles for untreated and torrefied materials.

Beyond the ultimate analysis, the ash yield provides supplementary information on the distinct effects of the applied pretreatment methods. The ash content of each sample was determined gravimetrically in an oxidising environment and is presented in Figure 4.22.

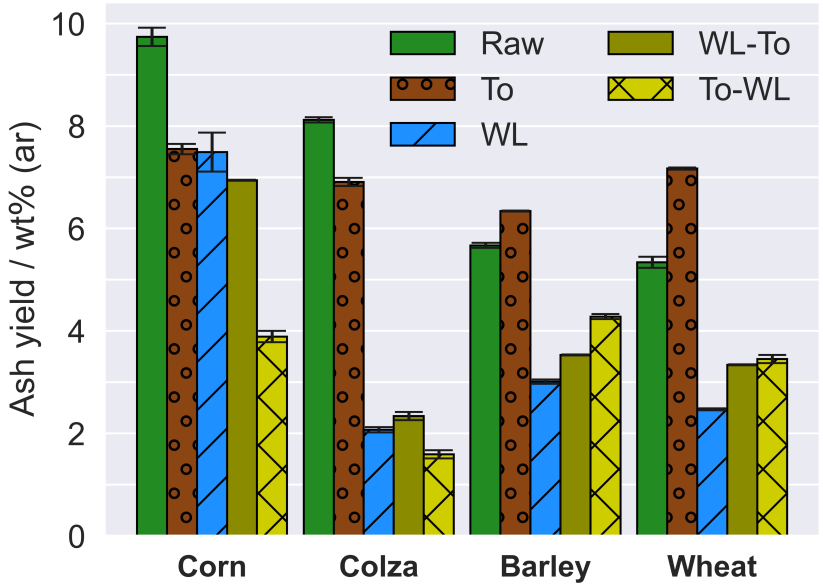

Figure 4.22: Ash yields for raw, torrefied, water-leached, torrefied and pre-washed, or post-washed straw samples at 550 °C for 36 h under atmospheric pressure.

The leached samples and pre- or post-washed materials showed the lowest ash content relative to raw and torrefied materials. This suggests that a significant portion of inorganic species was removed with the wash water. The torrefied fuels from barley and wheat showed a slightly increased ash yield, which is attributed to an increased bulk density of the sample material. Colza straw exhibited a significantly higher chloride content (Fig. 4.20), and torrefaction pre-treatment appeared to reduce the ash yield by approximately 1 wt%. Notably, Shang et al. [241] detected methyl chloride in the volatile products of torrefaction, but its impact on biomass chlorine content has not been extensively studied. Compared to biomass that had only been leached, the bulk density of pre-washed/post-washed and torrefied materials increased slightly, but remains lower than that of torrefied material.

4.2.2 Analysis of hot gases using MBMS (batch-type experiments)

The thermal conversion of biofuels under gasification-like conditions was simulated to investigate the fate and release of inorganic gaseous species. Figures 4.23 and 4.24 present the average normalised results of inorganic species released during the devolatilization phase and the ash/char reaction phase, respectively. Three measurements were taken for each sample, under conditions analogous to those described in Chapter 4.1.

The results of the semi-quantitative analysis were consistent with those of the chemical characterisation (Figure 4.20, Chapter 4.2.1). Compared to the untreated source materials, the torrefied samples showed a lower amount of chlorine released into the gas phase. In contrast, the water-leached samples exhibited more pronounced effects on the release behaviour of certain inorganics, particularly a significant reduction in the amounts of released Cl, HCl, and K. The release of sulphur-containing compounds (H_2S, SO_2, and COS) also tended to be slightly reduced. As previously observed in Fig. 4.3 (Chapter 4.1.2), the varying size of the error bars suggested an inhomogeneous distribution, which is consistent with biomass's typical fibrous and inhomogeneous properties. Based on these findings, it can be concluded that samples that underwent torrefaction and post-washing exhibited the most pronounced effects in reducing the levels of problematic, volatile species.

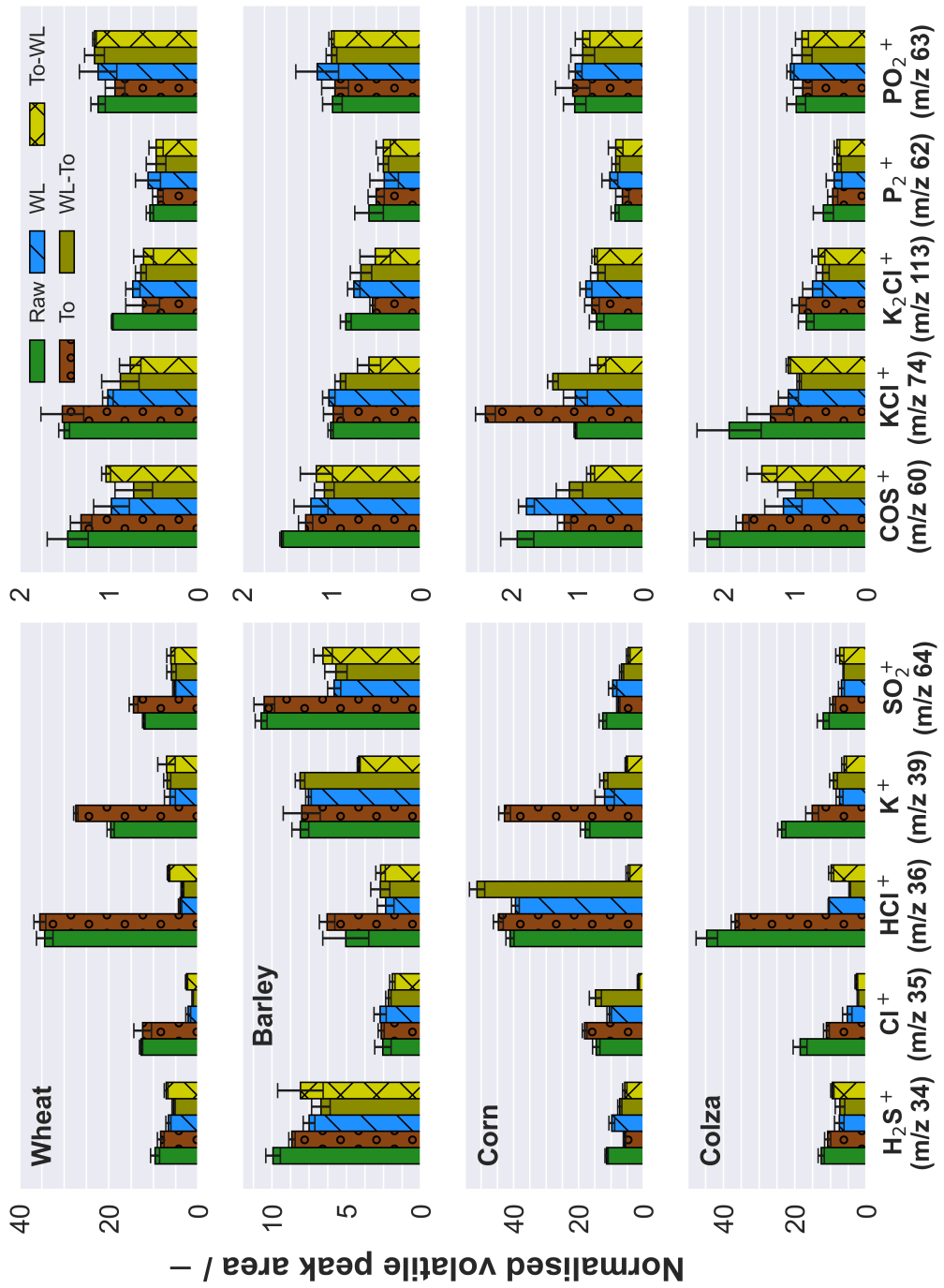

Figure 4.23: Averaged normalised peak areas of detected species released during devolatilization phase for raw and pre-treated wheat, barley, corn and colza straw.

Both raw and torrefied samples primarily exhibited secondary releases in the form of char gasification or ash reactions, as depicted in Figure 4.24. The main contributors to these releases were less volatile compounds in the ash, which primarily consisted of K, SO_2, and Cl. During this reaction phase, species were released that are less or non-volatile without a reaction partner, in contrast to the devolatilization phase. For example, sulphur was released as sulphur dioxide from stronger-bound organic compounds or sulphates. It is likely that the more strongly bound organic sulphur was released before the inorganic sulphur compounds. Additionally, a key observation was that the water-leached samples showed almost no releases during the ash/char reaction phases for nearly all inorganic compounds.

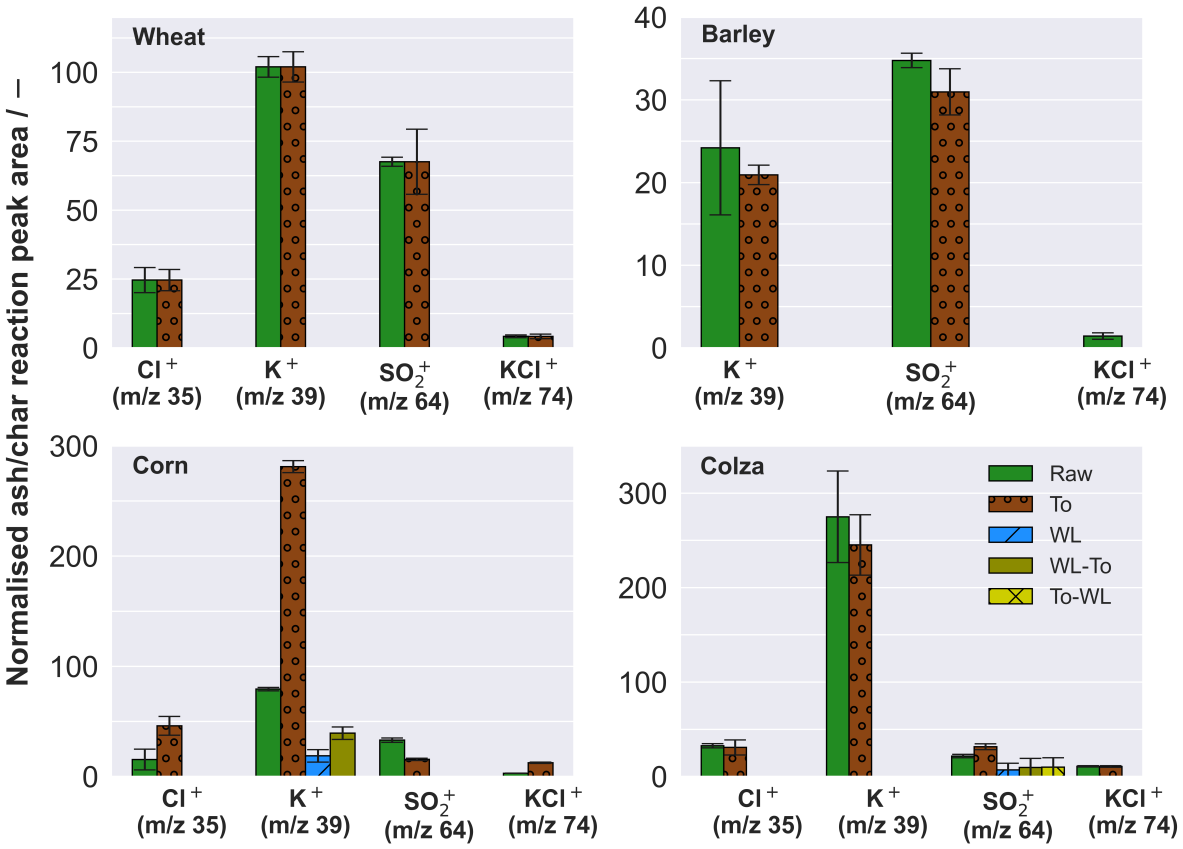

Figure 4.24: Averaged normalised peak areas of detected species released during the ash/char reaction phase (wheat, barley, corn and colza straw).

No further release of KCl or Cl was observed for samples that underwent water-leaching or torrefaction followed by pre- and post-washing. Due to their higher bulk density, the torrefied samples tended to exhibit a larger amount of released Cl and KCl. Additionally, a significant decrease in K or SO_2 was observed for washed samples during the second-release reaction phase.

Previous studies have shown that the molar Si/K ratio may be a reliable indicator of potassium release in the gas phase [242–244]. A high molar Si/K ratio is associated with the formation of potassium silicates, which are retained in the bottom ash. It is well established that alkali metal oxides can be chemically incorporated into silicate networks, making them less volatile [16, 245, 246]. Figure 4.25 presents data on the correlation between the molar Si/K ratio and K release, as obtained from the batch-type release experiments depicted in Fig. 4.23.

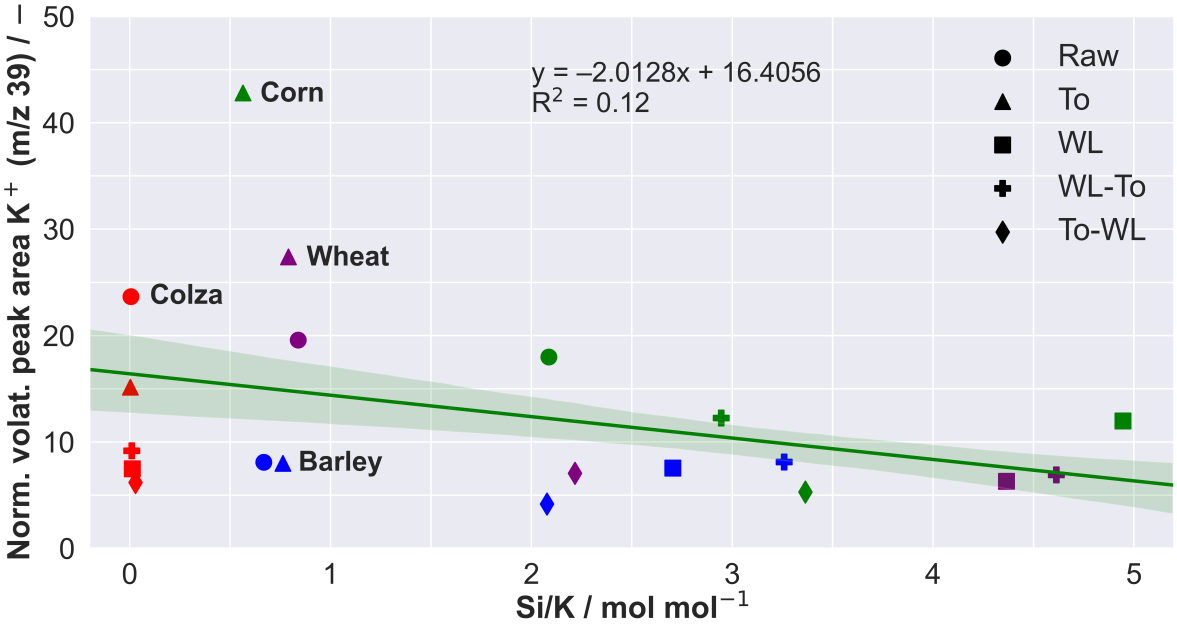

Figure 4.25: Comparison potassium release during devolatilization in relation to the molar ratio of Si/K for the (treated) herbaceous fuels. The confidence interval is set at 68 %.

A clear correlation was observed between the molar ratio of Si/K and the release behaviour of K. The release of K decreased with increasing molar Si/K ratio. Fig. 4.25 suggests that a higher concentration of Si relative to K limited the gas phase activity of K. In addition to these findings, the results also highlighted the effects of the pre-treatment methods applied. While the raw material and torrefied samples were associated with a higher release of potassium, the water-leached samples showed the opposite trend. A decrease in the fuel potassium content in the sample caused a shift in the ratio towards silicon, resulting in a corresponding decrease in potassium released. Sommersacher et al. [247] reported that other parameters, such as fuel bed temperatures and the presence of potassium in the fuel, also have a significant impact on potassium release.

4.2.3 Influence of pre-treatment measures on the release of N-species

So far, little is known about how different pre-treatment approaches affect the fate of fuel-N [157]. Besides gaseous Cl, S, or P species, it is expected that various pre-treatment technologies will also influence the formation of nitrogen species. This chapter focuses on investigating the fate and release behaviour of NO, NH_3, and HCN during devolatilization, combustion, and gasification-like conditions of upgraded wheat straw. The main focus of this work is on the thermochemical conversion of biofuels under gasification-based processes, although the chemistry and transformation of nitrogen are strongly dependent on oxygen partial pressure. Therefore, experimental investigations were conducted under both gasification and combustion conditions to provide an improved overview and reveal distinctions between these thermal conversions.

Figure 4.26 exemplifies the NO release curves from combustion (3 vol% O_2, rest N_2), gasification (14.5 vol% H_2O, 5 vol% CO_2, rest N_2), and devolatilization experiments (100 vol% N_2). The experiments to determine the N-species were conducted using a SPR, as described in Chapter 3.3.5 (Fig. 3.11).

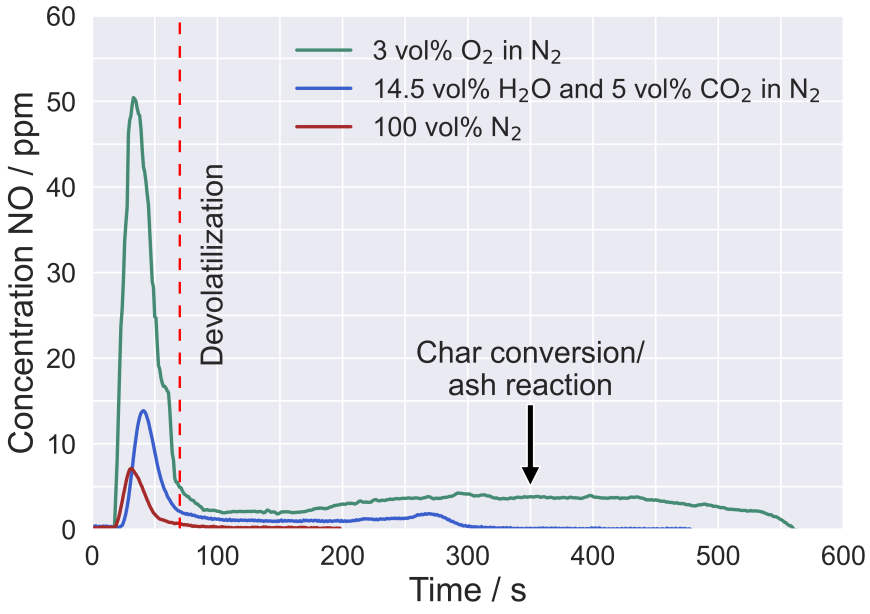

Figure 4.26: Release of NO during combustion (O_2 and N_2), gasification-like conditions (H_2O, CO_2 and N_2), and devolatilization (N_2) of raw wheat straw at 950 °C. The dashed line divides the devolatilization part from the char conversion/ash reaction part.

As shown in Fig. 4.26, the curves obtained from the combustion and gasification experiments exhibited both devolatilization and char conversion stages. Not surprisingly, in the devolatilization experiment performed under a nitrogen atmosphere (100 vol% N_2), no char gasification/ash reaction was observed. The devolatilization reaction typically involves a relatively rapid mass loss rate, whereas the ash/char conversion process occurs at a much slower rate, which is attributed to the chemical binding of nitrogen within the biofuel. This observation is consistent with the results of the batch-type release experiments, as described in Chapter 4.2.2 and supported by hot gas analyses using MBMS. The release of NO declined significantly in an oxygen-poor atmosphere, whereas a substantial peak was observed in an oxygen-rich environment. The amount of released NO was evaluated using a similar approach to the hot gas analyses, by integrating the peak intensity and dividing it into two parts: devolatilization and char conversion/ash reaction. The distribution of char-N, volatile-N, and removed-N is depicted in Figure 4.27.

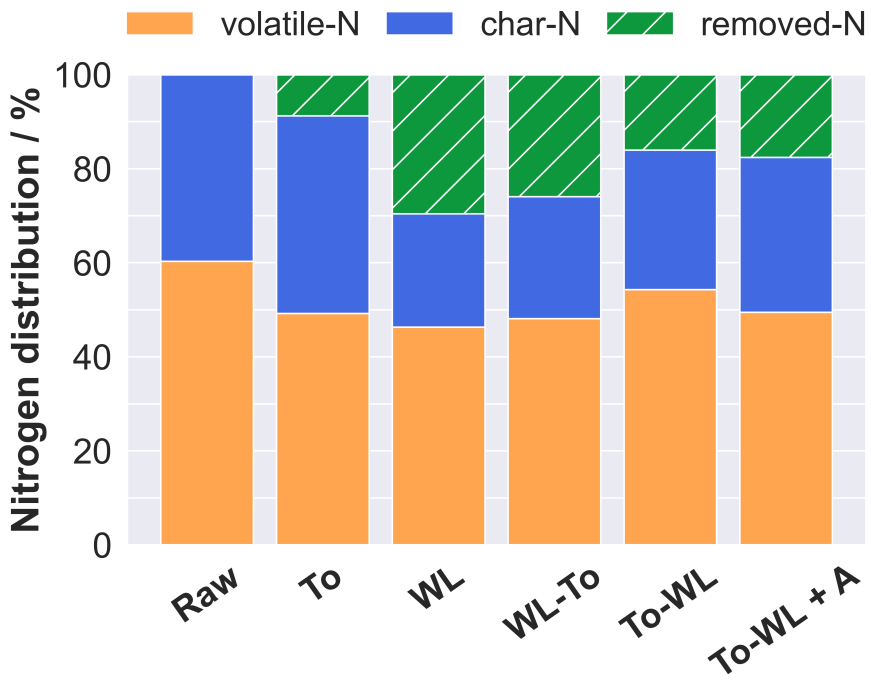

Figure 4.27: Distribution of volatile-N, char-N, and removed-N (estimated based on fuel-N content in raw wheat straw, the source material).

The N-content was determined as described in Chapter 3.3.5, and the results from CHNS analyses (fuel-N and char-N) were incorporated into the calculation of the N-distributions. As shown, approximately 40 % to 60 % of the nitrogen is volatile-N, while 20 % to 40 % of the nitrogen is present as char-N. Around 10 % to 30 % of the nitrogen

was removed during the pre-treatments, which is consistent with previous investigations [140, 248, 249]. Abelha et al. [250] found that pre-washing miscanthus and roadside grass reduced the nitrogen content, suggesting that a portion of the fuel-N is present in water-soluble forms such as ammonium salts or amines in the feedstock. This result is consistent with other studies [41, 251] that have reported a decrease in nitrogen content during water-leaching.

To better visualise the results presented in Fig. 4.27, Figure 4.28 shows the correlation between volatile-N and char-N distribution for fuel samples that were pre-treated and those that were not.

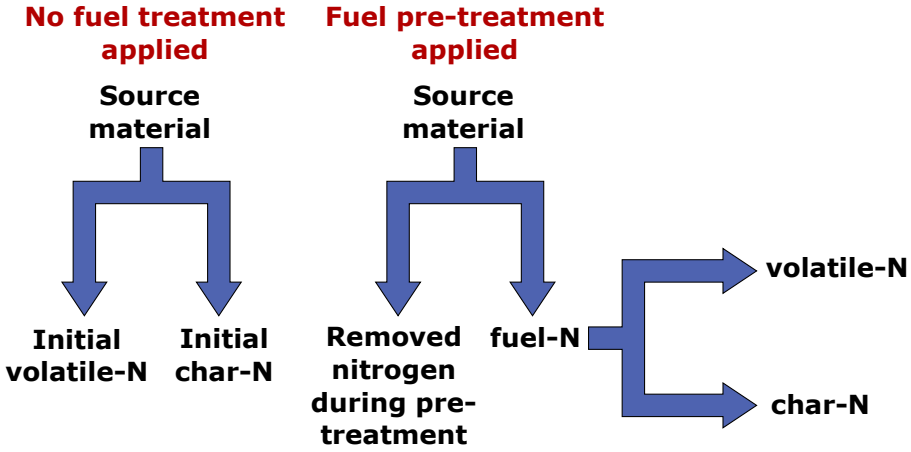

Figure 4.28: A schematic illustration of the fate of the nitrogen in a fuel. Modified after Schmid et al. [144].

The left sketch in Fig. 4.28 depicts the nitrogen distribution if no treatment was applied whereas the right sketch highlights the effect after pre-treatment (torrefaction, water-leaching or combination of both steps). It is worth noting that the initial amount of volatile-N is greater than the volatile-N itself, whereas the initial amount of char-N is approximately equal to the char-N concentration.

The removed nitrogen content was estimated based on the torrefaction grade (T_G = 27.8 %, Table 3.2, Chapter 3.1) or residual organic content after treatment. The organic fraction of the treated samples was determined from the ash content, assuming that the raw wheat straw has an ash content of 5.32 wt% (Table 3.2, Chapter 3.1), which corresponds to a residual organic content of 94.67 wt%. For the water-leached sample, an ash content of 2.47 wt% was measured, resulting in a residual organic content of 97.53 wt%. By calculating the ratio between the raw and washed samples, a factor of 0.97 was obtained. Multiplying this factor by the N-content of the washed sample (0.28 wt%) yields an estimated N-content of 0.27 wt%. This indicates that approximately

0.12 wt% of nitrogen must have been removed from the raw fuel, which had an initial nitrogen content of 0.39 wt%. For both washed and torrefied samples, the torrefaction degree was considered when estimating the removed nitrogen content.

The initial ratio of volatile-N to char-N for the raw material was 60:40. After torrefaction, this ratio changed to 49:40. In contrast, the volatile-N/char-N ratio remained relatively constant for the water-leached, torrefied, and either pre- or post-washed samples. The calculated approximation suggests that approximately 10 % of the initial nitrogen was removed during the torrefaction treatment, while around 30 % was removed during water-leaching.

The total amounts of NO released from combustion and gasification experiments are displayed in a three-dimensional bar chart in Figure 4.29.

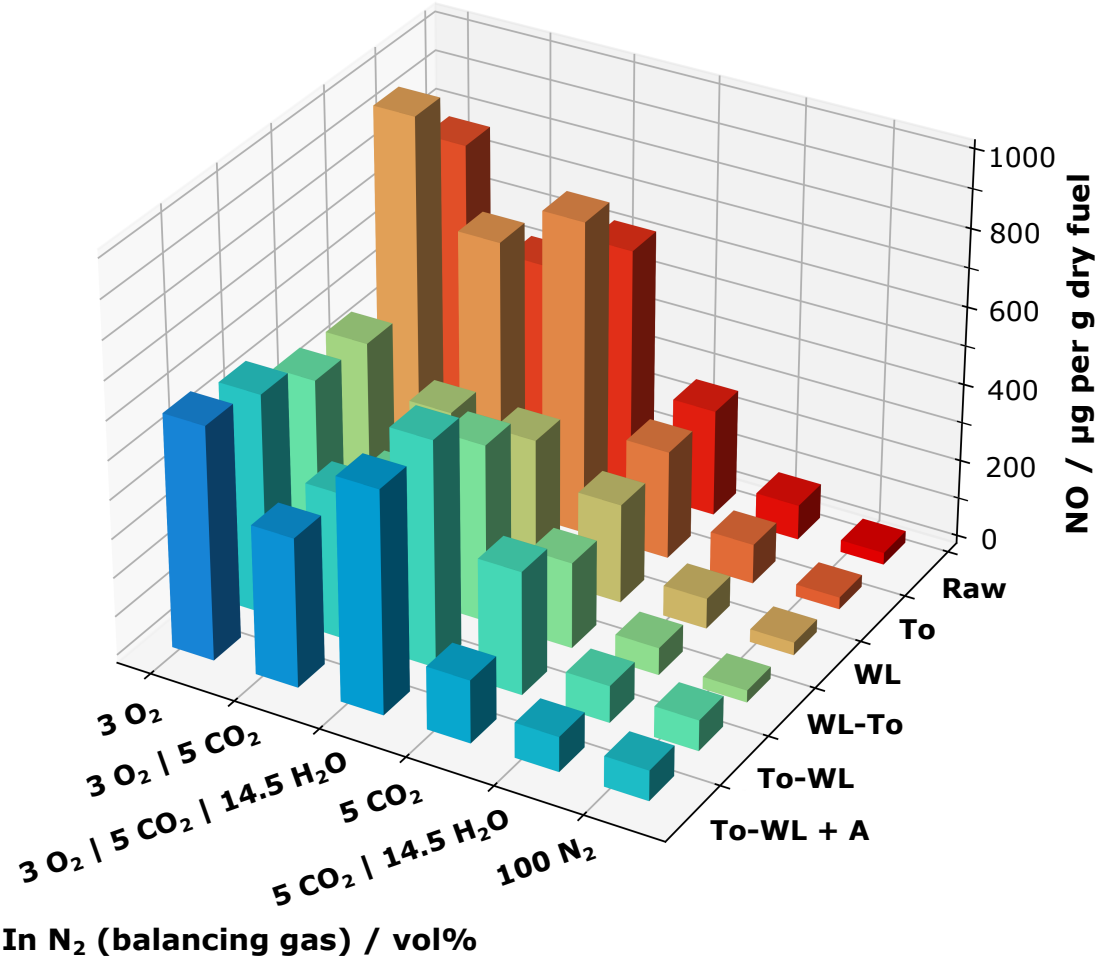

Figure 4.29: NO emission in µg g^{-1} dry fuel subject to different atmospheric conditions at 950 °C. The balancing gas was nitrogen.

During gasification, as expected, NO emissions were significantly lower than during combustion due to the absence of oxygen. The NO emissions from upgraded biofuels generally exhibited lower levels than those of the raw materials, except for torrefied fuels, which showed significantly higher emissions. During combustion at 3 vol% O_2, the raw material released approximately 790 µg of NO per gram of fuel, whereas the torrefied fuel emitted around 960 µg. It is noteworthy that the torrefied straw had a higher nitrogen content than the original straw (0.48 wt% vs. 0.39 wt%). In contrast, a substantial decrease in NO emissions was observed for water-leached samples, with an approximate reduction of 40 % to around 480 µg NO per gram of fuel. This decrease corresponds to a significant reduction in NO emissions.

Water-leached samples generally exhibited the lowest NO release rates, indicating that washing had a suppressing effect on the nitrogen chemistry. In contrast to the WL-To samples, the To-WL samples showed a slight increase in NO emissions, regardless of whether the reaction conditions were those of combustion or gasification. These observations provide additional evidence that the sequence of pre-treatment can have a corresponding impact on the release behaviour of inorganic species.

Interestingly, the addition of $CaCO_3$ to the To-WL sample resulted in a slight increase in NO emissions during combustion at 3 vol%, compared to the same sample without additive. This finding is consistent with previous studies on coal combustion, which have shown that limestone can increase NO emissions during combustion [252, 253]. Similarly, Liu et al. [254] reported that the addition of limestone to petroleum coke combustion can impact NO emissions, with the outcome dependent on the degree of contact between gas-solid components. If sufficient contact between calcium compounds and gaseous products is achieved, NO emissions may decrease. However, the underlying reaction mechanism remains unclear.

It is important to note that the amount of emitted NO does not directly correlate with the N-content in the parent fuel. Despite the higher N-content in the To-WL material compared to the untreated source material, significantly less nitrogen was released during combustion or gasification-like conditions. This is consistent with earlier findings by Ren et al. [157], who reported varying NO emissions for torrefied biomass samples depending on the type of biomass used. It is well established that the overall N-content in the parent fuel is an inadequate predictor of NO_x formation.

The conversion of fuel-N to NO is illustrated in Figure 4.30. It is noteworthy that the process has been broken down into two stages: devolatilization and char conversion, with corresponding conversion rates for volatile-N to NO and char-N to NO. In a combustion

environment (3 vol% O_2), fuel-N conversion to NO is expected to be higher than in a gasification-like atmosphere (14.5 vol% H_2O and 5 vol% CO_2). This difference is evident when comparing the release activity of the source material under these two conditions. Under 3 vol% O_2, 95 % of the fuel-N was converted to NO, whereas under 14.5 vol% H_2O and 5 vol% CO_2, only 12 % of the fuel-N was converted to NO. Furthermore, pre-processing had a suppressing effect on the fuel-N to NO conversion. For the torrefied-water-leached material, approximately 60 % of the fuel-N formed NO (in 3 vol% O_2), which represents a 35 % decrease compared to the raw sample.

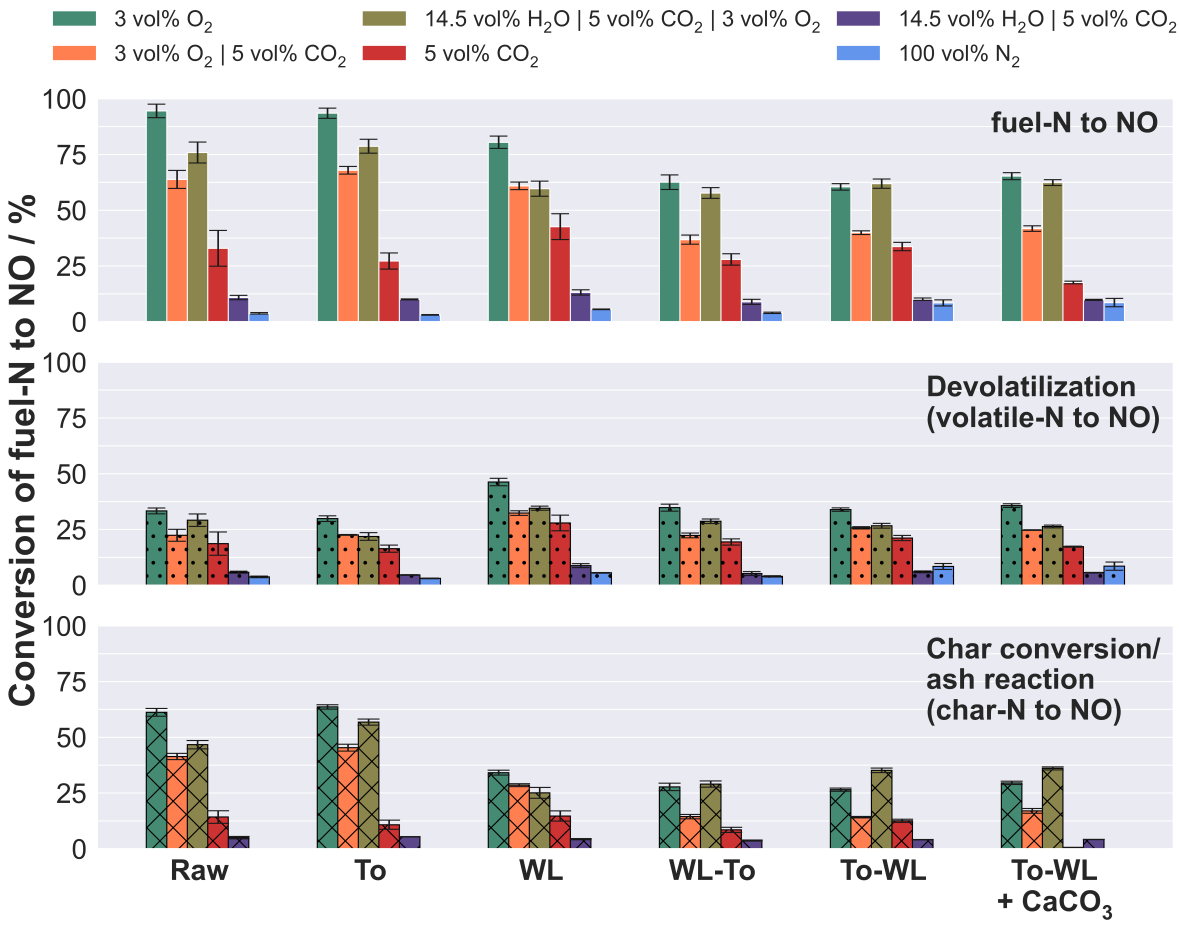

Figure 4.30: Conversion of fuel-N to NO at 950 °C: conversion of fuel-N to NO (top), volatile-N to NO or devolatilization (centre), and char-N to NO or char conversion (bottom).

Water-leached samples showed increased conversion of volatile-N to NO compared to raw or torrefied material, whereas all pre-treated samples, except the torrefied sample, produced lower NO emissions during char conversion. The raw and torrefied samples

formed approximately 62 % of char-N as NO, while the washed samples prior to or after thermal treatment produced 26 % to 35 % of char-N as NO. This supports the earlier statement that N-content is not a key factor in the conversion of volatile-N or char-N to NO. For combustion conditions, it appears that CO_2 reduces NO emissions, whereas H_2O increases them. These effects seemed to apply to CO_2 in both devolatilization and char conversion/ash reaction stages, but were more pronounced for H_2O during char burning. In gasification, H_2O decreased the formed NO, which was true for both conversion steps.

Previous studies [146, 155] reported that washing and subsequent torrefaction of samples led to the highest conversion of char-N to NO compared to raw or solely torrefied materials. In contrast, this study's findings do not align with those results, and the reason for this discrepancy is unclear. It is worth noting that the washing treatment in [144] was conducted at 50 °C, whereas in this study, it was performed at room temperature (20 °C). Furthermore, the decrease in nitrogen concentration observed in [144] was significantly higher than that seen in this work between raw and washed/torrefied straw samples.

During devolatilization, precursors such as NH_3 and HCN are released [140, 145]. The high-temperature chemistry of these nitrogen-containing species has been extensively studied (see, for example, [146]). HCN is the primary cyanide species, which can be further converted to NH_3 [135]. NH_3 and HCN can react to form imidogen (NH), a highly reactive radical. The reaction mechanism involves intermediate steps that depend on combustion parameters such as stoichiometry, gas temperature, and others [140, 255]. The nitrogen chemistry is primarily governed by NH_3 rather than HCN, with the selectivity for forming NO and N_2 controlled by combustion conditions in staged combustion processes [135]. The minimum in NO formation is due to competition between the reduction of NO by NH_3 and HCN and the oxidation of NH_3 or HCN [256]. The composition of the gas mixture can have a significant impact on the gas phase, with NH_3 being a notable example. However, its interaction with hydrocarbon oxidation chemistry, particularly under reduction conditions, is complex and multifaceted, as demonstrated in [135].

Figure 4.31 presents the conversion rates of volatile-N to NO, NH_3, and HCN during devolatilization at 950 °C. For the pre-treated samples, the conversion of volatile-N to NH_3 is slightly higher compared to the untreated sample. Notably, a significant increase in NH_3 formation is observed when the To-WL sample is blended with 2 wt% $CaCO_3$. A similar finding was reported by Schmid et al. [144] in a recent study using the same reactor system, where it was shown that biomass with a higher calcium and lower potassium content produced more NH_3. The results presented here support the

hypothesis that ash-forming elements, such as calcium or potassium, influence NH_3 formation [147, 154–156]. This effect is particularly evident in Figure 4.34 and is further discussed in the latter part of this chapter. In contrast, no trend was observed for HCN activity.

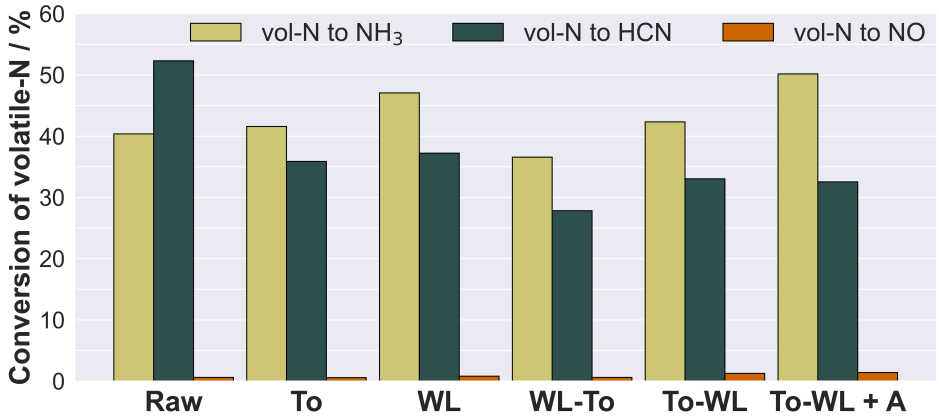

Figure 4.31: Conversion of volatile-N to NO, NH_3, and HCN during devolatilization in 100 vol% N_2 at 950 °C.

The effect of the precursors is further illustrated in Figure 4.32, which shows the formation of NO as a function of the proportion of precursors formed during devolatilization experiments conducted in 100 vol% N_2, under different atmospheric conditions (either oxidising or reducing).

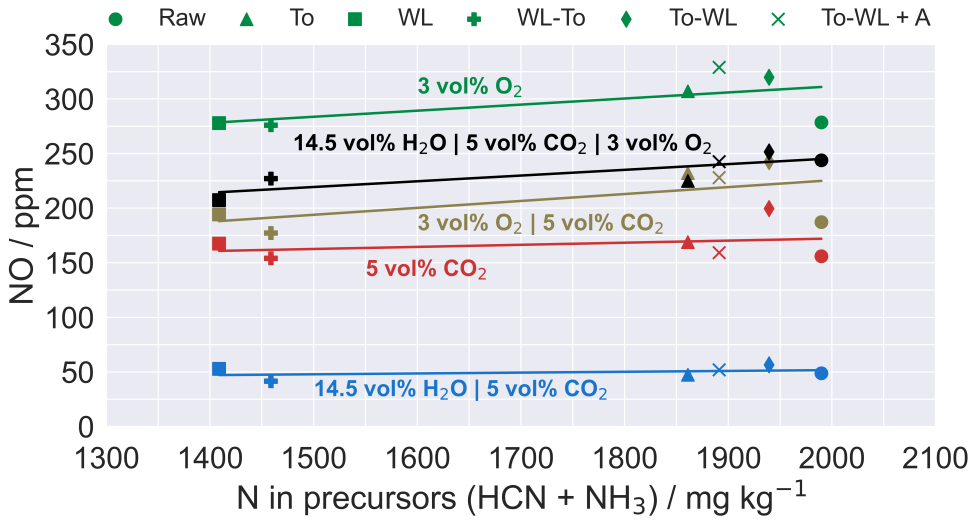

Figure 4.32: Comparison of NO release in various atmospheres and NH_3/HCN formation from devolatilization experiments (100 vol%) at 950 °C.

The data in Fig. 4.32 reveals a weak correlation between NO release and the precursors NH_3/HCN, with a slight increase in the trend with increasing nitrogen concentration in the precursors observed only under combustion conditions. However, the trend in Fig. 4.32 suggests that NO emission is primarily driven by the gas atmosphere rather than the nitrogen concentration in the precursors. This finding is consistent with the results presented in the 3D bar chart in Fig. 4.29, which showed that gas constituents have a decisive impact on NO release. Specifically, combustion conditions (e.g., O_2) led to the highest NO emissions, whereas gasification-like conditions (e.g., H_2O and CO_2) resulted in the lowest NO emissions.

Recent studies [144, 145] have shown that an increase in fuel-N content and a decrease in the H/N ratio result in a higher HCN/NH_3 ratio, which is closely related to the formation mechanisms of NH_3 and HCN. HCN can also be partly converted to NH_3 when hydrogen is present [144]. Figure 4.33 presents the experimentally determined molar HCN/NH_3 ratio for the pre-treated samples as a function of fuel-N content or molar H/N ratio. However, due to the relatively low nitrogen content in the examined samples, no direct trends or conclusions could be drawn from this data.

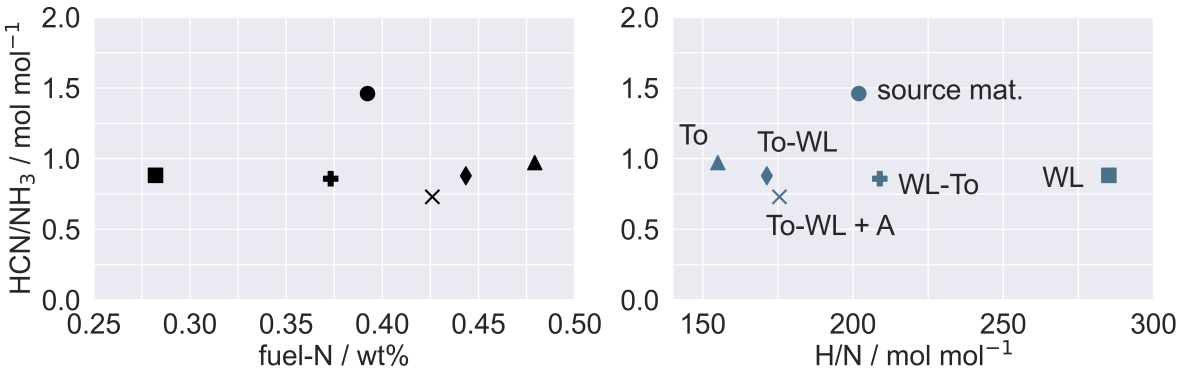

Figure 4.33: Molar HCN/NH_3 ratio plotted against fuel-N (left) or molar H/N ratio (right).

Several studies have reported that ash-forming elements, such as calcium and potassium, can exhibit catalytic effects on the formation of NH_3 and HCN during devolatilization [147, 154–156]. Figure 4.34 illustrates the conversion of volatile-N to NH_3 and HCN as a function of Ca or K concentration in pre-treated samples. Notably, there is no clear trend observed in HCN formation when comparing changes in calcium or potassium concentration. In contrast, the results suggest that more ammonia is formed in samples with higher calcium and lower potassium content.

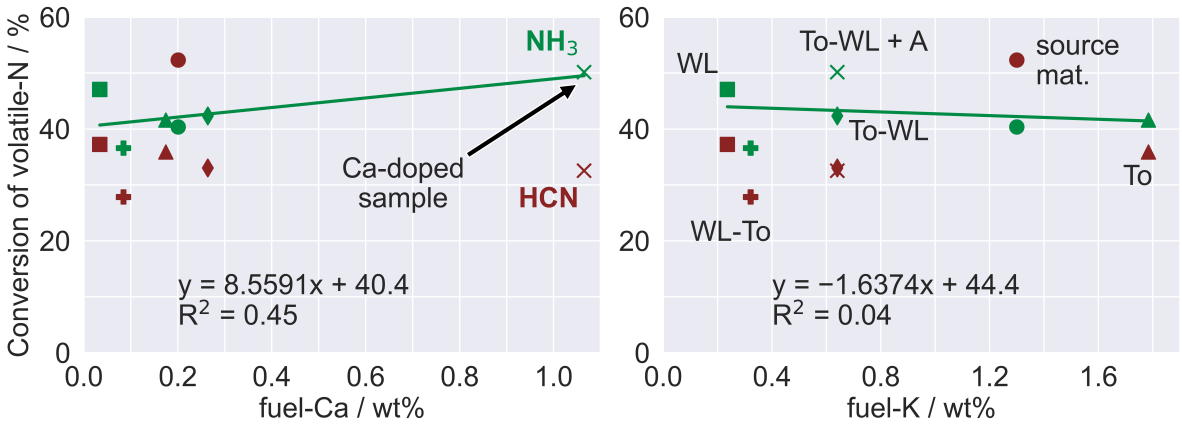

Figure 4.34: Conversion of volatile-N to NH_3 and HCN plotted against fuel-Ca (left) or fuel-K (right) concentration in the pre-treated wheat straw samples. The arrow marks the Ca-doped sample.

A previous study by Schmid et al. [144] observed similar trends in the conversion of volatile-N to NH_3 and HCN for both pre-treated bark and wheat straw. Yi et al. [156] found that during pyrolysis of proteins and amino acids in herbaceous feedstocks, calcium had a enhancing effect on NH_3 formation, while reducing HCN formation. It is clear that the nitrogen chemistry during char oxidation is influenced by ash-forming matter. Winter et al. [257] reported that during char conversion, char-N reacts with oxygen to form NO, which can then be heterogeneously reduced by char-C to nitrogen [258]. Calcium and potassium present in the char are thought to influence the conversion of char-N by catalysing the reduction reaction between NO and char [153]. A recent study showed that demineralised biomass exhibited significantly more NO release compared to raw biomass fuels [188].

4.2.4 Ash fusion testing and behaviour of ashes

Pre-treated ash samples were analysed using HSM to investigate the melting behaviour characteristics of the ashes. Figure 4.35 presents the height profile coefficients h_x/h_0 of ashes of pre-treated straw samples plotted against temperature. A single measurement was taken for each sample, and the conditions were identical to those described in Chapter 4.1. Upon comparing the h_x/h_0 coefficient, it is apparent that each biomass variety exhibits its own distinct profile. The melting behaviour of biofuel ashes exhibits variability due to their heterogeneous composition. Consequently, the geometric shape of the cylindrical samples, as specified in DIN 51730 (“Testing of solid fuels – Determination of fusibility of fuel ash”), cannot be accurately determined, just like for the

industrially pre-treated samples described in Chapter 4.1.4. However, when comparing the treated samples with each other and the untreated source materials, the geometric shape becomes more notable. In general, the fusion process of biomass ash involves moisture evaporation, oxidation of organic matter, and removal, as well as reactions between inorganic compounds at elevated temperatures [259].

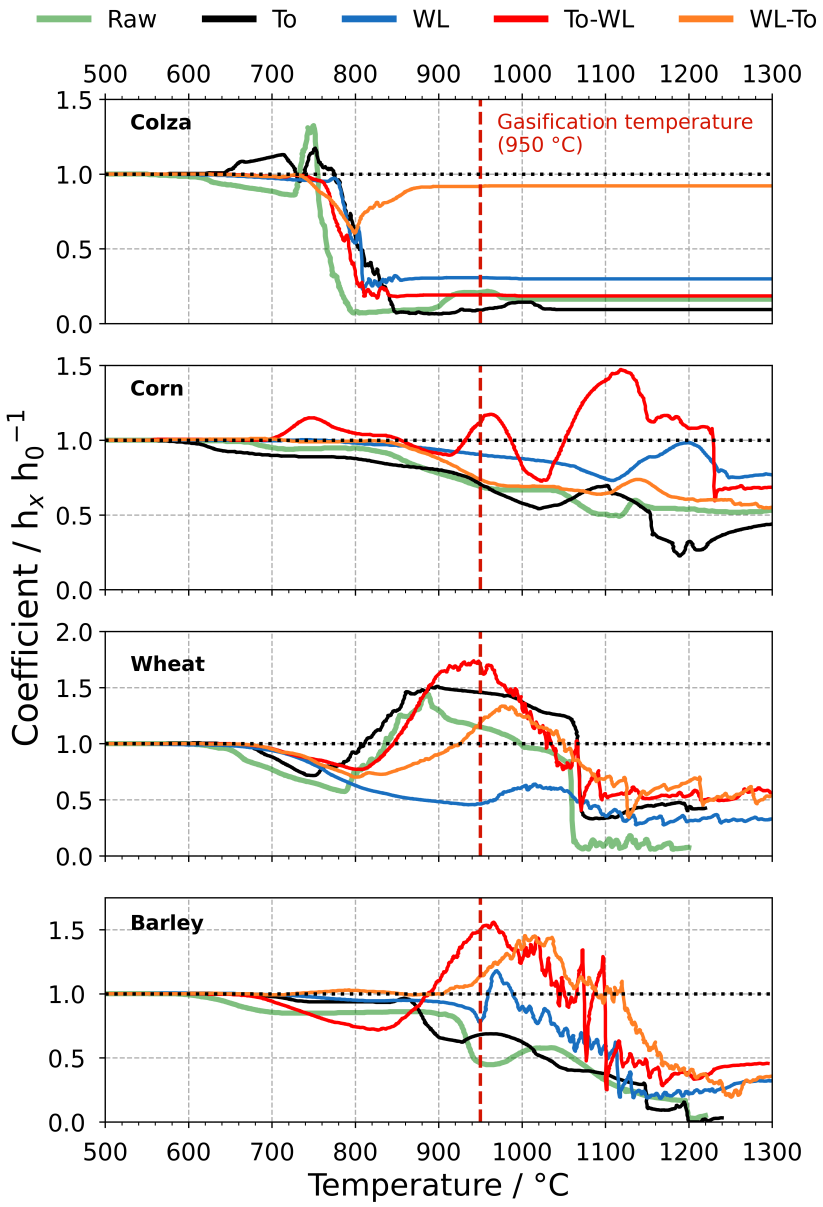

Figure 4.35: Height profile of ashes of raw and pre-treated colza, corn, wheat, and barley straw plotted against temperature (HSM). The red dashed line denotes the defined gasification temperature of 950 °C.

As anticipated, the height profile coefficient indicates a slight decrease in temperature within the range of 600 °C to 700 °C. Although initial sintering effects cannot be ruled out at this stage, it is possible that this temperature range may be attributed to reactions between residual carbon present in the ash and CO_2 in the atmosphere. The high amount of residual carbon in the ash produced in a gasification-like environment may have contributed to these reactions. The ash prepared under gasification-like conditions yielded a range of 12 wt% to 19 wt%, which clearly indicated a significantly increased residual carbon content in the ash compared to combustion at 550 °C, which yielded 5 wt% to 9 wt% (Table 3.2, Chapter 3.1). A blackish hue was observed in the ash samples, indicating that the organic matter was not fully converted (refer to Fig. 3.14 in Chapter 3.3.6). Regardless of the upgrading method employed, the colza straw ash displayed a noticeable low melting temperature, as evidenced by the steep decline in the coefficient h_x/h_0. In contrast, corn and barley straw ash began to melt at higher temperatures. In general, it can be stated that the ash samples either melted completely or swelled within a temperature range of 950 °C.

Biomass ashes are typically rich in oxides of K, Na, Mg, Ca, and P. As a result, they tend to have low melting points, often below 800 °C for straw varieties [160]. The experimental observations presented in 4.35 corroborate this finding. However, some subtle differences were noted: water-leached samples appeared to melt at higher temperatures compared to raw or torrefied fuel ashes.

Notably, untreated colza straw ash showed a change in the coefficient h_x/h_0 around 600 °C, while a more pronounced change was observed in the washed sample at temperatures above 750 °C. This phenomenon was further highlighted by comparing photographs of raw and water-leached samples under identical temperature conditions (Figure 4.36). This suggests that reactions involving ash components may be shifted to higher temperature ranges.

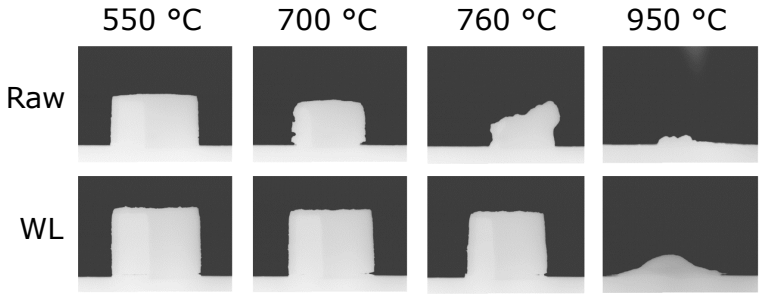

Figure 4.36: Photos (HSM) of colza straw ash during the ash fusion test, showing the effect of water leaching on pellet geometry and ash melting behaviour.

The first noticeable changes in the geometry of the cylindrical sample specimens became apparent at temperatures above 800 °C, which was consistent with the melting points of both alkali chlorides (771 °C for KCl and 802 °C for NaCl). Interestingly, the coefficient h_x/h_0 of the water-leached colza remained constant, in contrast to both raw and torrefied materials. The washing treatment removed water-soluble elements, such as alkali chlorides, from the biomass, which subsequently improved the biomass fuel characteristics at elevated temperatures. For most of the sample ashes, a volume increase began to occur around 1000 °C, likely due to the thermal decomposition of certain species (presumably potassium sulphate, as detected in ash samples via XRD analysis, see Table 4.4).

In summary, the washing pre-treatment has been found to influence the ash fusion behaviour by removing alkali chlorides, but this effect was not sufficient for optimal operation at gasification temperatures of 950 °C or higher. Not surprisingly, torrefaction alone was not effective in removing problematic species such as alkalis, and therefore, the ash fusion behaviour was not positively impacted by an increased ash melting point. In contrast, torrefaction pre-treatment did increase the carbon content and decrease the oxygen content in the biofuel, as shown in Table 4.3 (Chapter 4.2.1). However, this did not affect the ash fusion behaviour.

In Chapter 4.1 of this work, it was found that a causal relationship exists between Ca-blended wheat straw. The results indicated that the most promising outcomes regarding ash fusion characteristics were achieved when samples were blended with 2 wt% $CaCO_3$. The investigations showed that for samples blended with the Ca-based additive, the ash melting point can be significantly increased due to interactions with silicate compounds and the reduction of eutectic effects [14].

The sample ashes prepared in a gasification-like atmosphere (as described in Chapter 3.2) were investigated using XRD diffractometry to understand the crystalline phase formation of inorganic species and their interactions. The detected mineral phases are listed in Table 4.4 (see the last page of this chapter). Due to the need to quantify the identified crystalline phases and amorphous or unknown phases using an internal standard, the approximate fractions of the crystalline phases were determined. Although the measurements were subject to relatively high inaccuracies, the major trends presented can still provide general indications. The approximate quantities of the crystalline phases were estimated as weight percentages, with an estimated relative error of around 20 wt%. To improve the readability of the mineral fractions in Table 4.4, the approximate ranges of weight percentages for the crystalline phases are indicated using plus and minus symbols, as explained below.

–	<10 wt%
+	10 wt% to 30 wt%
++	30 wt% to 50 wt%
+++	>50 wt%

The diffractometric analyses revealed that the ash samples contained a significant proportion of amorphous phases, which are typically the dominant component of ash samples. This made it challenging to detect crystalline phases. As a result, not every individual Bragg reflection peak could be confidently assigned to a specific crystalline phase. For instance, the identification of $K_{9.6}Ca_{1.2}Si_{12}O_{30}$ in barley straw ash or illite in corn straw ash should be viewed with caution and considered as a possible phase rather than a definitive assignment. Notably, the presence of illite suggests that the corn straw sample was likely contaminated with soil impurities. It is worth noting that illite is a common clay mineral or layered silicate, and when combined with quartz, it increases the likelihood that the straw sample under investigation was contaminated with soil material. This observation is, in fact, desirable, as it aligns with the background idea of this work section, which aimed to significantly increase the sample size while also accounting for potential impurities in the fuels.

The major phases typically found in raw biomasses include KCl, SiO_2, carbonates (primarily in the form of $CaCO_3$), sulphates (mainly in the form of K_2SO_4), and phosphates [260, 261], which were also detected in the selected herbaceous feedstocks. Each sample series contained varying amounts of KCl, which could be significantly reduced by washing the fuel itself. The results are consistent with the ultimate analyses. Neither washing nor thermal treatment directly affects silica-based phases. However, both washing and torrefaction increase the bulk density of the materials, leading to a shift in certain inorganic proportions, such as SiO_2. The mineral phase proportions obtained through XRD investigations are also in good agreement with the ultimate analyses presented in Table 4.3 (Chapter 4.2.1).

It is important to reiterate that both ashing temperature and heating rate have a significant impact on the formation of crystalline phases [172, 220].

Table 4.4: Overview of the mineral phases present in the ashes of (treated) biofuels, which were found to be stable under gasification-like conditions.

Phase	Feedstock	Raw	To	WL	WL-To	To-WL
KCl (Sylvite)	wheat	++	++			
	barley	–	–			
	corn	+	+++	–	–	
	colza	+	+			
K_2SO_4 (Arcanite)	wheat	+++	+++			
	barley	+	++			
	corn					
	colza	+	+	–	–	–
$K_2CO_3(H_2O)_{1.5}$	wheat	+				
	barley	+	+			
	corn					
	colza					
$CaCO_3$ (Calcite)	wheat					
	barley	–	–	+++	+++	+++
	corn	–		–	–	+
	colza	+	+	+++	+++	+++
$K_2Ca(CO_3)_2$ (Fairchildite)	wheat					
	barley	–	–			
	corn					
	colza	++	++	++	+	++
$K_{9.6}Ca_{1.2}Si_{12}O_{30}$	wheat					
	barley	+	+			
	corn					
	colza					
SiO_2 (Quartz)	wheat					
	barley					
	corn	++	–	+++	+++	+++
	colza					
$KAl_4Si_2O_9(OH)_3$ (Illite)	wheat					
	barley					
	corn	+		+	+	+
	colza					
$Ca(OH)_2$ (Portlandite)	wheat					
	barley					
	corn					
	colza				+	–

4.2.5 Thermodynamic prediction of gas phase chemistry

Predictions on the condensation behaviour of inorganic compounds (alkali chlorides, carbonates, sulphides, and slag-mixtures) were performed starting from 950 °C for the pre-treated samples. The calculation of inorganic release from industrially pre-treated biofuels at 950 °C and atmospheric pressure, as described in the previous chapter, was performed first. The resulting gas phase was then used as input for the subsequent condensation computations.

Upon examining the results, it was found that the amounts of condensed alkali chlorides (KCl/NaCl) showed little difference between pyrolysis and char gasification/ash reaction. In contrast, carbonates, sulphides, and slag-mixtures exhibited slight variations. The calculated amounts of condensed alkali chlorides are depicted in Figure 4.37.

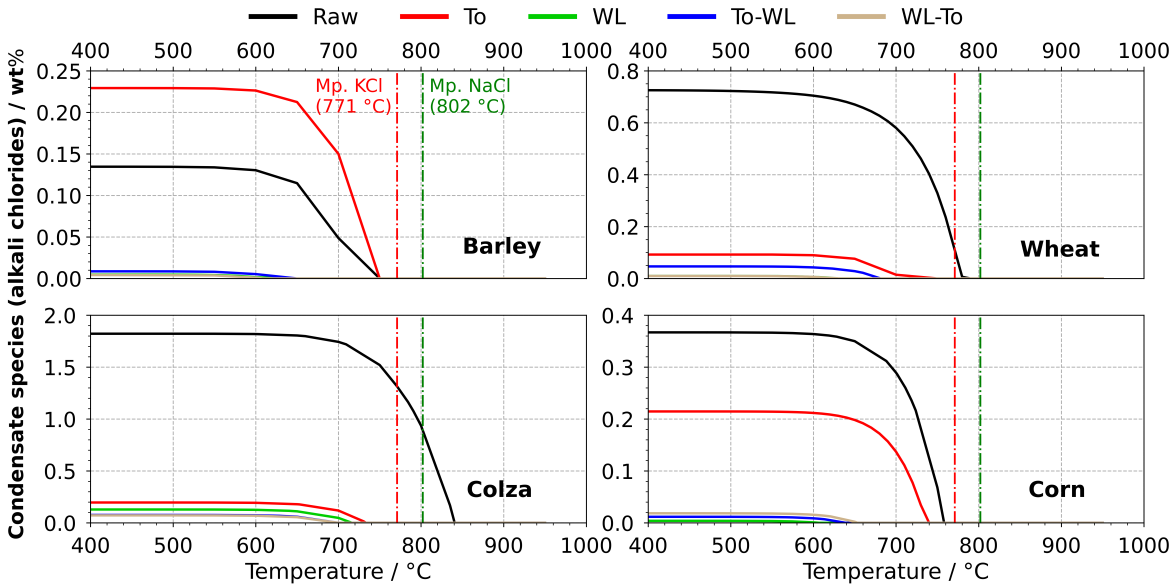

Figure 4.37: Condensation of alkali chlorides, primarily KCl, under gasification conditions. The red and green dashed lines indicate the melting temperatures of KCl and NaCl, respectively. The gasification temperature is 950 °C.

With regard to the source materials and torrefied samples, the condensation temperatures of both alkali chlorides were found to be close to or above the melting points of KCl and NaCl. Water-leaching, whether performed prior to or after torrefaction, shifted the condensation temperature to a lower range. Notably, the calculations showed a significant decline in the amount of condensed alkali chlorides. The washed samples exhibited the most pronounced impact in terms of reducing the amount of condensed alkali salts.

However, torrefaction pre-treatment of samples that had been pre- or post-washed did not result in any further differences in the amount of condensed chlorides below 950 °C. Interestingly, torrefied barley straw showed a slightly increased proportion of condensed alkali chlorides compared to the untreated raw material. This contrasts with the expectation that torrefaction would lead to a decrease in chloride content. According to the chemical characterisation (Figure 4.20, Chapter 4.2.1), an increased fraction of chlorine was detected in the torrefied barley straw compared to the source material. The presence of chloride is essential for the formation of KCl, and this relationship may explain the increase in condensation observed for the torrefied material.

In addition to alkali chlorides, other types of salt were also found to condense. Figure 4.38 illustrates the predicted formation of carbonates and slag-mixtures for both pyrolysis and gasification conditions.

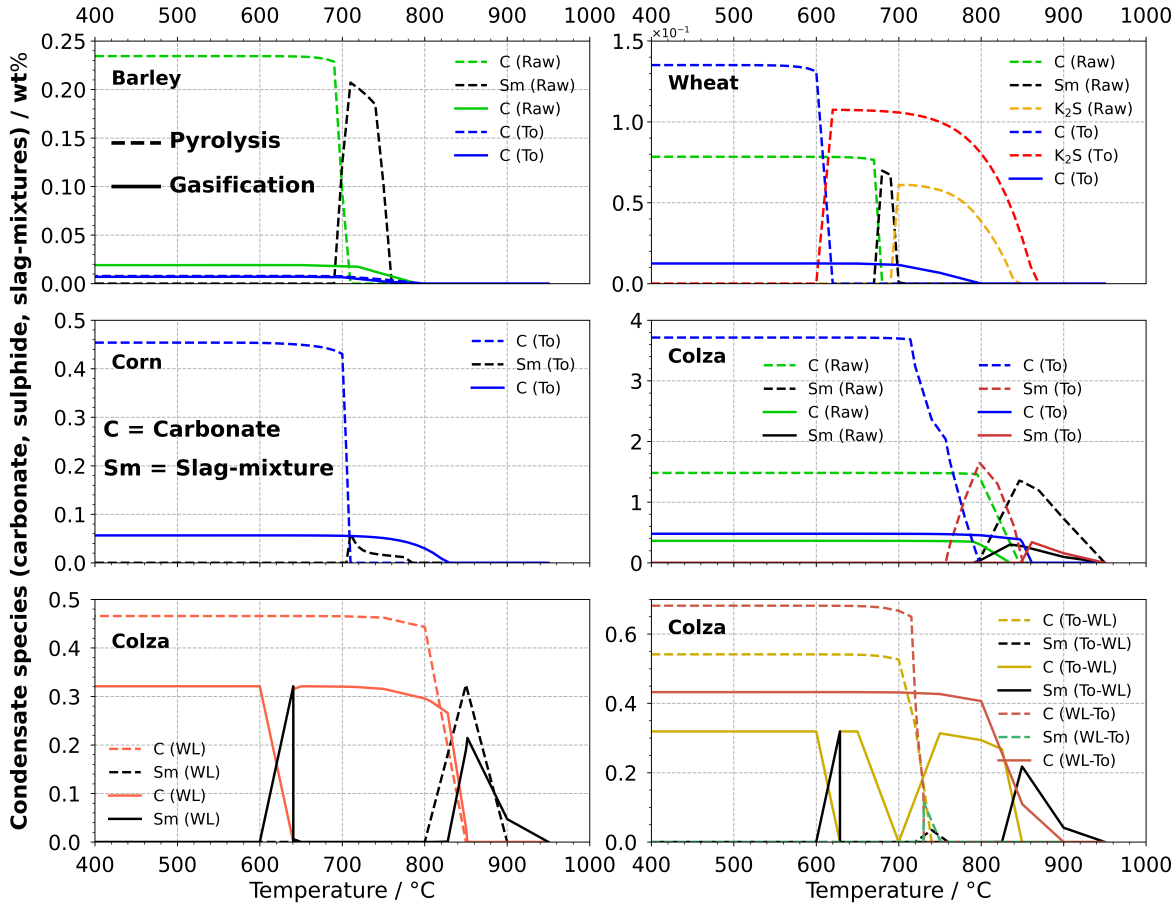

Figure 4.38: Condensation of carbonate (C), sulphide (K_2S), and slag-mixtures (Sm) under both pyrolysis and gasification conditions. The gasification temperature is 950 °C.

Notably, torrefied samples were observed to have a higher proportion of condensed species compared to the untreated source materials. The predicted results showed that colza straw yielded remarkable quantities of condensed carbonates or slag-mixtures for all pre-treated samples, regardless of the upgrading method, and the highest fractions of inorganics among all straw types investigated. Interestingly, a notable trend emerged, regardless of straw variety, where significantly more species condensed from the gas phase under pyrolysis conditions compared to gasification. The slag primarily consisted of molten carbonates (K_2CO_3 and small amounts of $CaCO_3$) and, in the case of wheat straw, K_2S. Below 900 °C, the slag gradually transformed into solid carbonates. One possible explanation for the increased formation of carbonates under pyrolysis conditions is that the rate of decomposition of K_2CO_3 is significantly accelerated in the presence of water vapour [242]. Although no steam was added under pyrolysis conditions, steam was present or accounted for in thermodynamic equilibrium calculations during gasification. In a pyrolysis environment, gas concentrations are lower, and decomposition pressures are significantly reduced compared to a gasification atmosphere, resulting in shifted equilibria. For instance, the partial pressure of oxygen is lower during pyrolysis, which in turn influences the composition and concentrations of other gases. A less oxidising environment favours carbonate formation.

It is important to note that in a real process, kinetic factors also play a key role. This is because CO_2 remains in the solid phase (biochar) for a longer period, allowing it to react with metal oxides such as K_2O or CaO. Although CO_2 content may be higher under gasification conditions, the limited gas flow during pyrolysis prevents CO_2 removal, instead favouring the reaction between CO_2 and metal oxides in the biochar.

The chemical characterisation revealed that colza has a remarkably low silicon content (Figure 4.20, Chapter 4.2.1). This suggests that both calcium and potassium must have reacted with other elements instead of silicon. Similarly, torrefied barley straw showed a higher fraction of condensed species compared to the original material. In particular, all straw types except colza straw showed no significant condensation of carbonates or slag-mixtures after washing. In contrast, colza straw displayed a smooth phase transition between the slag and carbonates, indicating that the inorganic compounds underwent a phase transformation.

4.2.6 Thermodynamic prediction of mineral phases formation

The predicted proportions of mineral phases under gasification conditions, dependent on process temperature, were evaluated for both pyrolysis and gasification processes. As reported in the previous chapter (Chapter 4.1.6), no significant differences were found between the two conditions. Consequently, this section will focus on gasification. The overview of the predicted mineral proportions for the upgraded feedstock varieties is depicted in Figure 4.39.

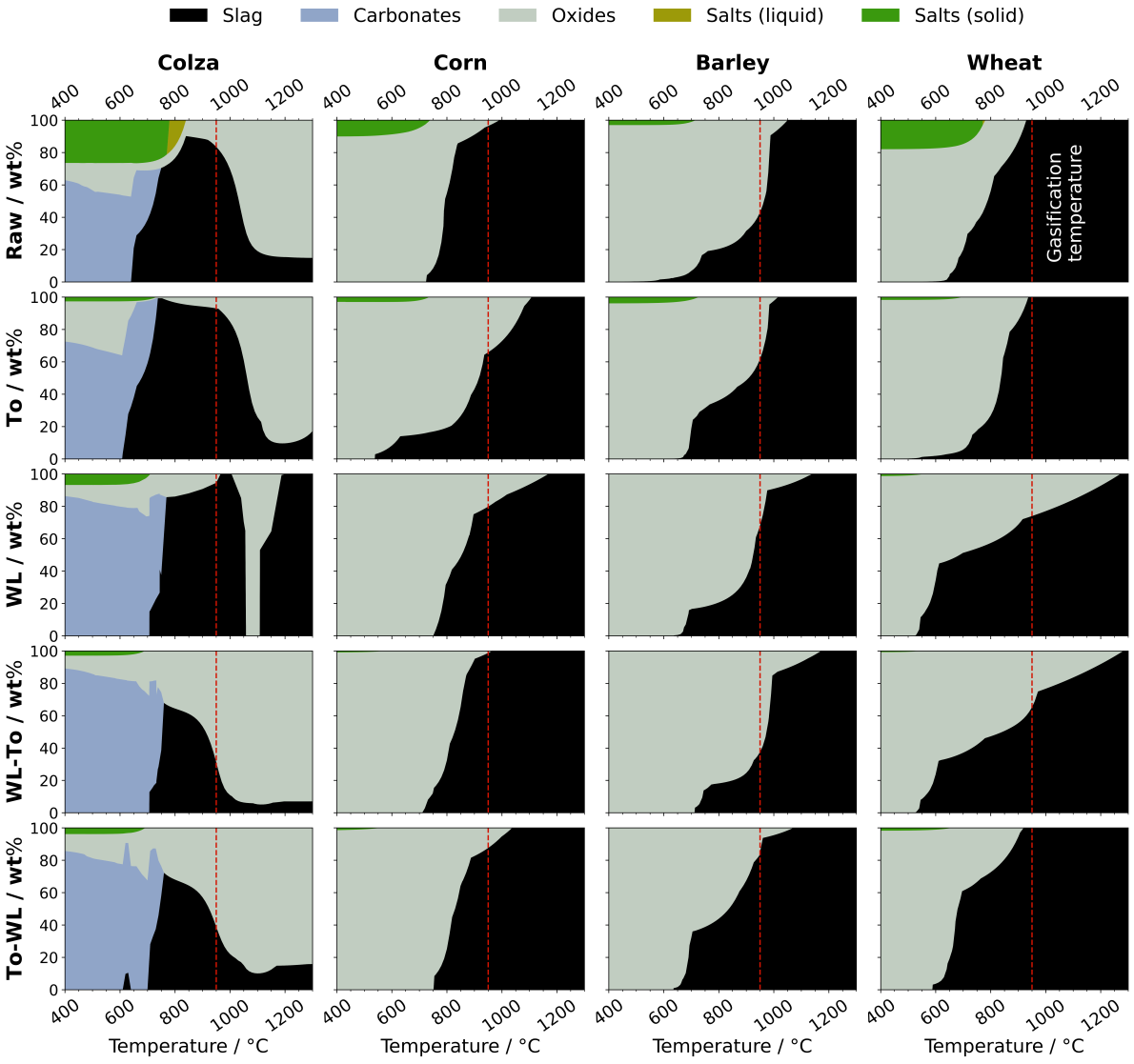

Figure 4.39: Calculated mineral proportions of ashes of upgraded straw varieties under gasification. The dashed line denotes the gasification temperature of 950 °C.

The mixed carbonate compounds, primarily composed of Ca and K, were found to mainly consist of carbonates. Additionally, various silicates and other mixed oxides were identified as belonging to the oxide category. The alkali salts primarily included KCl, though small amounts of NaCl were also detected in both the solid and liquid phases. As anticipated, the torrefied and water-leached samples demonstrated a significantly lower content of alkali chlorides compared to the original material due to a notable reduction in chlorine content resulting from the treatment process. Furthermore, as the temperature increases, the alkalis gradually transition into the gas phase, and their vaporisation raises the melting point of the ash.

Irrespective of the pre-treatment methods employed, colza straw ash demonstrated a notable tendency to form carbonates at low temperatures (between approximately 400 °C and 750 °C). However, above 800 °C, carbonate formation was no longer observable, likely due to thermal decomposition of $CaCO_3$ or the induction of reactions or melting processes by potassium-containing carbonates. Calcite decomposes into CaO and CO_2 at temperatures exceeding 600 °C [262]. It is noteworthy that the process resembled lime burning, with particular emphasis on the equilibrium between CaO and $CaCO_3$.

The thermodynamic modelling results for colza straw ash revealed that at temperatures above 900 °C, a significant proportion of CaO emerged as the primary oxide component. The slag contained carbonates, which explained the direct and smooth phase transition from carbonate to slag. Furthermore, the formation of solid oxides or silicates between 1050 °C and 1100 °C, within the solid phase range of the slag, was particularly noteworthy for the water-leached sample. In this temperature range, Ca_2SiO_4 showed a substantial increase in thermodynamic stability. This indicates that calcium-rich phases formed, resulting in the generation of high-melting calcium silicates that did not occur in the slag due to their relatively high melting point.

In addition, the untreated colza straw ash exhibited a high proportion of about 20 wt% alkali chlorides in the low-temperature range, primarily consisting of KCl. From around 770 °C, the alkali salts transformed into a liquid phase, coinciding with the melting point of KCl at 773 °C.

Upon examining the predicted phase formation of wheat straw ash, it became evident that washing had a significant impact on the ash's melting behaviour. While the raw material itself exhibited 100 wt% molten slag at 950 °C, the water-leached sample showed a much lower proportion of approximately 70 wt%. Additionally, a significant amount of KCl was removed through washing, which explained the higher proportion of solid oxides at 950 °C. Interestingly, pre-washing appeared to be more effective than post-washing: at 950 °C, approximately 60 wt% of the ash was molten in the pre-washed sample, whereas

the ash from the torrefied/water-leached sample showed almost 100 wt% molten slag under the same conditions.

However, this effect seemed to be reversed for barley straw ash. In contrast, corn and colza straw ash did not exhibit significant effects on the ash melting behaviour regardless of whether they were washed and then torrefied or vice versa.

At this point, it is essential to note that the thermodynamic calculations described ideal equilibrium conditions and may deviate from experimental melting processes due to kinetic influences.

To simplify the presentation, the mass fraction of molten slag at the operating temperature of 950 °C is illustrated in Figure 4.40, and the effect of the applied pre-processing methods on ash fusibility is thereby highlighted.

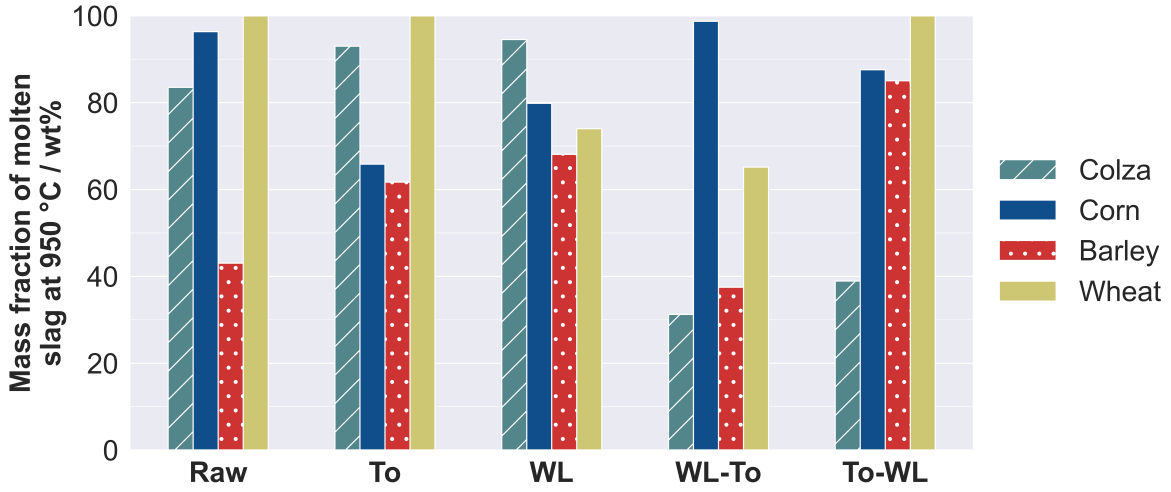

Figure 4.40: Comparison of the ash fusibility of the upgraded biofuels under gasification conditions. The bar chart shows the mass fraction of molten slag at 950 °C, and the results are sourced from Fig. 4.39.

Notably, pre-washed samples (excluding corn straw) exhibited a lower melt fraction compared to post-washed ones. This may be attributed to a higher fraction of alkali metals, primarily potassium, present in the post-washed material. It is well-established that torrefied samples generally enhance hydrophobic characteristics [263]. The hydrophobic nature of thermally pre-treated material may hinder subsequent leaching treatment, as the chemical matrix has likely changed, with alkali metals possibly bound in less water-soluble salts, such as sulphates or silicates. Furthermore, it can be assumed that alkali metals may be complexed with organic compounds as cationic associates with carboxylic acids or inorganic compounds.

The molar ratio of Si/(Ca+Mg) can serve as a suitable indicator for providing initial insights into ash-melting tendencies in systems dominated by Si, K, Mg, and Ca. A decreasing melting temperature has been correlated with an increasing molar ratio [247]. Furthermore, it has been reported that the molar Si/(Ca+Mg) ratio is effective in predicting slagging tendencies for residential heating appliances, with an increasing value corresponding to increased slagging [66]. Figure 4.41 illustrates a correlation between the molar ratio Si/(Ca + Mg) and the numerically predicted amount of molten slag formed at 950 °C for the pre-treated straw varieties summarised in Fig. 4.39.

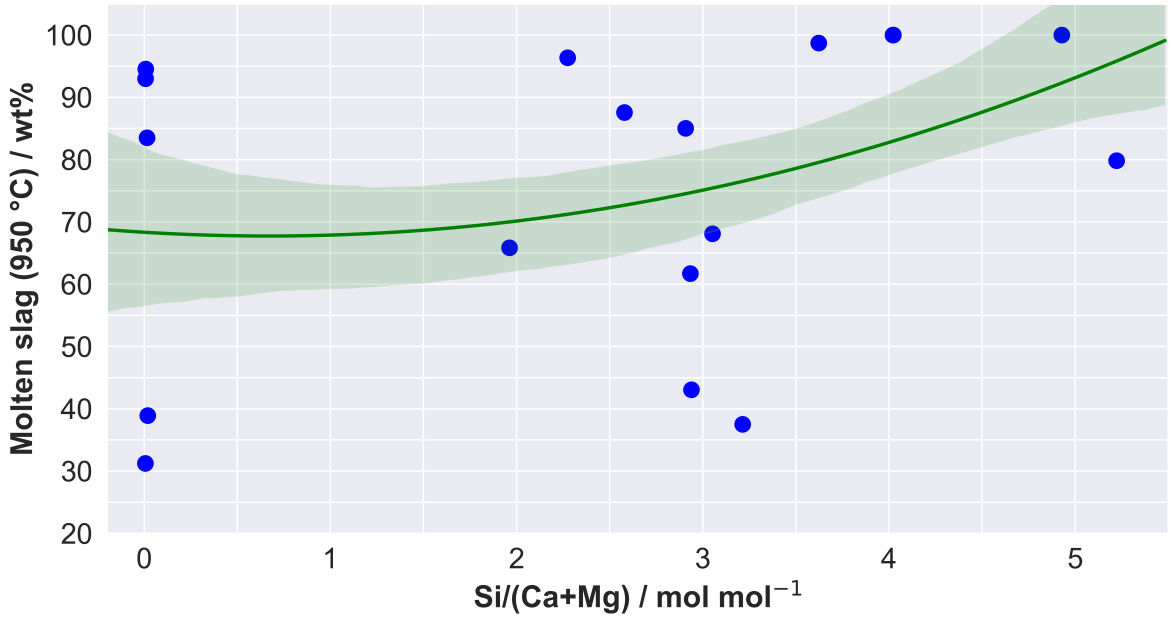

Figure 4.41: The predicted molten slag fraction, expressed as wt% (100 wt%), is plotted against the molar Si/(Ca+Mg) ratio of the ash from pre-processed herbaceous fuels. The slag amounts for each sample are sourced from Fig. 4.39. The confidence interval is set at 68 %.

The correlation between the molar ratio of Si/(Ca+Mg) and ash-melting behaviour tended to support the hypothesis. As the proportion of Si increases relative to Ca and Mg, the proportion of slag formed also increases, resulting in a lower melting point of the ash.

Figure 4.42 presents a comparison of the ash fusibility of the pre-treated straw varieties in ternary phase diagrams, considering the main ash-forming components CaO–K_2O–SiO_2. In addition to CaO and K_2O, small amounts of MgO and Na_2O were present, which were mathematically normalised by adding them to CaO and K_2O due to their

similar chemical properties. It can be seen that almost all ash samples, regardless of their pre-treatment, fell within the two-phase region (liquid-solid).

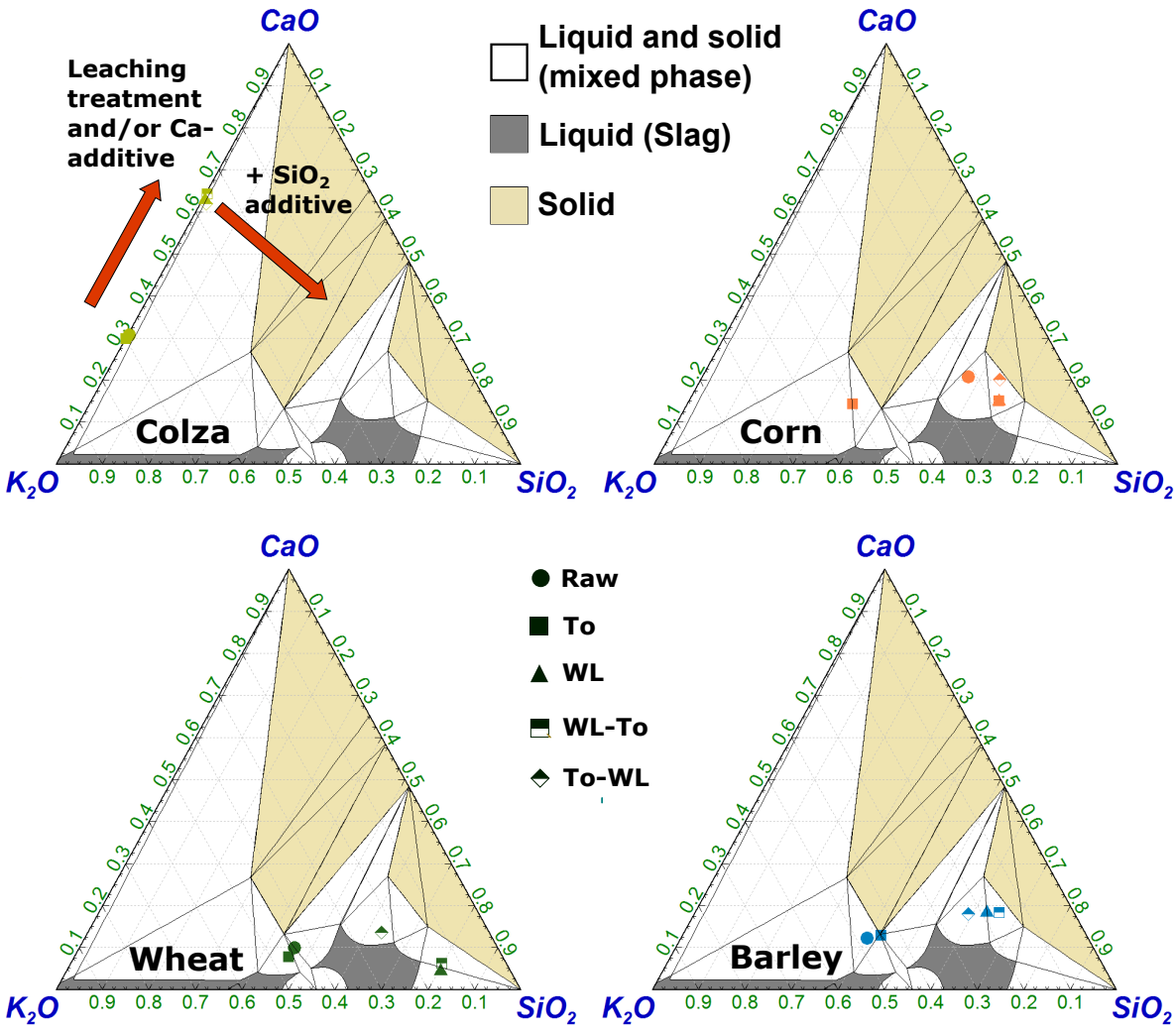

Figure 4.42: Ternary phase diagrams for the SiO_2–CaO–K_2O system, predicted using FactSage [202]. The phases were predicted for (pre-treated) colza, corn, wheat and barley straw. The calculations were performed under isothermal and isobaric conditions, at a temperature of 950 °C and at atmospheric pressure.

Notably, the SiO_2 content in colza straw ash was relatively low, whereas K was the dominant key component. This suggests that high-melting calcium silicates cannot be formed. A potential approach could be to combine water-leaching and/or Ca addition with a supplementary SiO_2 addition to achieve the solid phase area (as indicated by both arrows in Fig. 4.42, top left). Given the shift in ash composition (K_2O–CaO), washed samples would require significantly less SiO_2 compared to the raw material itself.

In summary, the central statement can be condensed to: predicted phase diagrams indicate that the applied pre-processing methods have distinct effects on increasing the solid phase fraction at 950 °C, but further (combined) approaches are needed to achieve a higher solid fraction, potentially through Ca- or Si-based additives or biomass blends. The investigation of these approaches is presented in the final part of this study (Chapter 4.3).

4.2.7 Discussion on the impact on fluidised-bed gasification and CLG

In this chapter, the impact of various biomass pre-treatment technologies, including torrefaction, water leaching, and combinations of both, on the behaviour of inorganic constituents was thoroughly investigated using a combination of experimental methods and numerical approaches. In contrast to the previous work (Chapter 4.1), the pre-treatment methods were conducted on a laboratory scale rather than on an industrial scale. Furthermore, the samples were washed twice with a consistent amount of washing water, and for a total duration of two hours, as opposed to the conventional 24 h.

In terms of the overall impact on thermochemical gasification, several conclusions can be drawn. The ultimate analysis revealed significant variations in the inorganic composition of different straw varieties, which were also reflected in the hot-gas analysis experiments. Notably, distinct differences were observed in the composition of the various biomass feedstocks examined. This highlights the importance of investigating a wide range of fuels to provide reliable conclusions about the inorganic composition and its corresponding impact on ash-related issues.

Thermodynamic calculations and XRD investigations further revealed that colza straw ash exhibited an intense formation of carbonates, whereas the other straw ashes did not exhibit this effect to the same extent. However, at temperatures above 900 °C, carbonates were no longer formed, regardless of sample composition. This means that at high gasification chamber temperatures and short ash residence times (high plant utilisation), low carbonate contents might be expected in the ash produced, similar to conditions found in a combustion environment [264]. Conversely, this implies that calcium is predominantly present as burnt lime in the ash under these conditions.

Torrefied samples generally exhibited an increase in ash content, whereas the opposite was observed for water-leached samples. Notably, torrefaction has been found to be an effective method for significantly reducing chlorine content in the fuel [208], which

should minimise the risk of high-temperature corrosion in the gasifier. However, the alkali content remained steady or even increased due to torrefaction, which may lead to increased risk of bed agglomeration, fouling, and slagging. Contrary to torrefied samples, water-leaching showed a positive impact on ash melting behaviour, as indicated by HSM and predicted ternary phase diagrams. In contrast to raw or torrefied samples, washed fuels demonstrated a slightly increased ash softening point. Nevertheless, these pre-treatment methods were not sufficient to ensure problem-free operation at 950 °C, as all ash samples virtually melted completely at temperatures above 950 °C.

A previous study by Gilbe et al. [216] suggested a correlation between the inorganic constituents and ash fusibility, particularly for woody biomass fuels. A "slagging index" was proposed, where high molar Si/(Ca+Mg) ratios indicate increased melt formation and a higher risk of slagging at a given temperature. The authors found that wood-derived fuels with low inherent Si content exhibited relatively moderate slagging tendencies. However, severe contamination of sand (SiO_2) in woody fuels can significantly enhance adverse slagging tendencies.

Similarly, investigations of herbaceous feedstocks in the present work revealed similar observations, and the predicted amount of formed slag correlated with the molar Si/(Ca+Mg) ratio. Thermodynamic equilibrium computations demonstrated a positive trend for lowering molten slag formation when the molar ratio of Si/(Ca+Mg) is lower.

Water-leached samples showed a significantly lower proportion of K_2O, which led to a shift in the inorganic components present in the ash and an increased proportion of SiO_2 as well as CaO/MgO. The presence of alkali metals, particularly potassium, in biomass fuel significantly impacts slagging, as it forms low-melting compounds that promote excessive slag formation [14]. This can lead to unwanted interactions with the bed material and fouling. The water-solubility of KCl, which is bound to chlorine, makes these treatment technologies promising in achieving the desired quality of woody biomass. Vapour-phase alkali compounds deposit on heat exchanger surfaces are causing severe fouling issues [265]. Hot gas analysis by MBMS showed that water-leaching treatment effectively reduced alkali chloride levels in the fuel. As a result, the condensation of alkali chlorides shifted to temperatures below their melting point, minimising fouling effects.

Besides Al and S, Si can trap alkali compounds before they are deposited, thereby reducing the amount of alkali released. Batch-type release experiments have shown that the release behaviour of K is dependent on the molar Si/K fuel ratio. An increased proportion of Si leads to a reduced release of K, which should have a beneficial impact on fouling-related problems. In fact, Sommersacher et al. [247] have reported that for

fuels with very high Si/K ratios (such as sewage sludge), K is well-embedded in the bottom ash, resulting in a very low K release.

Another key factor contributing to unfavourable side effects during gasification is nitrogen-induced air pollution, primarily caused by NO_x and its precursors, NH_3 and HCN. This differs from the ash-related issues mentioned earlier. As part of this study, the fuel-bound nitrogen was investigated, examining the influence of various pre-treatment methods and comparing their impact on the release of N-species.

The findings suggest that several factors influence NO emission, including the surrounding gas atmosphere and the contents of ash-forming elements. The formation of NH_3 was found to be inherently correlated with the Ca or K content in the fuel, likely due to catalytic effects. This suggests that nitrogen chemistry may be influenced by ash-forming matter. Consequently, fuel pre-processing indirectly affects N-related pollutant emission, indicating that the NO emission depends on how nitrogen is bound to the biofuel. Pre-processing modifies the chemical matrix of the feedstock, supporting the hypothesis that NO emission is influenced by the chemical form of nitrogen in the biofuel [140].

While most research on biofuels has focused on woody feedstocks, it is essential to investigate herbaceous feedstocks more thoroughly [266–270]. Herbaceous feedstocks are typically characterised by a high content of primarily ash-forming elements, which can make them challenging to utilise in thermal conversion processes. In contrast, woody biomass contains fewer problematic elements, which can cause issues such as high-temperature corrosion, ash deposition, and air emissions (SO_x and NO_x) [271]. According to Porbatzki et al. [272], the amount of inorganic trace elements released from herbaceous biomass is about one order of magnitude higher than from woody biomass. Additionally, woody biomass tends to have a lower moisture content than herbaceous biomass. Several studies [273–275] have demonstrated the advantages of torrefying woody biomass, which involves drying the material and increasing its bulk densification, resulting in a commodity fuel with enhanced energy content, hydrophobicity, grindability, and homogeneity. This upgraded woody biomass can then be handled similarly to coal and directly replaced.

While herbaceous feedstocks present several challenges, including lower calorific value, bulk density, and ash melting point, as well as higher ash impurity content [76], these drawbacks can be mitigated. For instance, leaving straw residues on the field after harvesting allows for natural leaching by rainfall, which can separate a significant portion of alkalis salts. Alternatively, dedicated facilities can wash the feedstocks at moderate or

room temperatures. It is crucial to consider the water waste streams generated by water-leaching pre-treatment and explore various resource recovery options. According to Tobin et al. [276], wastewater treatment is a vital component of a biorefinery operation. Although capital costs can be a challenge, evaporation of wastewater offers a promising means of treating wastewater while incorporating resource recovery options. Research has shown that specific biominerals like struvite, rich in nitrogen, phosphorous, and magnesium, can be recovered and used as a valuable fertilizer [277]. Various processes are used to recover struvite from wastewater, but the costs of these processes are difficult to compare due to varying operational conditions [277]. Therefore, it is essential to continue exploring the wastewater approach and promoting efficient processes in future studies.

It can be concluded that both experimental methods and thermodynamic modelling calculations have yielded similar trends, which are logically consistent. However, the significance of the predictions was partially limited, likely due to kinetic factors and the non-equilibrium nature of the experiments. To improve the accuracy of predictions, it is essential to develop an advanced numerical model that incorporates both thermodynamics and kinetics of biomass gasification in future studies. This will enable a more comprehensive understanding of the gasification process and provide a more reliable basis for prediction and optimisation.

4.3 Influence of additives and blending on behaviour of inorganic constituents

The final chapter of this work focuses on woody-biofuel blends and upgraded herbaceous samples with limestone as an additive. The woody components selected for blending were pine bark (PB), oak bark (OB), and pine forest residues (PFR). The same straw varieties used in the previous chapter (wheat, barley, corn, and colza) were employed for the fuel blends.

Three distinct sample series were designed to investigate various effects related to fuel blending approaches. Firstly, the impact of limestone (commercial quality) as an additive on upgraded barley straw was examined, with a focus not only on ash fusion behaviour but also on potential effects on gas phase chemistry. Previous studies (Chapters 4.1 and 4.2) have demonstrated the effectiveness of Ca as an active suppressor of S species and HCl release.

A second sample series investigated the effect of increasing mixing proportions by blending raw colza straw with varying amounts of pine bark (from 10 wt% to 90 wt%). The goal was to study and distinguish between different possible effects, such as whether blending alone is sufficient or if there is a linear relationship between the blending ratio and HCl release or melting ratio. Additionally, attention was paid to the possibility that side reactions may occur, leading to deviations from linearity.

The final sample series focuses on torrefied and post-washed fuel blends, which were chosen based on preliminary equilibrium calculations that predicted ternary phase diagrams ($CaO–K_2O–SiO_2$) to estimate the solid ash composition of each sample blend at 950 °C.

4.3.1 Chemical characterisation of woody blend components

As mentioned earlier in the introduction to this chapter, PB and OB were selected, in addition to PFR, as further blend components. PFR was previously studied in Chapter 4.1, as part of a comparison with other woody biomass alternatives. It is worth reiterating that, in contrast to woody biomass, herbaceous plant components are more challenging to gasify or combust due to their poorer fuel properties, specifically their higher ash content. This higher ash content can lead to several issues during high-temperature thermochemical conversion processes.

The composition of the inorganic constituents can be found in Table 4.1 and Figure 4.1, as described in Chapter 4.1.1. Table 4.5 presents the ultimate analysis of both woody blend components, while Figure 4.43 illustrates the selected chemical species present in the ash of PB and OB, highlighting inorganic compounds that are relevant to issues related to thermochemical conversion, making them of particular interest.

Table 4.5: Ultimate analysis of both blend components pine bark (PB) and oak bark (OB) in wt% or $mg\,kg^{-1}$. The results were not normalised.

wt% (ar)	**Pine bark (PB)**	**Oak bark (OB)**
Ash	3.67	4.20
C	42.10	45.50
H	5.66	6.22
N	0.40	0.43
O	38.70	43.40
S	0.10	0.10
$mg\,kg^{-1}$ (ar)	Ash forming components (major elements only)	
Cl	232	63
Al	830	239
Ca	7600	15560
Fe	830	158
K	1840	2810
Mg	676	516
Na	228	2810
P	409	368
Si	9200	3880

In contrast to the 2.0 wt% ash yield in PFR, both woody components exhibited elevated ash yields, as shown in Table 4.1 (Chapter 4.1.1). This was primarily due to the significant increase in Ca and Si concentrations observed in PB and OB. Notably, oak bark contained a high amount of Ca, making it a promising candidate as a biomass blend component. Given that both feedstocks had a relatively low proportion of critical components such as Cl, S, K, and Na, and a contrasting high proportion of Si and Ca, both blend components appear auspicious. Furthermore, the cheap purchase costs of pine and

oak bark residues make them attractive from an economic perspective. The chemical analysis highlights that woody biomass generally exhibits lower nutrient contents and higher lignin contents compared to herbaceous biomass. This trend is clearly evident when comparing the results with those of the herbaceous feedstock varieties presented in Chapter 4.2. Moreover, the ash yield of both biomass types provides further evidence of the presence of problematic species, which is typically much lower for woody materials.

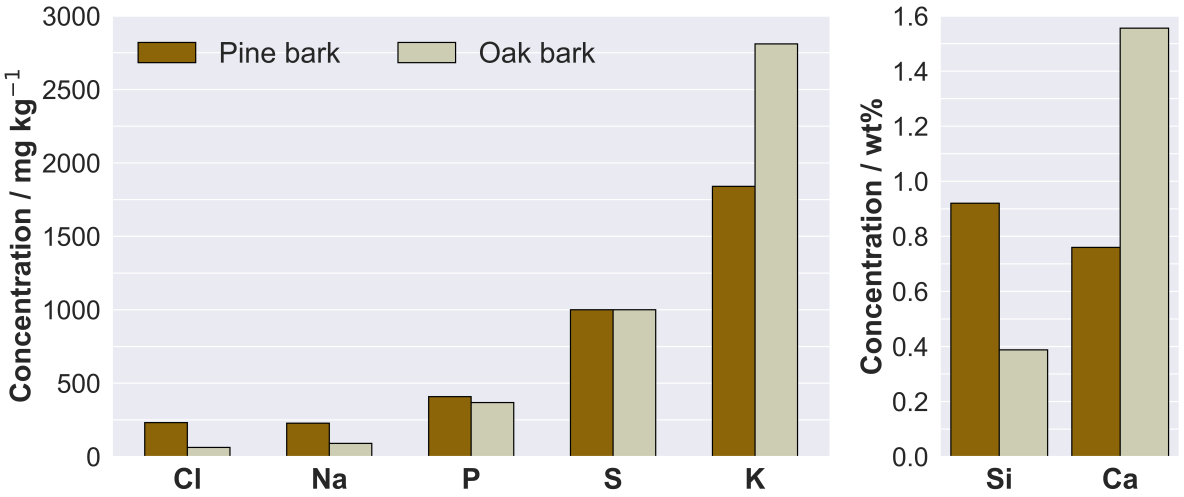

Figure 4.43: Chemical analysis (blending materials PB and OB), with an emphasis on species which are playing a crucial role in ash-related issues.

The results of the ultimate analysis for the feedstock blend series are presented in Table 4.6. It is important to note that the composition is based on the characterisation of the raw or upgraded fuels themselves, as listed in Chapter 4.1, Table 4.1, and Chapter 4.2, Table 4.3. This means that the composition was calculated on a percentage basis. For the pre-treated barley straw plus 2 wt% $CaCO_3$ (referred to as "+A" for clarity), the ultimate composition remains unchanged, except for a minor increase in Ca content, which has caused a slight shift in the ratio of inorganic constituents. For upgraded barley straw blended with 2 wt% $CaCO_3$, only the value for Ca was determined on a molar basis, as 2 wt% $CaCO_3$ (100.09 g mol^{-1}) corresponds to 0.8 wt% Ca (40.08 g mol^{-1}).

Table 4.6: Ultimate analysis of the blended fuel sample series in wt% or mg kg^{-1}. The results were not normalised. The results were calculated on a percentage basis, sourced from the data presented in the previous chapters on the initial fuels.

wt%	**Barley** + A	**To** + A	**WL** + A	**To-WL** + A	**WL-To** + A	**Barley/OB** 65/35	**Corn/PB** 70/30	**Corn/PFR** 60/40
C	43.50	50.50	44.50	47.30	49.70	46.50	46.30	49.90
H	6.20	5.91	6.37	5.85	5.95	5.98	5.83	6.10
N	0.56	0.73	0.39	0.37	0.63	0.63	0.52	0.48
O	44.80	38.70	45.70	40.70	41.20	41.00	39.80	40.40
S	0.13	0.12	0.10	0.10	0.10	0.10	0.10	0.08
mg kg^{-1}	Ash forming components (major elements only)							
Cl	618	1076	42	60	100	61	261	192
Al	20	20	20	40	20	110	634	400
Ca	11019	12319	10829	12409	12139	8306	4457	3222
Fe	7	7	7	49	7	87	438	216
K	15600	19550	3600	7170	4610	5644	3681	3230
Mg	377	550	271	515	405	515	1421	1225
Na	90	140	90	200	90	1114	138	74
P	890	1258	490	980	1010	766	524	431
Si	7480	10720	7000	10710	10800	8320	10320	6863
wt%	**Colza/PB** 65/35	**Wheat/PFR** 60/40	**Wheat/OB** 60/40	**Colza/PB** 90/10	**Colza/PB** 75/25	**Colza/PB** 50/50	**Colza/PB** 25/75	**Colza/PB** 10/90
C	45.70	50.70	47.80	41.30	41.40	41.70	41.90	42.00
H	5.87	6.06	5.99	5.98	5.92	5.84	5.75	5.70
N	0.37	0.42	0.45	0.50	0.48	0.46	0.43	0.41
O	41.00	39.80	41.00	43.60	42.80	41.40	40.10	39.20
S	0.10	0.08	0.10	0.31	0.27	0.22	0.16	0.12
mg kg^{-1}	Ash forming components (major elements only)							
Cl	308	207	204	7529	6313	4286	2259	1043
Al	317	106	132	111	231	431	630	750
Ca	5754	2940	7808	8347	8223	8015	7808	7683
Fe	302	99	109	89	213	419	624	748
K	2757	4388	4964	20317	17238	12105	6973	3893
Mg	401	534	559	564	583	614	645	664
Na	210	134	1244	1102	956	714	471	325
P	228	213	273	259	284	326	367	392
Si	3266	6503	7672	1008	2374	4649	6925	8290

4.3.2 Analysis of hot gases using MBMS (batch-type experiments)

In Figure 4.44 and 4.48, the normalised results of the evaluated MBMS peak areas are presented in bar chart format, displaying both devolatilization and char gasification/ash reaction data. Similar to previous parts of this work (Chapters 4.1 and 4.2), three measurements were taken per sample, and the conditions were replicated exactly to those used previously.

A comparison between upgraded barley straw (Figure 4.23, Chapter 4.2.2) and upgraded barley straw plus Ca-additive (Figure 4.44, top bar chart) revealed significant differences in the fate and release of inorganic species. The release of sulphur species (H_2S, SO_2, and COS) during devolatilization was significantly reduced in samples blended with calcium, with a notable decrease of approximately 50 wt%. Similarly, the release of HCl was also observed to decrease, although the magnitude of this decrease was less pronounced.

A noticeable decrease in HCl release was observed for the water-leached samples, similar to the upgraded samples without additives. However, a direct comparison between the two was challenging due to the relatively inhomogeneous composition of the samples, as evident from the error bars. In contrast to aluminosilicate-based additives, which react directly with alkali compounds [65], $CaCO_3$ exerts an indirect influence on the release behaviour of certain species, primarily sulphur-containing species and partly KCl, as previously demonstrated in Figure 4.5 (Chapter 4.1.2). Figure 4.45 illustrates the correlated effect of the upgraded and Ca-blended fuels on the release of KCl and SO_2 during devolatilization.

The samples that were blended with calcium additives showed a decrease in the release of KCl and SO_2 compared to non-blended samples. The higher the calcium content, the lower the amount of KCl or SO_2 released. In fact, when the calcium content exceeded 1 wt%, almost no KCl was detected in the washed, pre- and post-washed samples. Not surprisingly, the source material itself and the torrefied sample without calcium additive showed the highest levels of SO_2 release. However, the water-leached, post- and pre-washed samples revealed the most promising results, with a 50 % reduction in SO_2 release compared to the raw or torrefied material. The effect was amplified when the upgraded samples were also blended with $CaCO_3$.

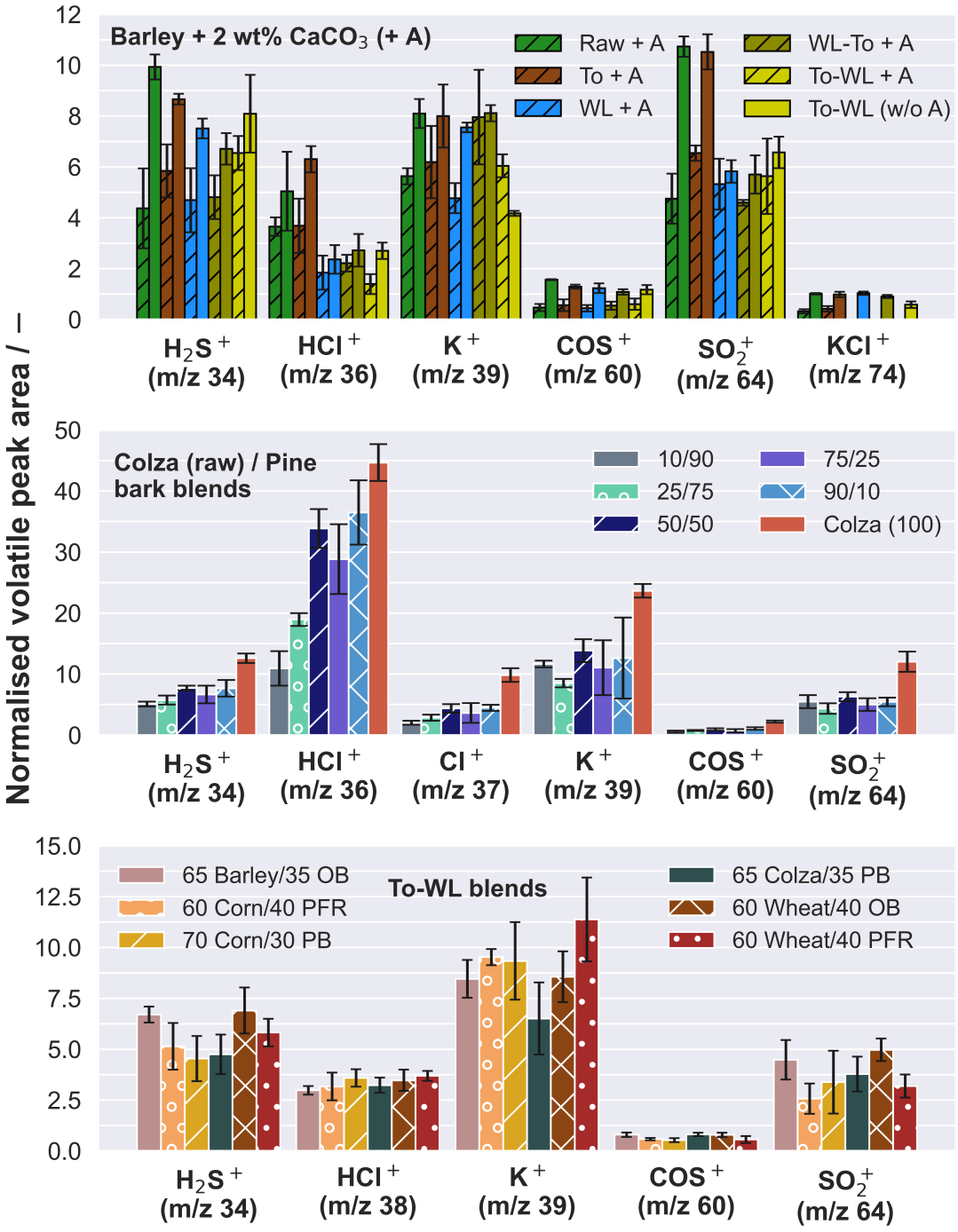

Figure 4.44: Averaged normalised peak areas of detected species released during pyrolysis/devolatilization phase. Top: comparison of pre-treated barley straw blended with 2 wt% $CaCO_3$ (including straw without additive for reference). Centre: raw colza straw blended with varying amounts of PB. Bottom: different straw varieties (To-WL) blended with different quantities of either PB, OB, or PFR.

The MBMS findings reinforced the results of the previous experimental series (Chapters 4.1 and 4.2), demonstrating that calcium effectively reduced sulphur species emission. It is likely that there is a cohesive interaction between K, Ca, and S species that explains the observed mechanisms. The high potassium content in herbaceous samples leads to the retention of sulphur through the formation of potassium sulphate, resulting in a suppression of SO_2 emission. Silica binds potassium, forming low-melting amorphous silicates that attenuate the formation of K_2SO_4 and promote SO_2 release. On the other hand, a high amount of Ca in the ash favours the formation of high-melting calcium silicates, which puts K and Ca in competition with each other, affecting SO_2 release.

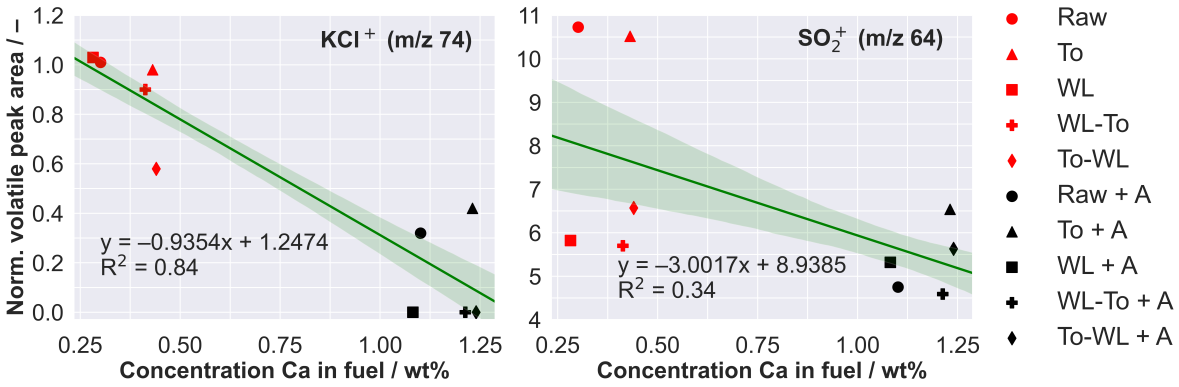

Figure 4.45: Comparison of the normalised peak area of KCl and SO_2 released during pyrolysis phase (pre-treated barley blended with 2 wt% $CaCO_3$, Fig. 4.44 and without $CaCO_3$, Fig. 4.23, Chapter 4.2.2) in relation to the Ca concentration in (treated) feedstock. The confidence interval is set at 68 %.

Calcium not only acts as a sulphur sorbent but also modifies the silica network by substituting K, promoting the formation of less harmful potassium sulphate. In a study published by Wu et al. [278], it was reported that sulphates can effectively convert KCl to K_2SO_4 by destroying KCl. Ultimately, the formation of K_2SO_4 can be regarded as a very promising additional effect, as it inherently restrains both KCl and SO_2 release due to increased Ca content in the fuel.

To summarise, calcium suppresses sulphur release through two distinct chemical mechanisms. Notably, similar findings have been reported for coal-straw blends under combustion conditions [244]. Additionally, the sequence of torrefaction and water-leaching was found to increase the release of sulphur-containing species (H_2S, COS and SO_2) in post-washed samples compared to pre-washed ones. This observation is consistent with the hypothesis that torrefaction enhances the hydrophobic properties of biomass.

For colza samples blended with varying proportions of PB, the main influence on the fate and release behaviour of inorganic compounds appears to be dilution. The sample blend containing 10 wt% PB exhibited similar amounts of released inorganic species to raw colza straw, although slightly lower on average. Compared to the untreated source material (Figure 4.23, Chapter 4.2.1), the PB-blended samples showed strikingly larger error bars, indicating increased inhomogeneity, which reduced the reliability of the results. This trend applies to all sample blend series investigated in this chapter.

Analysing the chemical composition, raw colza straw showed a higher fuel-S content than PB. A notable correlation was observed between fuel-S and the release of S-containing species such as H_2S, COS, and SO_2, with an increase in fuel-S corresponding to an increase in released S-species. Conversely, the proportion of PB was found to reduce the quantity of S-species released. The same trend applied to chlorine species, HCl and Cl. Interestingly, one sample with 25 wt% PB deviated from this trend, with a higher emission of HCl and Cl for the 50/50 colza/PB blend despite lower fuel-Cl. The ultimate analysis revealed no significant deviations in inorganic composition from other sample blends, including fuel-Ca. The reason for this observation was unclear, but may be attributed to increased observational error due to an inhomogeneous sample composition.

The final sample series investigated the impact of woody blend components on torrefied and post-washed straw samples. The ultimate analysis revealed that the parent straw samples had a fuel-Ca content of 0.2 wt% to 0.4 wt%, whereas the woody components, OB and PB, had fuel-Ca contents of 1.6 wt% and 0.8 wt%, respectively. The fuel-K content was significantly lower in the woody materials, averaging 0.2 wt%, compared to the upgraded straw samples at 0.5 wt%. The fuel-S remained constant, while the fuel-Cl content was similar for the upgraded fuels and woody components. It is not unexpected that the silicon content was lower for the woody materials. A comparison of ultimate analyses is essential to understand the fate of inorganics in the gas phase. The S-species and Cl-species were not affected by OB, but their quantities released were partially decreased compared to the upgraded straw material itself, likely due to a dilution effect caused by OB.

The observations for PB-blended colza straw were similar to those for OB-blended barley straw, and the quantities of released S- and Cl-species, as well as K, remained almost constant compared to the upgraded colza straw. This suggests that the woody blend components did not significantly impact the fate of inorganic species, with only minor dilution effects observed.

The corn straw was blended with either 30 wt% PB or 40 wt% PFR. At first glance, it appeared that both woody blends had a similar effect on the quantity of inorganic species released. The quantities of inorganic species released were approximately equal to those of the torrefied and post-washed colza material (refer to Figure 4.23 in Chapter 4.2.2 for comparison).

The wheat straw samples were blended with either 40 wt% OB or 40 wt% PFR. As shown in Figures 4.44 and 4.23 (Chapter 4.2.2), the blended samples exhibited a slight decrease in S-species (H_2S, SO_2, and COS) compared to the torrefied and post-washed wheat straw material. However, the release of S-species was found to be slightly increased for the upgraded blends with 40 wt% OB compared to the PFR-blended sample.

The ultimate analysis revealed that the fuel-S content in OB was twice as much as that of PFR. The sodium content was also remarkably high, suggesting that Na was likely bound to S in the form of Na_2SO_4, as is typically the case with Ca, K, Mg, and Na in biomass [279].

In Figure 4.48, it can be seen that for wheat straw blended with 40 wt% OB, the amount of SO_2 released during gasification was significantly increased, whereas for the PFR blend, the emission was only slightly increased. Previous studies have shown that the initial release of S from wheat straw is governed by the decomposition of low-thermal-stability organic S compounds [207, 280, 281]. Additionally, wheat straw contains a substantial amount of inorganic S in the form of sulphates [282], which is not volatilized during devolatilization. This suggests that the amount of released S during devolatilization is inherently correlated to the organic S fraction in the biomass [207].

The evidence from these findings suggests that various factors during devolatilization and gasification are related to various effects and interactions between ash constituents. Notably, the OB-blended wheat straw sample showed a higher amount of S species released compared to the PFR-blended sample, despite having a higher fuel-Ca content ($3880\,mg\,kg^{-1}$ vs. $958\,mg\,kg^{-1}$). As previously demonstrated, Ca affects the release of S species through physicochemical effects. One possible explanation lies with the higher concentration of fuel-Si in OB. According to thermodynamic equilibrium calculations [242], there is a significant correlation between sulphate and silicate, which may compete with cations such as Ca. Therefore, even though OB has a high concentration of fuel-Ca, it is not able to capture much of the sulphur.

These explanations complement each other and help illuminate the outcomes of hot gas analysis, as the findings for Si-rich fuels result in more sulphur being released into syngas, a phenomenon often reported for herbaceous feedstocks [283, 284]. Moreover, silicates are more stable at higher temperatures than sulphates, promoting their ability to sequester even more inorganic cations [279].

Figure 4.46 illustrates the correlation between the molar Si/Ca ratio and the release of H_2S or SO_2. To facilitate comparison, the summarised results of the sample series along with the corresponding non-blended materials are visualised in scatter plots. The data clearly shows that as the fuel-Si content increases, the release of both sulphur species also increases. Conversely, as the fuel-Ca content decreases, the amount of hydrogen sulphide or sulphur dioxide released into the gas phase decreases. These findings support the previous hypothesis about the interaction between the silicon network and Ca cations, which affects the fate of S-species during devolatilization and gasification.

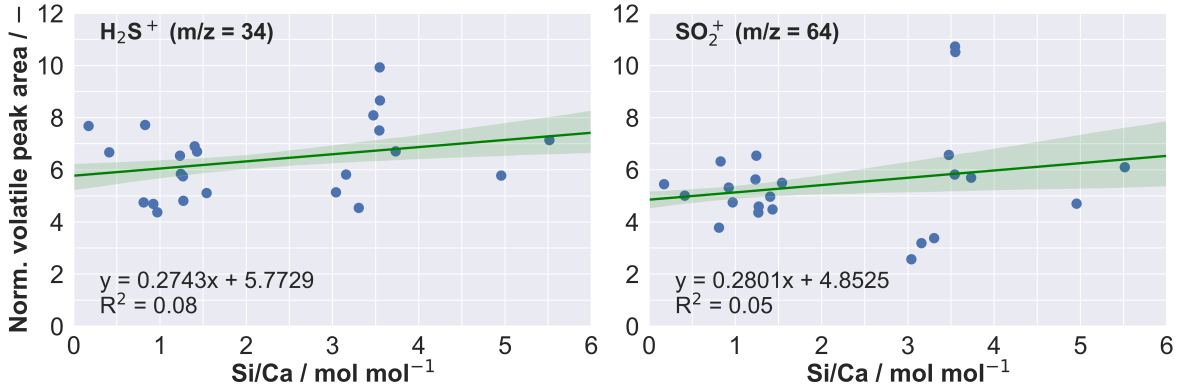

Figure 4.46: Comparison of molar Si/Ca ratios and the release of H_2S and SO_2 during devolatilization for the blended fuel series and their corresponding non-blended reference materials (see Chapter 4.2). The confidence interval is set at 68 %.

Compared to the upgraded wheat straw, the potassium release was found to be increased for both sample blends. Notably, the fuel-K content is significantly higher in the upgraded wheat straw itself (6400 mg kg^{-1}) compared to PFR (1370 mg kg^{-1}) or OB (2810 mg kg^{-1}). One possible explanation for this phenomenon is the difference in fuel-Si content. The upgraded wheat straw has the highest Si content (1 wt%), while PFR has the lowest content (958 mg kg^{-1}). As previously discussed, silica networks can incorporate alkali metals, making them less volatile. This hypothesis is consistent with the results in Figure 4.44.

A comparison of the sample blends with each other reveals distinct effects on the gas phase. The upgraded wheat straw blended with 40 wt% PFR showed a higher quantitative release than that blended with 40 wt% OB. The ultimate analysis of OB showed a lower fuel-Si content (3880 mg kg^{-1}), which explains why the release of K was lower for the OB-blend.

In summary, it can be concluded that the fate of inorganic species like K was primarily attributed to a dilution effect caused by a lower fuel-Si content, resulting from an inorganic shift in the sample blend composition.

In conclusion, it is essential to consider the impact of both Ca and K on the release of HCl. Figure 4.47 illustrates the relationship between the molar Ca/K ratio and HCl release during devolatilization for the blended fuel materials. The scatter plot summarises the results of the sample series, highlighting the effect of this ratio on the release behaviour of HCl. A distinct trend emerged from the data: as the Ca/K ratio increased, the amount of HCl released during devolatilization decreased. This phenomenon was consistently observed for the industrially pre-treated wheat straw fuels in Fig. 4.5, Chapter 4.1. CaO, present as a major ash component at high temperatures (950 °C), can act as a HCl sorbent, as described by Equation 4.3, Chapter 4.1.2.

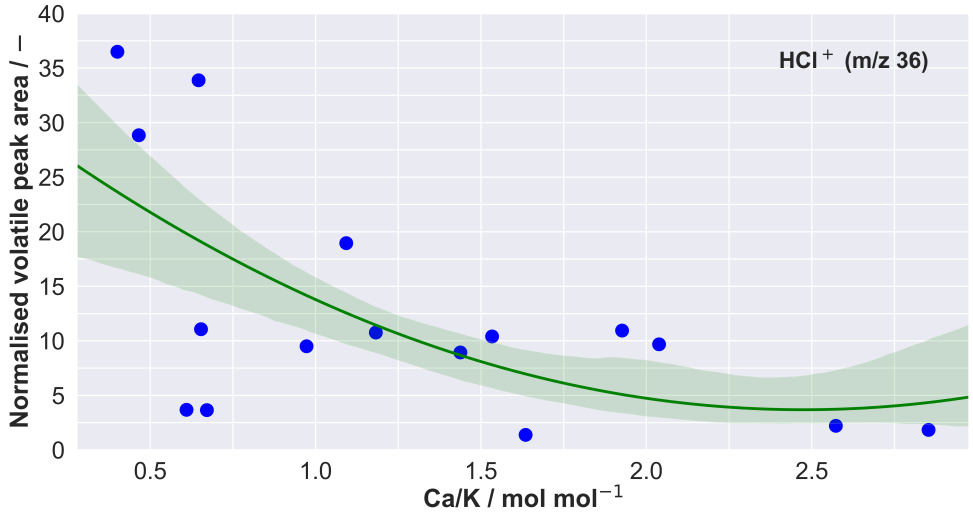

Figure 4.47: Molar Ca/K ratio as a function of HCl release during devolatilization for blended fuels. For the To-WL blends, where HCl was detected at $m/z = 38$ ($^{37}Cl^+$ isotope), the area measurements were adjusted by a factor of three to account for the presence of the $^{37}Cl^+$ isotope, thereby effectively converting the results to the equivalent $m/z = 36$ ($^{35}Cl^+$) signal. The confidence interval is set at 68 %.

This observation aligns with previous findings by Shemwell et al. [209], who reported that HCl gas can be removed using CaO, $CaCO_3$, and calcium formate, achieving maximum removal efficiencies of 76 %, 54 %, and 81 %, respectively. A recent DFT study published in 2022 [285] investigated the mechanism of HCl capture by CaO and suggested that oxygen atoms on the CaO surface play a crucial role in the HCl adsorption process.

The sorbent effect becomes more pronounced in Fig. 4.47, with a larger dataset available for comparison. It is likely that a competitive mechanism is at play between K and Ca, as the formation of KCl is thermodynamically more favoured and more stable than $CaCl_2$. As a result, CaO only binds additional HCl if there is no more K available in the gas phase.

On the other hand, the equilibrium with silicates, discussed earlier (Fig. 4.45), suggests that the explanation for this mechanism lies in the Ca/K ratio. However, the effectiveness of this mechanism depends on the amount of K relative to Cl, which could potentially reduce to Ca+K if Si is not present or is limited.

The results of the char gasification/ash reaction evaluation are presented in Figure 4.48, which shows that only K and SO_2 were detected. For upgraded barley straw samples with Ca-additive, only K and SO_2 were detected during the char gasification/ash reaction. Notably, no release was observed in samples that were washed prior to or after torrefaction. The water-leached sample exhibited a large error bar for SO_2 release, indicating that the result should be considered unreliable.

In summary, the release behaviour during char gasification/ash reaction did not show significant differences between samples with and without Ca-additive, except for SO_2 release, which was reduced in the Ca-blended sample. In contrast to the sample material without additive (Fig. 4.24, Chapter 4.2.2), no KCl release was observed. This finding is consistent with the results from the devolatilization part, suggesting that the Ca-additive may have some effect.

The results for the char gasification/ash reaction of colza/PB blends align with those observed during the devolatilization phase. A lower proportion of PB in colza resulted in a higher release of potassium, likely due to a dilution effect, as raw PB contains less fuel-K compared to colza straw. This means that the higher the proportion of PB, the lower the release of K.

Moreover, the fuel-Si content in PB is significantly higher than in colza straw, which suggests that it should exert a substantial influence on the fate of K. As previously observed and discussed in Chapter 4.2.2, the incorporation of alkali metals into silicate networks can occur. Regarding the SO_2 release, the ultimate analysis in Table 4.6 (Chapter 4.3.1) shows a decrease in sulphur fraction for sample blends with an increased proportion of PB. The lower fuel-S content limits the formation of SO_x, and this can be attributed to dilution effects.

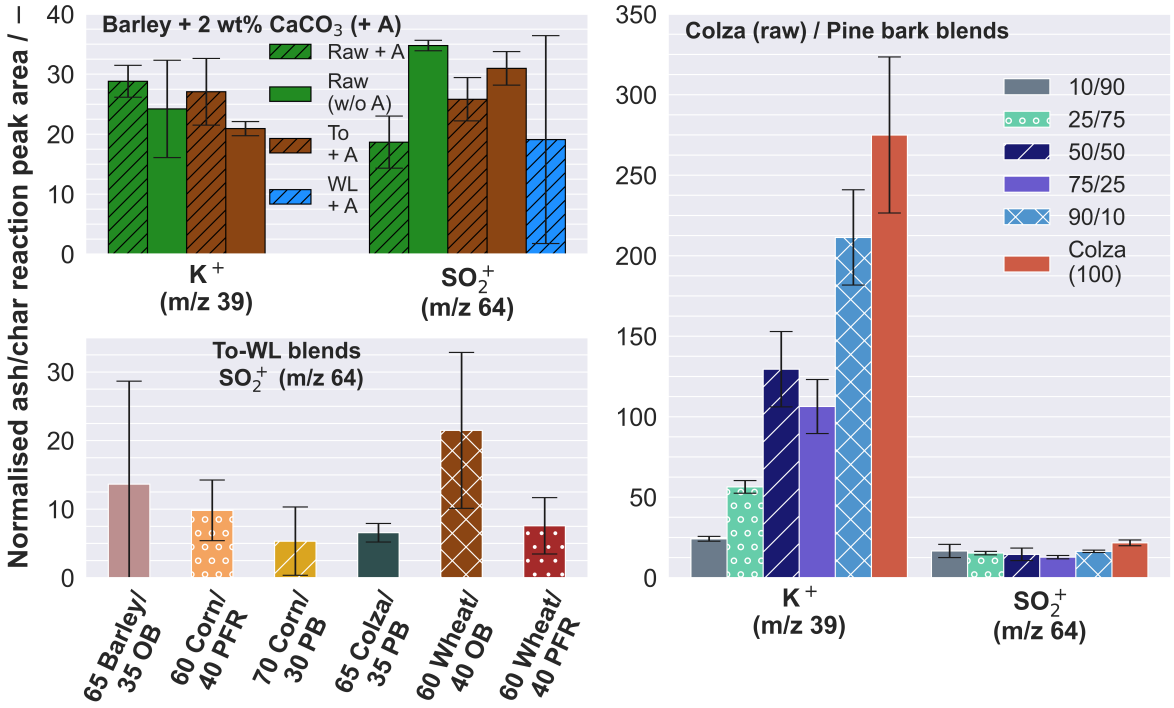

Figure 4.48: Averaged normalised peak areas of detected species released during the ash/char reaction phase. Top left: pre-treated barley straw blended with 2 wt% $CaCO_3$. Right: raw colza straw blended with varying amounts of PB. Bottom left: different straw varieties (To-WL) blended with different quantities of either PB, OB or PFR.

The char gasification/ash reaction of To-WL fuels blended with OB, PFR, or PB resulted in the detection of SO_2 releases only (Fig. 4.48, bottom left). However, the large error bars in the bar charts suggest that the values were less reliable and more spread out, making it challenging to accurately interpret the data.

Notably, wheat straw blended with PFR appeared to exhibit a significantly lower SO_2 release compared to wheat straw blended with OB. This observation is consistent with the findings during the devolatilization phase.

4.3.3 Ash fusion testing and behaviour of ashes

Similar to the previous sample series (Chapters 4.1.4 and 4.2.4), the blended biofuel series was investigated by HSM to elucidate the ash fusibility characteristics of the blended biofuels. It is essential to note that the fuel blends and their corresponding blending proportions (mass fractions) were based on the upgraded feedstock itself, rather than on the ash constituents. As previously specified in Chapters 4.1.4 and 4.2.4, one measurement was taken per sample, and the experimental conditions for ash fusion testing were identical to those used in previous experiments. Figure 4.49 displays the determined coefficients h_x/h_0 for the sample ashes plotted against temperature.

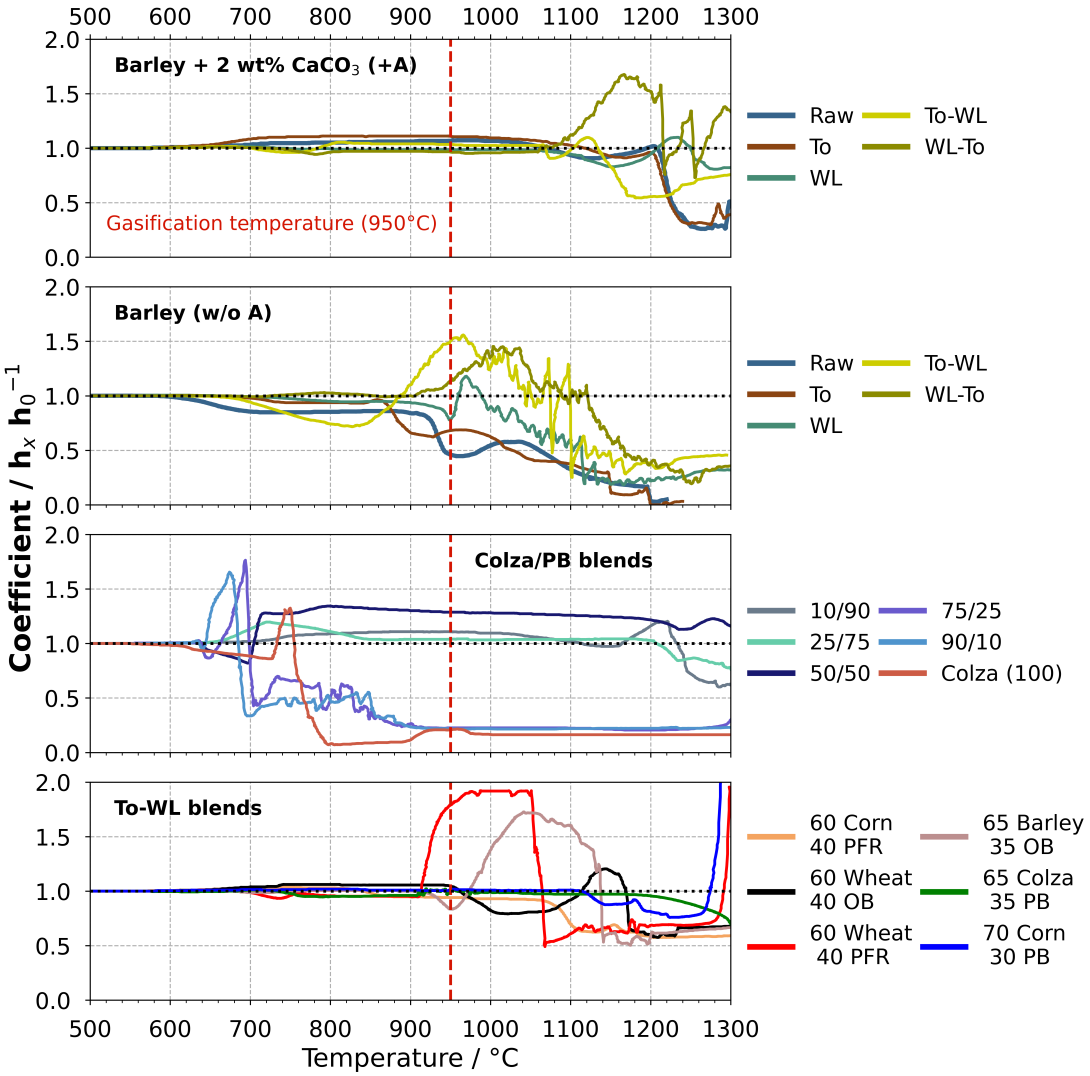

Figure 4.49: Height profile of ashes of pre-processed and blended herbaceous biofuels plotted against temperature (HSM).

The top diagram displays the ash melting curves for pre-treated barley straw blended with 2 wt% Ca-additive. As shown in the diagram, the melting curves exhibit either a slight decrease or increase at low temperature ranges (600 °C to 700 °C). This observation is consistent with the findings in both previous experimental parts of this work, where residual carbon content in the ash with CO_2 in the atmosphere may be attributed to shrinking or volume increase, as discussed in Chapter 4.2.4.

Comparing the upgraded materials (second diagram in Fig. 4.49) with the Ca-blended ones reveals noticeable effects on the ash melting curves. Barley straw ashes that were solely pre-treated before ashing show noticeable changes in terms of ash fusion effects at temperatures above 700 °C (except for the untreated material itself). In contrast, fuels blended with Ca-additive exhibit similar effects at temperatures starting from approximately 1050 °C. Notably, neither thermal nor leaching pre-treatment had a significant effect on ash melting behaviour at 1050 °C, and the ash fusion behaviour of the Ca-blended fuels was found to be identical. In other words, this suggests that only the Ca-additive exerts a decisive effect on ash melting behaviour by favouring the formation of high-melting calcium silicates, and it can be viewed as an independent factor from the upgrading method. Furthermore, it appears that the Ca-additive has a greater effect on ash fusion temperature compared to thermal and/or water-leaching pre-treatment.

The third diagram shows the ash melting curves for raw colza straw samples blended with varying proportions of PB. Interestingly, the blended sample ashes exhibited similar ash fusion characteristics to those of the raw colza straw ash, as observed in Fig. 4.35 (Chapter 4.2.4), and ash melting was observed to begin at temperatures above 630 °C. However, the sample blended with 90 wt% PB did not exhibit ash fusion effects below 700 °C. Samples with PB fractions of 75 wt% or less showed perceptible melting effects below 650 °C, and samples with PB fractions of 25 wt% or 10 wt% PB were completely molten at 700 °C.

It is not surprising that the colza straw ash samples had relatively low melting points, given that the raw material itself has a high fuel-K content and a low silicon fraction compared to other herbaceous biofuels (Table 4.3, Chapter 4.2.1). In contrast, PB has a relatively low fuel-K content and a much higher silicon content than raw colza straw. Therefore, it can be reasonably assumed that dilution effects played a key role in the observed ash fusion characteristics.

Based on these findings, it appears that simply blending K-rich feedstocks with woody components is not sufficient to increase the ash melting point, and biomass upgrading is necessary. In contrast, torrefying and post-washing colza straw and blending it with

35 wt% PB did increase the ash melting point. It is worth noting that raw colza straw has a very low fuel-Si content (98 mg kg^{-1}), which suggests that no high-melting silicates are formed regardless of whether the fuel-Ca content is increased or not. Given the high fuel-Ca content in raw colza straw, this further underscores the fact that no high-melting calcium silicates are formed due to the absence of a Si network component that could form such silicates at high temperatures. This example highlights the differences between herbaceous feedstocks and emphasizes the need for individual upgrading approaches to affect ash chemistry. In this case, the melting point can be successfully increased by adding biomass-based silicon-based additives or blending components with a distinct silicon content, as discussed in Chapter 4.2.6 (Fig. 4.42, top left diagram).

The lower diagram shows the ash melting curves for torrefied and post-washed samples blended with woody feedstock components. A comparison with the upgraded fuel samples in Fig. 4.35 (Chapter 4.2.4) suggests that an increase in the ash melting point was achieved for the blended sample varieties. For the upgraded fuels, ash melting was observed to begin at temperatures above 700 °C, whereas the upgraded and co-blended samples in Fig. 4.49 melted at an average temperature of 900 °C. The most promising results were obtained for corn straw, which was blended with 30 wt% PB, indicating that PB had a positive effect on ash melting. In contrast, PFR appeared to have the poorest results, as the samples blended with PFR showed lower ash melting temperatures compared to other woody blends.

According to the ultimate analysis in Table 4.6, it is clear that corn/PB had the highest fuel-Si fraction among all samples investigated (greater than 1 wt%). This suggests that Si can act as a network component, forming stable high-melting calcium silicates that positively affect the ash fusion temperature of the fuel samples. Additionally, it is evident why biomass upgrading through post-washing had a crucial side effect: the fuel-K content was reduced by half on average. In other words, this means that the effect of low-melting potassium silicates was diminished, and the competition between Ca and K silicate formation was reduced.

4.3.4 Thermodynamic prediction of gas phase chemistry

Building on the previous sample series (Chapters 4.1.5 and 4.2.5), predictions were made regarding the condensation behaviour of inorganic compounds (alkali chlorides, carbonates, and slag-mixtures) starting from 950 °C for both upgraded and blended sample series. Figure 4.51 illustrates the amount of condensed alkali chloride, while Figure 4.51

presents the amount of condensed carbonates and slag-mixtures. For alkali chlorides, no significant differences were observed between pyrolysis and gasification conditions. In contrast, some variations were found for carbonates and slag-mixtures. Therefore, the results in Fig. 4.51 are presented for both gasification and pyrolysis conditions. As seen in both previous parts of this work, the curves exhibit typical condensation formation patterns, which are promoted at lower temperatures, leading to an increased deposition rate.

The top diagram in Fig. 4.50 illustrates the condensation behaviour of alkali chlorides, primarily KCl and partly NaCl, for upgraded barley straw samples with 2 wt% calcium additive. A thorough examination of the data reveals that there were minimal disparities between the upgraded samples (Fig. 4.37, Chapter 4.2.5) and those additionally blended with Ca. This suggests that Ca did not impact the range of condensation temperatures or the fraction of condensed alkali salts. Interestingly, the torrefied sample with calcium addition showed a slightly increased fraction of condensed alkali chlorides compared to the untreated source material itself. This observation is consistent with findings for torrefied barley straw without calcium addition. As expected, given the thermally treated material's higher potassium fraction relative to the source material, it appears that Ca did not exert a noticeable effect on condensation behaviour.

It is also worth noting that the torrefied barley straw had a significantly higher fuel-Cl content ($1076\,\mathrm{mg\,kg^{-1}}$) compared to the source material ($618\,\mathrm{mg\,kg^{-1}}$). In the previous chapter, it was found that chlorine presence was essential for KCl formation, which explains the accelerated release of gaseous KCl. Given that the torrefied sample had a higher fuel-Cl content, more KCl was released into the gas phase, leading to an increased condensation temperature observed for the thermally treated material.

In addition to the condensation behaviour, another notable finding was that torrefied barley straw exhibited an exceptional fuel-Cl content, with significantly higher Cl fractions compared to the other thermally treated straw varieties. This suggests that chlorine was chemically bound in a distinct manner, differing from the other sample materials. For instance, during the ash/char reaction (see Fig. 4.24, Chapter 4.2.2), no chlorine release was observed for barley straw, whereas the other samples showed a release of chlorine into the gas phase.

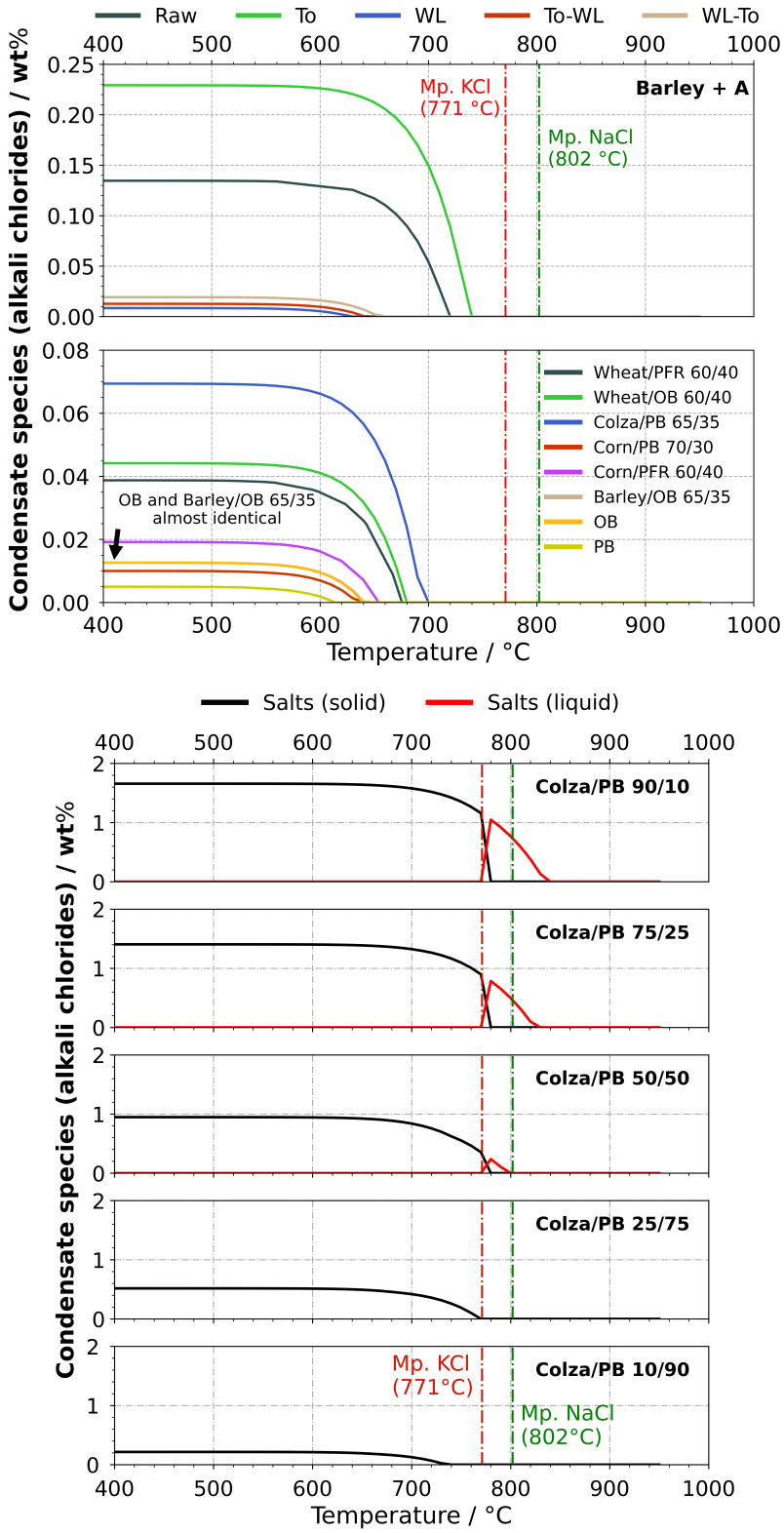

Figure 4.50: Condensation of alkali chlorides, primarily KCl, under gasification conditions. The red and green dashed lines indicate the melting temperatures of KCl and NaCl, respectively. The gasification temperature is 950 °C.

The predicted condensation behaviour of torrefied and post-washed straw varieties, which were subsequently blended with woody components, is illustrated in the centre diagram (Fig. 4.50). It is not surprising that the colza/PB (65/35) blend exhibited an increase in condensation temperature and produced a quantitatively larger amount of condensed alkali chlorides compared to blends containing wheat, barley, or corn straw. According to the ultimate analysis presented in Table 4.6 (Chapter 4.3.1), this colza straw sample blend demonstrated the highest fuel-Cl fraction among all the blends investigated; however, this fraction remains relatively low compared to that of the untreated source materials, as indicated in Table 4.3 (Chapter 4.2.1). The increased release of KCl is inherently linked to the fuel-Cl content, a relationship further emphasised by the colza/PB blends, which are discussed in the following section. Notably, the torrefied, post-washed, and blended fuels exhibited the lowest quantities of condensed alkali chlorides across all sample series analysed.

Another conclusion drawn from the investigation of all sample blends is that the condensation temperatures of the alkali chlorides were predominantly below 700 °C. In contrast, for the solely torrefied and post-washed samples, the salts were observed to condense at or just below their respective melting points, as illustrated in Fig. 4.37 (Chapter 4.2.5). The quantity of condensed salts across all samples was below 0.1 wt%, which is slightly lower compared to the non-blended, thermally treated, and post-washed materials.

In summary, torrefaction combined with post-washing demonstrated promising results concerning condensation behaviour at an operating temperature of 950 °C. The condensation temperatures of both alkali chlorides remained significantly below their respective melting points for all sample blends examined. This principal effect can primarily be attributed to biomass upgrading, while the blending approach with woody feedstock components offered an additional dilution effect, further enhancing the reduction in condensation temperature.

The results regarding the condensation behaviour of the colza sample blends are depicted in the lower diagram. Notably, the condensation temperature was closely related to the ratio of the woody blending component, PB, with a decrease observed as the fraction of PB increased. For the colza/PB blend at a ratio of 90/10, both the condensation temperature and the amount of alkali salts in the gas phase were identical to those seen in colza straw without any woody blending component (as shown in Fig. 4.37, Chapter 4.2.5).

For colza sample blends with a PB content of 50 wt% or higher, alkali salts in a liquid state were noted to condense in a temperature range of 770 °C to 830 °C. The fuel-Cl content of colza straw was typically at least two to three times greater than that of other feedstocks, facilitating a higher release of KCl, as indicated by the condensation calculations. Conversely, the fuel-Cl content in PB was 94 % lower, resulting in a negligible concentration of chlorine in that scenario.

The condensation temperature and the quantity of condensed KCl and NaCl were both influenced by the PB fraction. Thus, the relationship between condensation temperature and the amount of condensed alkali salts was primarily ascribed to dilution effects. This dilution effect was particularly evident in the 50:50 blending ratio, where the quantity of condensed alkali chlorides was effectively halved compared to the non-blended feedstock (refer to Fig. 4.37, Chapter 4.2.5).

In conclusion, the most favorable results for lowering condensation temperature were observed in samples with PB blending ratios of 75 wt% and 90 wt%. The fact that both the condensation temperature and the amount of condensed alkali chlorides were below their respective melting points suggests that these salts are unlikely to become overly sticky at the gasification temperature of 950 °C.

In addition to alkali chlorides, both carbonates and slag mixtures were observed to condense during pyrolysis and gasification conditions. The condensation curves for these species are presented in Figure 4.51.

In Chapter 4.38, it was previously established that the quantity of condensed carbonates and slag mixtures was generally higher under pyrolysis conditions than under gasification conditions for the upgraded biofuels. This difference was attributed to the distinct reaction environments associated with each process.

It is not surprising that phase transitions between the formation of carbonates and slag were observed, as indicated by the corresponding shape of the condensation curves. These observations were also noted for both series of samples in the earlier sections of this study. This suggests that the slag was rich in alkali carbonates – and to some extent, chlorides – which has been supported by the predicted thermodynamic activities.

In general, it can be stated that the upgraded barley straw with a calcium additive, as well as the torrefied/post-washed sample series, exhibited only low concentrations of condensed carbonates or slag mixtures. In contrast, the upgraded barley straw samples without the calcium additive displayed different results, as shown in Fig. 4.38 of Chapter 4.2.5. For the source material without the calcium additive, a concentration of 0.24 wt% of condensed carbonates was found, while the calcium-blended material indi-

cated only 0.01 wt%. This suggests that Ca significantly affected the gas phase chemistry, likely promoting a series of reactions among the ash constituents – K, Si, and Cl.

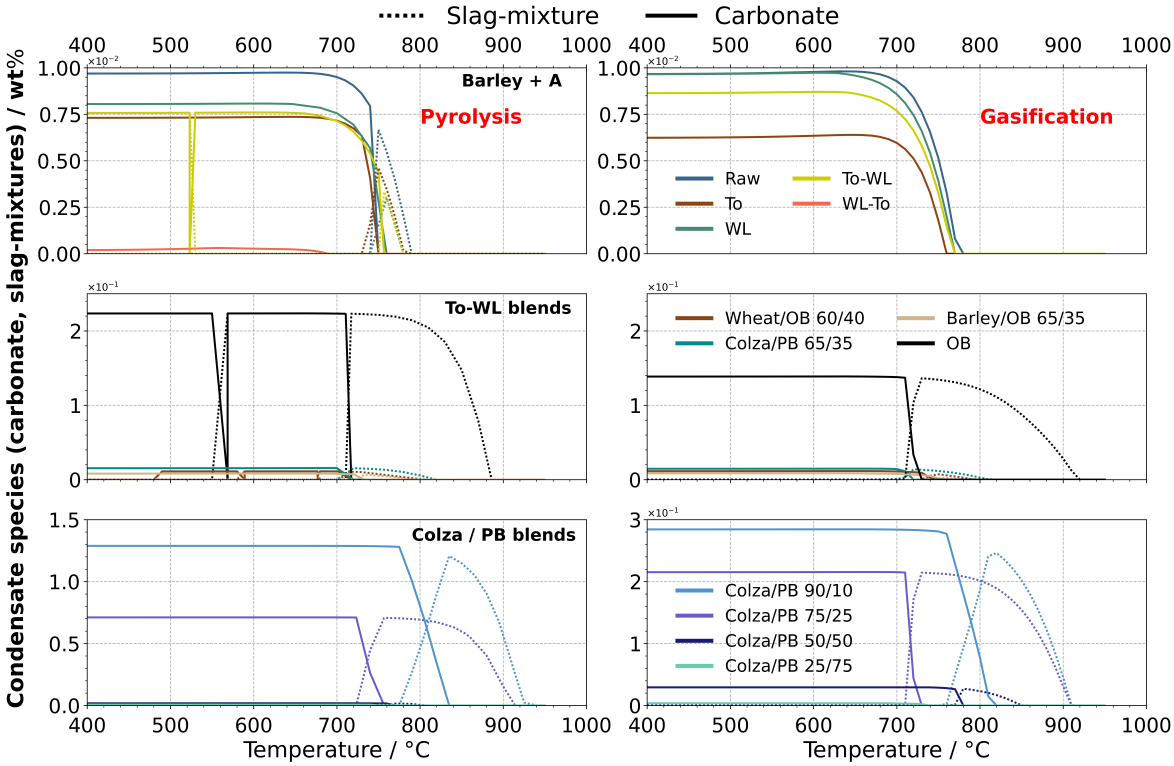

Figure 4.51: Condensation of carbonate and slag-mixtures under both pyrolysis (left Figure) and gasification conditions (right Figure). The gasification temperature is 950 °C.

The explanation for this phenomenon appears to be that Ca, acting as an active chlorine sorbent, suppressed the formation of HCl, which in turn reduced the amount of KCl released into the gas phase. This effect can also be viewed from another perspective: since KCl is one of the primary sources of HCl formation [210], its presence may contribute to the suppression of HCl production. Therefore, it can be assumed that K remained in the ash by forming high-melting silicates, with K and Ca likely forming mixed silicates. These ash components exhibit a distinctly lower vapour pressure than KCl.

It is notable that the normalised volatile peak area of K released during pyrolysis was lower for the Ca-blended straw series, averaging 6 arbitrary units (as shown in Fig. 4.44, Chapter 4.3.2). In contrast, it is evident that the upgraded material without the calcium additive displayed a higher concentration of potassium in the gas phase,

averaging 7.5 arbitrary units (see Fig. 4.23, Chapter 4.2.2). These findings support the previously discussed hypothesis that K may have formed chemical bonds with calcium silicates.

In summary, the increased Ca content in the fuel led to a shift in equilibrium. More specifically, competitive reactions among the species K, Ca, Cl, and Si were altered from a thermodynamic perspective.

The predicted condensation behaviour of the torrefied and post-washed sample blends is illustrated in the centre diagram of Fig. 4.51. This diagram also shows results for the woody blending component, OB. Based on equilibrium calculations, it can be noted that PB itself did not exhibit any condensation of carbonates during pyrolysis or gasification; instead, only alkali chlorides were detected in the gas phase. Similar observations were made for the corn/PFR (60/40), corn/PB (70/30), and wheat/PFR (60/40) samples, which also demonstrated no carbonate condensation and only alkali chlorides present in the gas phase during pyrolysis and gasification conditions.

For the upgraded and blended materials, the fraction of carbonates and slag in the gas phase was relatively low. It appears that the condensation of carbonates primarily originated from the woody component (OB), as non-blended samples of torrefied and post-washed wheat and barley straw exhibited only alkali chlorides in the gas phase. However, the concentration of inorganics was lower for the blended materials, which can be attributed to dilution effects. The colza/PB (65/36) blend displayed very low concentrations of carbonates in the gas phase, suggesting that the associated inorganics likely came from the herbaceous biofuel itself (see Fig. 4.38, Chapter 4.2.5). The carbonate fraction was significantly reduced in the blended material as well, also due to dilution effects.

From a quantitative perspective, it is noteworthy that the fraction of inorganics in the gas phase remained similar, regardless of whether the reaction took place during pyrolysis or gasification. The average condensation temperature for each sample blend was around 800 °C, with the most significant effect observed for the colza/PB (65/35) blend, which showed a notable reduction in condensation temperature, approximately 150 °C lower than that of the upgraded colza sample (as depicted in Fig. 4.38, Chapter 4.2.5).

The lower diagram presents the predicted outcomes regarding the condensation behaviour of ashes from PB-blended colza straw samples. Notably, the sample with the lowest PB fraction (10 wt%) exhibited the highest concentration of carbonates or slag. However, when compared to the herbaceous source material itself (as illustrated in Fig. 4.38, Chapter 4.2.5), it appears that the quantity of formed carbonates and slag was not significantly influenced by the presence of the woody blending component.

Specifically, the colza/PB (90/10) blend showed a carbonate fraction of 1.3 wt% during pyrolysis, while the non-blended material demonstrated a carbonate content of 1.3 wt%. This consistency in the carbonate content was observed under gasification conditions as well. No carbonates were detected in the gas phase for the colza/PB (10/90) sample. The condensation of carbonates/slag-mixtures shifted to lower temperature ranges as the ratio of colza to PB decreased, with an accompanying reduction in the fraction of inorganics present in the gas phase. The same trend was observed for the alkali chlorides, as shown in Fig. 4.50. These findings suggest that dilution effects played a significant role in the condensation behaviour observed.

4.3.5 Thermodynamic prediction of mineral phases formation

As mentioned in the introduction to this chapter, the experimental part focuses on the ash transformation chemistry of various straw blends. The motivation for introducing these blends was rooted in preliminary equilibrium calculations based on ternary phase diagrams ($CaO–K_2O–SiO_2$). The aim was to elucidate the context in which Ca or woody components affect interactions between inorganics, and whether these impacts can be attributed to dilution effects or if chemical interactions between ash components play a key role.

Figure 4.52 compares the ash fusibility of the pre-treated sample blends in ternary phase diagrams, considering the main ash-forming components CaO, K_2O, and SiO_2. In addition to CaO and K_2O, small amounts of MgO and Na_2O were also predicted to form, and these species were normalised for CaO and K_2O, respectively, due to their similar chemical properties.

In contrast to the solely upgraded barley straw (marked in orange in Fig. 4.52), the Ca-blended samples exhibited distinct effects on their ash melting behaviour. The red arrow indicates an increase in the fraction of CaO, and it is clear that the Ca additive shifted the sample ash from the mixed phase to the solid phase, resulting in dominant solid oxides. Therefore, no ash melting is expected at an operating temperature of 950 °C. Previous experimental investigations using HSM (as described in Chapter 4.3.3) have already confirmed the stability of the sample ashes at this specified gasification temperature. Consequently, the consistency between the ash fusibility results obtained from thermodynamic equilibrium calculations and experimental results was reasonably good.

Raw colza straw was blended with various proportions of PB, and a clear correlation was observed between the blend ratio and phase composition (right-hand Fig. 4.52). At a proportion of 50 wt% to 75 wt%, the ash of colza straw was found to be stable at 950 °C, due to the dominance of oxide phases. Consequently, no ash melting is expected. The observed effect was primarily attributed to dilution effects, and the arrows indicate a decrease in K_2O and an increase in SiO_2 with increasing proportions of PB.

The final sample series consisted of torrefied and post-washed straw varieties, which were then blended with woody components (bottom Fig. 4.52). It is noticeable that both woody components, OB and PFR, exhibited similar properties in terms of their phase composition at 950 °C. In contrast, PB was predicted to exist in the mixed phase.

In conclusion, the most promising results in terms of increasing the fraction of solid oxides were obtained by blending upgraded straw with Ca-additive. As a result, thermal stability can be expected at 950 °C. Notably, none of the Ca-blended samples investigated was found to be in the liquid phase. Furthermore, it appears that solely blending the source material with Ca was sufficient to shift the ash constituents from the mixed phase to the solid phase, and no prior pre-treatment was necessary to enhance this effect.

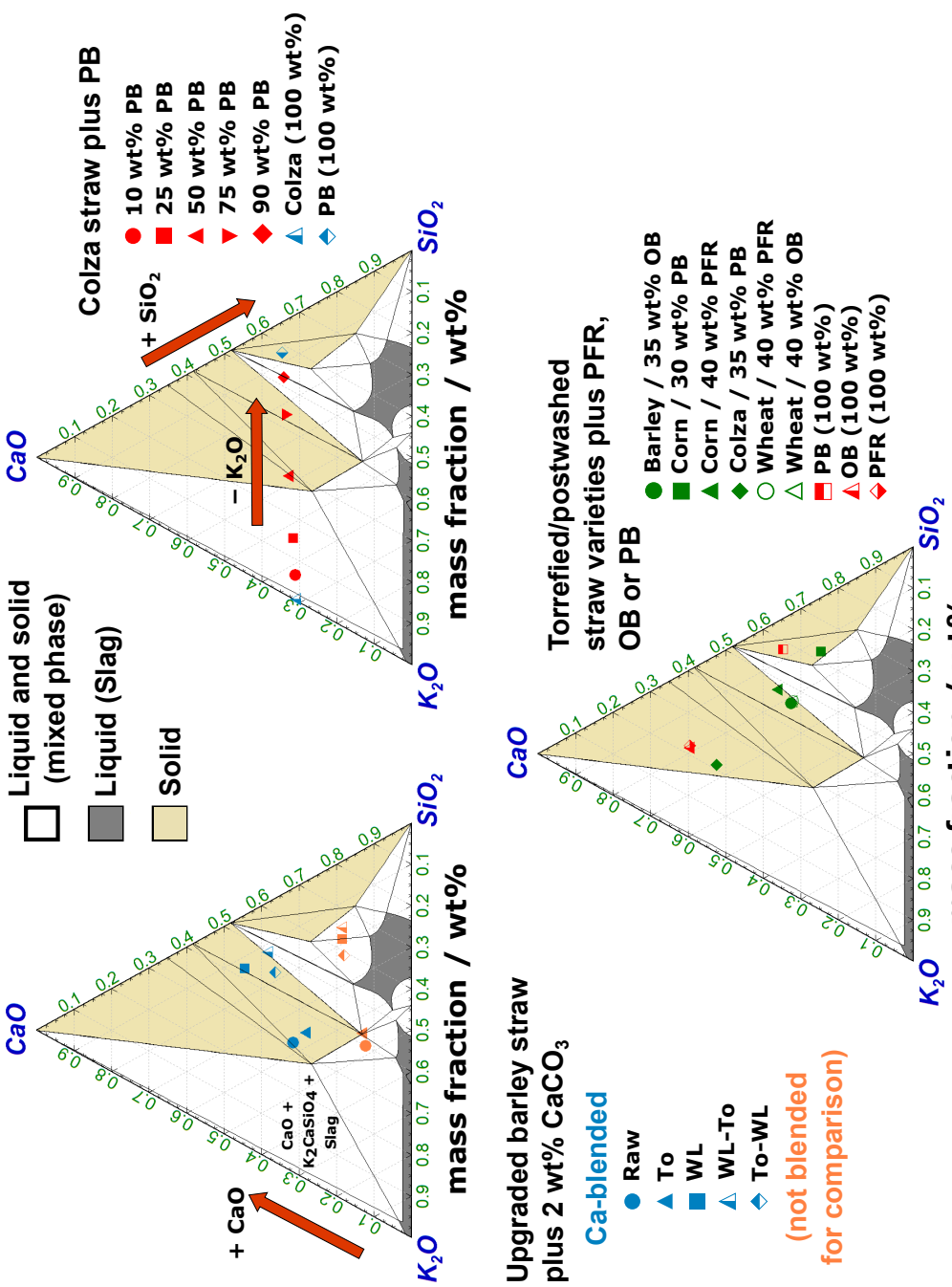

Figure 4.52: Ternary phase diagrams for the SiO_2–CaO–K_2O system, predicted using FactSage [202]. The phases were predicted for ashes of pre-treated barley plus 2 wt% $CaCO_3$ (top left), colza, blended with varying amounts PB (top right), and different straw varieties (To-WL) blended with different quantities of either PB, OB or PFR (bottom). The calculations were conducted under isothermal and isobaric conditions at a temperature of 950 °C and at atmospheric pressure.

In addition to ternary phase diagrams, mineral phase maps were predicted for the sample blends and are displayed in Figure 4.53. Notably, in the previous chapters of this work, no significant discrepancies were found between pyrolysis and gasification conditions, which is why the focus will be maintained on the latter.

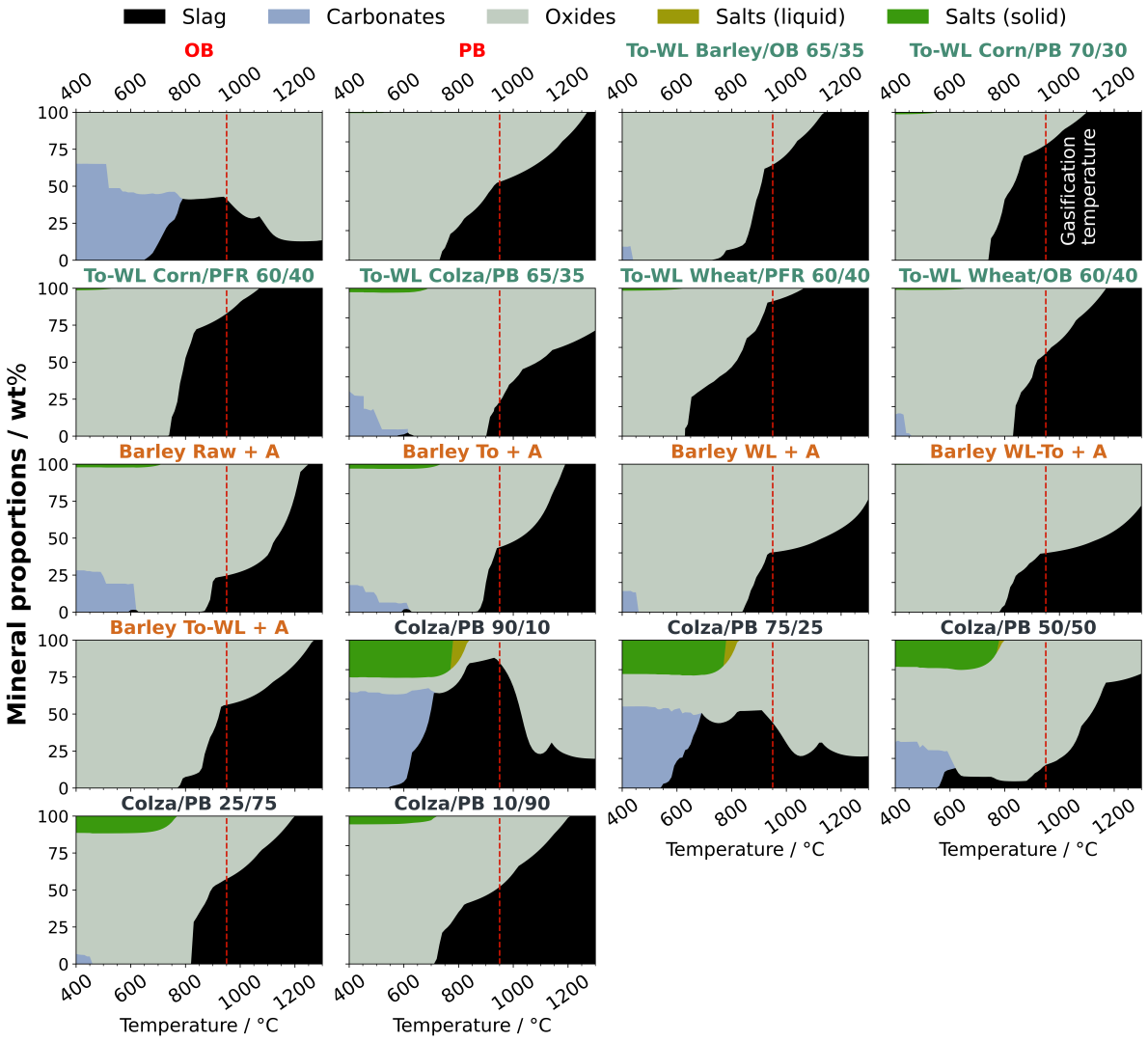

Figure 4.53: Calculated mineral compositions of the ashes from the upgraded straw blend varieties were determined under gasification conditions. The dashed line denotes the gasification temperature of 950 °C.

OB exhibited an increased formation of carbonates in the low-temperature range, unlike PB. The transition from solid carbonates to slag occurred smoothly, and based on the predicted thermodynamic activities of the species, the ash-slag mixture predominantly comprised molten carbonates.

Interestingly, the predicted composition of the ash phases for the torrefied and post-washed sample series matched well with the experimental observations obtained through HSM (Fig. 4.49, Chapter 4.3.3). The ashes from both sample blends, colza/PB (65/35) and corn/PB (70/30), did not exhibit any melting effects at 950 °C, as the inorganic constituents remained in a solid oxide phase. Previous HSM studies have shown that these sample blends are stable within this temperature range, with no significant changes in their geometric shape observed. The residual ash constituents of these sample blends were found near the phase boundary between solid oxides and the mixed phase, which may indicate thermal instability at 950 °C. In contrast, these samples showed a relatively high melt fraction of approximately 75 wt% on average. Experimental ash fusion testing using HSM confirmed the occurrence of melting or expanding effects.

In contrast to solely pre-processed barley straw, the Ca-blended samples exhibited altered phase formation at low temperatures. Not surprisingly, calcium promoted carbonate formation, which is consistent with the findings of the release experiments presented in Fig. 4.45, Chapter 4.3.2. A notable observation was the competitive interaction between potassium and calcium ions. It was hypothesised that Ca modified the silica network, favouring the formation of high-melting silicates, leading to an increased fraction of potassium remaining as a free reactant in the ash. Novaković et al. [243] reported that in the system K–Ca–Si, silicon dioxide preferentially reacts with calcium oxide at elevated temperatures, releasing more potassium to the gas phase rather than incorporating it into the silicate structure. This finding is consistent with the proposed hypothesis that potassium forms carbonates instead. It is not surprising that pre- or post-washed samples did not show carbonates in their phase maps. The carbonate fraction for the solely washed sample was significantly lower than that of the source material or torrefied sample, indicating that most of the potassium was leached out during the washing treatment.

The Ca-blended barley straw samples showed promising results regarding their melting behaviour, particularly with regards to slag formation. The predicted onset of liquid slag formation was around 800 °C to 850 °C, and it remained constant up to 950 °C.

When colza straw was blended with incremental ratios of PB, the formation of alkali salts (carbonates and chlorides) in the low-temperature range decreased significantly with increasing PB fraction. This is due to the high potassium concentration in the ash of the unblended colza straw. Interestingly, both sample ashes, colza/PB (90/10) and colza/PB (75/25), showed a noticeable decrease in molten slag formation above 950 °C. This phenomenon can be attributed to the enhanced release of K-containing

components, leading to a drop in slag formation and a major fraction of high-temperature stable oxides, such as CaO. The colza straw samples had a low fuel-Si content (as shown in Fig. 4.20, Chapter 4.2.1), which means that low-melting silicates are not expected to form at high temperatures. Silicon acts as a network agent that incorporates K, while an increased PB fraction led to an increased fuel-Si content, resulting in increased molten slag formation for PB fractions greater than 25 wt%. Despite having less K and traces of Na in the ash, which would typically react with SiO_2 to produce low-melting substances [286], the ash still fused progressively from 950 °C onwards. Furthermore, even with a high proportion of woody component (25 wt% or higher) and a corresponding decrease in fuel-K, the fuel-K content was sufficient to form low-melting silicates at high temperatures.

The results for PB-blended colza straw samples show that the ratio of woody component significantly impacts phase formation, which is heavily influenced by the ash-forming constituents, particularly potassium and silicon. The findings suggest that the chemical interactions between inorganic components play a crucial role in determining the ash fusibility.

In summary, Figure 4.54 provides a detailed comparison of the ash fusibility. The results are sourced from the predictions made in the mineral phase maps and provide a comprehensive overview of the ash fusion behaviour.

The addition of Ca to the sample was evident when comparing the melt fraction of the upgraded/Ca-blended and non-blended barley straw ashes (see Fig. 4.40 in Chapter 4.2.6). The results showed that the fraction of molten slag was significantly reduced by about half when Ca was added, particularly for the source material itself. This supports the assumption that blending with Ca without pre-processing is sufficient to minimise ash melt formation. Furthermore, the lowest temperature at which slag formation began (Fig. 4.54) was constant at around 800 °C, indicating a consistent effect.

The melting behaviour of ash from PB-blended colza straw was influenced by the presence of K and Si in the ash. The data showed that when the PB blending ratio was 75 wt% or higher, the ash temperature increased. The graph on the left-hand side illustrates how an increase in the woody component (indicated by the red arrow) correlates with an increase in K_2O and a decrease in SiO_2. Compared to the non-blended material (Fig. 4.40, Chapter 4.2.6), blending colza straw with 25 wt% PB reduced the amount of molten slag by about half. The ash from a 50/50 PB-blended colza straw sample showed a low amount of slag formation at 950 °C, but it was predicted to start fusing just below 600 °C. This outcome matches the experimental results obtained by

HSM, which showed distinct melting effects above 600 °C. Regardless of the woody component ratio, initial melting effects were found to occur just below 640 °C.

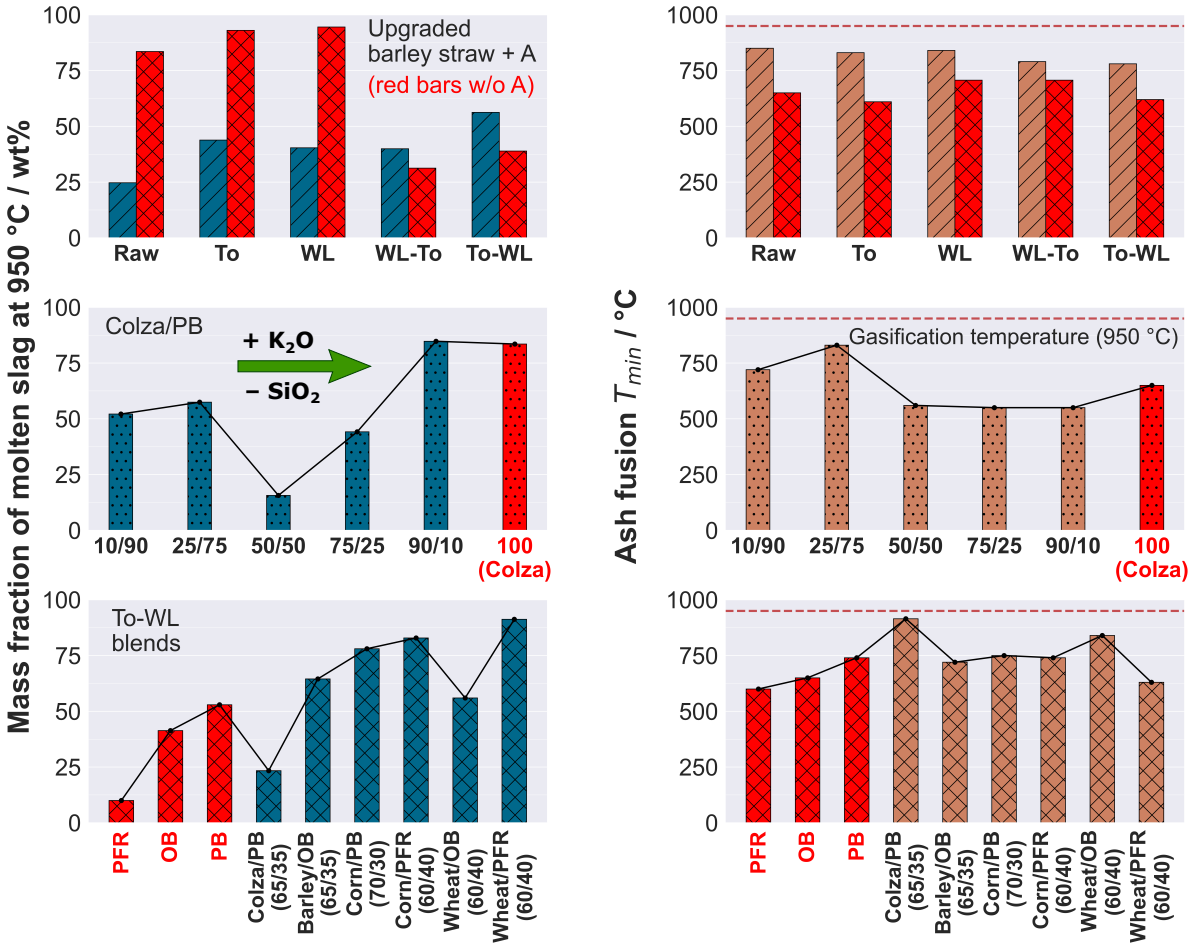

Figure 4.54: Comparison of the ash fusibility of the investigated sample blend ashes under gasification conditions. The graph on the left illustrates the percentage of molten slag formed at 950 °C, while the graph on the right shows the lowest temperature at which slag formation commenced. The results are sourced from the predicted data shown in Fig. 4.53. Red colour denotes the reference materials or blending components.

The bottom graph shows how woody biofuel components affect the formation of molten ash in torrefied and post-washed herbaceous fuels. As expected, the woody components PFR, OB, and PB produced the least amount of molten slag at 950 °C. The blends colza-/PB (65/35) and wheat/OB (60/40) showed the most significant reduction in molten slag formation, and the predicted data matched well with the experimental results ob-

tained by HSM (Fig. 4.49, Chapter 4.3.3). In contrast, the ash from wheat straw/PFR (60/40) predicted to form the highest fraction of molten slag at over 90 wt% at operating temperature. The experimental coefficient h_x/h_0 indicated severe deformation of the ash sample just below 950 °C, which aligns with the overall trend of ash fusion observed by HSM. Based on experimental findings, corn/PB (70/30) showed the best high-temperature stability, with ash melting occurring above 1100 °C. However, predicted results suggested an elevated molten slag fraction of almost 80 wt% at 950 °C, with the lowest temperature for molten slag formation found to be below 800 °C.

In conclusion, it is essential to note that this thesis did not include a kinetic analysis of the ash melting process, and the numerical results were solely based on thermodynamic data. As seen in [287] and [288], other studies have estimated the kinetic impacts on ash fusion behaviour as a crucial factor influencing ash melt formation. The Coats-Redfern method [289] has been widely used for determining the activation energy in kinetic analyses of coal and biomass thermal decomposition [290].

4.3.6 Discussion on the impact on fluidised-bed gasification and CLG

In addition to biomass upgrading through washing or thermal treatment, understanding the effects of additives and co-blending strategies on the ash fusion behaviour and the fate of inorganics during the gasification process is crucial for gasifier operators.

In the final part of this work, the influences and effects of calcium-based additives and biofuel co-blending approaches on the behaviour of inorganic constituents during gasification conditions were thoroughly examined. Based on preliminary thermodynamic calculations, including ternary phase diagrams designed to predict ash fusibility at 950 °C, a sample series was conceptualised and divided into three parts. Specifically, a set of upgraded barley straw samples (which were investigated in Chapter 4.2) were blended with an additional 2 wt% $CaCO_3$. Non-treated colza straw was then co-blended with incremental ratios of PB. Finally, various torrefied and post-washed straw varieties were blended with varying proportions (30 wt% to 40 wt%) of either PB, OB, or PFR. The results suggest that the Ca-based additive and the woody biofuel blending components exerted significant effects on gas phase and mineral phase formation, and the interactions of inorganics were attributed to chemical and dilution effects.

As previously established, Si, Ca, and K are crucial components when estimating slagging tendencies, and they can be considered fundamental factors in determining the slagging index. For example, colza straw ash has been found to contain a significant

fraction of KCl, but a relatively low level of fuel-Si. Compared to other herbaceous biofuels, the fraction of molten slag was found to be relatively low in the lower temperature range. Co-blending with woody biofuel components, such as PB, exhibited interesting effects on ash fusion behaviour, namely, a reduction in molten slag formation and an increase in ash melting point simultaneously. However, an excess of the PB blending component shifted the equilibrium chemistry back to favour enhanced molten slag phases at lower gasification temperatures, primarily due to the excess fuel-Si originating from the woody component. These outcomes emphasise the importance of considering the overall inorganic fuel composition.

In Chapter 4.1, a significant correlation was observed between the Ca content in the fuel and the release behaviour of KCl in batch-type release experiments. This effect became even more apparent here, as a direct comparison was made between Ca-blended barley straw and the same sample materials without additive (Fig. 4.45, Chapter 4.3.2). The results reinforce the assumption that calcium may play a role in capturing and depositing gaseous alkali chlorides (KCl or NaCl) [232–234]. When the fuel sample was washed before being blended with $CaCO_3$, almost no KCl release was observed. Moreover, Ca-blended barley straw showed a decrease in sulphur species released to the gas phase (H_2S, SO_2, and COS) compared to non-blended straw samples. This decrease in sulphur species release was due to sulphur capture by available calcium. Consequently, the presence of Ca did not only positively influence ash melting behaviour by increasing the eutectic temperature but also technologically influenced the release behaviour of KCl or S-containing species by chemically binding them and preventing their release into the gas phase. Due to its electrochemical nature, H_2S features corrosive effects, and a decreased release of H_2S may be therefore a significant advantage for gasifier operations.

Herbaceous feedstocks typically exhibit significant concentrations of Cl and S, which implies that potassium chloride KCl and K_2SO_4 become the dominant K-containing compounds [291, 292]. Unlike silicates, KCl and partially K_2SO_4 are known to be relatively volatile. It is worth noting that sulphates are less volatile than other alkali salts, such as chlorides. The release of these components can lead to increased deposition on heat exchanger surfaces, resulting in reduced heat transfer efficiency and higher corrosion rates. Furthermore, the release of these species into the gas phase may also lead to the formation of significant amounts of aerosols, including sub-micron particles, along with elevated emissions of sulphur compounds (mainly H_2S and partially its precursor SO_2) due to gasification conditions, as well as traces of organic sulphur compounds,

such as mercaptans. Additionally, a trend was observed for Ca-rich fuels to influence the HCl release behaviour. In batch-type release experiments, the HCl release was found to decrease in parallel with increasing Ca content in the fuel. When the molar ratio of K was higher than Ca, more HCl was released, since most potassium exists in the form of KCl in herbaceous feedstocks. As chlorine may accelerate high-temperature corrosion of reactor equipment during biomass thermochemical conversion [293, 294], HCl capture should have a highly favourable impact on this issue.

The colza/PB blends have demonstrated positive effects on both ash fusibility and the release behaviour of problematic species when the proportion of woody component PB was 50 wt% or higher. This suggests that woody/herbaceous fuel blends could be a viable alternative to expensive chemical additives, such as limestone or aluminosilicate minerals, for controlling ash melting and the release behaviour of inorganics. Consequently, valuable blends can be produced from low-cost fuels that offer additional economic and ecological benefits, as no additional chemical additives need to be manufactured.

As shown in the current study and previous experimental phases, alkali metals present in biomass fuels evaporate during gasification, causing significant damage to downstream components in a gasifier block. Therefore, alkali removal from high-temperature fuels gas is crucial for frictionless gasifier operation. Sorbent materials like aluminosilicate minerals are well-established for alkali removal approaches. In contrast, calcium-based minerals such as limestone are designed to increase the ash melting point by forming stable, high-melting calcium silicates. Interestingly, the findings suggest that Ca-based additives exhibit positive incidental effects, including sulphur and chlorine sorption mechanisms, which could have beneficial impacts on gas phase chemistry. Impurities in the gas phase, primarily Cl- and S-containing species, are the primary cause of corrosion of reactor components and poisoning of catalysts. While the concentration of these impurities can be controlled through operational conditions and gasification processes, it remains an inherent issue during CLG operation. Chemical sorption is therefore an additional advantage for minimising not only impurities but also harmful pollutant emissions.

The use of Ca-based additives and various biofuel blends has yielded promising results in enhancing the thermal stability of ashes at 950 °C. In terms of slagging trends, the most significant effects were observed for barley straw plus Ca-additive, regardless of whether a torrefaction or water-leaching treatment was applied beforehand. The additive was able to significantly increase the ash melting point of barley straw ash, as confirmed by both experimental investigations and thermodynamic equilibrium predictions. This suggests that slagging, fouling, and agglomeration problems in boilers should be mitigated.

In summary, it is important to note that the parameter thresholds for classifying biofuels are individualised for each feedstock, as this study highlights the significant differences between various herbaceous feedstocks in terms of their ash constituents and concentrations. This means that additives or co-blending should be tailored to each feedstock. Predictive approaches may be promising in generating valuable insights into ash fusion behaviour, mineral phase formation, and gas phase composition at process temperatures. However, they are limited by kinetic limitations. Notably, the comparative advantage of using small amounts of inexpensive additives or co-blending with other biofuels is an attractive option for enhancing the quality of low-grade fuels, thereby extending the range of agricultural or biogenic residues that can be processed. Overall, the mitigative effect of additives and co-blending with woody fuel components has a decisive impact on both gas and mineral phases.

Large-scale applications of biofuels may significantly benefit from preliminary screening and optimisation, as they require a high level of feedstock consumption. It is essential to emphasise that industrial applications differ significantly from those conducted on a laboratory scale. Unlike laboratory-scale production, industrial production typically operates continuously, as the costs associated with startup and shutdown of gasifiers are very high (requiring continuous operation to minimise downtime). Therefore, the selection of feedstock type and quality is a crucial key point for introducing new biofuels that are suitable for gasification operations. Further approaches are discussed in the Summary and Outlook (Chapter 5) of this work.

5 Summary and Outlook

Biomass is considered a non-conventional energy resource, and its relatively abundant availability and topographical independence make it a promising alternative to conventional renewable sources such as wind, solar, or hydroelectric power. Various techniques, such as biomass gasification, can serve as a key technology for producing products with higher value and potential applications than the original source material. During the gasification process, however, various ash-related issues are causing several operational problems. Inorganic, biomass-inherent constituents are the main origins and reason of those issues and play a fundamental role in that case. Therefore, a comprehensive knowledge about their behaviour and physical or chemical interactions among themselves or with the gasifier components is required. The present study offers a comprehensive summary of existing knowledge and suggests various promising approaches to address ash-related issues in fluidised-bed gasification systems combined with CLG technology, focusing on both economic and sustainable solutions. In particular, biomass preprocessing methods such as thermal treatment (torrefaction), water-leaching or blending with either Ca-based additives or various woody feedstocks were considered. Experimental investigations and thermodynamic modelling approaches in relation to one another were conducted, and the outcomes of both methods have been compared. Both, experiments and equilibrium predictions were carried out under well-defined gasification(-like) conditions at 950 °C with an emphasis on the influence of the applied upgrading methods on the release and phases formation. The results should help minimise ash-induced problems during fluidised-bed gasification, thereby enhancing performance from both an economic and ecological perspective.

It is worth noting that economic and ecological considerations play a more significant role in industrial applications than in laboratory-scale development. Unlike commercial scale production, laboratory research works completely different, because main goals are screening, exploring, and benchmarking new biofuels with existing technologies, mainly not focusing on production that makes a profit. Generally, the upgrading technologies and the operation of fluidised-bed gasification systems might be different from the in-

dustrial scale production. In large-scale fluidised-bed gasification systems, the selection of the type and quality of feedstock is crucial. As demonstrated in this study, it is important to consider a broader range of acceptable biofuel qualities to minimise feedstock costs.

Getting back to the general discussion on the outlook of this work, the combination of various biomass upgrading technologies can be instrumental in boosting the bioeconomy as a whole. The main objective is to enable the fuel flexibility and to reduce logistical challenges and high transportation costs. Treatment of biomass aims at converting a feedstock into a fuel showing similar characteristics to that of original fossil fuels, which, in turn, becomes attractive for saving efforts, costs, and lowering the impact on plant performance. Woody biomass are well-established biofuels, as their ash content is generally fairly low (lower than 1 wt%) and therefore almost ideal to fulfil quality classifications. In order to reduce the regional and seasonal dependency on woody biomass and minimise the overall fuel costs, biomass upgrading and co-blending or chemical additives such as limestone can be viewed as an adequate option to handle herbaceous fuels almost in the same way as woody residues and directly replace them.

In the scope of this work, applied pre-treatment methods were categorised into three different key subjects: firstly, industrially treated wheat straw samples were compared with woody biomass. In doing so, industrial wood pellets were selected as benchmark material, and pine forest residues were chosen as alternative woody waste biomass. Next, the focus was set on the influence of different pre-treatment measures, i.a. torrefaction, water-leaching, and either pre- or post-washing on behaviour of inorganic constituents. In the last part, the influence of a $CaCO_3$-based additive and feedstock co-blending with woody biomass, which is typically rich in calcium on behaviour of inorganic constituents was investigated. In the first and second working part, it has also been clarified how the water-leaching treatment of herbaceous biomass affects the sample chemistry. The industrially treated wheat straw samples were washed once (24 h), whereas four additional selected straw varieties (see second part of this study, Chapter 4.2) were washed twice (2 h in total), with due regard to the equal amount of washing water used. Washing twice in a shorter time period has proven to be more effective in washing out problem-causing inorganics, particularly alkali metal salts, but also partly inorganic sulphur compounds.

In summary, it can be concluded that additives or co-blending, torrefaction, washing, and pre- or post-washing can significantly influence the ash components of fuels. Specifically, these processes affect the behaviour of inorganic materials in the gas phase and modify the melting characteristics of ash – specifically, the mineral phases and slag

formation at gasification temperatures. It turned out, inter alia, that post-washed samples revealed hydrophobic characteristics in contrast to the pre-washed ones, which can be explained due to the fact that thermal treatment promotes the hydrophobic nature of the feedstock. It has been shown that the combination of torrefaction and washing might be an interesting route to upgrade low-quality biomass materials for energy applications, however, it strongly depended on the ash chemistry of the biofuel, and (inexpensive) additives or co-blending with appropriate (woody) feedstocks featuring a beneficial inorganic composition (e.g. low fraction of alkali salts, high fraction of Ca and/or Si) were partly of more effectiveness. The findings clearly highlight the different origin and chemical nature of biomass, reflecting the heterogeneousness in ash forming matter.

In Figure 5.1, a process indicated diagram is represented, in which the general concept of this work is centralised and summarised in a nutshell. Within this work, it has been demonstrated how different pre-processing approaches might be technically used for mitigating ash-related problems arising at elevated gasification temperatures in the range of 950 °C. The mineral phases formation (with regard to the ash melting behaviour) can be mainly adjusted through Ca-based additives or biofuel blends, whereas the thermodynamic properties or the gas phase composition are mainly influenced by pre-treatment methods, such as torrefaction, water-leaching, and either pre- or post-washing. Nonetheless, it could be demonstrated that additives and woody components as admixtures revealed some chemical effects on the fate of inorganics, indicating sorbent properties of the additive, as the comparison of solely upgraded fuels and their blended varieties implied distinctions in the gas phase (as it has been shown by means of MBMS measurements).

It has been clarified that low-melting ash or rather the "slagging index" should be considered as a main criterion for biomass-based fuels due to their relatively high fraction of alkali metals. The alkali nature of biomass ashes tends to lower the fusion point of ashes leading to several issues during fluidised-bed gasification, most notably fouling and slagging. By adding Ca-based additives or blending fuels with Ca/Si-rich feedstocks, the ash softening point was provably increased. However, account should be taken of the fact that Ca-based additives are considered to be inert substances that might have negative side-effects on relevant fuel properties, such as calorific value, ash content or abrasion behaviour. Thermodynamic equilibrium calculations pointed out that magnesium and potassium (originating from the fuel ash) seem to interact with mineral phases to form intermediates or mixtures when ilmenite was used as oxygen carrier. This may be a first indication of possible oxygen carrier poisoning.

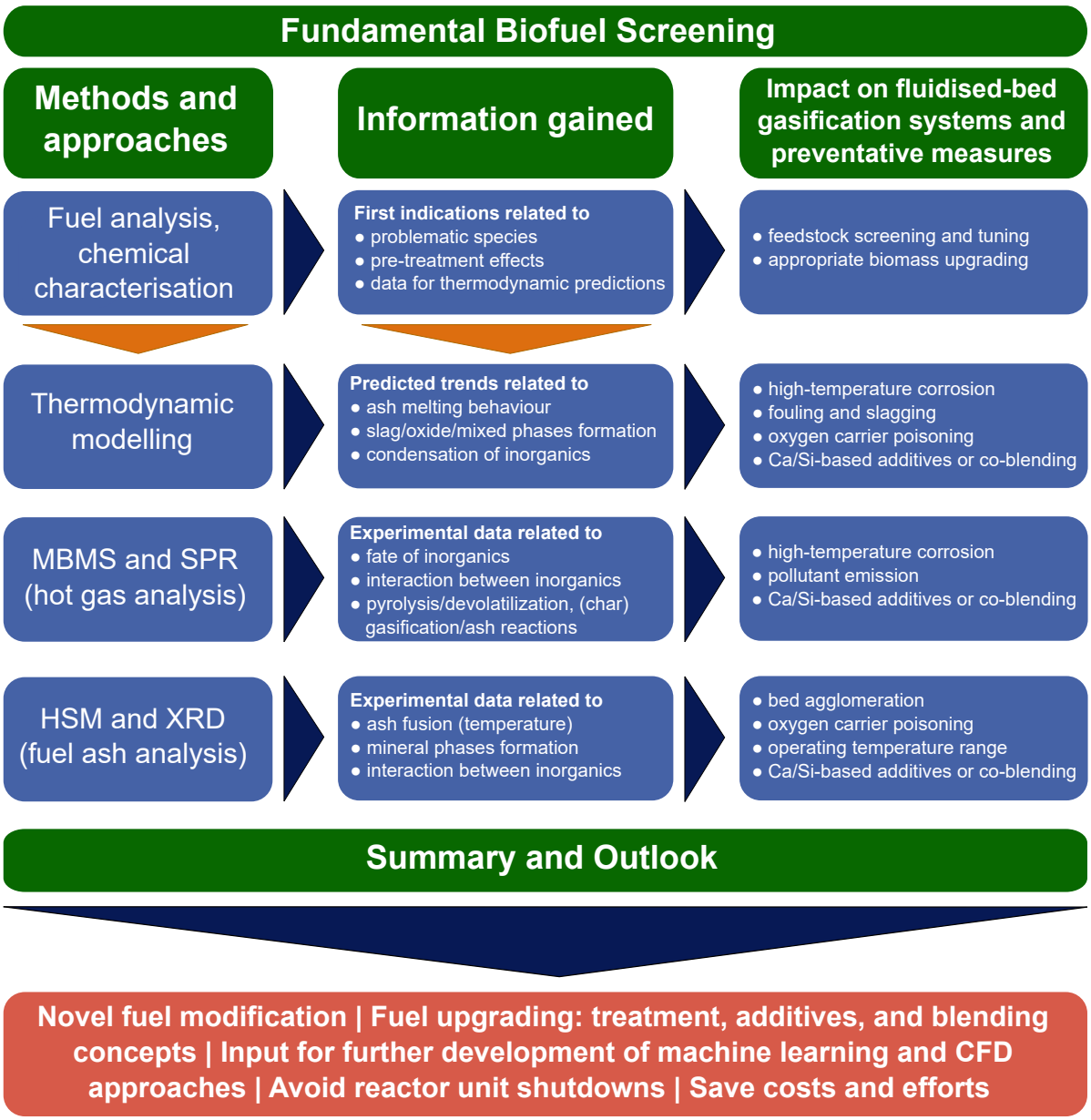

Figure 5.1: Schematic overview of novel fuel characterisation tools, outcomes, and impacts on fluidised-bed gasification and CLG systems. A proposed outlook completes the final conclusions and suggests approaches for further studies.

Besides the issues mentioned previously, nitrogen-based pollutant emissions should also be taken into account. The nitrogen content in the fuel might be a first indicator for NO_x emissions, which belong to the most critical gaseous emissions in thermal conversion of biomass [295, 296]. It was shown, among other things, that the nitrogen chemistry could be influenced by ash forming matter. E.g, the conversion of volatile nitrogen to

ammonia increased with increasing calcium content and decreasing potassium content in the fuel, which revealed a catalytic activity of both cations. The converse argument, then, is that biomass upgrading impacts indirectly on N-related pollutant emissions.

Generally, it can be concluded that both experimental methods and thermodynamic modelling calculations have shown similar trends. Nevertheless, the significance of the predictions were partially limited, which may be attributed to kinetic reasons and basically the non-equilibrium ("non-ideal") character of the experiments. It remains for future studies to design a representative model, which not only includes thermodynamics but also advanced kinetic aspects of ash-related issues during biomass gasification. In addition to thermochemical calculations and experimental investigations, numerical/predictive methods based on analyses of the ash composition as well as generated data from other recent studies should be considered in order to describe the fuel behaviour under gasification conditions reliably. The advantage lies in the low cost of materials and the fast generation of predictions. Developing significant strategies for modelling thermochemical conversion processes have the potential to maximise their productivity and performance. Machine learning methods, or more precisely, regression analyses may be employed to figure out ideal fuel compositions (in the sense of biomass upgrading) in order to estimate ash-related issues as well as H_2, CO, CO_2, CH_4, and HHV outputs for the gasification process. Due to a relatively varying inorganic composition of biomass in general (and the associated accumulation of data), machine learning approaches may make definitely sense and are highly recommended to be taken into account in further studies, as model complexity is a key consideration in machine learning. Reliable predictive model techniques such as artificial neural networks for biofuel quality would be of significant support to industrial operators. As has been shown within this thesis, there are several parameters, which might be considered as predictor or independent variables that a complex model needs to take into account in order to make accurate predictions. To the authors opinion, a new strategy is needed, and e.g. an organised collection of experimental and numerical predicted data stored and accessed electronically in the form of modern databases could be a useful first step. Given the fact that biomass-based fuels reveal inhomogeneous qualities, this would provide particular benefits, and facilitate the overview, the control of complexity and interactions of several factors during the thermochemical conversion.

Bibliography

[1] United Nations, *Paris Climate Agreement*, 2015, `https://unfccc.int/process-and-meetings/the-paris-agreement/the-paris-agreement` (accessed on 11/29/2022).

[2] N. Abas, A. Kalair and N. Khan, "Review of fossil fuels and future energy technologies", *Futures*, 2015, **69**, 31–49.

[3] D. Gielen, F. Boshell, D. Saygin, M. D. Bazilian, N. Wagner and R. Gorini, "The role of renewable energy in the global energy transformation", *Energy Strategy Reviews*, 2019, **24**, 38–50.

[4] M. Ram, D. Bogdanov, A. Aghahosseini, A. Gulagi, A. Oyewo, M. Child, U. Caldera, K. Sadovskaia, J. Farfan, L. Barbosa et al., "Global energy system based on 100% renewable energy–power, heat, transport and desalination sectors", *Study by Lappeenranta University of Technology and Energy Watch Group, Lappeenranta, Berlin*, 2019.

[5] T. Trainer, "Can renewables etc. solve the greenhouse problem? The negative case", *Energy Policy*, 2010, **38**, 4107–4114.

[6] T. L. Kelly-Yong, K. T. Lee, A. R. Mohamed and S. Bhatia, "Potential of hydrogen from oil palm biomass as a source of renewable energy worldwide", *Energy Policy*, 2007, **35**, 5692–5701.

[7] M. Ram and M. K. Mondal, in *Biofuels and Bioenergy*, ed. B. Gurunathan, R. Sahadevan and Z. A. Zakaria, Elsevier, 2022, pp. 253–276.

[8] M. Siedlecki, W. De Jong and A. H. Verkooijen, "Fluidized Bed Gasification as a Mature And Reliable Technology for the Production of Bio-Syngas and Applied in the Production of Liquid Transportation fuels—A review", *Energies*, 2011, **4**, 389–434.

[9] P. Dieringer, F. Marx, F. Alobaid, J. Ströhle and B. Epple, "Process Control Strategies in Chemical Looping Gasification—A Novel Process for the Production of Biofuels Allowing for Net Negative CO_2 Emissions", *Applied Sciences*, 2020, **10**, 4271.

[10] N. M. Nguyen, F. Alobaid, P. Dieringer and B. Epple, "Biomass-Based Chemical Looping Gasification: Overview and Recent Developments", *Applied Sciences*, 2021, **11**, 7069.

[11] Horizon 2020 project CLARA, *Chemical Looping Gasification for Sustainable Production of Biofuels*, `https://clara-h2020.eu/` (accessed on 11/29/2022).

[12] T. Zeng, A. Mlonka-Mędrala, V. Lenz and M. Nelles, "Evaluation of bottom ash slagging risk during combustion of herbaceous and woody biomass fuels in a small-scale boiler by principal component analysis", *Biomass Conversion and Biorefinery*, 2021, **11**, 1211–1229.

[13] A. Demirbas, "Demineralization of agricultural residues by water leaching", *Energy sources*, 2003, **25**, 679–687.

[14] D. Boström, A. Grimm, C. Boman, E. Björnbom and M. Ohman, "Influence of kaolin and calcite additives on ash transformations in small-scale combustion of oat", *Energy & Fuels*, 2009, **23**, 5184–5190.

[15] H. Kassman, J. Pettersson, B.-M. Steenari and L.-E. Åmand, "Two strategies to reduce gaseous KCl and chlorine in deposits during biomass combustion—injection of ammonium sulphate and co-combustion with peat", *Fuel Processing Technology*, 2013, **105**, 170–180.

[16] L. L. Baxter, T. R. Miles, T. R. Miles Jr, B. M. Jenkins, T. Milne, D. Dayton, R. W. Bryers and L. L. Oden, "The behavior of inorganic material in biomass-fired power boilers: field and laboratory experiences", *Fuel processing technology*, 1998, **54**, 47–78.

[17] L. Nikolaisen and P. Jensen, in *Biomass Combustion Science, Technology and Engineering*, ed. L. Rosendahl, Woodhead Publishing, 2013, pp. 36–57.

[18] G. W. Huber, S. Iborra and A. Corma, "Synthesis of transportation fuels from biomass: chemistry, catalysts, and engineering", *Chemical reviews*, 2006, **106**, 4044–4098.

[19] *Standard E1705, 1995 (2002) Standard technology relating to biotechnology ASTM international*, 1995, `https://www.astm.org/` (accessed on 08/25/2022).

[20] E. M. Rubin, "Genomics of cellulosic biofuels", *Nature*, 2008, **454**, 841–845.

[21] P. Pintana and N. Tippayawong, "Predicting ash deposit tendency in thermal utilization of biomass", *Engineering Journal*, 2016, **20**, 15–24.

[22] S. Channiwala and P. Parikh, "A unified correlation for estimating HHV of solid, liquid and gaseous fuels", *Fuel*, 2002, **81**, 1051–1063.

[23] A. Friedl, E. Padouvas, H. Rotter and K. Varmuza, "Prediction of heating values of biomass fuel from elemental composition", *Analytica chimica acta*, 2005, **544**, 191–198.

[24] K.-Y. Chiang, K.-L. Chien and C.-H. Lu, "Characterization and comparison of biomass produced from various sources: suggestions for selection of pretreatment technologies in biomass-to-energy", *Applied energy*, 2012, **100**, 164–171.

[25] W. O. Doherty, P. Mousavioun and C. M. Fellows, "Value-adding to cellulosic ethanol: Lignin polymers", *Industrial crops and products*, 2011, **33**, 259–276.

[26] T. Searchinger, R. Edwards, D. Mulligan, R. Heimlich and R. Plevin, "Do biofuel policies seek to cut emissions by cutting food?", *Science*, 2015, **347**, 1420–1422.

[27] J. Valentine, J. Clifton-Brown, A. Hastings, P. Robson, G. Allison and P. Smith, "Food vs. fuel: the use of land for lignocellulosic 'next generation' energy crops that minimize competition with primary food production", *Gcb Bioenergy*, 2012, **4**, 1–19.

[28] Z. Qin, Q. Zhuang, X. Zhu, X. Cai and X. Zhang, "Carbon consequences and agricultural implications of growing biofuel crops on marginal agricultural lands in China", *Environmental Science & Technology*, 2011, **45**, 10765–10772.

[29] F. H. Isikgor and C. R. Becer, "Lignocellulosic biomass: a sustainable platform for the production of bio-based chemicals and polymers", *Polymer Chemistry*, 2015, **6**, 4497–4559.

[30] H. V. Scheller and P. Ulvskov, "Hemicelluloses", *Annual review of plant biology*, 2010, **61**, 263–289.

[31] A. Barakat, H. de Vries and X. Rouau, "Dry fractionation process as an important step in current and future lignocellulose biorefineries: a review", *Bioresource technology*, 2013, **134**, 362–373.

[32] V. B. Agbor, N. Cicek, R. Sparling, A. Berlin and D. B. Levin, "Biomass pretreatment: fundamentals toward application", *Biotechnology advances*, 2011, **29**, 675–685.

[33] S. Moraïs, E. Morag, Y. Barak, D. Goldman, Y. Hadar, R. Lamed, Y. Shoham, D. B. Wilson and E. A. Bayer, "Deconstruction of lignocellulose into soluble sugars by native and designer cellulosomes", *mBio*, 2012, **3**, e00508–12.

[34] C.-H. Zhou, X. Xia, C.-X. Lin, D.-S. Tong and J. Beltramini, "Catalytic conversion of lignocellulosic biomass to fine chemicals and fuels", *Chemical Society Reviews*, 2011, **40**, 5588–5617.

[35] C. Somerville, H. Youngs, C. Taylor, S. C. Davis and S. P. Long, "Feedstocks for lignocellulosic biofuels", *science*, 2010, **329**, 790–792.

[36] E. Taarning, C. M. Osmundsen, X. Yang, B. Voss, S. I. Andersen and C. H. Christensen, "Zeolite-catalyzed biomass conversion to fuels and chemicals", *Energy & Environmental Science*, 2011, **4**, 793–804.

[37] A. Anukam, S. Mamphweli, P. Reddy, E. Meyer and O. Okoh, "Pre-processing of sugarcane bagasse for gasification in a downdraft biomass gasifier system: A comprehensive review", *Renewable and Sustainable Energy Reviews*, 2016, **66**, 775–801.

[38] B. Yang and C. E. Wyman, "Pretreatment: the key to unlocking low-cost cellulosic ethanol", *Biofuels, Bioproducts and Biorefining: Innovation for a sustainable economy*, 2008, **2**, 26–40.

[39] S. Barskov, M. Zappi, P. Buchireddy, S. Dufreche, J. Guillory, D. Gang, R. Hernandez, R. Bajpai, J. Baudier, R. Cooper et al., "Torrefaction of biomass: A review of production methods for biocoal from cultured and waste lignocellulosic feedstocks", *Renewable Energy*, 2019, **142**, 624–642.

[40] S. B. Saleh, J. P. Flensborg, T. K. Shoulaifar, Z. Sárossy, B. B. Hansen, H. Egsgaard, N. DeMartini, P. A. Jensen, P. Glarborg and K. Dam-Johansen, "Release of chlorine and sulfur during biomass torrefaction and pyrolysis", *Energy & Fuels*, 2014, **28**, 3738–3746.

[41] C. Yu, P. Thy, L. Wang, S. Anderson, J. VanderGheynst, S. Upadhyaya and B. M. Jenkins, "Influence of leaching pretreatment on fuel properties of biomass", *Fuel Processing Technology*, 2014, **128**, 43–53.

[42] S.-H. Gong, H.-S. Im, M. Um, H.-W. Lee and J.-W. Lee, "Enhancement of waste biomass fuel properties by sequential leaching and wet torrefaction", *Fuel*, 2019, **239**, 693–700.

[43] S. Zhang, Y. Su, D. Xu, S. Zhu, H. Zhang and X. Liu, "Effects of torrefaction and organic-acid leaching pretreatment on the pyrolysis behavior of rice husk", *Energy*, 2018, **149**, 804–813.

[44] V. Chaloupková, T. Ivanova, P. Hutla and M. Špunarová, "Ash melting behavior of rice straw and calcium additives", *Agriculture*, 2021, **11**, 1282.

[45] A. Zheng, Z. Zhao, S. Chang, Z. Huang, K. Zhao, G. Wei, F. He and H. Li, "Comparison of the effect of wet and dry torrefaction on chemical structure and pyrolysis behavior of corncobs", *Bioresource technology*, 2015, **176**, 15–22.

[46] J. G. Lynam, C. J. Coronella, W. Yan, M. T. Reza and V. R. Vasquez, "Acetic acid and lithium chloride effects on hydrothermal carbonization of lignocellulosic biomass", *Bioresource technology*, 2011, **102**, 6192–6199.

[47] R. Tu, E. Jiang, S. Yan, X. Xu and S. Rao, "The pelletization and combustion properties of torrefied Camellia shell via dry and hydrothermal torrefaction: a comparative evaluation", *Bioresource technology*, 2018, **264**, 78–89.

[48] H. Chen, X. Chen, Z. Qiao and H. Liu, "Release and transformation behavior of Cl during pyrolysis of torrefied rice straw", *Fuel*, 2016, **183**, 145–154.

[49] H. P. Nielsen, F. Frandsen, K. Dam-Johansen and L. Baxter, "The implications of chlorine-associated corrosion on the operation of biomass-fired boilers", *Progress in energy and combustion science*, 2000, **26**, 283–298.

[50] J. M. Johansen, J. G. Jakobsen, F. J. Frandsen and P. Glarborg, "Release of K, Cl, and S during pyrolysis and combustion of high-chlorine biomass", *Energy & Fuels*, 2011, **25**, 4961–4971.

[51] T. Bridgeman, J. Jones, I. Shield and P. Williams, "Torrefaction of reed canary grass, wheat straw and willow to enhance solid fuel qualities and combustion properties", *Fuel*, 2008, **87**, 844–856.

[52] H. Tukey Jr, "The leaching of substances from plants", *Annual review of plant physiology*, 1970, **21**, 305–324.

[53] B. Jenkins, R. Bakker and J. Wei, "On the properties of washed straw", *Biomass and bioenergy*, 1996, **10**, 177–200.

[54] T. Garbowski, "Changes in the physico-chemical parameters of water as a result of long-term contact with biomass, on the example of pine bark (Pinus sylvestris)", *Water, Air, & Soil Pollution*, 2019, **230**, 1–16.

[55] X. Liu and X. T. Bi, "Removal of inorganic constituents from pine barks and switchgrass", *Fuel processing technology*, 2011, **92**, 1273–1279.

[56] T. Wigley, A. C. Yip and S. Pang, "Pretreating biomass via demineralisation and torrefaction to improve the quality of crude pyrolysis oil", *Energy*, 2016, **109**, 481–494.

[57] K. Meesters, W. Elbersen, P. van der Hoogt and H. Hristov, *Biomass pre-treatment for bioenergy – Case study 5: Leaching as a biomass pre-treatment method for herbaceous biomass*, tech. rep., IEA Bioenergy, 2018.

[58] C. L. Williams, T. L. Westover, R. M. Emerson, J. S. Tumuluru and C. Li, "Sources of biomass feedstock variability and the potential impact on biofuels production", *BioEnergy Research*, 2016, **9**, 1–14.

[59] C. Li, J. E. Aston, J. A. Lacey, V. S. Thompson and D. N. Thompson, "Impact of feedstock quality and variation on biochemical and thermochemical conversion", *Renewable and Sustainable Energy Reviews*, 2016, **65**, 525–536.

[60] J. Hrbek, C. Oberndorfer, P. Zanzinger and C. Pfeifer, "Influence of $Ca(OH)_2$ on ash melting behaviour of woody biomass", *Carbon Resources Conversion*, 2021, **4**, 84–88.

[61] L. L. Baxter, T. R. Miles, T. Miles Jr, B. Jenkins, D. Dayton, T. Milne, R. Bryers and L. Oden, *Alkali deposits found in biomass boilers: The behavior of inorganic material in biomass-fired power boilers–Field and laboratory experiences. Volume 2*, tech. rep., National Renewable Energy Lab., Golden, CO (United States); Sandia National Laboratory, US Department of Energy, 1996.

[62] J. Werther, M. Saenger, E.-U. Hartge, T. Ogada and Z. Siagi, "Combustion of agricultural residues", *Progress in energy and combustion science*, 2000, **26**, 1–27.

[63] H. Vuthaluru and D. Zhang, "Remediation of ash problems in fluidised-bed combustors", *Fuel*, 2001, **80**, 583–598.

[64] M. F. Llorente, R. E. Cuadrado, J. M. Laplaza and J. C. García, "Combustion in bubbling fluidised bed with bed material of limestone to reduce the biomass ash agglomeration and sintering", *Fuel*, 2006, **85**, 2081–2092.

[65] L. J. Roberts, P. E. Mason, J. M. Jones, W. F. Gale, A. Williams, A. Hunt and J. Ashman, "The impact of aluminosilicate-based additives upon the sintering and melting behaviour of biomass ash", *Biomass and Bioenergy*, 2019, **127**, 105284.

[66] E. Lindström, M. Öhman, R. Backman and D. Boström, "Influence of sand contamination on slag formation during combustion of wood derived fuels", *Energy & Fuels*, 2008, **22**, 2216–2220.

[67] A. E. Ray, C. Li, V. S. Thompson, D. L. Daubaras, N. Nagle and D. S. Hartley, *Biomass blending and densification: impacts on feedstock supply and biochemical conversion performance*, tech. rep., Idaho National Lab.(INL), Idaho Falls, ID (United States), 2017.

[68] L. Ou, G. Luo, A. Ray, C. Li, H. Hu, S. Kelley and S. Park, "Understanding the impacts of biomass blending on the uncertainty of hydrolyzed sugar yield from a stochastic perspective", *ACS Sustainable Chemistry & Engineering*, 2018, **6**, 10851–10860.

[69] J. J. Jacobson, M. S. Roni, P. Lamers and K. G. Cafferty, *Biomass feedstock and conversion supply system design and analysis*, tech. rep., Idaho National Lab.(INL), Idaho Falls, ID (United States), 2014.

[70] A. Dutta, A. Sahir, E. Tan, D. Humbird, L. J. Snowden-Swan, P. A. Meyer, J. Ross, D. Sexton, R. Yap and J. Lukas, *Process design and economics for the conversion of lignocellulosic biomass to hydrocarbon fuels: Thermochemical research pathways with in situ and ex situ upgrading of fast pyrolysis vapors*, tech. rep., Pacific Northwest National Lab.(PNNL), Richland, WA (United States), 2015.

[71] S. Jones, P. Meyer, L. Snowden-Swan, A. Padmaperuma, E. Tan, A. Dutta, J. Jacobson and K. Cafferty, *Process design and economics for the conversion of lignocellulosic biomass to hydrocarbon fuels: fast pyrolysis and hydrotreating bio-oil pathway*, tech. rep., National Renewable Energy Lab.(NREL), Golden, CO (United States), 2013.

[72] P. K. Swain, L. Das and S. Naik, "Biomass to liquid: a prospective challenge to research and development in 21st century", *Renewable and Sustainable Energy Reviews*, 2011, **15**, 4917–4933.

[73] H. Goyal, D. Seal and R. Saxena, "Bio-fuels from thermochemical conversion of renewable resources: a review", *Renewable and sustainable energy reviews*, 2008, **12**, 504–517.

[74] W.-H. Chen, W.-Y. Cheng, K.-M. Lu and Y.-P. Huang, "An evaluation on improvement of pulverized biomass property for solid fuel through torrefaction", *Applied energy*, 2011, **88**, 3636–3644.

[75] S. S. Ail and S. Dasappa, "Biomass to liquid transportation fuel via Fischer Tropsch synthesis–Technology review and current scenario", *Renewable and sustainable energy reviews*, 2016, **58**, 267–286.

[76] J. G. Speight, *Gasification of unconventional feedstocks*, Gulf Professional Publishing, 2014.

[77] J. Phillips, "Different types of gasifiers and their integration with gas turbines", *The gas turbine handbook*, 2006, **1**.

[78] A. Molino, S. Chianese and D. Musmarra, "Biomass gasification technology: The state of the art overview", *Journal of Energy Chemistry*, 2016, **25**, 10–25.

[79] G. Evans and C. Smith, in *Comprehensive Renewable Energy*, ed. A. Sayigh, Elsevier, Oxford, 2012, pp. 155–204.

[80] A. K. Varma, R. Shankar and P. Mondal, "A review on pyrolysis of biomass and the impacts of operating conditions on product yield, quality, and upgradation", 2018, 227–259.

[81] S. Rönsch, J. Schneider, S. Matthischke, M. Schlüter, M. Götz, J. Lefebvre, P. Prabhakaran and S. Bajohr, "Review on methanation–From fundamentals to current projects", *Fuel*, 2016, **166**, 276–296.

[82] P. Breeze, *Coal-fired generation*, Academic Press, 2015, ch. 5 - Fluidized Bed Combustion and Coal Gasification, pp. 41–52.

[83] F. Scala, *Fluidized bed technologies for near-zero emission combustion and gasification*, Elsevier, 2013, ch. 13 - Economic evaluation of circulating fluidized bed combustion (CFBC) power generation plants, pp. 620–638.

[84] A. Pandey, C. Larroche, E. Gnansounou, S. K. Khanal, C.-G. Dussap and S. C. Ricke, *Biomass, biofuels, biochemicals: biofuels: alternative feedstocks and conversion processes for the production of liquid and gaseous biofuels*, Academic press, 2019.

[85] A. Kerester, "Gasification can help meet the world's growing demand for cleaner energy and products", *Cornerstone*, 2014, **2**, 5–10.

[86] D. Kunii and O. Levenspiel, *Fluidization engineering*, Butterworth-Heinemann, 1991.

[87] A. Pandey, T. Bhaskar, M. Stöcker and R. Sukumaran, *Recent advances in thermochemical conversion of biomass*, Elsevier, 2015.

[88] J. D. Morris, S. S. Daood, S. Chilton and W. Nimmo, "Mechanisms and mitigation of agglomeration during fluidized bed combustion of biomass: A review", *Fuel*, 2018, **230**, 452–473.

[89] H. Hofbauer, in *Energy from Organic Materials (Biomass)*, Springer, 2019, pp. 753–775.

[90] P. Basu, in *Biomass Gasification, Pyrolysis and Torrefaction (Second Edition)*, ed. P. Basu, Academic Press, Boston, Second Edition, 2013, pp. 249–313.

[91] M. Mayyas, R. K. Nekouei and V. Sahajwalla, "Valorization of lignin biomass as a carbon feedstock in steel industry: Iron oxide reduction, steel carburizing and slag foaming", *Journal of Cleaner Production*, 2019, **219**, 971–980.

[92] In *Electrochemistry and Corrosion Science*, ed. N. Perez, Springer US, Boston, MA, 2004, pp. 301–338.

[93] R. Elger, *High temperature corrosion in biomass-fired energy applications: Alloying effects and test environment comparisons (Ph.D. Thesis)*, KTH Royal Institute of Technology, 2016.

[94] H. J. Grabke, M. Spiegel and A. Zahs, "Role of alloying elements and carbides in the chlorine-induced corrosion of steels and alloys", *Materials Research*, 2004, **7**, 89–95.

[95] E. Björkman and B. Strömberg, "Release of chlorine from biomass at pyrolysis and gasification conditions", *Energy & Fuels*, 1997, **11**, 1026–1032.

[96] B. Gatternig, *Predicting agglomeration in biomass fired fluidized beds (Ph.D. Thesis)*, University of Erlangen-Nürnberg, 2015.

[97] A. Khan, W. de Jong, P. Jansens and H. Spliethoff, "Biomass combustion in fluidized bed boilers: Potential problems and remedies", *Fuel processing technology*, 2009, **90**, 21–50.

[98] J. Karl, *Decentralized power systems. Advanced technologies in a deregulated power market. 3. rev. and enl. ed.; Dezentrale Energiesysteme. Neue Technologien im liberalisierten Energiemarkt*, Oldenbourg Verlag, 2012.

[99] D. Vaughan, Chloride corrosion and its inhibition in refuse firing. Ash Deposits and Corrosion Due to Impurities in Combustion Gases, New York: Hemisphere Publishing Corporation, 1978, pp. 473–493.

[100] K. Kautz and J. Tichatschke, *Zusammenhänge zwischen Rauchgasverhältnissen, Kesselbelastung und Korrosionen in einer kommunalen Müllverbrennungsanlage*, VGB Kraftwerkstechnik, 1972, vol. 52, pp. 249–263.

[101] H. Latreche, S. Doublet and M. Schütze, "Development of corrosion assessment diagrams for high temperature chlorine corrosion. Part I: state of the art and development of the basis for a new extended approach", *Oxidation of metals*, 2009, **72**, 1–30.

[102] N. Sämann, *Einfluss von Oberflächenbehandlung und Legierungszusammensetzung auf die Hochtemperaturkorrosion von Chrom-Stählen (Ph.D. Thesis)*, TU Dortmund, 2002.

[103] M. Schmitt, *Investigations on high-temperature corrosion of commercial materials and model alloys in simulated waste and biomass combustion environments (Ph.D. Thesis)*, RWTH Aachen, 2013.

[104] C. C. Xu, B. Liao, S. Pang, L. Nazari, N. Mahmood, M. S. Tushar, A. Dutta and M. B. Ray, in *Comprehensive Energy Systems*, ed. I. Dincer, Elsevier, Oxford, 2018, pp. 770–794.

[105] M. Ottmann, *Verbrennung biogener Brennstoffe in stationären Wirbelschichtfeuerungen (Ph.D. Thesis)*, TU München, 2007.

[106] F. Zintl and B. Ljungdahl, *Alternativa bäddmaterial i FB/CFB-pannor*, tech. rep. 803, Termiska Processer (TPS), 2003.

[107] F. Kracek, N. Brown and G. Morey, "Equilibrium relations and factors influencing their determination in the system K_2SiO_3–SiO_2", *Journal of Physical Chemistry*, 1937, **41**, 1183–1193.

[108] L. Zhang, C. Schmetterer and P. J. Masset, "Thermodynamic description of the M_2O–SiO_2 (M = K, Na) systems", *Computational materials science*, 2013, **66**, 20–27.

[109] A. Hedayati, J. Falk, E. Borén, R. Lindgren, N. Skoglund, C. Boman and M. Öhman, "Ash Transformation during Fixed-Bed Combustion of Agricultural Biomass with a Focus on Potassium and Phosphorus", *Energy & Fuels*, 2022.

[110] E. Natarajan, M. Öhman, M. Gabra, A. Nordin, T. Liliedahl and A. Rao, "Experimental determination of bed agglomeration tendencies of some common agricultural residues in fluidized bed combustion and gasification", *Biomass and Bioenergy*, 1998, **15**, 163–169.

[111] V. Mettanant, P. Basu and J. Butler, "Agglomeration of biomass fired fluidized bed gasifier and combustor", *The Canadian Journal of Chemical Engineering*, 2009, **87**, 656–684.

[112] J. Van Caneghem, A. Brems, P. Lievens, C. Block, P. Billen, I. Vermeulen, R. Dewil, J. Baeyens and C. Vandecasteele, "Fluidized bed waste incinerators: Design, operational and environmental issues", *Progress in Energy and Combustion Science*, 2012, **38**, 551–582.

[113] M. Hupa, "Ash-related issues in fluidized-bed combustion of biomasses: recent research highlights", *Energy & Fuels*, 2012, **26**, 4–14.

[114] G. Morey, F. Kracek and N. Bowen, "The ternary system K_2O-CaO-SiO_2", *J. Glass. Technol*, 1930, **14**, 149–187.

[115] I.-H. Jung, S. A. Decterov and A. D. Pelton, "Critical thermodynamic evaluation and optimization of the CaO–MgO–SiO_2 system", *Journal of the European Ceramic Society*, 2005, **25**, 313–333.

[116] B.-M. Steenari and O. Lindqvist, "High-temperature reactions of straw ash and the anti-sintering additives kaolin and dolomite", *Biomass and bioenergy*, 1998, **14**, 67–76.

[117] M. Gyllenhammar, S. Herstad Svärd, K. Davidsson, L.-E. Åmand, B.-M. Steenari, N. Folkeson, J. Pettersson, J.-E. Svensson, A. Boss, L. Johansson and H. Kassman, *Measures for simultaneous minimization of alkali related operating problems, Phase 2; Åtgaerder för samtidig minimering av alkalirelaterade driftproblem, Etapp 2. Ramprogram*, tech. rep., 2007.

[118] J. Lachman, M. Baláš, M. Lisý, H. Lisá, P. Milčák and P. Elbl, "An overview of slagging and fouling indicators and their applicability to biomass fuels", *Fuel Processing Technology*, 2021, **217**, 106804.

[119] P. Teixeira, H. Lopes, I. Gulyurtlu, N. Lapa and P. Abelha, "Slagging and fouling during coal and biomass cofiring: chemical equilibrium model applied to FBC", *Energy & fuels*, 2014, **28**, 697–713.

[120] X. Yao, K. Xu, F. Yan and Y. Liang, "The influence of ashing temperature on ash fouling and slagging characteristics during combustion of biomass fuels", *BioResources*, 2017, **12**, 1593–1610.

[121] A. A. Tortosa-Masiá, F. Ahnert, H. Spliethoff, C. J. Loux and K. R. Hein, "Slagging and fouling in biomass co-combustion", *Thermal Science*, 2005, **9**, 85–98.

[122] U. Kleinhans, C. Wieland, F. J. Frandsen and H. Spliethoff, "Ash formation and deposition in coal and biomass fired combustion systems: Progress and challenges in the field of ash particle sticking and rebound behavior", *Progress in energy and combustion science*, 2018, **68**, 65–168.

[123] L. L. Baxter, "Ash deposition during biomass and coal combustion: a mechanistic approach", *Biomass and Bioenergy*, 1993, **4**, 85–102.

[124] U. Kleinhans, R. Rück, S. Schmid, T. Haselsteiner and H. Spliethoff, "Alkali Vapor Condensation on Heat Exchanging Surfaces: Laboratory-Scale Experiments and a Mechanistic CFD Modeling Approach", *Energy & fuels*, 2016, **30**, 9793–9800.

[125] A. Demirbas, "Potential applications of renewable energy sources, biomass combustion problems in boiler power systems and combustion related environmental issues", *Progress in energy and combustion science*, 2005, **31**, 171–192.

[126] G. Sorell, "The role of chlorine in high temperature corrosion in waste-to-energy plants", *Materials at high temperatures*, 1997, **14**, 207–220.

[127] M. Theis, B.-J. Skrifvars, M. Zevenhoven, M. Hupa and H. Tran, "Fouling tendency of ash resulting from burning mixtures of biofuels. Part 2: Deposit chemistry", *Fuel*, 2006, **85**, 1992–2001.

[128] T. R. Miles, T. R. Miles Jr, L. L. Baxter, R. W. Bryers, B. M. Jenkins and L. L. Oden, "Boiler deposits from firing biomass fuels", *Biomass and bioenergy*, 1996, **10**, 125–138.

[129] A. Garcia-Maraver and J. A. Pérez-Jiménez, *Biomass pelletization: standards and production*, Wit Press, 2015.

[130] D. J. Vega-Nieva, A. Garcia-Maraver and L. Ortiz, "Slagging and fouling risks derived from the combustion of solid biofuels", *WIT Transactions on State-of-the-art in Science and Engineering*, 2015, **85**, 137–147.

[131] S. Arvelakis, P. Vourliotis, E. Kakaras and E. Koukios, "Effect of leaching on the ash behavior of wheat straw and olive residue during fluidized bed combustion", *Biomass and Bioenergy*, 2001, **20**, 459–470.

[132] R. W. Bryers, "Fireside slagging, fouling, and high-temperature corrosion of heat-transfer surface due to impurities in steam-raising fuels", *Progress in energy and combustion science*, 1996, **22**, 29–120.

[133] M. Pronobis, "Evaluation of the influence of biomass co-combustion on boiler furnace slagging by means of fusibility correlations", *Biomass and bioenergy*, 2005, **28**, 375–383.

[134] I. Obernberger, T. Brunner and G. Bärnthaler, "Chemical properties of solid biofuels—significance and impact", *Biomass and bioenergy*, 2006, **30**, 973–982.

[135] P. Glarborg, J. A. Miller, B. Ruscic and S. J. Klippenstein, "Modeling nitrogen chemistry in combustion", *Progress in energy and combustion science*, 2018, **67**, 31–68.

[136] H. Chen, Y. Si, Y. Chen, H. Yang, D. Chen and W. Chen, "NO_x precursors from biomass pyrolysis: Distribution of amino acids in biomass and Tar-N during devolatilization using model compounds", *Fuel*, 2017, **187**, 367–375.

[137] V. Wilk and H. Hofbauer, "Conversion of fuel nitrogen in a dual fluidized bed steam gasifier", *Fuel*, 2013, **106**, 793–801.

[138] W. Ma, C. Ma, X. Liu, T. Gu, S. K. Thengane, A. Bourtsalas and G. Chen, "Nox formation in fixed-bed biomass combustion: Chemistry and modeling", *Fuel*, 2021, **290**, 119694.

[139] P. Grennfelt, A. Engleryd, M. Forsius, Ø. Hov, H. Rodhe and E. Cowling, "Acid rain and air pollution: 50 years of progress in environmental science and policy", *Ambio*, 2020, **49**, 849–864.

[140] P. Glarborg, A. Jensen and J. E. Johnsson, "Fuel nitrogen conversion in solid fuel fired systems", *Progress in energy and combustion science*, 2003, **29**, 89–113.

[141] A. Lucassen, N. Labbe, P. R. Westmoreland and K. Kohse-Höinghaus, "Combustion chemistry and fuel-nitrogen conversion in a laminar premixed flame of morpholine as a model biofuel", *Combustion and flame*, 2011, **158**, 1647–1666.

[142] I. Vermeulen, C. Block and C. Vandecasteele, "Estimation of fuel-nitrogen oxide emissions from the element composition of the solid or waste fuel", *Fuel*, 2012, **94**, 75–80.

[143] S. Yuan, Z.-j. Zhou, J. Li, X.-l. Chen and F.-c. Wang, "HCN and NH_3 released from biomass and soybean cake under rapid pyrolysis", *Energy & fuels*, 2010, **24**, 6166–6171.

[144] D. Schmid, O. Karlström and P. Yrjas, "Release of NH_3, HCN and NO during devolatilization and combustion of washed and torrefied biomass", *Fuel*, 2020, **280**, 118583.

[145] A. Anca-Couce, P. Sommersacher, N. Evic, R. Mehrabian and R. Scharler, "Experiments and modelling of NO_x precursors release (NH_3 and HCN) in fixed-bed biomass combustion conditions", *Fuel*, 2018, **222**, 529–537.

[146] J. Leppälahti, "Formation of NH_3 and HCN in slow-heating-rate inert pyrolysis of peat, coal and bark", *Fuel*, 1995, **74**, 1363–1368.

[147] H. Liu, L. Yi, H. Hu, K. Xu, Q. Zhang, G. Lu and H. Yao, "Emission control of NO_x precursors during sewage sludge pyrolysis using an integrated pretreatment of Fenton peroxidation and CaO conditioning", *Fuel*, 2017, **195**, 208–216.

[148] F.-J. Tian, J. Yu, L. J. McKenzie, J.-i. Hayashi and C.-Z. Li, "Conversion of fuel-N into HCN and NH_3 during the pyrolysis and gasification in steam: a comparative study of coal and biomass", *Energy & fuels*, 2007, **21**, 517–521.

[149] M. R. Mladenović, D. V. Dakić, S. Nemoda, M. Paprika, M. S. Komatina, B. Repić and A. Erić, "The combustion of biomass-the impact of its types and combustion technologies on the emission of nitrogen oxide", *Hemijska industrija*, 2016, **70**, 287–298.

[150] S. Koger and H. Bockhorn, "NO_x formation from ammonia, hydrogen cyanide, pyrrole, and caprolactam under incinerator conditions", *Proceedings of the Combustion Institute*, 2005, **30**, 1201–1209.

[151] E. C. Zabetta, M. Hupa and K. Saviharju, "Reducing NO_x emissions using fuel staging, air staging, and selective noncatalytic reduction in synergy", *Industrial & engineering chemistry research*, 2005, **44**, 4552–4561.

[152] M. U. Alzueta, R. Bilbao, A. Millera, P. Glarborg, M. Østberg and K. Dam-Johansen, "Modeling low-temperature gas reburning. NO_x reduction potential and effects of mixing", *Energy & Fuels*, 1998, **12**, 329–338.

[153] B. Ulusoy, H. Wu, W. Lin, O. Karlström, S. Li, W. Song, P. Glarborg and K. Dam-Johansen, "Reactivity of sewage sludge, RDF, and straw chars towards NO", *Fuel*, 2019, **236**, 297–305.

[154] Q. Ren and C. Zhao, "NO_x and N_2O precursors (NH_3 and HCN) from biomass pyrolysis: interaction between amino acid and mineral matter", *Applied energy*, 2013, **112**, 170–174.

[155] J. Zhou, P. Gao, C. Dong and Y. Yang, "Effect of temperature and mineral matter on the formation of NO_x precursors during fast pyrolysis of 2, 5-diketopiperazine", *Energies*, 2018, **11**, 629.

[156] L. Yi, H. Liu, G. Lu, Q. Zhang, J. Wang, H. Hu and H. Yao, "Effect of mixed Fe/Ca additives on nitrogen transformation during protein and amino acid pyrolysis", *Energy & Fuels*, 2017, **31**, 9484–9490.

[157] X. Ren, R. Sun, X. Meng, N. Vorobiev, M. Schiemann and Y. A. Levendis, "Carbon, sulfur and nitrogen oxide emissions from combustion of pulverized raw and torrefied biomass", *Fuel*, 2017, **188**, 310–323.

[158] M. Zevenhoven, P. Yrjas and M. Hupa, "Ash-Forming Matter and Ash-Related Problems", *Handbook of Combustion: Online*, 2010, 493–531.

[159] M. Zevenhoven, P. Yrjas, B.-J. Skrifvars and M. Hupa, "Characterization of ash-forming matter in various solid fuels by selective leaching and its implications for fluidized-bed combustion", *Energy & Fuels*, 2012, **26**, 6366–6386.

[160] C. Linderholm and A. Lyngfelt, in *Calcium and Chemical Looping Technology for Power Generation and Carbon Dioxide (CO_2) Capture*, ed. P. Fennell and B. Anthony, Woodhead Publishing, 2015, pp. 299–326.

[161] Y. De Vos, M. Jacobs, P. Van Der Voort, I. Van Driessche, F. Snijkers and A. Verberckmoes, "Development of stable oxygen carrier materials for chemical looping processes—A review", *Catalysts*, 2020, **10**, 926.

[162] J. Adánez, F. Garcá-Labiano, P. Gayán, F. Luis, A. Abad, C. Dueso and C. R. Forero, "Effect of gas impurities on the behavior of Ni-based oxygen carriers on chemical-looping combustion", *Energy Procedia*, 2009, **1**, 11–18.

[163] P. Moldenhauer, M. Rydén, T. Mattisson, A. Jamal and A. Lyngfelt, "Chemical-looping combustion with heavy liquid fuels in a 10 kW pilot plant", *Fuel Processing Technology*, 2017, **156**, 124–137.

[164] J. Adánez and A. Abad, "Chemical-looping combustion: Status and research needs", *Proceedings of the Combustion Institute*, 2019, **37**, 4303–4317.

[165] F. García-Labiano, L. de Diego, P. Gayán, A. Abad, A. Cabello, J. Adánez and G. Sprachmann, "Energy exploitation of acid gas with high H_2S content by means of a chemical looping combustion system", *Applied energy*, 2014, **136**, 242–249.

[166] J. Dai and K. J. Whitty, "Impact of fuel-derived chlorine on CuO-based oxygen carriers for chemical looping with oxygen uncoupling", *Fuel*, 2020, **263**, 116780.

[167] M. Zevenhoven, C. Sevonius, P. Salminen, D. Lindberg, A. Brink, P. Yrjas and L. Hupa, "Defluidization of the oxygen carrier ilmenite – Laboratory experiments with potassium salts", *Energy*, 2018, **148**, 930–940.

[168] F. Störner, F. Hildor, H. Leion, M. Zevenhoven, L. Hupa and M. Ryden, "Potassium Ash Interactions with Oxygen Carriers Steel Converter Slag and Iron Mill Scale in Chemical-Looping Combustion of Biomass—Experimental Evaluation Using Model Compounds", *Energy & Fuels*, 2020, **34**, 2304–2314.

[169] P. Piotrowska, A. Grimm, N. Skoglund, C. Boman, M. Öhman, M. Zevenhoven, D. Boström and M. Hupa, "Fluidized-bed combustion of mixtures of rapeseed cake and bark: the resulting bed agglomeration characteristics", *Energy & fuels*, 2012, **26**, 2028–2037.

[170] J. Bao, Z. Li and N. Cai, "Interaction between iron-based oxygen carrier and four coal ashes during chemical looping combustion", *Applied energy*, 2014, **115**, 549–558.

[171] M. M. Azis, H. Leion, E. Jerndal, B.-M. Steenari, T. Mattisson and A. Lyngfelt, "The Effect of Bituminous and Lignite Ash on the Performance of Ilmenite as Oxygen Carrier in Chemical-Looping Combustion", *Chemical Engineering & Technology*, 2013, **36**, 1460–1468.

[172] A. Mlonka-Mędrala, A. Magdziarz, M. Gajek, Nowińska and W. Nowak, "Alkali metals association in biomass and their impact on ash melting behaviour", *Fuel*, 2020, **261**, 116421.

[173] D. Yilmaz and H. Leion, "Interaction of Iron Oxygen Carriers and Alkaline Salts Present in Biomass-Derived Ash", *Energy & Fuels*, 2020, **34**, 11143–11153.

[174] A. Di Giuliano, I. Funcia, R. Pérez-Vega, J. Gil and K. Gallucci, "Novel application of pretreatment and diagnostic method using dynamic pressure fluctuations to resolve and detect issues related to biogenic residue ash in chemical looping gasification", *Processes*, 2020, **8**, 1137.

[175] F. Hildor, H. Leion, C. J. Linderholm and T. Mattisson, "Steel converter slag as an oxygen carrier for chemical-looping gasification", *Fuel Processing Technology*, 2020, **210**, 106576.

[176] F. Störner, F. Lind and M. Rydén, "Oxygen Carrier Aided Combustion in Fluidized Bed Boilers in Sweden—Review and Future Outlook with Respect to Affordable Bed Materials", *Applied Sciences*, 2021, **11**, 7935.

[177] A. Kumar, D. D. Jones and M. A. Hanna, "Thermochemical biomass gasification: a review of the current status of the technology", *Energies*, 2009, **2**, 556–581.

[178] E. Lemmon, "Vapor pressure and other saturation properties of water", *CRC Handbook of Chemistry and Physics*, 2009, **90**.

[179] H. Oleschko, *Freisetzung von Alkalien und Halogeniden bei der Kohleverbrennung (Ph.D. Thesis)*, RWTH Aachen, 2007.

[180] R. Campargue, "High intensity supersonic molecular beam apparatus", *Review of Scientific Instruments*, 1964, **35**, 111–112.

[181] T. A. Miller, "Chemistry and chemical intermediates in supersonic free jet expansions", *Science*, 1984, **223**, 545–553.

[182] R. Horn, K. Ihmann, J. Ihmann, F. C. Jentoft, M. Geske, A. Taha, K. Pelzer and R. Schlögl, "Molecular beam mass spectrometer equipped with a catalytic wall reactor for in situ studies in high temperature catalysis research", *Review of scientific instruments*, 2006, **77**, 054102.

[183] D. R. Miller, *Atomic and Molecular Beam Methods*, edited by G. Scoles (Oxford University Press, New York, 1998), vol. 1, chap. 2.

[184] J. B. Fenn, "Mass spectrometric implications of high-pressure ion sources", *International Journal of Mass Spectrometry*, 2000, **200**, 459–478.

[185] M. Bläsing, *Release of inorganic trace elements from high-temperature gasification of coal (Ph.D Thesis)*, RWTH Aachen, 2012.

[186] D. Porbatzki, *Freisetzung anorganischer Spezies bei der thermochemischen Umwandlung biogener Festbrennstoffe (Ph.D. Thesis)*, RWTH Aachen, 2008.

[187] O. Karlström, H. Wu and P. Glarborg, "Influence of H_2O on NO formation during char oxidation of biomass", *Fuel*, 2019, **235**, 1260–1265.

[188] O. Karlström, M. Perander, N. DeMartini, A. Brink and M. Hupa, "Role of ash on the NO formation during char oxidation of biomass", *Fuel*, 2017, **190**, 274–280.

[189] O. Karlström and L. Hupa, "Energy conversion of biomass char: Oxidation rates in mixtures of $O_2/CO_2/H_2O$", *Energy*, 2019, **181**, 615–624.

[190] J. P. Schupsky, *Crystallisation of oxidic gasifier slags (Ph.D. Thesis)*, RWTH Aachen, 2020.

[191] C. H. Pang, B. Hewakandamby, T. Wu and E. Lester, "An automated ash fusion test for characterisation of the behaviour of ashes from biomass and coal at elevated temperatures", *Fuel*, 2013, **103**, 454–466.

[192] M. Dohrn, *Ansatzverhalten von Aschen in Kohledampferzeugern bei brennstoff- und lastflexiblem Betrieb (Ph.D. Thesis)*, RWTH Aachen, 2018.

[193] M. Dohrn and M. Müller, "Influence of Load Changes on the Deposit Behavior during Combustion of Five Different Hard Coals", *Energy & Fuels*, 2018, **32**, 3985–3994.

[194] Y. Jiang, K. Ideta, J. Kim, J. Miyawaki, D.-H. Jung, S.-H. Yoon and I. Mochida, "The crystalline and microstructural transformations of two coal ashes and their quenched slags with similar chemical compositions during heat treatment", *Journal of Industrial and Engineering Chemistry*, 2015, **22**, 110–119.

[195] S. Seebold, M. Eberhard, G. Wu, E. Yazhenskikh, D. Sergeev, T. Kolb and M. Müller, "Thermophysical and chemical properties of bioliq slags", *Fuel*, 2017, **197**, 596–604.

[196] C. R. Friedrich, "100 Jahre Röntgenstrahlen Erster Nobelpreis für Physik", *Materialwissenschaft und Werkstofftechnik*, 1995, **26**, 598–607.

[197] C. Klein, B. Dutrow and J. D. Dana, *The 23rd edition of the manual of mineral science: (after James D. Dana)*, Hoboken, N.J. : J. Wiley, 2007.

[198] W. D. Nesse, *Introduction to optical mineralogy*, Oxford University Press, 2009.

[199] B. Fultz and J. M. Howe, *Transmission electron microscopy and diffractometry of materials*, Springer Science & Business Media, 2012.

[200] H. M. Rietveld, "A profile refinement method for nuclear and magnetic structures", *Journal of applied Crystallography*, 1969, **2**, 65–71.

[201] C. Rossi, L. Cardozo-Filho and R. Guirardello, "Gibbs free energy minimization for the calculation of chemical and phase equilibrium using linear programming", *Fluid Phase Equilibria*, 2009, **278**, 117–128.

[202] C. W. Bale, E. Bélisle, P. Chartrand, S. Decterov, G. Eriksson, A. Gheribi, K. Hack, I.-H. Jung, Y.-B. Kang, J. Melançon et al., "FactSage thermochemical software and databases, 2010–2016", *Calphad*, 2016, **54**, 35–53.

[203] N. Saunders and A. P. Miodownik, *CALPHAD (calculation of phase diagrams): a comprehensive guide*, Elsevier, 1998.

[204] M. Rieß, *Freisetzung und Einbindung von Schwermetallen bei der Hochtemperaturvergasung (Ph.D. Thesis)*, RWTH Aachen, 2010.

[205] E. Yazhenskikh, T. Jantzen, K. Hack and M. Müller, "A new multipurpose thermodynamic database for oxide systems", *Rasplavy/Melts*, 2019, 116–124.

[206] K. Hack, T. Jantzen, M. Müller, E. Yazhenskikh and G. Wu, Proceedings of the 5th International Congress on the Science and Technology of Steelmaking, Dresden, Germany, 2012, vol. 20.

[207] J. N. Knudsen, P. A. Jensen, W. Lin, F. J. Frandsen and K. Dam-Johansen, "Sulfur transformations during thermal conversion of herbaceous biomass", *Energy & Fuels*, 2004, **18**, 810–819.

[208] T. Keipi, H. Tolvanen, L. Kokko and R. Raiko, "The effect of torrefaction on the chlorine content and heating value of eight woody biomass samples", *Biomass and Bioenergy*, 2014, **66**, 232–239.

[209] B. Shemwell, Y. A. Levendis and G. A. Simons, "Laboratory study on the high-temperature capture of HCl gas by dry-injection of calcium-based sorbents", *Chemosphere*, 2001, **42**, 785–796.

[210] M. Bläsing, M. Zini and M. Muüller, "Influence of feedstock on the release of potassium, sodium, chlorine, sulfur, and phosphorus species during gasification of wood and biomass shells", *Energy & fuels*, 2013, **27**, 1439–1445.

[211] G. Toscano and F. Corinaldesi, "Ash fusibility characteristics of some biomass feedstocks and examination of the effects of inorganic additives", *Journal of Agricultural Engineering*, 2010, **41**, 13–19.

[212] S. V. Vassilev, D. Baxter, L. K. Andersen, C. G. Vassileva and T. J. Morgan, "An overview of the organic and inorganic phase composition of biomass", *Fuel*, 2012, **94**, 1–33.

[213] C. R. Ward, in *Impact of mineral impurities in solid fuel combustion*, Springer, 2002, pp. 23–32.

[214] M. S. Tiainen, J. S. Ryynänen, J. T. Rantala, H. T. Patrikainen and R. S. Laitinen, in *Impact of Mineral Impurities in Solid Fuel Combustion*, Springer, 2002, pp. 217–224.

[215] B.-M. Steenari, A. Lundberg, H. Pettersson, M. Wilewska-Bien and D. Andersson, "Investigation of ash sintering during combustion of agricultural residues and the effect of additives", *Energy & Fuels*, 2009, **23**, 5655–5662.

[216] C. Gilbe, M. Öhman, E. Lindström, D. Boström, R. Backman, R. Samuelsson and J. Burvall, "Slagging characteristics during residential combustion of biomass pellets", *Energy & Fuels*, 2008, **22**, 3536–3543.

[217] P. E. Mason, L. I. Darvell, J. M. Jones and A. Williams, "Observations on the release of gas-phase potassium during the combustion of single particles of biomass", *Fuel*, 2016, **182**, 110–117.

[218] D. Boström, N. Skoglund, A. Grimm, C. Boman, M. Ohman, M. Brostrom and R. Backman, "Ash transformation chemistry during combustion of biomass", *Energy & Fuels*, 2012, **26**, 85–93.

[219] A. Hedayati, R. Lindgren, N. Skoglund, C. Boman, N. Kienzl and M. Öhman, "Ash transformation during single-pellet combustion of agricultural biomass with a focus on potassium and phosphorus", *Energy & Fuels*, 2021, **35**, 1449–1464.

[220] J. Yang, Z. Feng, L. Ni, Q. Gao, Y. He, Y. Hou and Z. Liu, "Thermal Characteristics of Ash from Bamboo and Masson Pine Blends: Influence of Mixing Ratio and Heating Rate", *ACS Omega*, 2021, **6**, 7008–7014.

[221] X. Jin, J. Ye, L. Deng and D. Che, "Condensation behaviors of potassium during biomass combustion", *Energy & Fuels*, 2017, **31**, 2951–2958.

[222] K.-M. Hansson, J. Samuelsson, C. Tullin and L.-E. Åmand, "Formation of HNCO, HCN, and NH_3 from the pyrolysis of bark and nitrogen-containing model compounds", *Combustion and Flame*, 2004, **137**, 265–277.

[223] H. Risnes, J. Fjellerup, U. Henriksen, A. Moilanen, P. Norby, K. Papadakis, D. Posselt and L. Sørensen, "Calcium addition in straw gasification", *Fuel*, 2003, **82**, 641–651.

[224] M. T. Alam, B. Dai, X. Wu, A. Hoadley and L. Zhang, "A critical review of ash slagging mechanisms and viscosity measurement for low-rank coal and bio-slags", *Frontiers in Energy*, 2021, **15**, 46–67.

[225] N. Bao, X. Feng, X. Lu and Z. Yang, "Study on the formation and growth of potassium titanate whiskers", *Journal of materials science*, 2002, **37**, 3035–3043.

[226] C. Pettersson, J. Pettersson, H. Asteman, J.-E. Svensson and L.-G. Johansson, "KCl-induced high temperature corrosion of the austenitic Fe–Cr–Ni alloys 304L and Sanicro 28 at 600°C", *Corrosion Science*, 2006, **48**, 1368–1378.

[227] V. Manovic, B. Grubor, B. Repić, M. R. Mladenović and M. P. Jovanović, "Sulfur release during combustion of Serbian coals", *Fresenius Environmental Bulletin*, 2003, **12**, 1348–1353.

[228] K. Wieczorek-Ciurowa, "Physico-chemistry of the limestone sulphation process", *Journal of thermal analysis and calorimetry*, 1998, **54**, 85–91.

[229] İ. Atilgan, "Investigation of the effect of particle size of limestone added to lignite on emission behaviour in a fluidized bed combustion system", *Gazi University Journal of Science*, 2004, **17**, 89–101.

[230] N. Ilten and Ü. Sungur, "Removal of sulphur during combustion of coal by using lime", *Parlar Scientific Publications (PSP)*, 2009.

[231] S. V. Pisupati and S. Bhalla, "Influence of Calcium Content of Biomass-Based Materials on Simultaneous NO_x and SO_2 Reduction", *Environmental science & technology*, 2008, **42**, 2509–2514.

[232] L. Wang, G. Skjevrak, J. E. Hustad and Ø. Skreiberg, "Investigation of biomass ash sintering characteristics and the effect of additives", *Energy & Fuels*, 2014, **28**, 208–218.

[233] L.-E. Åmand, B. Leckner, D. Eskilsson and C. Tullin, "Deposits on heat transfer tubes during co-combustion of biofuels and sewage sludge", *Fuel*, 2006, **85**, 1313–1322.

[234] A. Pettersson, M. Zevenhoven, B.-M. Steenari and L.-E. Åmand, "Application of chemical fractionation methods for characterisation of biofuels, waste derived fuels and CFB co-combustion fly ashes", *Fuel*, 2008, **87**, 3183–3193.

[235] L. Wang, J. E. Hustad, Ø. Skreiberg, G. Skjevrak and M. Grønli, "A critical review on additives to reduce ash related operation problems in biomass combustion applications", *Energy Procedia*, 2012, **20**, 20–29.

[236] Y. Shao, J. Wang, F. Preto, J. Zhu and C. Xu, "Ash deposition in biomass combustion or co-firing for power/heat generation", *Energies*, 2012, **5**, 5171–5189.

[237] S. Fournel, J. H. Palacios, S. Godbout and M. Heitz, "Effect of additives and fuel blending on emissions and ash-related problems from small-scale combustion of reed canary grass", *Agriculture*, 2015, **5**, 561–576.

[238] P. Wang, N. Means, D. Shekhawat, D. Berry and M. Massoudi, "Chemical-looping combustion and gasification of coals and oxygen carrier development: a brief review", *Energies*, 2015, **8**, 10605–10635.

[239] S. Ren, H. Lei, L. Wang, Q. Bu, S. Chen and J. Wu, "Thermal behaviour and kinetic study for woody biomass torrefaction and torrefied biomass pyrolysis by TGA", *Biosystems engineering*, 2013, **116**, 420–426.

[240] R. B. Bates and A. F. Ghoniem, "Biomass torrefaction: Modeling of reaction thermochemistry", *Bioresource technology*, 2013, **134**, 331–340.

[241] L. Shang, J. Ahrenfeldt, J. K. Holm, S. Barsberg, R.-z. Zhang, Y.-h. Luo, H. Egsgaard and U. B. Henriksen, "Intrinsic kinetics and devolatilization of wheat straw during torrefaction", *Journal of Analytical and Applied Pyrolysis*, 2013, **100**, 145–152.

[242] J. N. Knudsen, P. A. Jensen and K. Dam-Johansen, "Transformation and release to the gas phase of Cl, K, and S during combustion of annual biomass", *Energy & Fuels*, 2004, **18**, 1385–1399.

[243] A. Novaković, S. C. van Lith, F. J. Frandsen, P. A. Jensen and L. B. Holgersen, "Release of potassium from the systems K–Ca–Si and K–Ca–P", *Energy & Fuels*, 2009, **23**, 3423–3428.

[244] M. Müller, K.-J. Wolf, A. Smeda and K. Hilpert, "Release of K, Cl, and S species during co-combustion of coal and straw", *Energy & fuels*, 2006, **20**, 1444–1449.

[245] B. Sander, N. Henriksen, O. Larsen, A. Skriver, C. Ramsgaard-Nielsen, J. N. Jensen, K. Stærkind, H. Livbjerg, M. Thellefsen, K. Dam-Johansen et al., 1st World Conference and Exhibition on Biomass for Energy and Industry, 2000.

[246] P. A. Jensen, F. Frandsen, K. Dam-Johansen and B. Sander, "Experimental investigation of the transformation and release to gas phase of potassium and chlorine during straw pyrolysis", *Energy & fuels*, 2000, **14**, 1280–1285.

[247] P. Sommersacher, T. Brunner and I. Obernberger, "Fuel indexes: a novel method for the evaluation of relevant combustion properties of new biomass fuels", *Energy & Fuels*, 2012, **26**, 380–390.

[248] J. Konttinen, S. Kallio, M. Hupa and F. Winter, "NO formation tendency characterization for solid fuels in fluidized beds", *Fuel*, 2013, **108**, 238–246.

[249] K. M. Broer and R. C. Brown, "The role of char and tar in determining the gas-phase partitioning of nitrogen during biomass gasification", *Applied Energy*, 2015, **158**, 474–483.

[250] P. Abelha, C. M. Vilela, P. Nanou, M. Carbo, A. Janssen and S. Leiser, "Combustion improvements of upgraded biomass by washing and torrefaction", *Fuel*, 2019, **253**, 1018–1033.

[251] Q. Ma, L. Han and G. Huang, "Evaluation of different water-washing treatments effects on wheat straw combustion properties", *Bioresource technology*, 2017, **245**, 1075–1083.

[252] C. Lupiáñez, L. I. Díez and L. M. Romeo, "NO emissions from anthracite oxy-firing in a fluidized-bed combustor: effect of the temperature, limestone, and O_2", *Energy & fuels*, 2013, **27**, 7619–7627.

[253] T. Shimizu, Y. Tachiyama, A. Kuroda and M. Inagaki, "Effect of SO_2 removal by limestone on NO_x and N_2O emissions from a bubbling fluidized-bed combustor", *Fuel*, 1992, **71**, 841–844.

[254] X. Liu, Z. Luo, X. Yang, G. Xie, Y. Yu and C. Yu, "Effect of limestone addition on no emission during petroleum coke combustion in CFBB", *Fuel*, 2020, **270**, 117475.

[255] T. Li, Ø. Skreiberg, T. Løvås and P. Glarborg, "Skeletal mechanisms for prediction of NO_x emission in solid fuel combustion", *Fuel*, 2019, **254**, 115569.

[256] P. G. Kristensen, P. Glarborg and K. Dam-Johansen, "Nitrogen chemistry during burnout in fuel-staged combustion", *Combustion and Flame*, 1996, **107**, 211–222.

[257] F. Winter, C. Wartha and H. Hofbauer, "NO and N_2O formation during the combustion of wood, straw, malt waste and peat", *Bioresource technology*, 1999, **70**, 39–49.

[258] F. Pereira, J. Beer, B. Gibbs and A. Hedley, Symposium (International) on Combustion, 1975, vol. 15, pp. 1149–1156.

[259] Z. Liu, Z. Feng, H. Xiang, J. Yang and J. Zhang, "The ash fusion characteristics of bamboo and coal co-firing process", *Journal of Thermal Analysis and Calorimetry*, 2021, **146**, 461–468.

[260] A. Magdziarz, M. Gajek, D. Nowak-Woźny and M. Wilk, "Mineral phase transformation of biomass ashes – Experimental and thermochemical calculations", *Renewable Energy*, 2018, **128**, 446–459.

[261] S. Link, P. Yrjas, D. Lindberg and A. Trikkel, "Characterization of Ash Melting of Reed and Wheat Straw Blend", *ACS Omega*, 2022, **7**, 2137–2146.

[262] I. Carević, N. Štirmer, M. Serdar and N. Ukrainczyk, "Effect of wood biomass ash storage on the properties of cement composites", *Materials*, 2021, **14**, 1632.

[263] R. H. Ibrahim, L. I. Darvell, J. M. Jones and A. Williams, "Physicochemical characterisation of torrefied biomass", *Journal of Analytical and Applied Pyrolysis*, 2013, **103**, 21–30.

[264] I. Obernberger, *Aschen aus Biomassefeuerungen-Zusammensetzung und Verwertung*, Inst. für Verfahrenstechnik, Techn. Univ. Graz, 1997.

[265] M. Aho and E. Ferrer, "Importance of coal ash composition in protecting the boiler against chlorine deposition during combustion of chlorine-rich biomass", *Fuel*, 2005, **84**, 201–212.

[266] I. Aigner, C. Pfeifer and H. Hofbauer, "Co-gasification of coal and wood in a dual fluidized bed gasifier", *Fuel*, 2011, **90**, 2404–2412.

[267] K. Matsuoka, T. Shimbori, K. Kuramoto, H. Hatano and Y. Suzuki, "Steam reforming of woody biomass in a fluidized bed of iron oxide-impregnated porous alumina", *Energy & fuels*, 2006, **20**, 2727–2731.

[268] I. Samprón, F. Luis, F. García-Labiano, M. T. Izquierdo, A. Abad and J. Adánez, "Biomass Chemical Looping Gasification of pine wood using a synthetic Fe_2O_3/Al_2O_3 oxygen carrier in a continuous unit", *Bioresource Technology*, 2020, **316**, 123908.

[269] I. Ahmed and A. Gupta, "Kinetics of woodchips char gasification with steam and carbon dioxide", *Applied Energy*, 2011, **88**, 1613–1619.

[270] I. Sircar, A. Sane, W. Wang and J. P. Gore, "Experimental and modeling study of pinewood char gasification with CO_2", *Fuel*, 2014, **119**, 38–46.

[271] M. J. Dirbeba and J. Werkelin, in *Biomass, Biorefineries and Bioeconomy*, IntechOpen, 2022.

[272] D. Porbatzki, M. Stemmler and M. Müller, "Release of inorganic trace elements during gasification of wood, straw, and miscanthus", *Biomass and bioenergy*, 2011, **35**, S79–S86.

[273] P. Nanou, M. C. Carbo and J. H. Kiel, "Detailed mapping of the mass and energy balance of a continuous biomass torrefaction plant", *Biomass and Bioenergy*, 2016, **89**, 67–77.

[274] A. Janssen and M. Carbo, "Report on Requirements of End Users on Densified and Torrefied Materials, FP7 EU Project SECTOR, 2013 Dec", *Deliverable No. D*, **4**, 18.

[275] D. Thrän, J. Witt, K. Schaubach, J. Kiel, M. Carbo, J. Maier, C. Ndibe, J. Koppejan, E. Alakangas, S. Majer et al., "Moving torrefaction towards market introduction–Technical improvements and economic-environmental assessment along the overall torrefaction supply chain through the SECTOR project", *Biomass and bioenergy*, 2016, **89**, 184–200.

[276] T. Tobin, R. Gustafson, R. Bura and H. L. Gough, "Integration of wastewater treatment into process design of lignocellulosic biorefineries for improved economic viability", *Biotechnology for biofuels*, 2020, **13**, 1–16.

[277] A. Siciliano, C. Limonti, G. M. Curcio and R. Molinari, "Advances in struvite precipitation technologies for nutrients removal and recovery from aqueous waste and wastewater", *Sustainability*, 2020, **12**, 7538.

[278] H. Wu, M. N. Pedersen, J. B. Jespersen, M. Aho, J. Roppo, F. J. Frandsen and P. Glarborg, "Modeling the use of sulfate additives for potassium chloride destruction in biomass combustion", *Energy & fuels*, 2014, **28**, 199–207.

[279] S. Cheah, S. C. Malone and C. J. Feik, "Speciation of sulfur in biochar produced from pyrolysis and gasification of oak and corn stover", *Environmental science & technology*, 2014, **48**, 8474–8480.

[280] D. C. Dayton, R. J. French and T. A. Milne, "Direct observation of alkali vapor release during biomass combustion and gasification. 1. Application of molecular beam/mass spectrometry to switchgrass combustion", *Energy & Fuels*, 1995, **9**, 855–865.

[281] D. Dayton, B. Jenkins, S. Turn, R. Bakker, R. Williams, D. Belle-Oudry and L. Hill, "Release of inorganic constituents from leached biomass during thermal conversion", *Energy & Fuels*, 1999, **13**, 860–870.

[282] R. G. Beerkens, "Modeling the kinetics of volatilization from glass melts", *Journal of the American Ceramic Society*, 2001, **84**, 1952–1960.

[283] S. Cheah, D. L. Carpenter and K. A. Magrini-Bair, "Review of mid-to high-temperature sulfur sorbents for desulfurization of biomass-and coal-derived syngas", *Energy & Fuels*, 2009, **23**, 5291–5307.

[284] D. L. Carpenter, R. L. Bain, R. E. Davis, A. Dutta, C. J. Feik, K. R. Gaston, W. Jablonski, S. D. Phillips and M. R. Nimlos, "Pilot-scale gasification of corn stover, switchgrass, wheat straw, and wood: 1. Parametric study and comparison with literature", *Industrial & Engineering Chemistry Research*, 2010, **49**, 1859–1871.

[285] X. Ma, X. Huang, T. Feng, M. Mu and X. Hu, "A DFT study on the mechanism of HCl and CO_2 capture by CaO", *Reaction Chemistry & Engineering*, 2022.

[286] X. Wang, Y. Liu, H. Tan, L. Ma and T. Xu, "Mechanism research on the development of ash deposits on the heating surface of biomass furnaces", *Industrial & engineering chemistry research*, 2012, **51**, 12984–12992.

[287] Y. Lv, Y. Niu, G. Wang, L. Xu, Y. Lei, S. Hui and D. Wang, "Experimental and kinetic studies on ash fusion behavior: a high-precision acquisition method for ash fusion temperatures", *Asia-Pacific Journal of Chemical Engineering*, 2021, **16**, e2644.

[288] X. Yao, H. Zhou, K. Xu, Q. Xu and L. Li, "Investigation on the fusion characterization and melting kinetics of ashes from co-firing of anthracite and pine sawdust", *Renewable Energy*, 2020, **145**, 835–846.

[289] A. W. Coats and J. Redfern, "Kinetic parameters from thermogravimetric data", *Nature*, 1964, **201**, 68–69.

[290] J. Cai and L. Bi, "Precision of the Coats and Redfern method for the determination of the activation energy without neglecting the low-temperature end of the temperature integral", *Energy & Fuels*, 2008, **22**, 2172–2174.

[291] Y. Niu, H. Tan et al., "Ash-related issues during biomass combustion: Alkali-induced slagging, silicate melt-induced slagging (ash fusion), agglomeration, corrosion, ash utilization, and related countermeasures", *Progress in Energy and Combustion Science*, 2016, **52**, 1–61.

[292] P. Glarborg and P. Marshall, "Mechanism and modeling of the formation of gaseous alkali sulfates", *Combustion and Flame*, 2005, **141**, 22–39.

[293] H. Kassman, M. Broström, M. Berg and L.-E. Åmand, "Measures to reduce chlorine in deposits: Application in a large-scale circulating fluidised bed boiler firing biomass", *Fuel*, 2011, **90**, 1325–1334.

[294] R. Saidur, E. Abdelaziz, A. Demirbas, M. Hossain and S. Mekhilef, "A review on biomass as a fuel for boilers", *Renewable and sustainable energy reviews*, 2011, **15**, 2262–2289.

[295] P.-W. Li and C.-S. Chyang, "A comprehensive study on NOx emission and fuel nitrogen conversion of solid biomass in bubbling fluidized beds under staged combustion", *Journal of the Energy Institute*, 2020, **93**, 324–334.

[296] O. Karlström, E. Vainio, M. Engblom, A. Brink and M. Hupa, "Effect of air staging on NOx emissions in biomass combustion in a bubbling fluidized bed", *Fuel*, 2022, **330**, 125565.

Acknowledgements

While I am writing this section of the thesis – the very last one, it is already after midnight and I cannot help to think my short but incredible journey in this wonderful research community. Life is like a road. Sometimes it can be tumultuous. But it is always taking you somewhere. I took to the open road, healthy, free, the uncharted territory before me. I have reached my destination and now is the perfect time to pursue a new beginning and embrace a new perspective towards the future life.

However, this work would not have been possible without the help of many individuals around this research community. I would like to express my most heartfelt gratitude to my supervisor, Priv.-Doz. Dr. Michael Müller, who has been so generous with his time, support, and advice – not forgetting about his excellent sense for humour! I feel so incredibly lucky to have had the opportunity to study and work with you. I am deeply grateful to Univ.-Prof. Dr.-Ing. habil. Manfred Christian Wirsum for serving as my second academic examiner. His valuable feedback and insightful suggestions significantly enhanced the quality and impact of this thesis prior to its publication.

I would like to express my gratitude to all CLARA project partners from all over Europe for making this exciting project happen. I deeply appreciated the excellent working atmosphere, the help and assistance that you have provided to me. It was my pleasure to work in this community. The research of this thesis was funded and supported by the Horizon 2020 Framework program of the European Union, CLARA project, G.A. 817841.

I have received great support from my external mentor D.Sc. Patrik Yrjas, Assoc. Prof. Oskar Karlström, Daniel Schmid (PhD), Luis Bezerra, Tor Laurén, colleagues and friends back in Finland, which have made one part of my thesis once again substantial. Thank you to all members and the board of HITEC, the graduate school of energy and climate research at Forschungszentrum Jülich for expanding my network and enlarging my soft skills.

I would like to extend my heartfelt thanks to Dr. Elena Yazhenskikh for her invaluable support with the thermochemical predictions using FactSage. Without your guidance and expertise, I would have struggled to carry out all those model calculations. Thank you for your help and teaching.

With many thanks for the technical and IT support service to Manuel Hucko, Marita Offerman, Monika Marx, Max Borzikow, Christoph Bütow, Ralf Küppers, and Inge Dreger.

From the bottom of my heart I would like to say big thank you to my close friends Tuan Vo, Dr. Xiaoqiang Li, and Nobuhisa Ata for all those unforgettable moments, excellent and inspiring ideas, and coffee time chats.

Thank you also to all my fantastic colleagues and friends from the IMD-1 (Thermochemistry) group, as well as the past group members who have helped me along the way. I also would like to say special thank you to my office colleagues Dr. Ursula Gude and Marcel Siepmann, your easygoing nature has helped me to calm down when I was in trouble. Thank you all for being there for me, and for making work such a happy place to be.

Last but not least, I cannot name everything my parents have done for me, nor can I express in words how much gratitude I feel to them. And so I would like to offer heartfelt thanks to my grandfathers, André Fauré and Eberhard Steudt, who have been both a huge blessing and genuine influence on my life. You were a great role model for me, this work is dedicated to you.